Modelling and image processing of microtubule dynamics and organisation

Chris Rookyard

Supervisors:

Dr. Barry-John Theobald

Dr. Mette Mogensen

Dr. Scott Grandison

A thesis submitted for the degree of

Doctor of Philosophy

October 2014

University of East Anglia

School of Computing Sciences

Acknowledgements

First of all, thanks to my supervisors, Barry-John Theobald and Mette Mogensen, for their guidance and willingness to discuss and critique the work presented in this thesis. I am grateful to Barry for agreeing to supervise the latter half of my PhD. Thanks also to my previous supervisor, Scott Grandison, with whom I enjoyed many idea-bouncing discussions that started off the work presented here. More thanks to Richard Morris, for smoothing over the transition between supervisors, and also to Andrew Mayes and Simon Turner, who have both given up a lot of their time to assist with various projects that have not made it into this thesis, but which helped with the development of my work.

I am very grateful to other members of the Mogensen lab for always being happy to talk over ideas and help in the lab. Thanks especially to Jonathan Gadsby for his support at the beginning of my PhD, and also to Debbie Goldspink for collaborating on some of the work in this thesis, and providing images for analysis.

Thanks to my family; to Charlie, whose unfailing support combined with just the right amount of impatience is a fool-proof recipe for getting a thesis written; this work could not have happened without it, and to Arthur and Rufus for their smiles and important critical discussion of my work.

Thanks to Mum and Dad for their continual help and interest in my work, and for teaching me so much.

Finally, thanks to everybody else who has helped!

Chris Rookyard,

17th October, 2014

Abstract

Microtubules, dynamic protein polymers, form networks that are essential for intracellular organisation. Involved in many cellular processes that are vital in development and homeostasis, improper regulation of the microtubule network is implicated in various diseases. This work addresses the relationships between microtubule dynamics and organisation, using image processing and modelling, focussing on two features of microtubule organisation: radiality and alignment. The hypothesis that radiality results from modulation of dynamics at the cell periphery was tested. Firstly, cells in which the small GTPase Rac1 was inhibited were used as a model for perturbed radiality. Measurements of microtubule dynamics in central and peripheral regions showed that Rac1 inhibition alters microtubule dynamics and the orientation of their growth at the cell periphery. Further investigation was carried out with a simple 1-dimensional, two-area dynamics model, which confirmed that a two-area dynamics system is sufficient to target microtubules to a given length. The propensity to grow of any given dynamics parameters is a major determinant of the accuracy of length targeting, while the extent of pausing and the average length have a modulatory effect on accuracy. Simulation of measured dynamics indicated that two-area dynamics may contribute to radiality in reality, but that this mechanism may work in concert with other cortex-specific processes. The alignment of microtubules was quantified with a new application of the Fourier transform. Depletion of +TIP protein EB2 produced highly-aligned microtubules, and inhibition of formins rescued this phenotype. Inhibition of Rac1 produced less-aligned microtubules in otherwise unperturbed cells, while in EB2-depleted cells, microtubules were further aligned. The method was also used to quantify alignment in plant microtubule arrays. This work presents a set of analyses that test ideas as to how the microtubule network is organised, and highlight interesting relationships between dynamics and organisation that will yield exciting future investigation.

Contents

Terms/abbreviations list

Biased transition frequency. Where the transition frequency is calculated using all of the time spend in the relevant phase.

Corrected transition frequency. Where the transition frequency is calculated using only the time in the relevant phase that precedes the transition in question.

F_{cat}. The catastrophe frequency – see transition frequency.

F_{g2p}. The grow-to-pause frequency – see transition frequency.

F_{p2g}. The pause-to-grow frequency – see transition frequency.

F_{p2s}. The pause-to-shrink frequency – see transition frequency.

F_{res}. The rescue frequency – see transition frequency.

F_{s2p}. The shrink-to-pause frequency – see transition frequency.

Growth distance. The average distance covered in the growth phase of pooled microtubule tracks.

Growth speed (V_g). The average speed of growth phases of pooled microtubule tracks.

Growth time. The average time spent in the growth phase of pooled microtubule tracks.

MTOC. Microtubule organising centre. Microtubules are polymerised from an MTOC, and often, minus ends are anchored here.

Pause time. The average time spent in the pause phase of pooled microtubule tracks.

SBC. Spatial boundary condition. Refers to physical obstacles that constrain or influence microtubule growth.

Shrinking distance. The average distance covered in the shrinking phase of pooled microtubule tracks.

Shrinking speed (V_s). The average speed of shrinking phases of pooled microtubule tracks.

Shrinking time. The average time spent in the shrinking phase of pooled microtubule tracks.

Transition frequency. Calculated as the number of transitions over the time spent in the relevant phase.

V_g. See growth speed.

V_s. See shrinking speed.

Chapter 1

Introduction

A. MICROTUBULE DYNAMICS AND ORGANSIATION

a. Introduction to microtubules

Every cell in our bodies contains microtubules, as do the cells in other animals, in plants and fungi, and there are similar structures in bacteria. *Why? What are microtubules?* An individual microtubule is a polymer of the protein tubulin: a hollow cylinder of 25 nm in diameter, and on the order of tens of microns in length; in a typical cell, there can be hundreds of microtubules. What do microtubules do? In general, they contribute to the structure of the cell, though the exact nature of the job depends on the organism, the type of cell, and the particular activity of that cell at any given moment. Microtubules are not only essential for normal development and homeostasis, but if not regulated properly, they can also contribute to disease; indeed, many therapies for cancer act on microtubules.

Along with actin filaments and intermediate filaments, microtubules form the eukaryotic cell cytoskeleton. At 25 nm in external diameter, microtubules are the largest of the three cytoskeletal constituents, with intermediate filaments at approximately 10 nm and actin filaments at 5-9 nm (Alberts, 2008). Both actin and intermediate filaments help to impart rigidity to the cell; actin filaments form what is known as the cortex, a thin layer just beneath the plasma membrane, while some intermediate filaments perform a similar role beneath the nuclear lamina, and others form networks to give mechanical strength to tissues (Alberts, 2008). Within this cytoskeletal network, microtubules are fundamental to the structuring, and thus the correct functioning, of the cell. Their best-known role is the creation of the mitotic spindle, a miracle of molecular engineering whereupon chromosomes are segregated, but away from cell division, microtubules also provide tracks for transport of molecules and organelles, are involved in cell shape and migration, and sensing physical stimuli.

Polymerisation of tubulin occurs from monomers which diffuse freely in the cytosol, forming hollow cylinders of length on the order of micrometres, though this is not fixed. In the cell, the many hundreds of microtubules are arranged by an organelle called the microtubule organising centre (MTOC), and in animal cells, the MTOC is the centrosome. A typical microtubule arrangement is known as the radial array: microtubules are anchored at one end to the centrosome, usually in the vicinity of the nucleus, and extend out towards the cell periphery, probing the intracellular space. In many circumstances, which include cell migration and changes in cell morphology, the microtubule array must be re-organised so as to serve certain cellular requirements. Such re-organisations are effected through a special property of microtubules, known as dynamic instability.

b. Overview of thesis

This thesis is for the most part concerned with microtubules in animal cells; specifically, how microtubule dynamics are controlled so as to generate proper organisation of the microtubule network. In all of the roles of microtubules described above, the appropriate organisation of

microtubules, in relation to one another and to certain cellular structures, is requisite for proper function. Understanding this organisation, how it is generated, maintained, and how it can be measured, is the aim of this thesis. To do this, a specific example of microtubule organisation is used: the radial array, and this is elaborated upon in the next chapter. There is also a very small part of this work given to plant microtubules; here, microtubules are involved in specification of the physical properties of cells, vital for development.

B. THESIS CHAPTERS

a. Overview

There are four chapters containing original research; these are chapters 3 to 6, while before this, in chapter 2, the introduction to microtubule biology continues with a literature review of microtubule dynamics and organisation. Thus chapter 2 serves to illustrate the background to the research that follows in subsequent chapters: what we know about microtubule dynamics and how that relates to organisation of the microtubule network, how it is modulated, and what we still do not know about microtubule dynamics-organisation relationships.

Although the research in chapters 3-6 is united by the common themes introduced above, there are various methodologies, and within each, different aspects of microtubule organisation are considered. Thus, there is a discussion of the findings at the end of each chapter, and after the research chapters, in chapter 7, a short summary discussion is given, along with some conclusions and a consideration of future work. Briefly, a summary of each of the research chapters is given below.

b. Chapter 3: Measuring microtubule dynamics in a radial array

As was mentioned above, the radial array, a common type of microtubule network organisation in animal cells, is taken as a reference organisation throughout the whole thesis. In this chapter, the dynamics of microtubules are measured, involving use of previously published image processing software, and original extensions to analyse dynamics further. The aim of this chapter is to understand how dynamics are controlled to maintain the "radiality" of the radial array; specifically, to test the hypothesis that microtubule dynamics are modulated at the cell periphery to maintain radiality. Thus, unperturbed cells that exhibit a radial array, and cells in which the radial array is disrupted by inhibition of the small GTPase Rac1, are subject to dynamics measurements. I find that inhibition of Rac1 affects both microtubule dynamics and the orientation of their growth, and that Rac1-inhibited microtubules take shallower growth trajectories relative to the cell cortex. The results of this work hint at possible reasons for loss of radiality in the cortex-specific dynamics framework, such as a lower proportion of time spent in pause in Rac1-inhibited microtubule networks relative to control microtubules.

c. Chapter 4: Modelling microtubules and radiality

In this chapter, a model of microtubule dynamics is used to try to elucidate what the combinations of dynamics must be if microtubules are to be organised in a radial array. The

work is based on the idea that microtubule dynamics are modulated in some way at the periphery of the cell so as to maintain radiality, which has some empirical support (discussed further in the next chapter). Thus, a simple model whereby microtubules grow in two areas: an inner and outer area, each with different dynamics, is implemented. I find here that the two-area dynamics model is sufficient to target microtubules to a target length, and thus could be a mechanism of radiality.

The tendency towards growth of any dynamics set is a major determinant of the accuracy of such length targeting. Characterising this propensity for growth with the random walk analogy of drift leads to the introduction of "drift space", which acts as a tool with which we can assess the likelihood of any given combinations of dynamics being good microtubule length targeting strategies. Furthermore, introduction of pausing in the model demonstrated that it if in the outer area, it enhances targeting, but if in the inner area, it reduces targeting accuracy. Likewise, the theoretical average length, another random walk analogy, has area-specific effects: increases in the inner area give better targeting accuracy, while increases in the outer area worsen targeting accuracy.

d. Chapter 5: Comparing and modelling measured microtubule dynamics

Here, the work from chapters 3 and 4 is united to try to understand how the measured dynamics contribute to the organisation of the radial array. The dynamics from chapter 3 are first compared to previously reported measurements of microtubule dynamics, and then they are considered in the context of the modelling from chapter 4, and additional modelling is implemented to better understand dynamics and radiality. Plotting the measured dynamics sets in drift space indicated that the control condition should have better microtubule length targeting, and thus more radial microtubules, but its location in drift space suggest that it may act in concert with other cell cortex-specific microtubule targeting mechanisms.

e. Chapter 6: Frequency-based quantification of microtubule organisation

Where in previous chapters, attention was given to microtubule organisation in the context of interactions between microtubules and the periphery of the cell, in this chapter, other properties of microtubule organisation, the alignment between microtubules and the orientation of microtubules, are considered. To quantify these properties, a new method based on analysing the frequencies in images of the microtubule network is developed, involving extensive characterisation of how the method behaves with synthetic images. The new method, called "MtFT", is then applied to real biological problems, some previously studied, some novel, and in one case, in plant cells, and indicates interesting and relatively unexplored mechanisms of microtubule alignment.

Firstly, depletion of the +TIP protein (see next chapter for more details of +TIP proteins) EB2 produced better-aligned microtubules, in agreement with previous measures made manually. Also in agreement with those measurements, inhibition of formins, which promote actin polymerisation and also interact with microtubules, returned microtubule networks to the less-aligned state. Interestingly, inhibition of Rac1 gave less-aligned microtubules, in agreement with chapter 3 results, but simultaneous inhibition and depletion of Rac1 and EB2,

respectively, produced networks with enhanced alignment relative to the EB2-depleted-only case.

Finally, two plant cell types with differing microtubule alignment, petiole (well-aligned) and pavement (disordered) cells, were analysed in wild-type and two mutant backgrounds. MtFT detected the cell type-specific differences, and quantified a decrease in alignment in a katanin (a microtubule severing protein) mutant in both cell types, and an increase in alignment in a spiral 2 mutant in both cell types. These results are consistent with the postulated roles and interplay between katanin and spiral 2: katanin severs microtubules at crossover sites, allowing them to align with one another, while spiral 2 protects these sites from severing by katanin, leading to a disordered microtubule network.

REFERENCES

Alberts, B. 2008. Molecular Biology of the Cell: Reference edition. Garland Science.

Chapter 2

Background review

A. MICROTUBULE DYNAMICS

I. Fundamentals of microtubule dynamic instability

a. History

The term "microtubule" was first introduced by Slautterback (1963) and Ledbetter and Porter (1963), at a time when, although fibril-like structures, which were indeed microtubules, had been observed in many instances, it was not clear exactly what they were and furthermore, whether they were the same in each instance. Studying electron micrographs of the cortices of plant cells (Ledbetter and Porter, 1963) and the Cnidarian organism Hydra (*Hydra oligactis* and *Hydra littoralis*), it became evident that microtubules were a common constituent of animal and plant cells. Following on from this, further electron microscopy was used to determine that microtubules were constructed from "13 subunits in the wall of the tubule" (Ledbetter and Porter, 1964), which we know now as the 13 protofilament structure of the microtubule (more of which follows below).

Once microtubules had been described, the matter of determining their constituent protein was addressed. At the time it was known that colchicine, isolated from plants and long-used to treat gout, destroyed the mitotic spindle, and also had an array of other effects. Using radioactive labelling of colchicine to identify its target within cells, Borisy and Taylor (1967a) found a correlation between binding activity and the presence of tubulin; thus, dividing cells and brain cells had high binding activity, while cell extracts in which microtubules were not present had low activity. Next, Borisy and Taylor (1967b) isolated microtubules from the mitotic spindle of the sea urchin, and demonstrated that they were responsible for the binding of colchicine to the spindle. They then went on to characterise the protein, and later, Mohri (1968) gave it the name "tubulin".

Following on from this, it was assumed that microtubules obeyed standard polymer kinetic principles (Oosawa and Asakura, 1975) in their growth and shrinkage, by addition and loss of tubulin. In this framework, a microtubule population would be uniform, so that all microtubules would either be growing or shrinking, and this assumption underlay the interpretation of previous experimental results. For example, continual uptake of a radioactively labelled-tubulin from solution into the microtubule polymer, whilst total polymer remained constant, was taken as evidence of net assembly and disassembly being confined to opposite ends of individual microtubules (Cote and Borisy, 1981; Margolis and Wilson, 1978).

Although this interpretation is valid in special cases of microtubule behaviour, these data can also be explained by the existence of a two-phase population, in that the depolymerisation and subsequent regrowth can account for constant label incorporation, and indeed, this behaviour was documented in two seminal papers by Mitchison and Kirschner (1984a;

1984b). Termed "dynamic instability", it was not directly observed until 2 years later by Horio and Hotani (1986). These studies showed that a microtubule population, whether centrosome-bound (Mitchison and Kirschner, 1984b) or free (Mitchison and Kirschner, 1984a) could consist of two sub-populations, some growing, some shrinking; the ratio between them ultimately depending on the concentration of free tubulin. The co-existence of these growth and shrinking phases, which occur through addition and loss of tubulin monomers, respectively, and infrequent transitions between them, are the main tenets of dynamic instability (Kirschner and Mitchison, 1986).

Subsequent work has shown that dynamic instability is the main mechanism of microtubule assembly in the cell, and much effort has been dedicated to understanding and quantifying dynamic instability and the factors that influence the process (Desai and Mitchison, 1997). This body of work has demonstrated that, not only is dynamic instability an intrinsic feature of the microtubule that arises from its structure and biochemistry, it is the underlying mechanism for the organisation and manipulation of the microtubule network.

b. Microtubule structure

Structural studies of the microtubule had yielded much information before the time dynamic instability was proposed (Stephens, 1970), yet with continual improvement of conventional techniques (Meurer-Grob et al., 2001) and utilisation of newer technology (Wu et al., 2012), present-day studies still add to our knowledge. As has already been discussed, the basic unit of the microtubule is the protein tubulin (Mohri, 1968), which is a heterodimer of α- and β-tubulin (Bryan and Wilson, 1971). Tubulin molecules assemble end-to-end to make a protofilament, a linear polymer of tubulin, so that α- and β-tubulin alternate along its length. Note that, in the context of the microtubule assembly and disassembly, the tubulin heterodimer is often referred to simply as a subunit. In the most common microtubule structure, 13 protofilaments associate laterally (Amos and Klug, 1974), known as the microtubule lattice, and this forms the hollow cylindrical structure recognised as the microtubule (Alberts, 2008) (fig. 1).

In the microtubule lattice, neighbouring protofilaments do not line up subunit-against-subunit, but are instead offset with respect to one another by a distance of approximately 0.9 nm along the microtubule axis (Amos and Klug, 1974; Wade, 2009). It is apparent that there are two possibilities with regard to the arrangement of the two types of tubulin in adjacent protofilaments: in one configuration, different tubulins are in contact with one another, while in the other arrangement, similar tubulins interact. These are known as "A-type" and "B-type" lattices, respectively, named after the A- and B-tubules of the flagellum in which they were thought to occur (Amos and Klug, 1974; Song and Mandelkow, 1993) (fig. 2). Investigations based on microtubule binding of the motor domain of kinesin proteins, which transport cargo around the cell by moving along microtubules, have shown that microtubules have a B-type lattice (Song and Mandelkow, 1993).

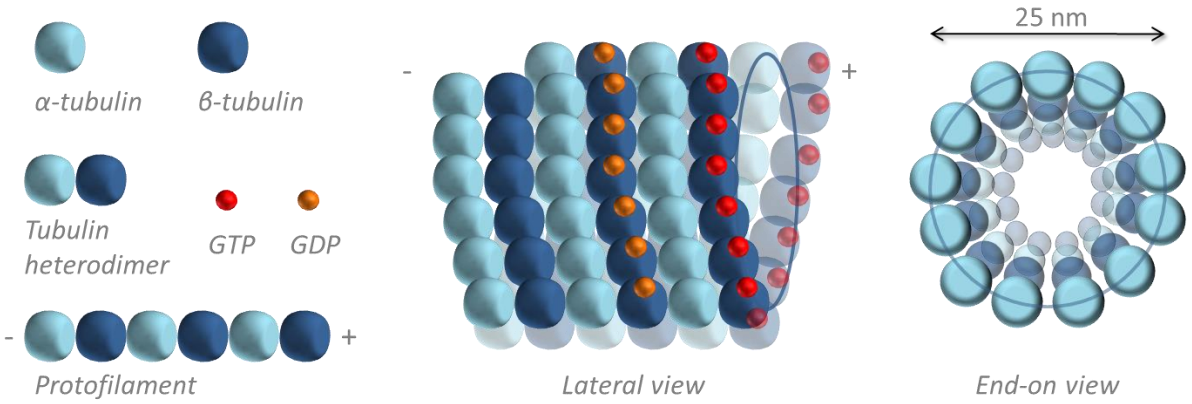

Figure 1. Structure and components of the microtubule. α- and β-tubulin form the tubulin heterodimer, or "subunit", and these associate end-to-end to form a protofilament. 13 protofilaments interact laterally to form the hollow cylindrical microtubule structure, which is 25 nm in external diameter. All protfilaments are oriented in the same direction with regard to their tubulin subunits; this confers polarity to the microtubule. The end with β-tubulin exposed is the plus end, and the other end, where α-tubulin is the terminal subunit, is the minus end. Though both α- and β-tubulin can bind GTP, only β-tubulin hydrolyses this to GDP once it is incorporated into the microtubule.

Since the subunits in adjacent protofilaments are offset longitudinally, following either α- or β-tubulin from one protofilament to the next actually draws a helix along the microtubule axis. The lengthwise shift combined with the number of protofilaments means that, at regular points along the path of this helix, there are discontinuities, where different tubulins contact (Song and Mandelkow, 1993) (fig 2). This discontinuity is commonly known as the microtubule "seam" (Song and Mandelkow, 1993; Wade, 2009). It is thought that the seam may act as a recognition site for microtubule-associated proteins (MAPs), and that it may be important in microtubule disassembly by providing a structural fault from which to effectively peel apart the lattice (Wade, 2009).

Although offset relative to one another, all protofilaments are oriented in the same manner with respect to tubulin subunits, and this confers polarity to the microtubule (Allen and Borisy, 1974). At one end, α-tubulin is the terminal subunit (Fan et al., 1996), referred to as the minus-end, and at the other, the final subunit is β-tubulin (Hirose et al., 1995; Mitchison, 1993), referred to as the plus end (fig. 1). In the cell, microtubules are anchored to the MTOC at the minus end, and the plus end explores the intracellular space (fig. 3). Hence growth and shrinkage occur predominantly at the plus end *in vivo*; in *in vitro* assays, the minus end does exhibit dynamic instability but with slower kinetics compared to the plus end (Farrell and Jordan, 1982; Margolis and Wilson, 1978; Mitchison and Kirschner, 1984a; Walker et al., 1988).

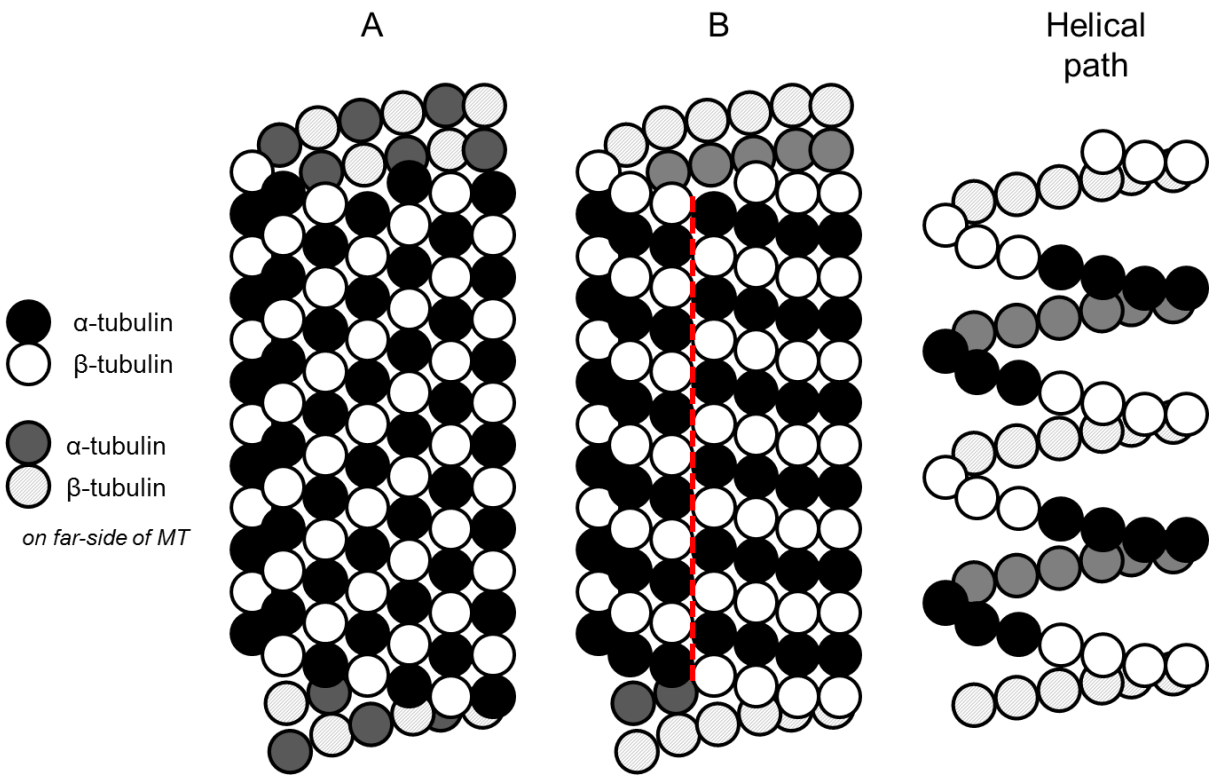

Figure 2. Possible arrangements of protofilaments in the microtubule (MT). In the A-type lattice (A), α- and β-tubulin interact between adjacent protofilaments, whereas in the B-type lattice (B), same-species interactions occur. The B-type lattice is the conventional microtubule structure (see text for details), and there is a discontinuity, known as the seam, where α- and β-tubulin are adjacent to one another (dashed red line). Following the path of subunits across protofilaments draws a helical structure (helical path), shown here for the B-type lattice. Subunits on the far side of the cylindrical MT structure are shown in grey (α-tubulin) and patterned white/grey (β-tubulin). This figure is based on Desai and Mitchison (1997), figure 1.

So the structure of the microtubule provides the physical context for dynamic instability, but to understand what governs the occurrences of these phase transitions, we must also understand the biochemistry of microtubule assembly.

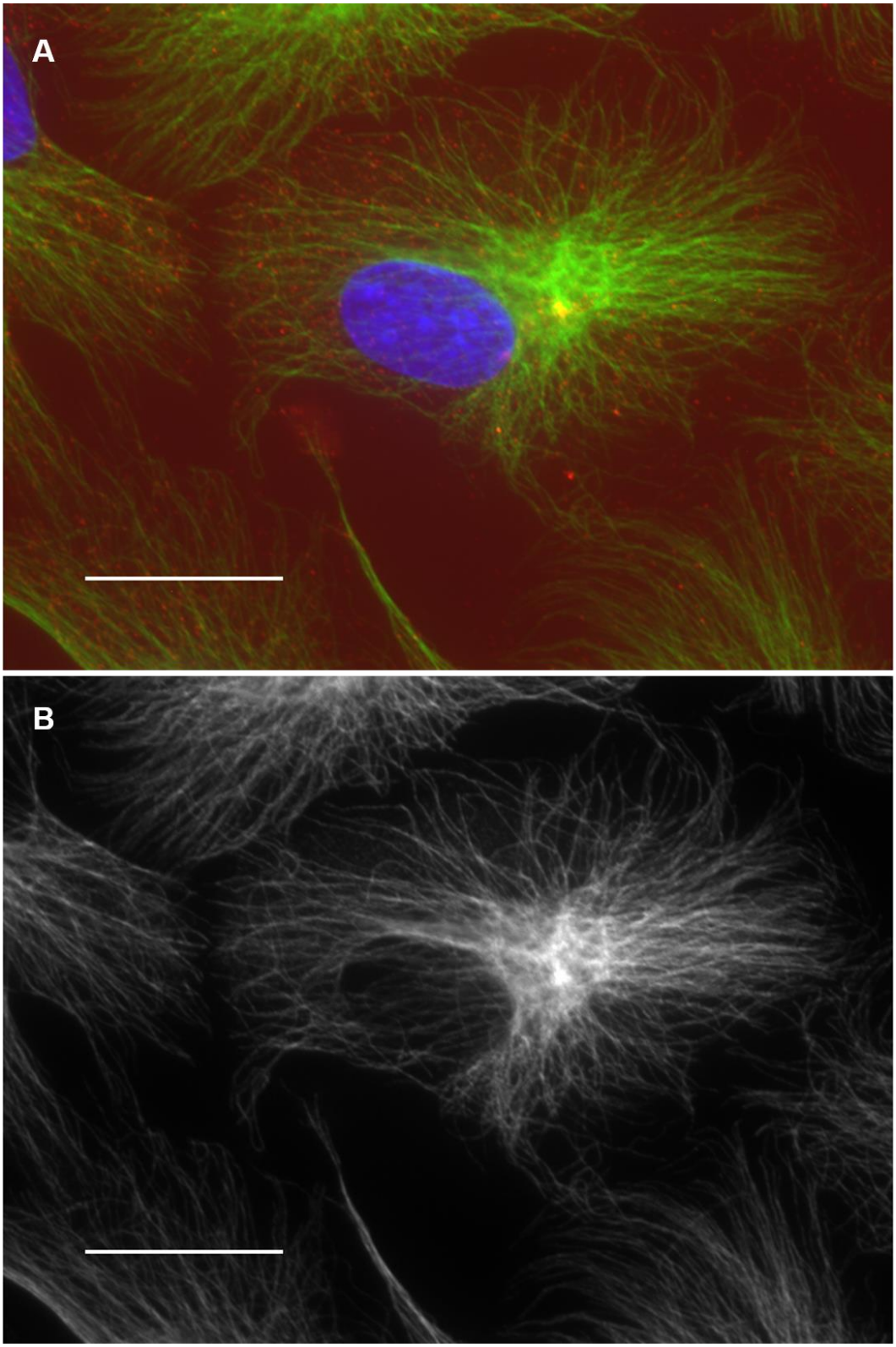

Figure 3. The microtubule radial array, visualised by immunofluorescence microscopy. In A, microtubules (green) radiate from the centrosome (red channel, visible as yellow spot at centre of main cell) to probe intracellular space. Nuclei are also labelled in blue. In B, a greyscale image of just the microtubule cytoskeleton is shown. Plus ends are located near the cell periphery, while minus ends are anchored at the centrosome. Scale bar 20 μm.

c. Microtubule biochemistry: introducing the GTP cap

A common feature of microtubules and actin filaments is their ability to bind and hydrolyse nucleotide triphosphate (NTP) molecules (Carlier, 1991). In the case of actin, this is adenosine triphosphate (ATP), while microtubules interact with guanosine triphosphate (GTP). Both α- and β-tubulin can bind one molecule of GTP, and in the cytosol, GTP-binding occurs quickly so that essentially all free tubulin is GTP-bound. However, when incorporated into the microtubule lattice, β-tubulin, but not α-tubulin, can hydrolyse GTP to guanosine diphosphate (GDP) (David-Pfeuty et al., 1977; MacNeal and Purich, 1978; Spiegelman et al., 1977; Weisenberg et al., 1976). For this reason, the GTP-binding sites on α- and β-tubulin are known as the N- (for non-exchangeable) and E-sites (exchangeable), respectively. Initially, observations of a lag between polymerisation and GTP hydrolysis (Carlier and Pantaloni, 1981) lead to the proposition of the "GTP cap" model, whereby this kinetic disparity leads to the accumulation of GTP-bound β-tubulin at the plus-end (Carlier and Pantaloni, 1981; Kirschner and Mitchison, 1986; Mitchison and Kirschner, 1984b).

The GTP cap was proposed as the distinguishing feature between the two phases of the microtubule, and that it acted to stabilise the growing plus end (Mitchison and Kirschner, 1984b). The theory of this stabilising effect is that the GTP cap is effectively a structural support, helping to maintain protofilament interactions by keeping them straight, but the mechanism for this has not been elucidated (Maurer et al., 2012). Indeed, GDP-bound protofilaments take on a curved conformation (Hyman et al., 1995; Mandelkow et al., 1991; Melki et al., 1989; Simon and Salmon, 1990) which would destabilise the microtubule and consequently, cause a transition to the shrinking phase (fig. 4). So the stability of the microtubule, and therefore its current phase, is dependent on the relative rates of polymerisation and GTP hydrolysis: in some cases, hydrolysis "catches up" with polymerisation, the GTP cap is lost, and shrinkage occurs. For example, free tubulin concentration could be low enough so as to limit growth, or the plus end may be prevented from growing by a boundary.

So the GTP cap model provided a convincing account of the events occurring at the microtubule plus end, and was consistent with macroscopic observations of microtubule dynamics. For example, shearing of microtubules along their length resulted in immediate depolymerisation (Mitchison and Kirschner, 1984b), suggesting a stabilising structure only present toward the plus end. Furthermore, the GTP cap model was supported by theoretical analyses (Hill and Chen, 1984). However, the model was based only on indirect observations, and for a long period following its proposition, there was a long period of uncertainty over the existence and size of the GTP cap.

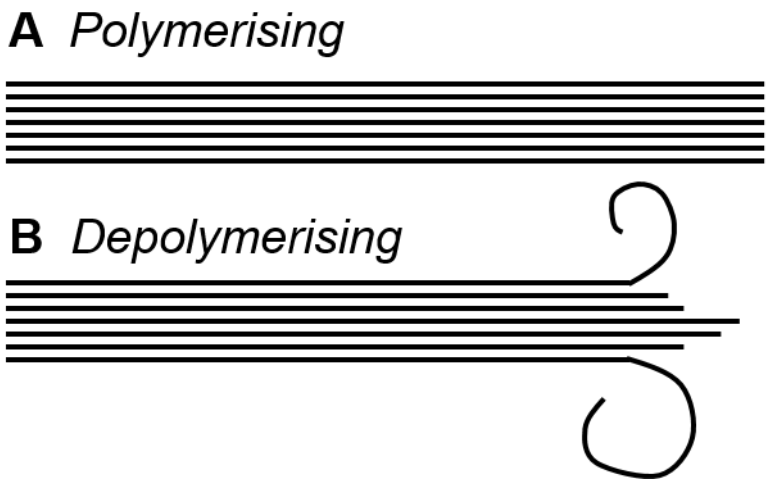

Figure 4. Differences in microtubule structure with phase. Microtubules undergoing growth (A, polymerisation) have straight protofilaments, whereas microtubules in the shrinking phase (B, depolymerisation) have curled protofilaments that give a "ram's horns" appearance.

d. Evidence for the GTP cap

Obtaining direct evidence to support the GTP cap model proved difficult. The GTP cap, not only a temporally dynamic structure, could also potentially be as small as one layer of tubulin subunits (i.e., 8 nm deep) (reviewed in Desai and Mitchison (1997)). Recent work using end-binding (EB) proteins, a family of MAPs that bind to the microtubule plus end, has clarified the issue.

Firstly, three studies verified that EB proteins bound to microtubules according to the nucleotide state of the microtubule. Zanic et al. (2009) and Maurer et al. (2011) demonstrated that EB proteins (in the former, EB1, the most-studied EB protein, and in the latter, EB1 and Mal3, a yeast EB protein) preferentially bind to microtubules bound to slowly hydrolysable analogues of GTP over those with bound GDP. These studies provided evidence that the mechanism for the tip-tracking behaviour of the EB proteins is related to the bound-nucleotide state of tubulin, and later, Maurer et al. (2012) provided a high-resolution reconstruction of the Mal3-microtubule interaction, suggesting that EB proteins recognise a GTP-hydrolysis-dependent tubulin conformation.

The finding that EB proteins recognise the bound nucleotide state of tubulin was a big step towards verifying the existence of the GTP cap. These findings were then used with fluorescence recovery after photobleaching (FRAP) to estimate its size. Seetapun et al. (2012) estimate the cap to be around 750 tubulin subunits, corresponding to approximately 60 subunit-layers. This figure is far greater than previous estimates, which were as small as a single layer of subunits (reviewed in Desai and Mitchison (1997)), but it is supported by measurements using optical tweezers that indicate an extended GTP cap (Schek et al., 2007).

Interestingly, the manner in which Mal3 binds GTP-bound microtubules, bridging protofilaments, suggests that they act to stabilise the lattice (Maurer et al., 2012), though whether this is in addition to the straightening effect attributed to GTP, or it is in fact the sole

mechanism for stabilisation, is unknown. Note that the latter would mean that GTP cap regions would have no intrinsic stability; they would need to permanently bind EB proteins, or perhaps other MAPs with similar functions, in order to stabilise the microtubule end.

Understanding the nature of the GTP cap is further complicated by taking into consideration the discrete steps of GTP hydrolysis and the possibility of further tubulin conformational changes as a result of the reaction (Brouhard and Sept, 2012). On the microtubule lattice, GTP hydrolysis has a minimum of two stages: first is the actual hydrolysis event, which results in GDP and phosphate, or GDP-Pi, and the second stage is phosphate release. So this raises the possibility of 3 domains in the lattice: GTP-bound, GDP-Pi-bound, and GDP-bound. The precise nature of the GTP cap is an active area of research; fortunately, given the recent EB protein data, we can be more confident of its existence. These data, around 30 years later, lend support to the original proposals of the GTP cap model and that it has a stabilising effect at the microtubule plus end (Carlier and Pantaloni, 1981; Mitchison and Kirschner, 1984b).

e. Consequences of the GTP cap

The initial lack of direct evidence for the GTP cap did not inhibit analyses and of the effects such a structure would have on the properties of the microtubule population; moreover, these analyses leant support to the idea, even necessitating the need of the cap or a similar stabilising structure. Not only can the GTP cap account for the phase transitions of individual microtubules, it also has other important implications for microtubule behaviour, especially *in vivo* (Kirschner and Mitchison, 1986).

Perhaps the best starting point to appreciate the effect of the GTP cap is with an analysis of conventional polymers, that is, polymers without the kinetic properties conferred by the GTP cap. Common ideas employed in the analysis of polymer formation are those of equilibrium and critical concentration; in a system where a polymer is forming from a pool of monomer, there is a critical concentration of monomer at which an equilibrium state is achieved, where the net exchange between polymer and monomer is zero. Types of polymer that follow this theory can be called equilibrium polymers (Kirschner and Mitchison, 1986).

Incorporation of monomer into polymer of length n can be simply defined by the monomer addition (or "on") and loss ("off") rates, α and α', respectively. The former interacts with the concentration of free monomer, C, while the latter is independent of it. For simplicity, reactions only at one end of the polymer are considered, and this is quite applicable to microtubules, since in the cell they are anchored at their minus ends to the MTOC. The net rate of assembly of a polymer, dn/dt, is thus the addition rate multiplied by the free monomer concentration, minus the monomer loss rate (after Kirschner and Mitchison (1986)):

$$\frac{dn}{dt} = \propto C - \propto', \quad (1).$$

The critical concentration is defined when the system is in equilibrium, that is, when there is no net assembly:

$$\frac{dn}{dt} = 0,$$

$$C_c = \propto'/\propto = K_{diss}, \quad (2),$$

where K_{diss} is the dissociation constant, and C_c is the critical concentration. Note that in the case of microtubules, there is constant exchange between monomer and polymer pools even at this equilibrium point. For this reason, equilibrium of the microtubule system is often referred to as steady-state, rather than equilibrium state.

The above theory assumes that there is a single reversible association reaction for incorporation of monomer into polymer, and thus that the free and polymer-incorporated monomer is of the same type. Since GTP hydrolysis essentially accompanies tubulin monomer addition to the microtubule lattice, the assembly reaction involves GTP-bound tubulin, while GDP-bound tubulin is participant in the disassembly reaction; GTP hydrolysis partitions the assembly and disassembly reactions, and the above assumptions do not hold (Kirschner and Mitchison, 1986). Thus, microtubules cannot be considered as simple equilibrium polymers.

The consequences of decoupling microtubule assembly and disassembly reactions are fundamental to the characteristics of the microtubule cytoskeleton (Kirschner and Mitchison, 1986) and its self-organising behaviour (Kirschner et al., 2000). Most importantly, it permits an extremely rapid disassembly reaction, that, were microtubules simple equilibrium polymers, would hinder assembly to the extent that very little polymer would form. So the rapid disassembly reaction allows high turnover of polymer without inhibiting the total level of polymer, and this is proposed to be advantageous to the cell since greater turnover gives better responsiveness should the network need to be re-arranged (Kirschner and Mitchison, 1986), as is often the case.

Thus, GTP hydrolysis frees the microtubule system from the confines of eqs. 1 and 2. As a demonstrative example, (Kirschner and Mitchison, 1986) discuss the sperm aster in the *Xenopus* egg, which we will expand upon here. Individual microtubules in the aster are up to 500 μm in length, yet they must depolymerise within 10 minutes (Ubbels et al., 1983), giving a net disassembly rate of 50 μm min^{-1}. Even at a very low tubulin concentration, this would demand a high α', and a low α. However, these values of α and α' would prohibit polymerisation to any sort of substantial length, not least the 500 μm that is observed. In order to adequately satisfy the requirements of long microtubules and fast depolymerisation, the concentration would have to be varied. Not only would this be a slow means of re-organising the network, since tubulin would either have to be sequestered or synthesised, it would also restrict the system to being homogenous; all microtubules would be polymerising or all microtubules would be depolymerising. By partitioning polymerisation and depolymerisation, this problem is solved.

Note that, for the assembly reaction, there is still an on- and off-rate; it is just that the disassembly reaction, which occurs as another microtubule phase, is not defined according to

the values of those rates; instead, it has its own off-rate. This is discussed further below (see "*Dynamic instability parameters*").

Other consequences arising from the non-equilibrium polymer properties of the microtubule include an increased sensitivity of the growing phase to the tubulin concentration (since it is not confined by a high off-rate) and it also permits growth of individual microtubules below the critical concentration. With regard to this point, it is an important point that the critical concentration refers to the bulk critical concentration, that is, on the whole, microtubule polymer will decrease below C_c, however, the stabilisation afforded by the GTP cap permits individual microtubules to continue growing (Kirschner and Mitchison, 1986).

f. Microtubule treadmilling

Clearly, there are differences in the bound nucleotide states between the two microtubule ends. Tubulin is GTP-bound at the plus-end and GDP-bound at the minus-end, which is usually anchored at the MTOC. However, in some cases, the minus-end is, or can become, free of the MTOC, so that there are two free ends with different nucleotides. As mentioned already, the minus-end does undergo dynamic instability, albeit with slower kinetics compared to the plus-end, and with only GDP-bound tubulin present, the critical concentration for the minus-end is greater than that of the plus-end. So within a certain range of free tubulin concentrations, that is, bounded by the critical concentrations for each end, the minus-end will undergo net loss of tubulin, while the plus-end will generally continue growth. This produces a subunit flux through the polymer, a phenomenon known as "treadmilling" (Margolis and Wilson, 1981), and is a special case of microtubule behaviour. This type of assembly process was first proposed for actin filaments, another constituent of the cytoskeleton, by (Wegner, 1976), who gave it the term "head-to-tail" polymerisation.

Treadmilling is an interesting manifestation of the biochemistry that drives dynamic instability, but the extent to which it features in nature is not clear (this is true for actin filaments, too). It is possible to observe treadmilling *in vitro* (Margolis and Wilson, 1978; Rothwell et al., 1985; Walker et al., 1988) and it has also been observed in the cell in some instances, such as in the lamellae of migrating newt lung epithelial cells (Waterman-Storer and Salmon, 1997), and in melanophore cell fragments (Rodionov and Borisy, 1997). Although it is not overtly common in animal cells, observation of its occurrence in migration is suggestive of specific, but potentially important, roles. Treadmilling is commonplace in plant cells (see Ehrhardt and Shaw (2006) for a review), which lack a single, defined MTOC.

II. Measurements of dynamic instability

a. Dynamic instability parameters

Soon after the discovery of dynamic instability, efforts were made to describe the parameters that define it. For an anchored microtubule (at the centrosome or MTOC) undergoing dynamic instability, it is relatively straightforward to see that there are just a few pertinent parameters: growth rate, shrink rate, and the transitions from growth to shrinkage and *vice versa*, known respectively as catastrophe and rescue. There is also a third phase, pause, seen

both *in vitro* (Walker et al., 1988) and *in vivo* (Shelden and Wadsworth, 1993), where no net growth or shrinkage occurs. In growth and pausing phases, shortening "excursions" of individual protofilaments may occur (Brun et al., 2009; Schek et al., 2007), where a single protofilament shrinks while others are in the pausing or growing state. Transitions between all three states, including pause, are possible. Thus, excluding pause, there are four parameters to describe dynamic instability: growth rate, shrinking rate, catastrophe frequency and rescue frequency. Including pause introduces four additional transition frequencies: growth to pause and back again, and shrinking to pause and back again; unlike catastrophe and rescue, these transitions do not have particular names; a naming convention is explained in the next chapter. Importantly, it is clear that the transitions from one state to another are not dependent on the current state, nor the length of time a microtubule has been in that state (O'Brien et al., 1990; Walker et al., 1988).

The factors that contribute to the dynamic instability parameters differ between *in vitro* and *in vivo* conditions; *in vitro*, it is the core properties of tubulin that give rise to dynamic instability, while *in vivo*, these properties are modulated by associated proteins and chemical modifications of tubulin. The dynamic instability parameters have been investigated in both conditions, described below.

b. Dynamic instability in vitro

As discussed, initially, dynamic instability was inferred from biochemical methods and fixed immunofluorescence and electron microscopy studies (Mitchison and Kirschner, 1984a; Mitchison and Kirschner, 1984b). From the fixed microscopy data, the second of these studies provided an indirect estimate of the growth rate, the on- and off-rates of tubulin during growth, and the depolymerisation and off-rate as a function of tubulin concentration, for both microtubule ends (Mitchison and Kirschner, 1984b). These data indicated that microtubule polymerisation, as briefly mentioned already, is linearly dependent on the free tubulin concentration; while depolymerisation appeared not to be (thus there is only an off-rate for this phase).

The first direct observations of dynamic instability were made by Horio and Hotani (1986), who, using dark-field microscopy, measured two of the dynamics parameters, growth and shrink rates. Later, Walker et al. (1988) provided a more comprehensive study of microtubule dynamics, providing rate constants and transition frequencies in addition to growing and shrinking rates. This study extended our understanding of microtubule polymerisation dynamics, showing that not only is growth rate dependent on free tubulin concentration, the frequencies of catastrophe and rescue are also. Catastrophe events, as one might expect, decreased with increasing free tubulin concentration, while rescue events increased, albeit quite weakly, with increasing tubulin concentration. Thus, the rate of addition of tubulin to the microtubule, and the likelihood of an individual microtubule being in the growth phase, through decreased catastrophe and increased rescue, increases with increasing free tubulin concentration. On the other hand, the likelihood of a microtubule being in the shrinking phase, through increased catastrophe and decreased rescue, increases

with decreasing free tubulin concentration, but the rate of depolymerisation is similar for any given concentration.

Similar studies followed, aimed at further characterising rates and transitions. These give support to the free tubulin concentration-independence of depolymerisation rate, while the relationship between rescue frequency and free tubulin concentration is not clear. Reported off-rate values during microtubule polymerisation are rather variable, while catastrophe frequency is generally found to decrease with increasing free tubulin concentration. Finally, nucleation also shows free tubulin concentration-dependence, increasing with it (Walker et al., 1988).

c. Dynamic instability in vivo

In the cell, precise experimental variation of the free tubulin concentration is not possible; thus, the dynamics parameters are often measured as functions of rather different data, such as cell type, cell cycle stage, cell morphology, developmental stage, and even subcellular position. Obviously, without manipulation of the tubulin concentration, derivation of some information, such as the on- and off-rates of the growth phase, is not possible.

Broadly speaking, the differences between microtubule dynamics in vivo to those in vitro are that microtubules exhibit greater polymerisation rates and have higher transition frequencies (Cassimeris, 1993; Desai and Mitchison, 1997). Desai and Mitchison (1997) make the point that the higher frequencies of transition, particular that for catastrophe, change the relationship between some of the dynamics parameters. They show, for example, that if the ratio between polymerisation rate and catastrophe frequency were conserved from the *in vitro* situation, then we would expect essentially no catastrophe events.

This change in dynamics, of course, must be due to the dynamic instability modulators, of which most appear to act by altering transition frequencies (Desai and Mitchison, 1997). For example, at the transition from interphase to mitosis, there is a dramatic re-arrangement of the microtubule population, and this is brought on by a higher turnover of microtubules (McNally, 1996). The increased turnover results from changes in transition frequencies; Belmont et al. (1990) and Verde et al. (1992) report increased catastrophe, without alteration of other transition frequencies. However, Rusan et al. (2001) found that both catastrophe and rescue frequencies were altered at mitosis; catastrophe frequency increased and rescue frequency decreased, while no change was found in growth and shrink rates. Interestingly, this study also found that there was a reduction in the length of time spent in the pause phase, too.

An exception to the rule that dynamic instability modulators target transition frequencies rather than assembly/disassembly rates must be XMAP215 (Gard and Kirschner, 1987a), which promotes greater polymerisation rates through the catalysis of tubulin subunit addition to the growing microtubule end (Vasquez et al., 1994). However, this MAP increases microtubule turnover through increased depolymerisation rates, and importantly, also decreases rescue frequency (Vasquez et al., 1994), so it still retains transition frequency-targeting activities characteristic of dynamic instability modulators.

Indeed, an emerging theme of *in vivo* microtubule dynamics is that of differential stabilisation of microtubules, rather than alteration of growth rates. That is to say, the transition frequencies of microtubules change, either through different states of cellular differentiation, or between different areas, or sub-populations of microtubules, within a cell. During polarisation of MDCKII cells, for example, the growth rates of microtubules are not altered, but the rate of microtubule turnover decreases (Bre et al., 1990). Stabilisation of microtubules by septin GTPases, filamentous guanine triphosphatases, which associated with microtubules, may provide the decreased turnover seen during polarisation (Bowen et al., 2011). There is evidence for a sub-population of microtubules that are more stable, that is, undergo decreased turnover, within cells that are not undergoing any over processes (i.e., not polarising, migrating, dividing, etc.) (Schulze and Kirschner, 1986; Schulze and Kirschner, 1987).

Microtubule dynamics also differ over developmental stage, and between different cell types. Gard and Kirschner (1987b) compared microtubule dynamics in *Xenopus* oocytes, the immature egg, and mature activated eggs. They found that there was no assembly in oocytes, whereas in the activated eggs, microtubule polymerisation did occur. Thus developmental events are also intertwined with regulation of the microtubule network. Once development is complete, differences in cell type, reflecting different functions, are also reflected in differences in microtubule dynamics. However, unlike the mode of regulation discussed above, whereby dynamics are altered by changes in transition frequencies and growth and shortening rates do not change, Shelden and Wadsworth (1993) found that microtubules in fibroblast cells have higher rates of growing and shortening than in epithelial cells, while the frequency of catastrophe was unchanged. Still, rescue frequency was greater in epithelial cells.

Interestingly, the levels of unpolymerised tubulin are effectively self-regulated in the cell. This was determined through experiments where, firstly, colchicine was again used to depolymerise microtubules, which resulted in a decrease in synthesis of both α- and β-tubulin (Ben-Ze'ev et al., 1979), and in subsequent experiments where microinjected tubulin was also found to decrease tubulin synthesis (Cleveland et al., 1983). It was found that the effect of synthesis was by reduction of tubulin mRNA levels (Cleveland et al., 1981), and that this effect depends on free tubulin subunits in the cell binding to the nascent tubulin peptide as it is being translated (Yen et al., 1988). Such a feedback mechanism suggests that free tubulin levels are maintained at some target levels in the cell, and hence that the concentration effects observed *in vitro* may not be as pertinent inside the cell. Indeed, in a situation where dynamics can be modulated by a vast array of proteins, it may well be advantageous to have a constant, i.e. predictable, level of substrate.

Finally, it is important to realise the potential bias in measurement of microtubule dynamics *in vivo*. This could arise due to the fact that many microtubules, when visualised with fluorescent probes/proteins, cannot be differentiated from others in regions of the cell that are densely packed with microtubules. Thus, *in vivo* studies may measure the dynamics of only a subset of the microtubule population. This is evident in the study by Rusan et al. (2001) cited above, where only the dynamics of microtubule ends near the cell periphery were measured.

This is, of course, no fault of the experimenter; to measure the dynamics of microtubules in more dense regions is near-impossible, and at best, would be unreliable. However, given the nature of many proteins that interact with microtubules, which also interact with other cellular components, many enriched at the cell periphery (e.g. actin), the results of these studies must be interpreted with caution.

To circumvent this problem, Komarova et al. (2002) employed various techniques to visualise microtubule behaviour in the cell interior. They used photobleacing to effectively clear an area of the cell of fluorescence from labelled tubulin, so that they could see microtubule growth in interior areas of the cell, and they also tracked microtubule growth with fluorescently-labelled proteins that bind to the growing plus end of the microtubule (see section AIIIc). The results of their study indicated that estimates of microtubule dynamics at the cell periphery are indeed not representative, finding that microtubule often grow persistently from the interior to the periphery without undergoing catastrophe, in contrast to the relatively frequent transitions made at the periphery. An interesting point arising here is that, once the radial array is established during interphase, it is often seen as a relatively static structure, especially when compared to the mitotic spindle. That is not to say that it is not acknowledged that it is indeed dynamic, but potential subtle re-arrangements of the radial array have not been investigated. The fact that microtubules are seen to depolymerise all the way from the periphery to the interior and beyond, and the difference in dynamics between these areas, suggests that this is a possibility worth considering further.

The general picture of microtubule dynamics *in vivo* is thus a lot more complex than that *in vitro*. The additional levels of regulation and interaction that give rise to this complexity allow precise manipulations and refinement of the microtubule network, which must be required to meet the demands of organising the cell.

III. Modulation of dynamic instability in the cell

a. Tools for tuning microtubule dynamics

The basic properties of the microtubule described so far are enough to give rise to all aspects of dynamic instability. Thus, *in vitro* preparations of purified tubulin reproduce *in vivo* microtubule behaviour. However, these similarities are only qualitative; although each parameter of dynamic instability is present *in vitro*, they are usually quantitatively different to those seen in the cell. Generally, microtubules *in vivo* are more dynamic than *in vitro* (Cassimeris, 1993); for example, sea urchin egg extract microtubules polymerise 6-times faster than purified sea urchin tubulin (Simon et al., 1992). Published descriptions of microtubule dynamics show that there is indeed a high degree of variability within *in vitro* data and, *in vivo*, between cell types, and also that such measurements are made with varying techniques and precision. However, the discrepancy between *in vitro* and *in vivo* microtubule dynamics is also due to the presence in the cell of modulators of dynamic instability. These modulatory factors, predominantly MAPs, but also tubulin post-translational modifications (PTMs) and microtubule motor proteins, modify the basic properties of microtubules in the cell, thus affecting the cellular functions of the microtubule network.

b. Nucleation

Nucleation is the process by which a microtubule is initially generated. In animals and fungi, it takes place at an MTOC, and in animal cells, as was discussed above, the main MTOC is the centrosome, but depending on cellular circumstances, this may vary.

Nucleation involves another member of the tubulin family, γ-tubulin. This tubulin isoform, along with γ-tubulin ring proteins and complex proteins (GRIPs and GCPs, respectively), forms a ring structure known as the γ-tubulin small complex (γTuSC) (Moritz et al., 1995). Many copies of the γTuSC create the γ-tubulin ring complex (γTuRC) in conjunction with a number of associated proteins, and it is this structure that nucleates microtubules (Zheng et al., 1995). The mechanism for nucleation by the γTuRC centres on stabilisation of the first tubulin heterodimer by γ-tubulin, and, upon hydrolysis of γ-tubulin-bound GTP, γ-tubulin undergoes a conformational change, allowing lateral interactions between tubulin heterodimers, and subsequent microtubule polymerisation (Wiese and Zheng, 2006).

c. MAPs

This class of proteins, as the name suggests, is delineated by the interaction of the member proteins with microtubules. This being the sole criterion, the class has a broad and diverse membership, consisting of proteins that interact with different regions of the microtubule and that do so through different mechanisms, with varied domains and evolutionary origin. Accordingly, the MAP literature is extensive; below, I summarise the MAPs that have links to influencing dynamic instability, grouping them according to the region of the microtubule which they recognise. For a thorough review of MAPs in general, see Mimori-Kiyosue (2011).

Plus end tracking MAPs are proteins are referred to simply as +TIPs, and although other MAPs have the ability to track microtubule plus ends, for example, the Dam1 complex (Lampert et al., 2010), the term +TIPs is generally reserved for those proteins whose binding gives rise to comet-like formations at the plus end (Jiang and Akhmanova, 2011; Schuyler and Pellman, 2001), and they can be grouped according to the presence of particular domains.

The +TIPs, due to their position, have the potential to mediate microtubule interactions with other proteins, organelles and other cellular components, as they probe intracellular space (Galjart, 2010). The most important +TIPs are those of the end-binding (EB) family, since they not only target the microtubule plus end without need for binding partners (Bieling et al., 2007) through recognition of the GTP cap (Maurer et al., 2011; Zanic et al., 2009), they also act as binding partners for other +TIPs. Such +TIPS include cytoplasmic linker protein 170 KDa (CLIP-170), adenomatous polyposis coli protein (APC), microtubule-actin crosslinking factor (MACF), CLIP-associating proteins (CLASPs). Some of these, and many other +TIPs, not only interact with EB family proteins, but with each other (reviewed in Akhmanova and Steinmetz (2008) and Galjart (2010)). As a result, determining how each +TIP affects the dynamics of the microtubule is difficult.

Many +TIPs are thought to be involved in microtubule stabilisation, for example, loss of MACF, also known as actin-crosslinking family-7 (ACF7), which links microtubules and actin, results in less-stable microtubules (Kodama et al., 2003). Other such stabilising +TIPs include APC (Etienne-Manneville and Hall, 2003), CLIP-170 (Fukata et al., 2002) and CLASPs (Akhmanova et al., 2001), which all associate with the actin network too (Galjart, 2010). EB family proteins are associated with an increase in microtubule dynamics and lower incidence of catastrophe (Lansbergen and Akhmanova, 2006), while XMAP215 promotes microtubule growth by catalysing the addition of subunits at the plus end (Brouhard et al., 2008; Vasquez et al., 1994). CLIP proteins have been reported to promote rescue (Komarova et al., 2002), despite apparently not binding depolymerising microtubules (Akhmanova and Steinmetz, 2008).

Finally, it is noteworthy that some of the +TIPs, those with a cytoskeleton-associated protein Gly-rich domain (CAP-Gly), only bind to tyrosinated microtubules (Peris et al., 2006). Given the nature of the tubulin detyrosination/tyrosination cycle in cells (see "Tubulin PTMs", below), the tyrosinated-tubulin preference results in fewer binding events of CAP-Gly +TIPs over time. It is possible that there may be more as-yet-undiscovered examples of MAP-PTM interactions.

As was discussed above, the minus end of the microtubule does undergo dynamic instability, albeit with slower kinetics (Mitchison and Kirschner, 1984a). The lack of dynamic minus ends *in vivo* is due to the fact that microtubules are usually anchored at this end at the MTOC. Moreover, microtubules usually initiate, that is, undergo nucleation, at the MTOC. The MTOC can thus be considered as an effector of dynamic instability, and it is γ-tubulin, another member of the tubulin family, that is responsible for this. γ-tubulin is evolutionarily-conserved, found in a complex with other proteins to form the γ-tubulin ring complex, or γ-TuRC, and is essential for microtubule nucleation (Raynaud-Messina and Merdes, 2007). Other minus-end MAPs, including ninein, pericentrin and centrosomin function to link γ-tubulin to centrosomes or other structures (Jiang and Akhmanova, 2011). The kinetic advantage conferred by γ-tubulin for microtubule nucleation is crucial to microtubule dynamics.

The MAP2/tau family of MAPs, traditionally associated with expression in neurons, is another important class of MAPs that can affect microtubule dynamics. Members are the various isoforms of MAP2 and tau, and MAP4 (Dehmelt and Halpain, 2005). These proteins stabilise microtubules, binding to the side of the microtubule along its length; moreover, microtubules are more rigid with MAP2 and tau bound. Although members of this family are generally considered to be restricted to neuronal cells, MAP4 is expressed elsewhere and displays similar microtubule-stabilising functions. It is thought that these proteins stabilise microtubules by inhibiting catastrophe, possibly by forming clusters on the microtubule

d. Tubulin PTMs

There is a number of tubulin PTMs known; some are general modifications that are known to apply to other proteins, while others are specific for tubulin (Janke and Bulinski, 2011). It

has been proposed that the heterogeneity of tubulin PTMs incorporated into the microtubule lattice acts as a "tubulin code", which acts to provide information to the various MAPs in analogy to the histone code and chromatin function (Verhey and Gaertig, 2007). Although the first example of tubulin PTM was documented nearly 40 years ago (Arce et al., 1975; Hallak et al., 1977), generally, tubulin PTM is an active area of research. Non-exclusive PTMs of tubulin include phosphorylation, ubiquitylation, sumoylation, and palmitoylation, while those specific to tubulin are detyrosination and generation of Δ2-tubulin, acetylation, polyglutamylation, and polyglycylation (Janke and Bulinski, 2011).

Tubulin undergoes cycles of addition and removal of a tyrosine functional group, and although tyrosination was observed first (Arce et al., 1975), in the majority of α-tubulin genes, upon which this modification occurs, a tyrosine residue is encoded at the carboxy-terminal (Valenzuela et al., 1981). Thus detyrosination (Hallak et al., 1977) occurs first. Detyrosination takes place preferentially on tubulin incorporated into the lattice (Kumar and Flavin, 1981), whereas soluble tubulin is very quickly tyrosinated (Raybin and Flavin, 1977). Generation of Δ2-tubulin is a related tubulin PTM, and it results from the removal of the glutamate residue that is exposed on detyrosinated tubulin (Paturle-Lafanechere et al., 1991). Detyrosination is associated with stable microtubules (Webster et al., 1987), and this occurs as a result of the preference for tyrosinated microtubules of depolymerising kinesins (Peris et al., 2009), a special family of the microtubule motor protein that are involved in microtubule destabilisation (Desai et al., 1999). Moreover, detyrosination enhances binding of kinesin-1 (Dunn et al., 2008; Liao and Gundersen, 1998), a conventional kinesin protein (Lawrence et al., 2004), while binding of the CAP-Gly domain plus tip MAPs requires tyrosinated α-tubulin (Peris et al., 2006; Weisbrich et al., 2007); these are examples of the aforementioned tubulin code (Verhey and Gaertig, 2007).

The best-studied example of acetylation is that of Lys40 on α-tubulin (L'Hernault and Rosenbaum, 1985), which also occurs on the microtubule polymer (Maruta et al., 1986). As with detyrosination, acetylation is considered as a marker for stabilised microtubules, yet, this seems not to be supported by a great deal of evidence, and the apparent promotion of kinesin-1 and dynein binding in response to acetylation is also subject to debate (both aspects are reviewed in Janke and Bulinski (2011)).

Polyglutamylation and polyglycylation are related tubulin PTMs; they both involve the addition of glutamate (Edde et al., 1990) or glycine (Redeker et al., 1994) residues, respectively, to the γ-carboxyl group of one or more of the glutamate residues toward the C-terminus of both polymerised α- and β-tubulin. The number of residues added is variable, and since both modifications occur at the same sites on the tubulin molecule, they are competitive (Janke and Bulinski, 2011). Polyglutamylation has the interesting potential role in mediating microtubule severing, since *in vitro* experiments have shown that long Glu chains promote severing, while shorter chains (which are generated by a different enzyme to that which catalyses long chain-formation) did not (Lacroix et al., 2010). (Janke and Bulinski, 2011) point out that, since many microtubules are polyglutamylated *in vivo*, for example in axons, there must be protective mechanisms in place so that they are not randomly severed. Polyglutamylation may also affect motor protein binding (Janke and Bulinski, 2011).

B. MICROTUBULE ORGANISATION

I. Microtubules in minimal systems

a. A framework for consideration of microtubule organisation

There is a complex interplay between a variety of cellular processes and organisation of the microtubule cytoskeleton. This relationship goes in both directions, thus, the state of the cell, its differentiation programme, and other factors such as adhesions with surrounding matrix and with other cells all influence the organisation of the microtubule network, and the organisation of the network, in turn, has the capability to influence those processes. Therefore, there is a general cell-wide self-organisational process that contributes to the form of not only the microtubule network, but the cell as a whole. In this section, the organisation of the microtubule network is considered.

How do various cellular processes affect the organisation of the microtubule network? By definition of organisation, such processes must affect the behaviour of microtubules in space, and somehow maintain this over time. Targets of organising processes include microtubule dynamics, and modulation of interactions of microtubules with each other and with other cellular components.

Although this thesis is concerned with microtubule organisation in animal cells, many enlightening studies on microtubule organisation have been conducted *in vitro*. In these minimal systems, where there are a small number of components, the reduction of the intricacy of the problem helps to understand mechanisms of organisation. Firstly, then, these minimal systems studies are described, with the aim of highlighting some of the general principles of microtubule organisation without the bewildering complexity of the cell. After this, the additional layers of regulation that have been discovered to be in operation within the cell are discussed.

b. Microtubule-motor self-organisation

When microtubules are mixed with motor proteins, various large-scale and stable patterns can form. Two classic studies of microtubule-motor protein self-organisation first demonstrated and explained the formation of these patterns. First, Nedelec et al. (1997) showed that multimeric kinesin molecules could give rise to different microtubule organisations that was dependent on the concentration of the motor protein and also the confining geometry of the system. At fixed concentrations of multimeric kinesin in a confined cylindrical container (but almost 2-D, i.e. circular), microtubules consistently formed first a symmetrical aster, then a vortex. It was also found that vortices could form without an aster first forming if a torus-like geometry was used. When unconfined, the concentration of kinesins was important; low concentrations produced a network of vortices, while if the concentration was increased, a network of asters was organised; still greater concentration produced networks of bundled microtubules in a manner also sensitive to microtubule nucleation rate and potentially other dynamics parameters.

Surrey et al. (2001) expanded upon the work of Nedelec et al. (1997). In this study, microtubules with plus end-directed motors formed asters with plus ends oriented toward the focus of the aster, while those with minus end-directed motors are oriented with minus ends at the centre of the aster. Interestingly, Surrey et al. (2001) found that the vortices described in Nedelec et al. (1997) are dependent on the concentration of the motor: increasing concentration leads to an aster. Reconstruction of the system *in silico* indicated that the ability of the motor (whether plus or minus end-directed) to form asters was dependent on the residence time at the microtubule end; longer times meant a greater likelihood of aster formation. This work also presented evidence of an unusual network organisation, whereby microtubules were arranged in large parallel bundles in mixtures of both plus end- and minus end-directed motors; at one end of the bundle would be a concentration of plus end-directed motors, and at the other end, minus end-directed motors.

In addition to demonstrating that large-scale patterns can be generated by just a few components, these studies demonstrate that changes to a simple kinetic parameter, in this case the characteristic residence time of a motor protein at the end of a microtubule, can effect large-scale changes in network organisation, (a theme expanded upon by Huber and Kas (2011)).

c. Microtubules and forces

As microtubules grow, they can in theory generate force if this growth takes place against some form of barrier. On the other hand, if microtubules are attached in some way to a structure of some sort, then their shrinkage could potentially generate a pulling force. Vignaud et al. (2012) call these "spatial boundary conditions" (SBCs). Furthermore, if a microtubule motor is attached to some kind of substrate away from its microtubule-binding parts, then by walking on the microtubule, the motor could generate a pulling force. Many minimal systems, often complemented by theoretical analyses, have addressed the issue of microtubule forces generation in the organisation of microtubule networks.

Since a microtubule aster *in vivo* generally has minus ends clustered at its centre, the most commonly addressed mode of motor-mediated force generation is that by the minus end-directed motor dynein, as, by walking towards the aster centre along a microtubule, it could in theory exert a force on the aster.

Microtubule asters that were formed in micro-fabricated chambers were used to demonstrate that the aster will centre itself by the pushing forces generated by microtubule polymerisation against the chamber border (Holy et al., 1997). In a related study, addition of dynein to the system, where it was anchored at the borders of the chamber, leads to more stable aster centring, so long as the micro-fabricated chamber dimensions are smaller than microtubule lengths, allow interaction of microtubules around the chamber perimeter (Laan et al., 2012). Indeed, in the former study, dimensions are also important, so as to allow isotropic interaction of microtubules and the SBC, if centring is to occur. This is an excellent example of the basic network organisational properties conferred by inherent microtubule dynamics and how interaction with appropriately-positioned microtubule motors re-enforces this.

Aster off-centring, or so-called symmetry-breaking, can arise from a certain type of microtubule-SBC interaction (Vignaud et al., 2012). In this case, in vitro systems that do not permit force-generation by microtubules at the SBC have been used to demonstrate that microtubule sliding along the SBC results in off-centring of the aster (Cosentino Lagomarsino et al., 2007; Pinot et al., 2009). As with the previous example, the exact outcome depends on the relative dimensions of the microtubules and the SBC: if the SBC is large, centring is still observed; the smaller the SBC, the further off-centre the aster becomes (see Vignaud et al. (2012), for a review). Eventually, as microtubules slip along the SBC, the network can become arranged as a ring, with microtubules running parallel to the SBC. Thus, as a result of energy minimisation (i.e. microtubules becoming as straight as the SBC permits), the network takes on a specific type of organisation.

d. Microtubule interaction with actin

One interaction that is commonly acknowledged to be an underlying contributor in many cellular functions is that between microtubules and actin (Rodriguez et al., 2003), yet it remains somewhat neglected in the domain of *in vitro* reconstituted systems. Recently, however, López et al. (2014) addressed the effects of each cytoskeletal system on the other. In this study, a minimal version of the microtubule and actin binding protein ACF7 was created, named "TipAct", consisting of an N-terminal GFP, an F-actin binding domain, and a C-terminal SxIP motif allowing binding of EB proteins.

The authors found that TipAct could capture and guide microtubule growth along actin bundles, whereas in the absence of TipAct, initially-redirected microtubules often "snapped" off the actin tracks; this forced and continual alignment was found to be due to the presence of TipAct along actin bundles, and subsequent redistribution of EB proteins to the lattice of aligned microtubules. Moreover, initially disorganised microtubule arrays were found to gradually co-align with actin bundle orientation to a greater extent in the presence of TipAct than without it. Note, however, that just mechanical interactions between microtubule plus tips and actin bundles could redirect microtubule growth in the 2-dimensional system under study. When microtubules and non-bundled actin filaments were studied, it was found that microtubules could transport and reshape the actin filaments; thus the two cytoskeletal systems can influence the organisation of one another.

II. Microtubules *in vivo*

a. From minimal systems to the cell

The studies of purified components in controlled conditions described above have contributed to our understanding of what such minimal systems are capable of in terms of organisation; they set a reference against which the organisation of the microtubule network in the complex environment of the cell can be compared. In many cases, the actual patterns formed *in vivo* are similar to the set of organisations that have been described *in vitro* (Dogterom and Surrey, 2013); as Nedelec et al. (1997) pointed out, those types of experiments serve to catalogue the "vocabulary" of microtubule organisation.

The many types of microtubule-MAP associations, microtubule PTMs etc. may indeed have their own set of self-organising properties when isolated with microtubules in a minimal system. Further studies of that kind will determine whether certain organisations emerge from simple combinations of microtubules and other associated proteins and processes yet to be fully investigated; it is likely that the use of patterning molecules at specific locations within fabricated microchambers (e.g. Laan et al. (2012)), will enable further investigation of the influence of one or a few molecules at a time on the mechanisms of organisation of the microtubule network. Below, some of the plethora of modifications to the simple pattern-forming systems behaviours described previously are described; the specific examples are chosen with the aim of highlighting the more pertinent factors of *in vivo* microtubule organisation in general, and also to be relevant to the material presented in subsequent chapters.

b. Microtubule nucleation and anchorage

Unlike the microtubule asters in Nedelec et al. (1997) and Surrey et al. (2001), the microtubule asters in animal cells are based around the centrosome. In undifferentiated cells with a radial array, microtubule anchorage is confined to the centrosome, and disruption of anchorage by depletion of anchoring proteins, including ninein, a prominent minus end-anchoring protein (Delgehyr et al., 2005; Mogensen et al., 2000) leads to a change in organisation, or rather, disorganisation, of the microtubule array (Dammermann and Merdes, 2002). Generally, microtubules remain anchored at the centrosome, though release from the centrosome, again under the control of ninein, has been documented in migrating cells (Abal et al., 2002).

Deviations from the basic radial array often involve changes in the location of microtubule anchorage, and thus, microtubule anchorage is a major determinant of microtubule organisation. For example, in differentiated columnar epithelial cells, ninein is redistributed to apical sites associated with cell-cell junctions, where microtubule minus ends terminate (Mogensen et al., 2000; Moss et al., 2007).

c. Selective microtubule stabilisation by cortical factors

After discovering dynamic instability, in their typically prescient manner, Kirschner and Mitchison (1986) proposed that selective stabilisation of microtubules in certain locations within the cell could be one means of regulating microtubule organisation. As Li and Gundersen (2008) point out, in animal cells, microtubules are generally first nucleated and anchored at the centrosome, and specialisation in organisation follows, thus, re-organisations that depend on stabilising a select population of microtubules are perhaps best effected at the location of the plus tips: the cortex. Moreover, this also confers localisation proximal to external signals. Thus, the idea that microtubule could search cellular space and be selectively stabilised or captured (Mimori-Kiyosue and Tsukita, 2003) took shape, and indeed, re-organisation of the microtubule cytoskeleton by selective stabilisation, mediated by cortical factors, is an acknowledged feature of cellular microtubule organisation.

The common theme behind most instances of microtubule stabilisation at the cortex is a reduction of the dynamicity of the microtubule and an increase in occurrence of the pausing phase (Li and Gundersen, 2008). This is mediated by various +TIPs and specialised clusters of molecules at the cortex, so-called "cortical platforms". These platforms contain a phosphatidylinositol-3,4,5-triphosphate (PIP3) binding protein, LL5β, and ELKs (Lansbergen et al., 2006), while the +TIP CLASP proteins mediate capture of microtubules at the cortex (Mimori-Kiyosue et al., 2005) and are also found within these platforms through interaction with LL5β (Lansbergen et al., 2006). LL5β knockdown was found to alter microtubule dynamics so that there was an increased tendency to transit from the pausing state and a decreased tendency to transit towards it (Lansbergen et al., 2006) and this resulted in a decreased density of microtubule plus ends at the cortex; CLASP knockdown had a similar but more pronounced effect (Mimori-Kiyosue et al., 2005).

The regulation of microtubule dynamics at the periphery of the cell so as to allow cortical capture appears to be in a delicate balance. For example, the protein 4.1R, which contains a FERM domain, was recently found to contribute to the capture of microtubule plus ends by the LL5β/ELKS platforms (Ruiz-Saenz et al., 2013). Upon knockdown of 4.1R, microtubules exhibited lower catastrophe frequency, and longer times in growth to the detriment of time spent in shrinkage and pausing, relative to control microtubules.

Indeed, further evidence for this balance of effectors of microtubule dynamic instability at the cortex is provided by the recently discovered role of the kinesin-4 KIF21A in inhibition of microtubule growth at the cortex, and *in vitro*, KIF21A also suppressed catastrophe (van der Vaart et al., 2013). It was proposed that growth inhibition at the cortex contributes to cortical capture and correct microtubule organisation at the cortex.

The modulation of microtubule dynamics at the cortex is also mediated by many other +TIPs. One example is CLIP-170, which, in conjunction with IQGAP, is involved in cortical targeting of microtubules to distinct sites marked by Rac1/Cdc42 (Fukata et al., 2002); this is expanded upon in the next chapter. Interestingly, protein 4.1 has been shown to be involved in recruitment of IQGAP to distinct cortical sites in migrating cells (Ruiz-Saenz et al., 2011). Microtubules have been shown to be selectively stabilised downstream of signalling by Rho GTPase in response to lysophosphatidic acid (Cook et al., 1998), a component of serum, and that this is mediated by an interaction between diaphanous formins, mDia, and +TIPs EB1 and APC (Palazzo et al., 2001; Wen et al., 2004).

The mechanisms discussed above are located downstream of particular signalling cascades, though a full elucidation of the interplay between various signalling cascades and the cortical microtubule interacting proteins is yet to be availed. A comprehensive discussion of these signalling systems is beyond the scope of this thesis; suffice to say that microtubule organisation is responsive to external signals (Gundersen and Cook, 1999), the PIP3-binding activity of LL5β and the FERM domain of protein 4.1R are examples of the capability of these molecules to respond to external signals.

d. Microtubule guidance

In two studies that utilised micropatterned substrates to control cell shape, Thery et al. (2006) and Huda et al. (2012) investigated whether microtubule growth was guided within the cell. In cells with anisotropic substrate adhesion, the former study demonstrated that upon reaching a non-adhesive cell boundary, microtubules continued to grow along the boundary and accumulated at adhesive sections; interestingly the accumulation coincided with accumulation of APC (Thery et al., 2006). Huda et al. (2012) showed that microtubule growth was guided by actin bundles toward adhesive vertices of the cell. Notably, such guidance was dependent upon focal adhesions; on a substrate that promoted focal adhesion-independent substrate adhesion, microtubule guidance was no longer in effect (Huda et al., 2012).

Before the micropatterning studies, it was observed that microtubules persistently targeted focal adhesions (Kaverina et al., 1998), and that these adhesions could capture and stabilise microtubules. This association with focal adhesions only occurred for growing microtubules, and indeed occurred at high precision (Krylyshkina et al., 2003), suggesting some mechanism of non-random, i.e. guided, microtubule growth. However, initially, it was not found to be dependent upon actin, or indeed intermediate filaments (Kaverina et al., 1998), and apparently not re-tested in subsequent studies. Interestingly, repeated targeting of microtubules to focal adhesions results in their disassembly (Kaverina et al., 1999), contributing to adhesion turnover.

An apparent departure from the trend of guidance to and subsequent stabilisation of microtubules at particular cellular landmarks (i.e. focal adhesions, localised signalling cascades) has been described by Stehbens et al. (2006). Here, dynamic microtubules were observed growing toward E-cadherin puncta at cell-cell adhesions. Indeed, reduction of dynamicity with low doses of the microtubule-depolymerising drug nocodazole lead to reduced targeting of microtubule plus ends to these puncta. In another study, septins were found to have a microtubule-guiding role in polarising epithelial cells, and this involved suppressing catastrophe frequency and promoting growth (Bowen et al., 2011). These studies highlight the balance between the relative degrees of dynamicity and guidance: in an unguided system, a more dynamic microtubule should search space better (Holy and Leibler, 1994), whereas, in a guided system, persistent growth will permit better targeting.

Finally, an interesting potential system for microtubule guidance must be interaction with the actin cytoskeleton, given the findings described above in *in vitro* studies. The actin cytoskeleton is organised in a variety of ways within the cell, depending on the activity of a number of interacting proteins that modulate the assembly dynamics of actin filaments (Blanchoin et al., 2014). The actin cortex is a thin layer (approximately 190 nm) underlying the plasma membrane (Clark et al., 2013), while, in migratory cells, a network of branched and cross-linked filaments is found in the lamella, a thin, almost 2-dimensional region at the front of the cell, and in filopodia, protrusions resembling cell "fingers" at the front of the cell, the actin cortex is organised into bundles (Blanchoin et al., 2014).

Microtubules are known to affect the organisation of actin. For example, it has been shown that microtubule growth into lamellipodial regions promotes actin polymerisation through activation of the small GTPase Rac1 (Waterman-Storer et al., 1999). Here, clever use of the microtubule-affecting drugs nocodazole and taxol demonstrated that it was indeed microtubule growth, and not dynamics *per se*, that induced actin polymerisation. Indeed, Rac1 appears to be important in regulating both cytoskeletal systems; it has been shown that its activation can promote microtubule growth into lamellipodial areas, while a dominant negative Rac1 has the opposite effect (Wittmann et al., 2003), suggesting some sort of positive feedback mechanism is at work to promote growth of microtubules and actin together. Exactly how these *in vivo* findings relate to those documented *in vitro* remains to be determined. Notably, these studies were conducted in motile cells; Rac1 and its effect on microtubule growth at the cortex in non-migrating cells is investigated in chapter 3.

e. Forces on microtubules

One of the most obvious features of undifferentiated, non-motile cells in culture is the approximately central location of the centrosome. Centrosome positioning has the potential to influence microtubule organisation, but forces generated by microtubules may also influence centrosome positioning. In any case, centrosome relocation can be taken as a re-organisation of the microtubule network. Does centrosome positioning occur as a result of the centring mechanisms described in minimal systems?

The additional regulation of microtubule dynamics at the cell cortex suggest that the principles of centring that are based on microtubule pushing when polymerising against or slipping on a barrier are modified; in the cell, it is unlikely that there will be many surfaces or spatial boundary conditions that are so inert as to allow microtubule slipping along it.

Even in physical terms, the cell is far more complex than the minimal systems already considered; there are many SBCs here, for example the nucleus excludes microtubules from a large part of the cell volume, and given the association between the centrosome and nucleus, this introduces an asymmetry in the microtubule network (Bornens, 2012). Other organelles must have a similar SBC effect, though these may be more uniformly distributed. The pushing effect of microtubules growing against cytosol components has been postulated as a potential contributing mechanism for centring of the microtubule network (Zhu et al., 2010), but has not been investigated.

Rather than pushing forces generated by microtubules growing against a barrier, pulling forces have been demonstrated in the *Caenorhabditis elegans* embryo spindle (Grill et al., 2001; Grill and Hyman, 2005). Indeed, reliance on pushing force becomes problematic when microtubules become long, because longer microtubules will buckle more readily than shorter microtubules (Dogterom et al., 2005). Indeed, there is evidence that dynein pulls on microtubules to organise the network (Burakov et al., 2003; Koonce et al., 1999).

The organisation of the microtubule network is not simply a case of default centring. In a cell with an asymmetric microtubule network, the centrosome can maintain its central position (Vignaud et al., 2012). When adhesive micropatterns have been used to produce particular

cell shapes, the consistency of centrosome positioning in many cells of the same shape (Thery et al., 2006) suggests this is an integral part of cellular organisation, and centrosome positioning is predictable, given cell type and behaviour, for example in the wound healing response, where centrosomes localise between the nucleus and the leading edge of migrating cells (reviewed in Tang and Marshall (2012)), but the extent to which microtubule-mediated forces play a role in this is not clear.

In a comprehensive modelling study by Zhu et al. (2010), it is suggested that fine-tuning between forces generated by microtubules and actin can reliably off-centre the network, and this is a possibility. Indeed, in some cases of microtubule network re-organisation, modulation of microtubule dynamics is required, for example in centrosome relocation to the immunological synapse, where casein kinase 1δ promotes microtubule growth through EB1 (Zyss et al., 2011). In a different system, cellular polarisation after making cell-cell contacts, both actin and microtubules have been shown to have a role in centrosome relocation (Desai et al., 2009; Dupin et al., 2009; Vignaud et al., 2012).

To summarise, it is likely that forces on and generated by microtubules play an important role in microtubule organisation *in vivo*, but the complexity of the cell and the sheer number of potential force-mediated processes, and the fact that they are in operation at the same time as biochemical regulation, means that they are yet to be fully elucidated. As the study of mechanics within cells in general catches up with the more traditional biochemical and molecular focus, these processes should become clearer.

C. SUMMARY

Overall, the literature reviewed here shows that microtubules are fascinating cellular structures, and although there is a great deal known about their dynamics, we are a long way from understanding how microtubule dynamics are controlled within the cell to generate various organisations. Moreover, in many cases, other factors, such as physical interactions between microtubules and other cellular components, can contribute to microtubule network organisation, and this further complicates the issue. In subsequent chapters, the ways in which some of these phenomena contribute to microtubule organisation are addressed.

REFERENCES

Abal, M., M. Piel, V. Bouckson-Castaing, M. Mogensen, J.B. Sibarita, and M. Bornens. 2002. Microtubule release from the centrosome in migrating cells. *The Journal of cell biology*. 159:731-737.

Akhmanova, A., C.C. Hoogenraad, K. Drabek, T. Stepanova, B. Dortland, T. Verkerk, W. Vermeulen, B.M. Burgering, C.I. De Zeeuw, F. Grosveld, and N. Galjart. 2001. Clasps are CLIP-115 and -170 associating proteins involved in the regional regulation of microtubule dynamics in motile fibroblasts. *Cell*. 104:923-935.

Akhmanova, A., and M.O. Steinmetz. 2008. Tracking the ends: a dynamic protein network controls the fate of microtubule tips. *Nature reviews. Molecular cell biology*. 9:309-322.

Alberts, B. 2008. Molecular Biology of the Cell: Reference edition. Garland Science.

Allen, C., and G.G. Borisy. 1974. Structural polarity and directional growth of microtubules of Chlamydomonas flagella. *Journal of molecular biology*. 90:381-402.

Amos, L., and A. Klug. 1974. Arrangement of subunits in flagellar microtubules. *Journal of cell science*. 14:523-549.

Arce, C.A., J.A. Rodriguez, H.S. Barra, and R. Caputo. 1975. Incorporation of L-tyrosine, L-phenylalanine and L-3,4-dihydroxyphenylalanine as single units into rat brain tubulin. *European journal of biochemistry / FEBS*. 59:145-149.

Belmont, L.D., A.A. Hyman, K.E. Sawin, and T.J. Mitchison. 1990. Real-time visualization of cell cycle-dependent changes in microtubule dynamics in cytoplasmic extracts. *Cell*. 62:579-589.

Ben-Ze'ev, A., S.R. Farmer, and S. Penman. 1979. Mechanisms of regulating tubulin synthesis in cultured mammalian cells. *Cell*. 17:319-325.

Bieling, P., L. Laan, H. Schek, E.L. Munteanu, L. Sandblad, M. Dogterom, D. Brunner, and T. Surrey. 2007. Reconstitution of a microtubule plus-end tracking system in vitro. *Nature*. 450:1100-1105.

Blanchoin, L., R. Boujemaa-Paterski, C. Sykes, and J. Plastino. 2014. Actin dynamics, architecture, and mechanics in cell motility. *Physiological reviews*. 94:235-263.

Borisy, G.G., and E.W. Taylor. 1967a. The mechanism of action of colchicine. Binding of colchincine-3H to cellular protein. *The Journal of cell biology*. 34:525-533.

Borisy, G.G., and E.W. Taylor. 1967b. The mechanism of action of colchicine. Colchicine binding to sea urchin eggs and the mitotic apparatus. *The Journal of cell biology*. 34:535-548.

Bornens, M. 2012. The centrosome in cells and organisms. *Science (New York, N.Y.)*. 335:422-426.

Bowen, J.R., D. Hwang, X. Bai, D. Roy, and E.T. Spiliotis. 2011. Septin GTPases spatially guide microtubule organization and plus end dynamics in polarizing epithelia. *The Journal of cell biology*. 194:187-197.

Bre, M.H., R. Pepperkok, A.M. Hill, N. Levilliers, W. Ansorge, E.H. Stelzer, and E. Karsenti. 1990. Regulation of microtubule dynamics and nucleation during polarization in MDCK II cells. *The Journal of cell biology*. 111:3013-3021.

Brouhard, G., and D. Sept. 2012. Microtubules: sizing up the GTP cap. *Current biology : CB*. 22:R802-803.

Brouhard, G.J., J.H. Stear, T.L. Noetzel, J. Al-Bassam, K. Kinoshita, S.C. Harrison, J. Howard, and A.A. Hyman. 2008. XMAP215 is a processive microtubule polymerase. *Cell*. 132:79-88.

Brun, L., B. Rupp, J.J. Ward, and F. Nedelec. 2009. A theory of microtubule catastrophes and their regulation. *Proceedings of the National Academy of Sciences of the United States of America*. 106:21173-21178.

Bryan, J., and L. Wilson. 1971. Are cytoplasmic microtubules heteropolymers? *Proceedings of the National Academy of Sciences of the United States of America*. 68:1762-1766.

Burakov, A., E. Nadezhdina, B. Slepchenko, and V. Rodionov. 2003. Centrosome positioning in interphase cells. *The Journal of cell biology*. 162:963-969.

Carlier, M.F. 1991. Nucleotide hydrolysis in cytoskeletal assembly. *Current opinion in cell biology*. 3:12-17.

Carlier, M.F., and D. Pantaloni. 1981. Kinetic analysis of guanosine 5'-triphosphate hydrolysis associated with tubulin polymerization. *Biochemistry*. 20:1918-1924.

Cassimeris, L. 1993. Regulation of microtubule dynamic instability. *Cell motility and the cytoskeleton*. 26:275-281.

Clark, A.G., K. Dierkes, and E.K. Paluch. 2013. Monitoring actin cortex thickness in live cells. *Biophysical journal*. 105:570-580.

Cleveland, D.W., M.A. Lopata, P. Sherline, and M.W. Kirschner. 1981. Unpolymerized tubulin modulates the level of tubulin mRNAs. *Cell*. 25:537-546.

Cleveland, D.W., M.F. Pittenger, and J.R. Feramisco. 1983. Elevation of tubulin levels by microinjection suppresses new tubulin synthesis. *Nature*. 305:738-740.

Cook, T.A., T. Nagasaki, and G.G. Gundersen. 1998. Rho guanosine triphosphatase mediates the selective stabilization of microtubules induced by lysophosphatidic acid. *The Journal of cell biology*. 141:175-185.

Cosentino Lagomarsino, M., C. Tanase, J.W. Vos, A.M. Emons, B.M. Mulder, and M. Dogterom. 2007. Microtubule organization in three-dimensional confined geometries: evaluating the role of elasticity through a combined in vitro and modeling approach. *Biophysical journal*. 92:1046-1057.

Cote, R.H., and G.G. Borisy. 1981. Head-to-tail polymerization of microtubules in vitro. *Journal of molecular biology*. 150:577-599.

Dammermann, A., and A. Merdes. 2002. Assembly of centrosomal proteins and microtubule organization depends on PCM-1. *The Journal of cell biology*. 159:255-266.

David-Pfeuty, T., H.P. Erickson, and D. Pantaloni. 1977. Guanosinetriphosphatase activity of tubulin associated with microtubule assembly. *Proceedings of the National Academy of Sciences of the United States of America*. 74:5372-5376.

Dehmelt, L., and S. Halpain. 2005. The MAP2/Tau family of microtubule-associated proteins. *Genome biology*. 6:204.

Delgehyr, N., J. Sillibourne, and M. Bornens. 2005. Microtubule nucleation and anchoring at the centrosome are independent processes linked by ninein function. *Journal of cell science*. 118:1565-1575.

Desai, A., and T.J. Mitchison. 1997. Microtubule polymerization dynamics. *Annual review of cell and developmental biology*. 13:83-117.

Desai, A., S. Verma, T.J. Mitchison, and C.E. Walczak. 1999. Kin I kinesins are microtubule-destabilizing enzymes. *Cell*. 96:69-78.

Desai, R.A., L. Gao, S. Raghavan, W.F. Liu, and C.S. Chen. 2009. Cell polarity triggered by cell-cell adhesion via E-cadherin. *Journal of cell science*. 122:905-911.

Dogterom, M., J.W. Kerssemakers, G. Romet-Lemonne, and M.E. Janson. 2005. Force generation by dynamic microtubules. *Current opinion in cell biology*. 17:67-74.

Dogterom, M., and T. Surrey. 2013. Microtubule organization in vitro. *Current opinion in cell biology*. 25:23-29.

Dunn, S., E.E. Morrison, T.B. Liverpool, C. Molina-Paris, R.A. Cross, M.C. Alonso, and M. Peckham. 2008. Differential trafficking of Kif5c on tyrosinated and detyrosinated microtubules in live cells. *Journal of cell science*. 121:1085-1095.

Dupin, I., E. Camand, and S. Etienne-Manneville. 2009. Classical cadherins control nucleus and centrosome position and cell polarity. *The Journal of cell biology*. 185:779-786.

Edde, B., J. Rossier, J.P. Le Caer, E. Desbruyeres, F. Gros, and P. Denoulet. 1990. Posttranslational glutamylation of alpha-tubulin. *Science (New York, N.Y.)*. 247:83-85.

Ehrhardt, D.W., and S.L. Shaw. 2006. Microtubule dynamics and organization in the plant cortical array. *Annual review of plant biology*. 57:859-875.

Etienne-Manneville, S., and A. Hall. 2003. Cdc42 regulates GSK-3beta and adenomatous polyposis coli to control cell polarity. *Nature*. 421:753-756.

Fan, J., A.D. Griffiths, A. Lockhart, R.A. Cross, and L.A. Amos. 1996. Microtubule minus ends can be labelled with a phage display antibody specific to alpha-tubulin. *Journal of molecular biology*. 259:325-330.

Farrell, K.W., and M.A. Jordan. 1982. A kinetic analysis of assembly-disassembly at opposite microtubule ends. *The Journal of biological chemistry*. 257:3131-3138.

Fukata, M., T. Watanabe, J. Noritake, M. Nakagawa, M. Yamaga, S. Kuroda, Y. Matsuura, A. Iwamatsu, F. Perez, and K. Kaibuchi. 2002. Rac1 and Cdc42 capture microtubules through IQGAP1 and CLIP-170. *Cell*. 109:873-885.

Galjart, N. 2010. Plus-end-tracking proteins and their interactions at microtubule ends. *Current biology : CB*. 20:R528-537.

Gard, D.L., and M.W. Kirschner. 1987a. A microtubule-associated protein from Xenopus eggs that specifically promotes assembly at the plus-end. *The Journal of cell biology*. 105:2203-2215.

Gard, D.L., and M.W. Kirschner. 1987b. Microtubule assembly in cytoplasmic extracts of Xenopus oocytes and eggs. *The Journal of cell biology*. 105:2191-2201.

Grill, S.W., P. Gonczy, E.H. Stelzer, and A.A. Hyman. 2001. Polarity controls forces governing asymmetric spindle positioning in the Caenorhabditis elegans embryo. *Nature*. 409:630-633.

Grill, S.W., and A.A. Hyman. 2005. Spindle positioning by cortical pulling forces. *Developmental cell*. 8:461-465.

Gundersen, G.G., and T.A. Cook. 1999. Microtubules and signal transduction. *Current opinion in cell biology*. 11:81-94.

Hallak, M.E., J.A. Rodriguez, H.S. Barra, and R. Caputto. 1977. Release of tyrosine from tyrosinated tubulin. Some common factors that affect this process and the assembly of tubulin. *FEBS letters*. 73:147-150.

Hill, T.L., and Y. Chen. 1984. Phase changes at the end of a microtubule with a GTP cap. *Proceedings of the National Academy of Sciences of the United States of America*. 81:5772-5776.

Hirose, K., J. Fan, and L.A. Amos. 1995. Re-examination of the polarity of microtubules and sheets decorated with kinesin motor domain. *Journal of molecular biology*. 251:329-333.

Holy, T.E., M. Dogterom, B. Yurke, and S. Leibler. 1997. Assembly and positioning of microtubule asters in microfabricated chambers. *Proceedings of the National Academy of Sciences of the United States of America*. 94:6228-6231.

Holy, T.E., and S. Leibler. 1994. Dynamic instability of microtubules as an efficient way to search in space. *Proceedings of the National Academy of Sciences of the United States of America*. 91:5682-5685.

Horio, T., and H. Hotani. 1986. Visualization of the dynamic instability of individual microtubules by dark-field microscopy. *Nature*. 321:605-607.

Huber, F., and J. Kas. 2011. Self-regulative organization of the cytoskeleton. *Cytoskeleton (Hoboken, N.J.)*. 68:259-265.

Huda, S., S. Soh, D. Pilans, M. Byrska-Bishop, J. Kim, G. Wilk, G.G. Borisy, K. Kandere-Grzybowska, and B.A. Grzybowski. 2012. Microtubule guidance tested through controlled cell geometry. *Journal of cell science*. 125:5790-5799.

Hyman, A.A., D. Chretien, I. Arnal, and R.H. Wade. 1995. Structural changes accompanying GTP hydrolysis in microtubules: information from a slowly hydrolyzable analogue guanylyl-(alpha,beta)-methylene-diphosphonate. *The Journal of cell biology*. 128:117-125.

Janke, C., and J.C. Bulinski. 2011. Post-translational regulation of the microtubule cytoskeleton: mechanisms and functions. *Nature reviews. Molecular cell biology*. 12:773-786.

Jiang, K., and A. Akhmanova. 2011. Microtubule tip-interacting proteins: a view from both ends. *Current opinion in cell biology*. 23:94-101.

Kaverina, I., O. Krylyshkina, and J.V. Small. 1999. Microtubule targeting of substrate contacts promotes their relaxation and dissociation. *The Journal of cell biology*. 146:1033-1044.

Kaverina, I., K. Rottner, and J.V. Small. 1998. Targeting, capture, and stabilization of microtubules at early focal adhesions. *The Journal of cell biology*. 142:181-190.

Kirschner, M., J. Gerhart, and T. Mitchison. 2000. Molecular "vitalism". *Cell*. 100:79-88.

Kirschner, M., and T. Mitchison. 1986. Beyond self-assembly: from microtubules to morphogenesis. *Cell*. 45:329-342.

Kodama, A., I. Karakesisoglou, E. Wong, A. Vaezi, and E. Fuchs. 2003. ACF7: an essential integrator of microtubule dynamics. *Cell*. 115:343-354.

Komarova, Y.A., I.A. Vorobjev, and G.G. Borisy. 2002. Life cycle of MTs: persistent growth in the cell interior, asymmetric transition frequencies and effects of the cell boundary. *Journal of cell science*. 115:3527-3539.

Koonce, M.P., J. Kohler, R. Neujahr, J.M. Schwartz, I. Tikhonenko, and G. Gerisch. 1999. Dynein motor regulation stabilizes interphase microtubule arrays and determines centrosome position. *The EMBO journal*. 18:6786-6792.

Krylyshkina, O., K.I. Anderson, I. Kaverina, I. Upmann, D.J. Manstein, J.V. Small, and D.K. Toomre. 2003. Nanometer targeting of microtubules to focal adhesions. *The Journal of cell biology*. 161:853-859.

Kumar, N., and M. Flavin. 1981. Preferential action of a brain detyrosinolating carboxypeptidase on polymerized tubulin. *The Journal of biological chemistry*. 256:7678-7686.

L'Hernault, S.W., and J.L. Rosenbaum. 1985. Chlamydomonas alpha-tubulin is posttranslationally modified by acetylation on the epsilon-amino group of a lysine. *Biochemistry*. 24:473-478.

Laan, L., N. Pavin, J. Husson, G. Romet-Lemonne, M. van Duijn, M.P. Lopez, R.D. Vale, F. Julicher, S.L. Reck-Peterson, and M. Dogterom. 2012. Cortical dynein controls microtubule dynamics to generate pulling forces that position microtubule asters. *Cell*. 148:502-514.

Lacroix, B., J. van Dijk, N.D. Gold, J. Guizetti, G. Aldrian-Herrada, K. Rogowski, D.W. Gerlich, and C. Janke. 2010. Tubulin polyglutamylation stimulates spastin-mediated microtubule severing. *The Journal of cell biology*. 189:945-954.

Lampert, F., P. Hornung, and S. Westermann. 2010. The Dam1 complex confers microtubule plus end-tracking activity to the Ndc80 kinetochore complex. *The Journal of cell biology*. 189:641-649.

Lansbergen, G., and A. Akhmanova. 2006. Microtubule plus end: a hub of cellular activities. *Traffic (Copenhagen, Denmark)*. 7:499-507.

Lansbergen, G., I. Grigoriev, Y. Mimori-Kiyosue, T. Ohtsuka, S. Higa, I. Kitajima, J. Demmers, N. Galjart, A.B. Houtsmuller, F. Grosveld, and A. Akhmanova. 2006. CLASPs attach microtubule plus ends to the cell cortex through a complex with LL5beta. *Developmental cell*. 11:21-32.

Lawrence, C.J., R.K. Dawe, K.R. Christie, D.W. Cleveland, S.C. Dawson, S.A. Endow, L.S. Goldstein, H.V. Goodson, N. Hirokawa, J. Howard, R.L. Malmberg, J.R. McIntosh, H. Miki, T.J. Mitchison, Y. Okada, A.S. Reddy, W.M. Saxton, M. Schliwa, J.M. Scholey, R.D. Vale, C.E. Walczak, and L. Wordeman. 2004. A standardized kinesin nomenclature. *The Journal of cell biology*. 167:19-22.

Ledbetter, M.C., and K.R. Porter. 1963. A "MICROTUBULE" IN PLANT CELL FINE STRUCTURE. *The Journal of cell biology*. 19:239-250.

Ledbetter, M.C., and K.R. Porter. 1964. Morphology of Microtubules of Plant Cell. *Science (New York, N.Y.)*. 144:872-874.

Li, R., and G.G. Gundersen. 2008. Beyond polymer polarity: how the cytoskeleton builds a polarized cell. *Nature reviews. Molecular cell biology*. 9:860-873.

Liao, G., and G.G. Gundersen. 1998. Kinesin is a candidate for cross-bridging microtubules and intermediate filaments. Selective binding of kinesin to detyrosinated tubulin and vimentin. *The Journal of biological chemistry*. 273:9797-9803.

López, M.P., F. Huber, I. Grigoriev, M.O. Steinmetz, A. Akhmanova, G.H. Koenderink, and M. Dogterom. 2014. Actin–microtubule coordination at growing microtubule ends. *Nat Commun*. 5.

MacNeal, R.K., and D.L. Purich. 1978. Stoichiometry and role of GTP hydrolysis in bovine neurotubule assembly. *The Journal of biological chemistry*. 253:4683-4687.

Mandelkow, E.M., E. Mandelkow, and R.A. Milligan. 1991. Microtubule dynamics and microtubule caps: a time-resolved cryo-electron microscopy study. *The Journal of cell biology*. 114:977-991.

Margolis, R.L., and L. Wilson. 1978. Opposite end assembly and disassembly of microtubules at steady state in vitro. *Cell*. 13:1-8.

Margolis, R.L., and L. Wilson. 1981. Microtubule treadmills--possible molecular machinery. *Nature*. 293:705-711.

Maruta, H., K. Greer, and J.L. Rosenbaum. 1986. The acetylation of alpha-tubulin and its relationship to the assembly and disassembly of microtubules. *The Journal of cell biology*. 103:571-579.

Maurer, S.P., P. Bieling, J. Cope, A. Hoenger, and T. Surrey. 2011. GTPgammaS microtubules mimic the growing microtubule end structure recognized by end-binding proteins (EBs). *Proceedings of the National Academy of Sciences of the United States of America*. 108:3988-3993.

Maurer, S.P., F.J. Fourniol, G. Bohner, C.A. Moores, and T. Surrey. 2012. EBs recognize a nucleotide-dependent structural cap at growing microtubule ends. *Cell*. 149:371-382.

McNally, F.J. 1996. Modulation of microtubule dynamics during the cell cycle. *Current opinion in cell biology*. 8:23-29.

Melki, R., M.F. Carlier, D. Pantaloni, and S.N. Timasheff. 1989. Cold depolymerization of microtubules to double rings: geometric stabilization of assemblies. *Biochemistry*. 28:9143-9152.

Meurer-Grob, P., J. Kasparian, and R.H. Wade. 2001. Microtubule structure at improved resolution. *Biochemistry*. 40:8000-8008.

Mimori-Kiyosue, Y. 2011. Shaping microtubules into diverse patterns: molecular connections for setting up both ends. *Cytoskeleton (Hoboken, N.J.)*. 68:603-618.

Mimori-Kiyosue, Y., I. Grigoriev, G. Lansbergen, H. Sasaki, C. Matsui, F. Severin, N. Galjart, F. Grosveld, I. Vorobjev, S. Tsukita, and A. Akhmanova. 2005. CLASP1 and CLASP2 bind to

EB1 and regulate microtubule plus-end dynamics at the cell cortex. *The Journal of cell biology*. 168:141-153.

Mimori-Kiyosue, Y., and S. Tsukita. 2003. "Search-and-capture" of microtubules through plus-end-binding proteins (+TIPs). *Journal of biochemistry*. 134:321-326.

Mitchison, T., and M. Kirschner. 1984a. Dynamic instability of microtubule growth. *Nature*. 312:237-242.

Mitchison, T., and M. Kirschner. 1984b. Microtubule assembly nucleated by isolated centrosomes. *Nature*. 312:232-237.

Mitchison, T.J. 1993. Localization of an exchangeable GTP binding site at the plus end of microtubules. *Science (New York, N.Y.)*. 261:1044-1047.

Mogensen, M.M., A. Malik, M. Piel, V. Bouckson-Castaing, and M. Bornens. 2000. Microtubule minus-end anchorage at centrosomal and non-centrosomal sites: the role of ninein. *Journal of cell science*. 113 (Pt 17):3013-3023.

Mohri, H. 1968. Amino-acid composition of "Tubulin" constituting microtubules of sperm flagella. *Nature*. 217:1053-1054.

Moritz, M., M.B. Braunfeld, J.W. Sedat, B. Alberts, and D.A. Agard. 1995. Microtubule nucleation by gamma-tubulin-containing rings in the centrosome. *Nature*. 378:638-640.

Moss, D.K., G. Bellett, J.M. Carter, M. Liovic, J. Keynton, A.R. Prescott, E.B. Lane, and M.M. Mogensen. 2007. Ninein is released from the centrosome and moves bi-directionally along microtubules. *Journal of cell science*. 120:3064-3074.

Nedelec, F.J., T. Surrey, A.C. Maggs, and S. Leibler. 1997. Self-organization of microtubules and motors. *Nature*. 389:305-308.

O'Brien, E.T., E.D. Salmon, R.A. Walker, and H.P. Erickson. 1990. Effects of magnesium on the dynamic instability of individual microtubules. *Biochemistry*. 29:6648-6656.

Oosawa, F., and S. Asakura. 1975. Thermodynamics of the polymerization of protein. Academic Press.

Palazzo, A.F., T.A. Cook, A.S. Alberts, and G.G. Gundersen. 2001. mDia mediates Rho-regulated formation and orientation of stable microtubules. *Nature cell biology*. 3:723-729.

Paturle-Lafanechere, L., B. Edde, P. Denoulet, A. Van Dorsselaer, H. Mazarguil, J.P. Le Caer, J. Wehland, and D. Job. 1991. Characterization of a major brain tubulin variant which cannot be tyrosinated. *Biochemistry*. 30:10523-10528.

Peris, L., M. Thery, J. Faure, Y. Saoudi, L. Lafanechere, J.K. Chilton, P. Gordon-Weeks, N. Galjart, M. Bornens, L. Wordeman, J. Wehland, A. Andrieux, and D. Job. 2006. Tubulin tyrosination is a major factor affecting the recruitment of CAP-Gly proteins at microtubule plus ends. *The Journal of cell biology*. 174:839-849.

Peris, L., M. Wagenbach, L. Lafanechere, J. Brocard, A.T. Moore, F. Kozielski, D. Job, L. Wordeman, and A. Andrieux. 2009. Motor-dependent microtubule disassembly driven by tubulin tyrosination. *The Journal of cell biology*. 185:1159-1166.

Pinot, M., F. Chesnel, J.Z. Kubiak, I. Arnal, F.J. Nedelec, and Z. Gueroui. 2009. Effects of confinement on the self-organization of microtubules and motors. *Current biology : CB*. 19:954-960.

Raybin, D., and M. Flavin. 1977. Modification of tubulin by tyrosylation in cells and extracts and its effect on assembly in vitro. *The Journal of cell biology*. 73:492-504.

Raynaud-Messina, B., and A. Merdes. 2007. Gamma-tubulin complexes and microtubule organization. *Current opinion in cell biology*. 19:24-30.

Redeker, V., N. Levilliers, J.M. Schmitter, J.P. Le Caer, J. Rossier, A. Adoutte, and M.H. Bre. 1994. Polyglycylation of tubulin: a posttranslational modification in axonemal microtubules. *Science (New York, N.Y.)*. 266:1688-1691.

Rodionov, V.I., and G.G. Borisy. 1997. Microtubule treadmilling in vivo. *Science (New York, N.Y.)*. 275:215-218.

Rodriguez, O.C., A.W. Schaefer, C.A. Mandato, P. Forscher, W.M. Bement, and C.M. Waterman-Storer. 2003. Conserved microtubule-actin interactions in cell movement and morphogenesis. *Nature cell biology*. 5:599-609.

Rothwell, S.W., W.A. Grasser, and D.B. Murphy. 1985. Direct observation of microtubule treadmilling by electron microscopy. *The Journal of cell biology*. 101:1637-1642.

Ruiz-Saenz, A., L. Kremer, M.A. Alonso, J. Millan, and I. Correas. 2011. Protein 4.1R regulates cell migration and IQGAP1 recruitment to the leading edge. *Journal of cell science*. 124:2529-2538.

Ruiz-Saenz, A., J. van Haren, C. Laura Sayas, L. Rangel, J. Demmers, J. Millan, M.A. Alonso, N. Galjart, and I. Correas. 2013. Protein 4.1R binds to CLASP2 and regulates dynamics, organization and attachment of microtubules to the cell cortex. *Journal of cell science*. 126:4589-4601.

Rusan, N.M., C.J. Fagerstrom, A.M. Yvon, and P. Wadsworth. 2001. Cell cycle-dependent changes in microtubule dynamics in living cells expressing green fluorescent protein-alpha tubulin. *Molecular biology of the cell*. 12:971-980.

Schek, H.T., 3rd, M.K. Gardner, J. Cheng, D.J. Odde, and A.J. Hunt. 2007. Microtubule assembly dynamics at the nanoscale. *Current biology : CB*. 17:1445-1455.

Schulze, E., and M. Kirschner. 1986. Microtubule dynamics in interphase cells. *The Journal of cell biology*. 102:1020-1031.

Schulze, E., and M. Kirschner. 1987. Dynamic and stable populations of microtubules in cells. *The Journal of cell biology*. 104:277-288.

Schuyler, S.C., and D. Pellman. 2001. Microtubule "plus-end-tracking proteins": The end is just the beginning. *Cell*. 105:421-424.

Seetapun, D., B.T. Castle, A.J. McIntyre, P.T. Tran, and D.J. Odde. 2012. Estimating the microtubule GTP cap size in vivo. *Current biology : CB*. 22:1681-1687.

Shelden, E., and P. Wadsworth. 1993. Observation and quantification of individual microtubule behavior in vivo: microtubule dynamics are cell-type specific. *The Journal of cell biology*. 120:935-945.

Simon, J.R., S.F. Parsons, and E.D. Salmon. 1992. Buffer conditions and non-tubulin factors critically affect the microtubule dynamic instability of sea urchin egg tubulin. *Cell motility and the cytoskeleton*. 21:1-14.

Simon, J.R., and E.D. Salmon. 1990. The structure of microtubule ends during the elongation and shortening phases of dynamic instability examined by negative-stain electron microscopy. *Journal of cell science*. 96 (Pt 4):571-582.

Slautterback, D.B. 1963. CYTOPLASMIC MICROTUBULES. I. HYDRA. *The Journal of cell biology*. 18:367-388.

Song, Y.H., and E. Mandelkow. 1993. Recombinant kinesin motor domain binds to beta-tubulin and decorates microtubules with a B surface lattice. *Proceedings of the National Academy of Sciences of the United States of America*. 90:1671-1675.

Spiegelman, B.M., S.M. Penningroth, and M.W. Kirschner. 1977. Turnover of tubulin and the N site GTP in Chinese hamster ovary cells. *Cell*. 12:587-600.

Stehbens, S.J., A.D. Paterson, M.S. Crampton, A.M. Shewan, C. Ferguson, A. Akhmanova, R.G. Parton, and A.S. Yap. 2006. Dynamic microtubules regulate the local concentration of E-cadherin at cell-cell contacts. *Journal of cell science*. 119:1801-1811.

Stephens, R.E. 1970. Thermal fractionation of outer fiber doublet microtubules into A- and B-subfiber components. A- and B-tubulin. *Journal of molecular biology*. 47:353-363.

Surrey, T., F. Nedelec, S. Leibler, and E. Karsenti. 2001. Physical properties determining self-organization of motors and microtubules. *Science (New York, N.Y.)*. 292:1167-1171.

Tang, N., and W.F. Marshall. 2012. Centrosome positioning in vertebrate development. *Journal of cell science*. 125:4951-4961.

Thery, M., V. Racine, M. Piel, A. Pepin, A. Dimitrov, Y. Chen, J.B. Sibarita, and M. Bornens. 2006. Anisotropy of cell adhesive microenvironment governs cell internal organization and orientation of polarity. *Proceedings of the National Academy of Sciences of the United States of America*. 103:19771-19776.

Ubbels, G.A., K. Hara, C.H. Koster, and M.W. Kirschner. 1983. Evidence for a functional role of the cytoskeleton in determination of the dorsoventral axis in Xenopus laevis eggs. *Journal of embryology and experimental morphology*. 77:15-37.

Valenzuela, P., M. Quiroga, J. Zaldivar, W.J. Rutter, M.W. Kirschner, and D.W. Cleveland. 1981. Nucleotide and corresponding amino acid sequences encoded by alpha and beta tubulin mRNAs. *Nature*. 289:650-655.

van der Vaart, B., W.E. van Riel, H. Doodhi, J.T. Kevenaar, E.A. Katrukha, L. Gumy, B.P. Bouchet, I. Grigoriev, S.A. Spangler, K.L. Yu, P.S. Wulf, J. Wu, G. Lansbergen, E.Y. van Battum, R.J. Pasterkamp, Y. Mimori-Kiyosue, J. Demmers, N. Olieric, I.V. Maly, C.C. Hoogenraad, and A. Akhmanova. 2013. CFEOM1-associated kinesin KIF21A is a cortical microtubule growth inhibitor. *Developmental cell*. 27:145-160.

Vasquez, R.J., D.L. Gard, and L. Cassimeris. 1994. XMAP from Xenopus eggs promotes rapid plus end assembly of microtubules and rapid microtubule polymer turnover. *The Journal of cell biology*. 127:985-993.

Verde, F., M. Dogterom, E. Stelzer, E. Karsenti, and S. Leibler. 1992. Control of microtubule dynamics and length by cyclin A- and cyclin B-dependent kinases in Xenopus egg extracts. *The Journal of cell biology*. 118:1097-1108.

Verhey, K.J., and J. Gaertig. 2007. The tubulin code. *Cell cycle (Georgetown, Tex.)*. 6:2152-2160.

Vignaud, T., L. Blanchoin, and M. Thery. 2012. Directed cytoskeleton self-organization. *Trends in cell biology*. 22:671-682.

Wade, R.H. 2009. On and around microtubules: an overview. *Molecular biotechnology*. 43:177-191.

Walker, R.A., E.T. O'Brien, N.K. Pryer, M.F. Soboeiro, W.A. Voter, H.P. Erickson, and E.D. Salmon. 1988. Dynamic instability of individual microtubules analyzed by video light microscopy: rate constants and transition frequencies. *The Journal of cell biology*. 107:1437-1448.

Waterman-Storer, C.M., and E.D. Salmon. 1997. Actomyosin-based retrograde flow of microtubules in the lamella of migrating epithelial cells influences microtubule dynamic instability and turnover and is associated with microtubule breakage and treadmilling. *The Journal of cell biology*. 139:417-434.

Waterman-Storer, C.M., R.A. Worthylake, B.P. Liu, K. Burridge, and E.D. Salmon. 1999. Microtubule growth activates Rac1 to promote lamellipodial protrusion in fibroblasts. *Nature cell biology*. 1:45-50.

Webster, D.R., G.G. Gundersen, J.C. Bulinski, and G.G. Borisy. 1987. Differential turnover of tyrosinated and detyrosinated microtubules. *Proceedings of the National Academy of Sciences of the United States of America*. 84:9040-9044.

Wegner, A. 1976. Head to tail polymerization of actin. *Journal of molecular biology*. 108:139-150.

Weisbrich, A., S. Honnappa, R. Jaussi, O. Okhrimenko, D. Frey, I. Jelesarov, A. Akhmanova, and M.O. Steinmetz. 2007. Structure-function relationship of CAP-Gly domains. *Nature structural & molecular biology*. 14:959-967.

Weisenberg, R.C., W.J. Deery, and P.J. Dickinson. 1976. Tubulin-nucleotide interactions during the polymerization and depolymerization of microtubules. *Biochemistry*. 15:4248-4254.

Wen, Y., C.H. Eng, J. Schmoranzer, N. Cabrera-Poch, E.J. Morris, M. Chen, B.J. Wallar, A.S. Alberts, and G.G. Gundersen. 2004. EB1 and APC bind to mDia to stabilize microtubules downstream of Rho and promote cell migration. *Nature cell biology*. 6:820-830.

Wiese, C., and Y. Zheng. 2006. Microtubule nucleation: gamma-tubulin and beyond. *Journal of cell science*. 119:4143-4153.

Wittmann, T., G.M. Bokoch, and C.M. Waterman-Storer. 2003. Regulation of leading edge microtubule and actin dynamics downstream of Rac1. *The Journal of cell biology*. 161:845-851.

Wu, Z., E. Nogales, and J. Xing. 2012. Comparative studies of microtubule mechanics with two competing models suggest functional roles of alternative tubulin lateral interactions. *Biophysical journal*. 102:2687-2696.

Yen, T.J., P.S. Machlin, and D.W. Cleveland. 1988. Autoregulated instability of beta-tubulin mRNAs by recognition of the nascent amino terminus of beta-tubulin. *Nature*. 334:580-585.

Zanic, M., J.H. Stear, A.A. Hyman, and J. Howard. 2009. EB1 recognizes the nucleotide state of tubulin in the microtubule lattice. *PloS one*. 4:e7585.

Zheng, Y., M.L. Wong, B. Alberts, and T. Mitchison. 1995. Nucleation of microtubule assembly by a gamma-tubulin-containing ring complex. *Nature*. 378:578-583.

Zhu, J., A. Burakov, V. Rodionov, and A. Mogilner. 2010. Finding the cell center by a balance of dynein and myosin pulling and microtubule pushing: a computational study. *Molecular biology of the cell*. 21:4418-4427.

Zyss, D., H. Ebrahimi, and F. Gergely. 2011. Casein kinase I delta controls centrosome positioning during T cell activation. *The Journal of cell biology*. 195:781-797.

Chapter 3

Measuring microtubule dynamics in a radial array

A. INTRODUCTION

I. Microtubule dynamics and organisation in cells

a. Dynamics and organisation

The aim of this thesis is to better understand microtubule organisation in animal and plant cells. As chapter 2 made clear, one of the main contributing factors to any type of microtubule organisation is their dynamics. There are a great number of MAPs and other processes that function to modulate microtubule dynamics in some way, and microtubule organisation changes as a result of the activity of these many factors in order to serve some cellular function. Making sense of at least some of the relationships between dynamics and organisation is the focus of this chapter, wherein the results of extensive processing of time-lapse recordings of microtubule dynamics are presented.

b. Microtubule organisation as a system property

One important question which generally remains unanswered is: how is the microtubule array maintained? To put the question another way, we might ask: what are the factors that contribute to the homeostasis of the microtubule network? Taking the radial array, for example, it is fascinating that the microtubules, which are of course extremely dynamic and constantly changing, are part of this network which, at a macroscopic level, does not change. How delicate, or sensitive, is this unchanging state? Indeed, an alternative premise might be that microtubule dynamics can change a great deal and the organisation of the network does not change, i.e. that the network organisation is robust, to use systems terminology; in this view, the stasis of the network is not so remarkable.

However, it is possible to disrupt the organisation of the network, as thousands of experiments have demonstrated, and of which we will see more below. Therefore, if we take microtubule network organisation being the manifestation of a precise balance of contributing homeostatic processes as a given, a systems biology-type view of microtubule organisation emerges. Here, a number of processes contribute to the properties of the network; these properties, collectively referred to under the umbrella term organisation, can vary, depending on the type of array. For example, in the radial array, a pertinent property might be what has been termed "radiality" (van der Vaart et al., 2013), i.e. the proportion of microtubules that point away from the centrosome; here, the array is characterised by microtubules that are relatively straight and extend to the cortex, and stop there. In mitotic cells, a pertinent organisational property might be the length distribution (and perhaps bias in orientation, e.g. Wollman et al. (2005)) of microtubules which is important for proper capture of chromosomes (Hill, 1985; Holy and Leibler, 1994).

In this systems view of the microtubule network, it is clear from chapter 2 that a lot of work has been dedicated to understanding how the microtubule network becomes asymmetrically

organised (reviewed in Sugioka and Sawa (2012)), which often assume a symmetric starting point. Such asymmetries are important in cell polarisation and migration, for example. In addition to symmetry breaking, a lot of attention has been dedicated to understanding the maintenance of any given state. Here, I consider the maintenance of the radial array, characteristic of undifferentiated cells. To do this, I analyse time-lapse recordings of microtubule dynamics in normal cells, and also in cells where the system has been perturbed; this is the subject of the next section.

II. Perturbing the system

a. Pertinent processes

What are the candidate processes for a role in radial array maintenance? Clearly, there are some system components that are requisite. Nucleation of microtubules must balance loss of microtubules by extinction. After this, we might want to know how it is that the radiality of the system is maintained. The systems view of radial array maintenance is depicted in figure 1. There are two explanations: first, that microtubule dynamics are tuned so that the steady-state length is appropriate for the size of the cell, so that on average, microtubules are of the length equal to the distance between the centrosome and the cortex of the cell. The second explanation is that microtubule dynamics within the cell and at the cortex are different, so that microtubules reach the cortex, and stay there.

The first explanation for radiality suffers from one main weakness: first of all, assuming the centrosome is at the centre of the cell, then in any cell that is not circular, the centrosome-cortex distance is not constant, so in some areas, microtubules would be too long, and in others, too short. The second radiality explanation has some empirical support from van der Vaart et al. (2013), who find that the kinesin-4 KIF21A acts to inhibit microtubule growth at the cortex. Some complementary modelling based on their experimental data demonstrated that certain differences in dynamics between central and peripheral regions of the cell could produce radiality.

In addition to growth inhibition in peripheral regions of the cell, microtubules can be "captured" at the cortex. This involves +TIP proteins, and other proteins at the cortex and still other that act to link between the two (see chapter 2; and also reviewed in Gundersen et al. (2004)). What is the nature of these microtubule-cortex interactions? In chapter 2, we saw that there are a number of types of interaction, and various proteins that mediate them. *In vitro* experiments have elucidated that boundary-bound dynein, the microtubule minus end motor, can bind to microtubule plus ends and, by walking toward the minus end, pull on the microtubule (Laan et al., 2012). Moreover, it was shown before that, again *in vitro*, that pushing forces are also produced at boundaries when microtubules grow into them (Holy et al., 1997). Proteins such as CLASPs, CLIPs, IQGAP, 4.1R, and APC, all mediate "capture" of microtubule plus ends at the cortex, resulting in their stabilisation there.

Thus, we have a picture of microtubule-cortex interactions where microtubules are capable of continuation of growth into a barrier, producing force, though whether this is the case *in vivo* is not clear, where there are mediators of this growth. Furthermore, it is possible that growth

rate may be reduced whilst growing against a barrier, reducing the size of the GTP cap, destabilising the microtubule and resulting in catastrophe. Previously, a simple model of microtubule dynamics in the context of cell growth found that it was necessary to have an increased catastrophe rate at the cell periphery in order to explain observed cell growth (Picone et al., 2010), while the notion of cortex-induced catastrophe is supported by an analysis of the microtubule "life cycle" throughout the cell, finding intracellular catastrophe is low compared to boundary catastrophe (Komarova et al., 2002).

Thus, one of the main determinants of microtubule radiality is microtubule-cortex interactions. Here, I use image processing of time-lapse recordings of the +TIP protein CLIP-170, introduced in chapter 2, to characterise the dynamics of microtubules in ordinary cells, and in cells in which Rac1, a protein involved in microtubule-cortex interactions, has been inhibited. In the next section, I summarise what is known about Rac1, and why it is of interest here.

b. Rac1 and microtubule organisation

Rac1 is a member of the Rho family of small GTPases, along with many other members, including the well-studied Cdc42 and Rho proteins (A, B and C) (Hall, 2012). They act as molecular switches, cycling between inactive GDP-bound and active GTP-bound states, and are involved in a variety of cellular processes by regulating downstream "effector" molecules (Hall, 2012). One of the most prominent cellular activities that the Rho GTPases are involved in is cell migration (Ridley, 2001), where Rho proteins promote formation of contractile actin structures, "stress fibres", in response to lysophosphatidic acid (Ridley and Hall, 1992), while Rac1 causes membrane ruffles (Ridley et al., 1992) by promotion of branched actin filament formation by the Arp2/3 complex (Eden et al., 2002). Cdc42 is involved in formation of cellular protrusions rich in actin, known as filopodia (Hall, 2012)

Previously, Rac1 was also found to be involved with not only actin but also microtubules in migrating cells (Fukata et al., 2002), through one of its effector molecules, IQ motif containing GTPase-activating-like protein (IQGAP). This protein was originally identified as a potential Ras GTPase activating protein (GAP) (Weissbach et al., 1994), hence its name. However, rather than possessing GAP activity, instead, IQGAP binds Rac1 and Cdc42 in their activated GTP-bound forms (Kuroda et al., 1996). IQGAP is also an intermediary between Rac1 and Cdc42 and actin (Bashour et al., 1997; Hart et al., 1996). When IQGAP is bound to active Rac1 or indeed Cdc42, it binds via its C-terminus to the +TIP protein CLIP-170 (Fukata et al., 2002).

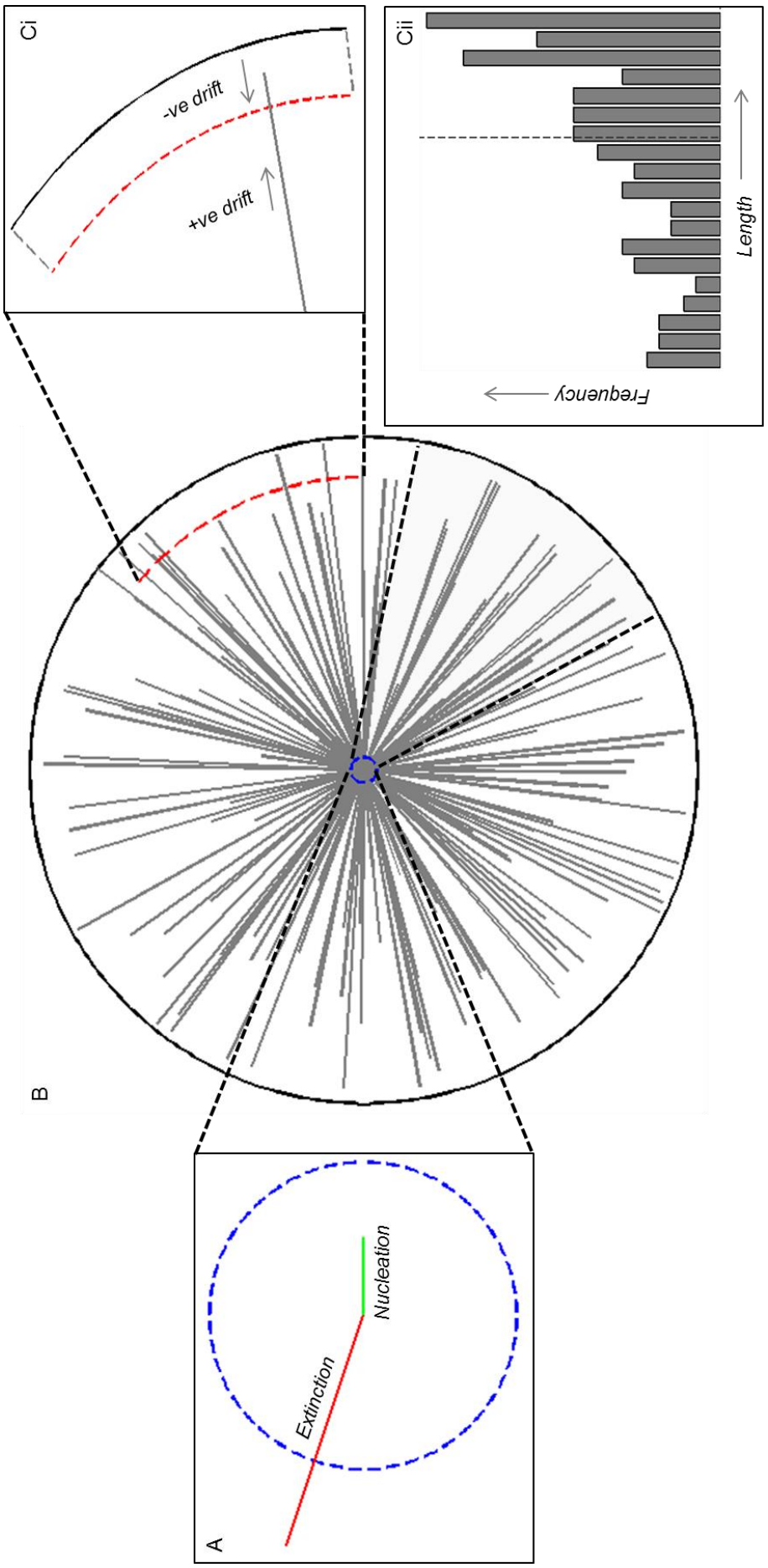

Figure 1. A systems view of microtubule organisation in the radial array. The organisation of the radial array (B), characterised by overt radiality, i.e. a high proportion of microtubules pointing away from the centrosome, is maintained by the processes above. First, to maintain constant numbers of microtubules, nucleation balances extinction (A). Secondly, the microtubules have a characteristic length distribution that permits this radiality; this could be maintained by differing dynamics in the peripheral zones compared to central zones (Ci), where the drift, i.e. the average displacement, of microtubules is negative in the former and positive in the latter, or microtubule dynamics might be finely tuned to give the correct length distribution (Cii).

Fukata et al. (2002) found that a constitutively-active (CA) form of Rac1 (Rac^{v12}) caused EGFP-CLIP-170 comets to remain relatively immobile compared to the control condition (displacement of < 0.5 μm over 24 seconds), while a C-terminal fragment of IQGAP caused a change in localisation of EGFP-CLIP-170 from microtubule plus ends to diffuse in the cytoplasm. They also found that a mutant IQGAP that cannot bind to Rac1 (or Cdc42) induced formation of multiple leading edges in migratory cells (Fukata et al., 2002), suggesting that, in an analogous manner to the role of the yeast CLIP-170 homologue tip1p, which produces a polarised microtubule morphology by modulating microtubule behaviour at the cortex (Brunner and Nurse, 2000), CLIP-170 may permit the "safe passage" of microtubules along the cortex until they reach appropriate locations, which would be indicated by the presence of IQGAP and Rac1/Cdc42 (Brunner, 2002).

An ongoing investigation in the Mogensen laboratory is the mechanism of re-organisation of the microtubule population from a radial array to the apico-basal array characteristic of differentiated epithelial cells (Bacallao et al., 1989). In the apico-basal array, microtubules are no longer anchored at the centrosome but at apical sites instead (Mogensen et al., 2000), and, rather than being nucleated there, a "release and capture" model has been proposed, whereby microtubules are originally nucleated at the centrosome and relocate to the apical sites, where they are subsequently anchored (Bellett et al., 2009; Mogensen, 1999).

One of the main anchoring molecules is the protein ninein, an acidic coiled-coil protein which localises to the centrosome (Bouckson-Castaing et al., 1996). Depletion of ninein causes disorganisation of the microtubule radial array (Dammermann and Merdes, 2002), and its overexpression prevents the release of microtubules from the centrosome in migrating cells (Abal et al., 2002). Furthermore, ninein can also affect nucleation through its interaction with microtubule nucleating machinery (Delgehyr et al., 2005; Stillwell et al., 2004). Ninein has been shown to mimic the movement of microtubule from centrosomal anchorage to apical anchorage in supporting epithelial cells of the mouse cochlea (Mogensen et al., 2000), and it is transported along microtubules, in both a plus end- and minus end-directed fashion, during the polarisation process (Moss et al., 2007). The apical sites at which the microtubules are anchored is apparently associated with adherens junctions (Moss et al., 2007), although ninein and another anchoring molecule, nezha, which has been found at adherens junctions, do not co-localise (Meng et al., 2008).

These data suggest that efficient redeployment of ninein to the junctions would require targeting of microtubule plus ends to those sites. Since IQGAP localises to cell-cell junctions (Kuroda et al., 1996), the mechanisms outlined above that control microtubule behaviour at the cortex in migrating cells may also contribute to microtubule capture, and thus facilitate ninein redeployment and later, formation of the apico-basal array and epithelieal polarisation.

Since Rac1 regulates the positioning of IQGAP-based CLIP-170 interaction, one of the first questions to be answered is: how does Rac1 affect microtubule behaviour at the cortex in cells with a radial array? One such cell line is the retinal pigment epithelial (ARPE-19) cell in an undifferentiated state (as in fig. 2). When grown in culture to confluence, these cells make contacts with one another, with the localisation of β-catenin to these sites indicative of

adherens junctions. Rac1 has been observed to localise to the adherens junctions in these cells; thus, ARPE-19 cells will make a good study system for the effects of Rac1 on microtubule behaviour at the cortex, and of course elsewhere in the cell.

It is clear that Rac1 inhibition has a major effect on the organisation of the microtubule cytoskeleton (compare figs. 2 and 3), and as it is localised to adherens junctions and is involved in microtubule-cortex interactions in other cell types, the disorganised phenotype may be a consequence of disrupted microtubule-cortex dynamics. Previously, it has been shown that a dominant negative (DN)-Rac1 reduced the abundance of "pioneer" microtubules, which grow into lamellipodia, and made microtubule dynamics similar to those of more centrally-located microtubules (Wittmann et al., 2003). Here, it might be expected that Rac1-inhibited cells and cells with a DN-Rac1 might have similar microtubule organisation. In that study, the analysis was performed in the PtK1 cells, a marsupial kidney epithelial cell line, and indeed, the lack of these pioneer microtubules produces a more compact array; however, many microtubules do apparently reach the border of the cell at a perpendicular angle, contrary to the appearance of the Rac1-inhibited cells (Nishimura et al., 2012). However, in this system, cells were migrating, without forming junctions with one another.

Interestingly, CA-Rac1 has been shown to induce microtubule organisation more similar to that shown in figure 3 than that of DN-Rac1 cells (Nishimura et al., 2012). In that case, both the DN- and CA-Rac1 were introduced (separately) into human U2-OS oteosarcoma cells, and indeed, the CA-Rac1, but not the DN-Rac1, produced a microtubule organisation similar to that shown in figure 3, where microtubules tend to be parallel to the cell edge, often forming bundles there. The discrepancies between the studies of a DN-Rac1 and the Rac1 inhibition in the Mogensen lab may be to do with the fact that the mechanisms of interfering with Rac1 function are different; indeed, it could be the case that the two strategies of interfering with Rac1 affect its interaction with IQGAP differently. Alternatively, the source of the differences could be due to the different cell lines used, or the fact that the other studies were interested in migrating cells, rather than cells at confluence that had formed junctions with one another. Ultimately, the differences will be better addressed once the CA-, DN-Rac1 and inhibition are conducted in the same cell line, in the same lab.

In any case, the Rac1-inhibited microtubule organisation phenotype is reproducible in the Mogensen lab, and the fact that it has been shown to have an active role in cortical capture of microtubules supports the notion that inhibiting Rac1 will lead to microtubule disorganisation. Thus, inhibition of Rac1 will be taken here as a model for disrupted microtubule-cortex interaction. Of course, given the involvement of Rac1 in organisation of the actin cytoskeleton as well as microtubules, it is probable that inhibition of Rac1 will interfere with actin cytoskeleton organisation. Given the cross-talk between the two cytoskeletal systems, it is therefore also probable that the documented roles, here and elsewhere, of Rac1 in the organisation of either system, is a result of interplay between microtubules and actin, and Rac1 in organising both of them. The argument taken here is that while this may be the case, Rac1 inhibition still leads to disrupted microtubule organisation, especially at the cortex. Such disorganisation may operate through actin, or be direct, or indeed both; mechanisms at this level are not the focus of this work, instead, here we are interested in understanding how

microtubule dynamics differ between central and peripheral regions of the cell and how that affects dynamics in unperturbed and Rac1-inhibited cells.

To better understand the role of microtubule cortex interactions in organisation of the microtubule network, I process time-lapse recordings of CLIP-170-GFP in ARPE-19 cells, with and without inhibition of Rac1. CLIP-170, as discussed already, labels growing microtubule plus ends (Perez et al., 1999), and thus, can be used to measure microtubule dynamics, as has been done before (Komarova et al., 2002). Of course, other +TIP proteins (discussed in chapter 2) labelled with fluorescent proteins could be used for a similar purpose. To date, no extensive investigation into whether these are equivalent, or somehow bias measurements of microtubule dynamics by labelling only a subset of microtubules, has been made, and is beyond the scope of this work. Tracking is done with the aid of the tracking software "plusTipTracker" (Applegate et al., 2011), and further analysis to fully characterise microtubule dynamics in this system. The software, and subsequent processing, which makes use of directional statistics and computational geometry, are described in the next sections.

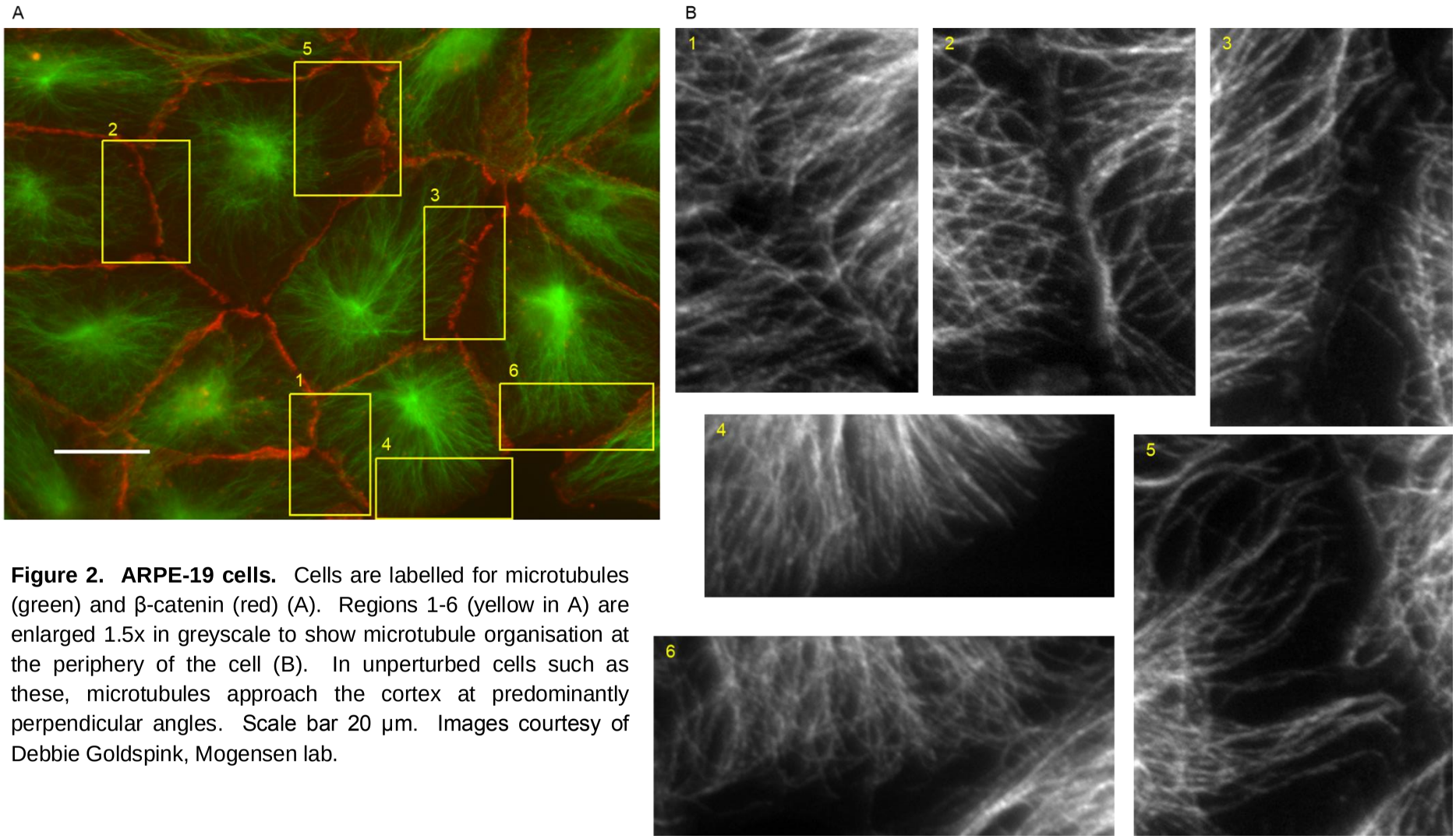

Figure 2. ARPE-19 cells. Cells are labelled for microtubules (green) and β-catenin (red) (A). Regions 1-6 (yellow in A) are enlarged 1.5x in greyscale to show microtubule organisation at the periphery of the cell (B). In unperturbed cells such as these, microtubules approach the cortex at predominantly perpendicular angles. Scale bar 20 µm. Images courtesy of Debbie Goldspink, Mogensen lab.

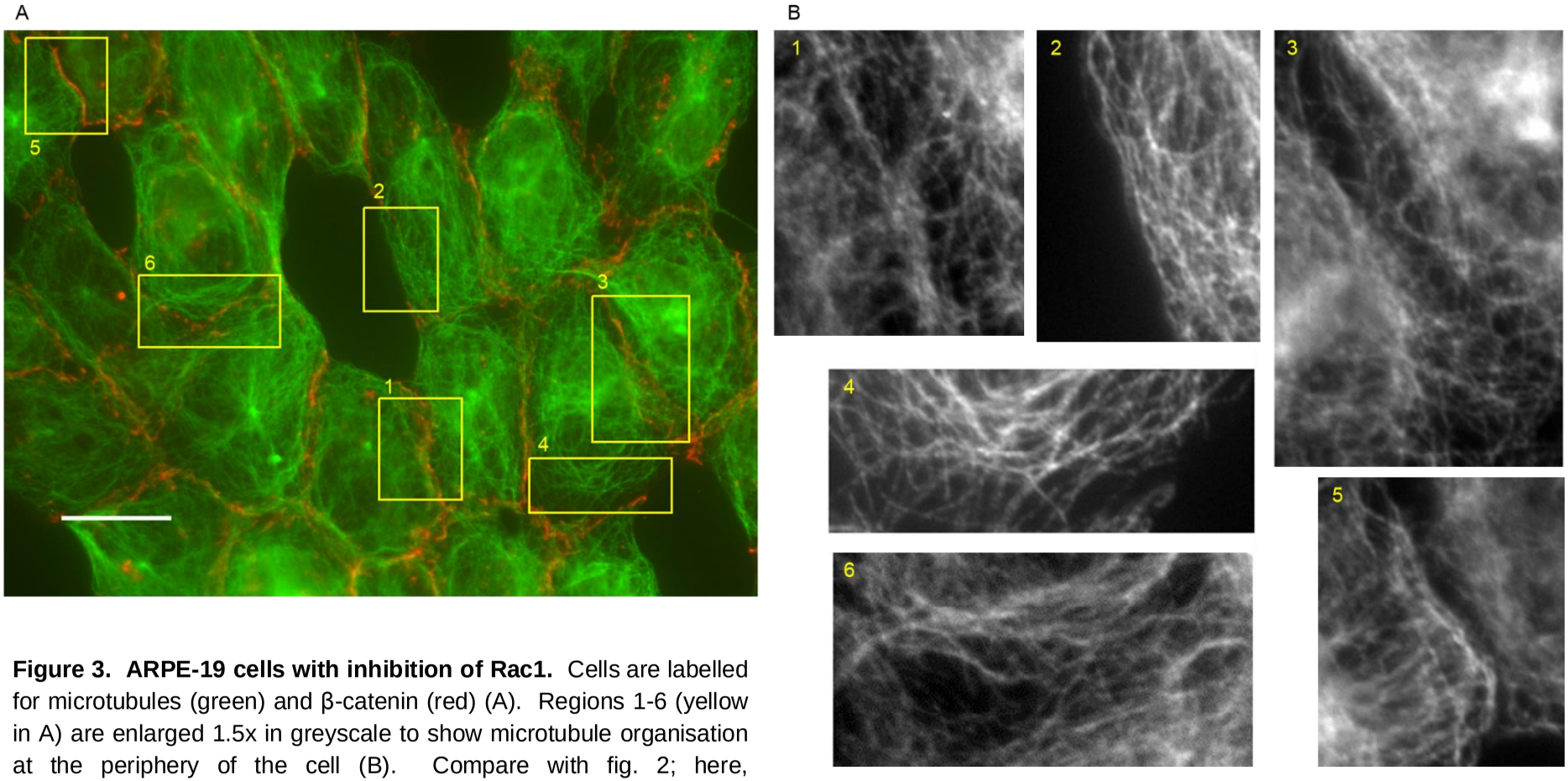

Figure 3. ARPE-19 cells with inhibition of Rac1. Cells are labelled for microtubules (green) and β-catenin (red) (A). Regions 1-6 (yellow in A) are enlarged 1.5x in greyscale to show microtubule organisation at the periphery of the cell (B). Compare with fig. 2; here, microtubules contact the cortex at shallower angles. Scale bar 20 μm. Images courtesy of Debbie Goldspink, Mogensen lab.

B. METHODOLOGY

I. Comet tracking

a. plusTipTracker

plusTipTracker takes input films as series of TIFF file images. Method pertaining to maintenance and preparation of cells are in appendix (section F). Time-lapse recordings of CLIP-170-GFP comets of 60 frames, 2.5 seconds apart (see appendix I for wet lab methodology), were passed to plusTipTracker, which was run with its default tracking parameters. Note that cells were analysed when confluent, so they were not migrating, as in figures 2-3. Although +TIP comets only mark microtubule growth phases, plusTipTracker infers the other two states by linking growth tracks together (Applegate et al., 2011).

The following description of the analysis of microtubule dynamics, based on the output of plusTipTracker, warrants a short summary of what this output is exactly, so that it will be clear what the data are and where they are coming from. All of the matrices and structures discussed below are the basis for both the processing of data carried out within plusTipTracker itself, or my subsequent analysis of microtubule dynamics.

The main output of plusTipTracker is an index of "sub-tracks": these are the detected comets that have been linked across frames to make microtubule trajectories. These trajectories may be growth, pause or shrinkage phases, and depending on whether a sub-track has been linked to another sub-track to make a "compound" track, the sub-tracks may have the same index. Thus, the sub-track matrix is an array with m_p rows, where m_p is the number of sub-tracks before reclassification (see below), and the columns contain information about the track:

1. Compound track index
2. Start frame
3. End frame
4. Growth rate ($\mu m\ min^{-1}$)
5. Track type (i.e., growth, shrinkage, pausing, unclassified)
6. Lifetime (frames)
7. Displacement (pixels)

The compound track index indicates which row to refer to in the co-ordinate matrices; these, one for x- and another for y-co-ordinates, are of size *n*-by-*f*, where *n* is the number of compound tracks, and *f* is the number of film frames. Thus, the co-ordinates of any sub-track can be obtained using the compound track index as the row, and the start and end frames as the first and last column, respectively, in the co-ordinate matrices.

There are two more matrices of which we should be aware; they are the "reclassified matrix" and the "statistics matrix": the former is the same as the sub-track matrix, but after reclassification of sub-tracks that were initially determined to be pausing as growth, and those that were considered to be shrinking as pause. If a sub-track is reclassified as growth from pause, then it is merged with the growth tracks that were adjacent to it (a pause, by definition,

must be flanked by growth); thus, the reclassified matrix tends to have fewer rows than the sub-track matrix, designated *m*. The reclassified matrix has some other differences to the sub-track matrix; first, sub-track lifetime is now in seconds, not frames, and displacement is in microns, not pixels. Moreover, the reclassified matrix contains additional information in three extra columns:

8. A logical (i.e., "yes" or "no") for nucleation, i.e., whether this is the first instance of the compound track or not
9. Only relevant for growth tracks, it indicates the event that resulted in the growth track ending (i.e., "termination", pause, shrinkage, or unclassified)
10. A logical for whether the sub-track is part of a compound track or not

The statistics matrix is called so because it contains the data that plusTipTracker uses for its statistics calculations. So as not to bias some of these statistics, for example nucleation rate, the sub-tracks that were detected in the first frame, and the first linked pause or shrinkage track, are removed, as are the sub-tracks that were present in the last frame, along with the last linked pause or shrinkage track. Therefore, it contains m_s rows, reduced from *m*, while the columns remain the same as in the reclassified matrix.

b. Sub-cellular analysis

In order to easily measure dynamics in central and peripheral areas, I designed an interactive tool in Matlab, called "analysetracks", that allows the user to delineate the areas, and then the tracks (so defined by plusTipTracker) in each area are then analysed. The algorithm runs thus:

1. User input: the first frame of the image, and the projData structure from plusTipTracker (this contains the matrices described above). Check that the image and projData structure match by plotting all tracks on the image and asking the user to verify they are correct (fig. 4).
2. Obtain original data from projData; among these are the pixel size, the number of and time between frames, and the sub-track, reclassified and statistics matrices described above.
3. Display the first frame and ask user to define the border of the cell by clicking on the image with the mouse at positions along the border. Clicks must be in a clockwise direction (since later parts of the process require that the direction of the points is known; see 6), and terminated with a click on the first point (fig. 4).
4. Ask the user to define a relevant cell axis by clicking on the first frame images, and then to enter a value for the "relative border size", the percentage of the length of the defined cell axis that will determine the "thickness" of the border region (fig. 5A).
5. Based on the cell axis and relative border size, the outer and inner borders are plotted on the image, and the user is asked to verify that they are happy with them (fig. 5B). The inner border is found by moving the specified distance from each vertex of the outer border, in the resultant direction of the edges adjacent to each vertex. Where two outer vertices are close together and the inner vertices result in crossed lines for

the inner border, the offending inner vertices are removed and replaced by the point at which the crossed lines intersect.

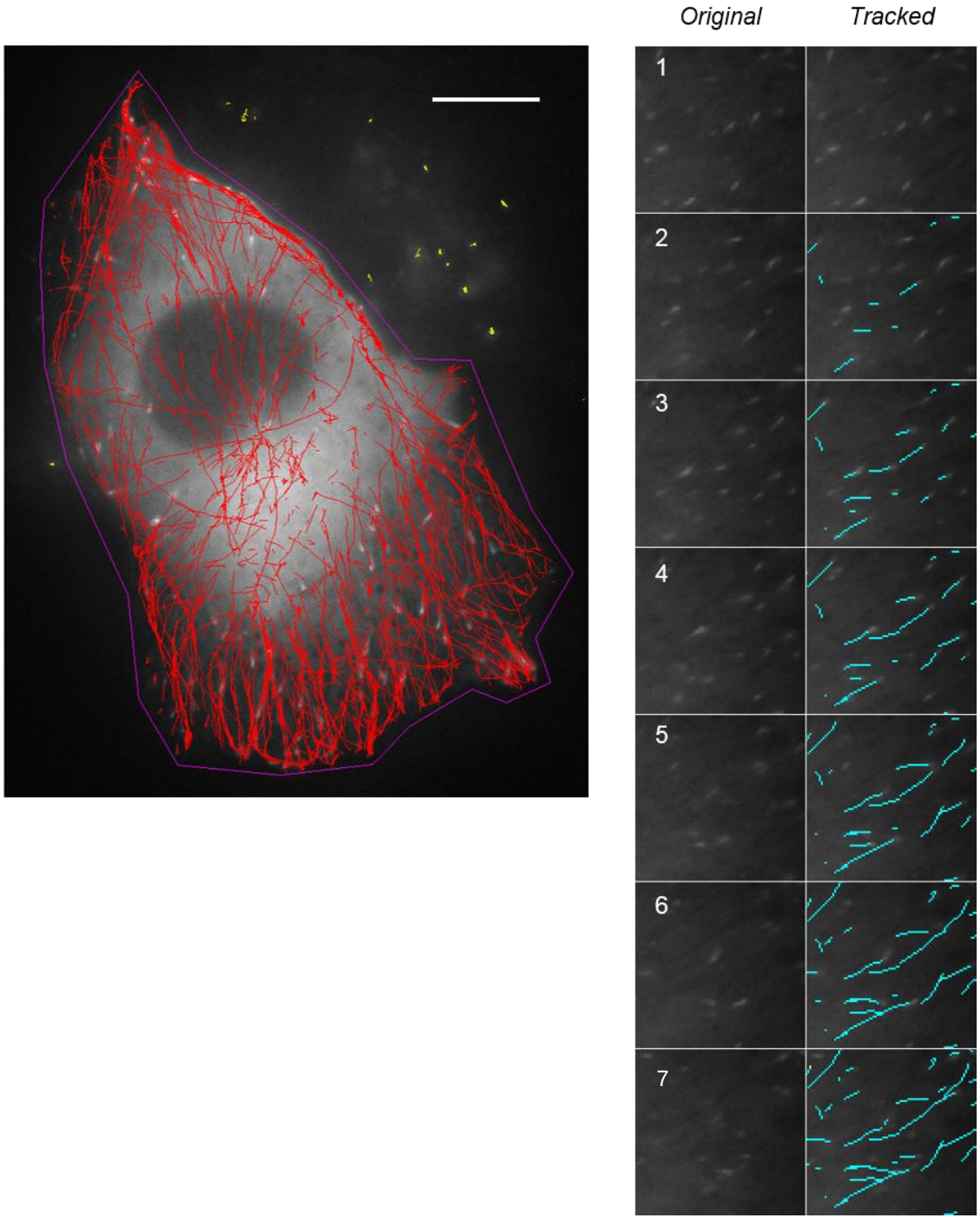

Figure 4. Example image and time-lapse. All tracks (red) and user-defined border (purple) plotted on left panel; **t**racks located outside border are coloured yellow. Scenes from frames (right panel, frames indicated by numbers) of a time-lapse film, showing untracked (left column) and tracked (cyan, right column) comets. Scale bar 10 μm. Image courtesy of Debbie Goldspink, Mogensen lab. Note that cell is in confluent culture, and not migrating.

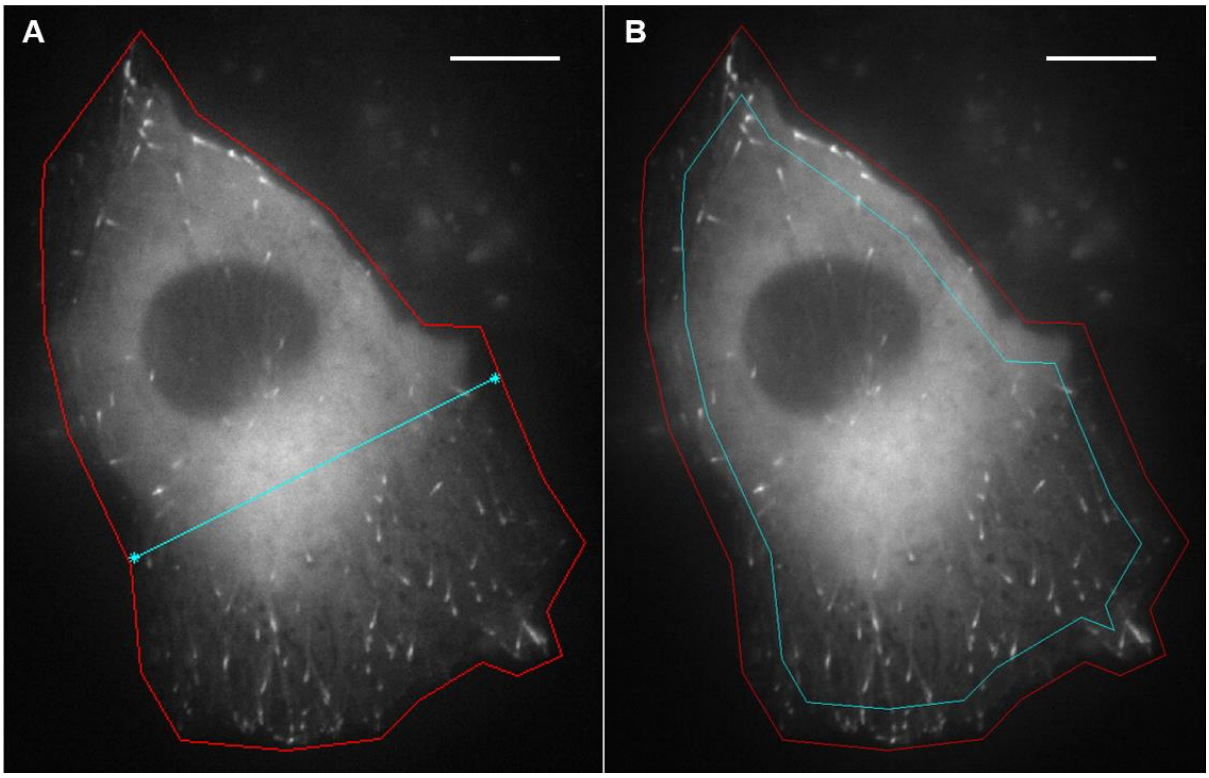

Figure 5. Defining the "inner border". The user defines a relevant cell axis (A, cyan) by clicking on the image with the outer border plotted (A, red), and these are then processed to produce the inner border (B, cyan), which, together with the outer border (B, red), defines a border region of the cell. Scale bar 10 μm. Images courtesy of Debbie Goldspink, Mogensen lab. Note that cell is in confluent culture, and not migrating.

6. Next, in order to identify which tracks, or which parts of a track, are in a given area, I use an algorithm based on defining the area by the midpoints of its edges and vectors that are orthogonal to each edge (fig. 6A). Here, for each co-ordinate of a track, the vectors from each midpoint to that co-ordinate are calculated, and the dot product of each of these with the corresponding orthogonal is found. If the co-ordinate is within the area, all of these dot products are positive, since the vectors from each edge midpoint point in the same direction as the edge orthogonal vectors, whereas if the co-ordinate is outside the area, then at least one of the dot products will be negative (fig. 6A). However, this algorithm only works for areas that are convex; thus, if the outer and inner regions are not convex already, they must be converted into a set of convex shapes. My algorithm for splitting the area into a set of convex shapes, based on a common "triangulation" method, is contained in the function "makeconvex". Briefly, it relies on the fact that the co-ordinates that define each area have been given in a clockwise direction. In fact, it does not matter whether it is clockwise or anti-clockwise, as long as the direction is always the same, and, just to confuse the issue, the directions are actually reversed in an image, since the y-axis runs in the other direction (i.e. y = 0 is at top-left). In Cartesian space, to identify a concave shape, we use the fact that in a convex shape, every angle between adjacent edges is always less than 180° in the anticlockwise direction. To convert the concave shape into a set of convex shapes, one draws a line from the right-turn to the next-but-one vertex (fig.

6A), so long as the next turn is not a right turn; if the next turn is a right turn, then the current right turn is abandoned until the next right turn is no longer a right turn by having made that sub-shape convex. Doing this iteratively gives the set of convex shapes (fig. 6B).

7. Now, for every track co-ordinate, the orthogonal dot-product test is conducted to determine if it lies within the area. This is done for the whole area, and the inner area alone. Those that are exclusive to the outer area are defined by being in the first set and not the second. Thus, there is now a set of arrays of tracks that lie within the defined areas.
8. Point 7 can produce tracks of a single point, if a track started in an area and then had left by the next frame, or moved into an area in its final frame, or indeed, briefly entered an area and then left by the next frame. These are removed.
9. The tracks are plotted in their areas and the user is asked to verify that they have been allocated to the correct area (fig. 7A).
10. Information about each set of tracks is collected. Such information includes the descriptive statistics regarding growth and shrinkage etc., much like the output of plusTipTracker, the orientations of each track at each frame, and the relative orientation between a comet trajectory and the nearest cell edge (fig 7B). For each track in a given area, its speed, displacement, lifetime, etc., are found by searching the reclassified matrix with the row and column indices of the co-ordinates of the track in that area; the statistics are based on these. The orientation of each track is found using the co-ordinates, which are defined in co-ordinate matrix described above, while the nearest edge is found by taking the edge with the minimum perpendicular distance to the co-ordinate.

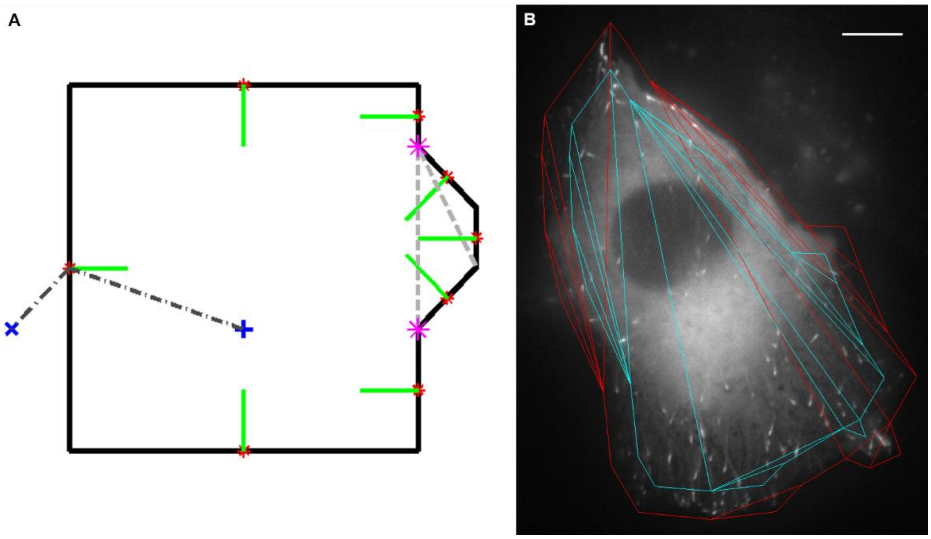

Figure 6. Convex shapes and the "orthogonal dot-product" method. A shape (A) is defined by its edge midpoints (red asterisks) and orthogonal vectors (green lines). If a point is inside the shape (blue plus), the dot products of each of the orthogonal vectors and the vectors from the midpoints to the point will be positive (example midpoint-point vector shown in dark grey dash-dot line to plus). If a point is outside the shape (blue cross), then at least one of the dot products of the orthogonal vectors and the vectors from the midpoints to the point will be negative (example negative midpoint-point vector shown in dark grey dash-dot line to cross). This algorithm requires convex shapes, so shapes with "left-turns" (in the clockwise case, shown here with magenta asterisks) must be split into convex sub-shapes (light grey dotted lines). An example image (B) is shown with outer (red) and inner (cyan) areas split into convex shapes. Scale bar 10 μm, images courtesy of Debbie Goldspink. Note that cell is in confluent culture, and not migrating.

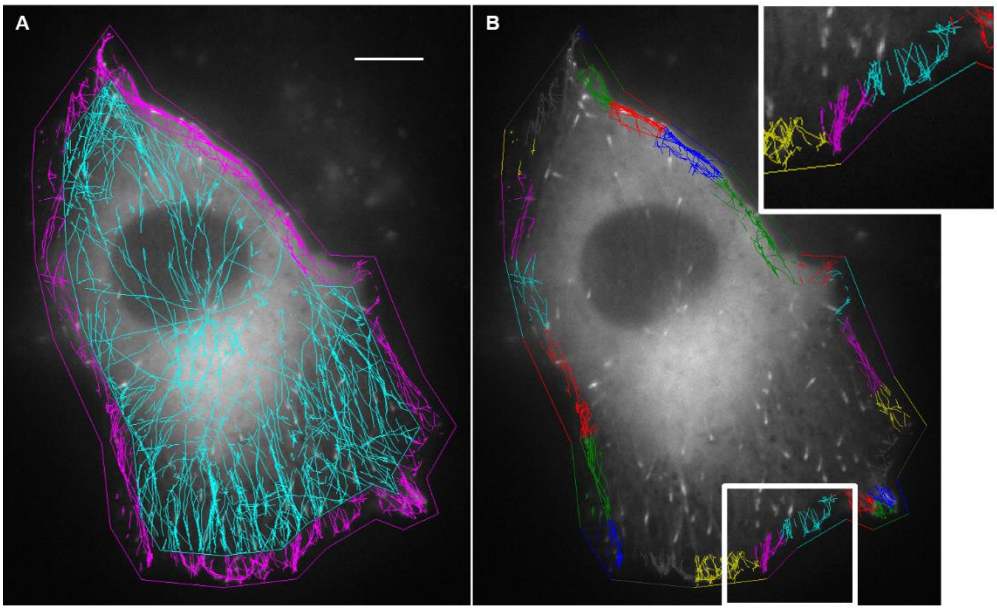

Figure 7. Area tracks and track-edge coupling. Tracks exclusive to the inner area (A, cyan) and outer area (A, magenta) are displayed, while the outer area tracks are colour-coded to indicate their closest edge (B, and enlarged area in white in inset). Scale bar 10 μm, images courtesy of Debbie Goldspink, Mogensen lab. Note that cell is in confluent culture, and not migrating.

II. Statistics and calculations

a. Microtubule dynamics

The data obtained from plusTipTracker and the subsequent processing as described in the previous sub-section can be used to make estimates of parameters used in traditional descriptions of microtubule dynamics, i.e. growth and shrinkage rates, and transition frequencies. A diagram of microtubule dynamics is shown in figure 8, with adjustments made to indicate the extent of information available from +TIP protein tracking.

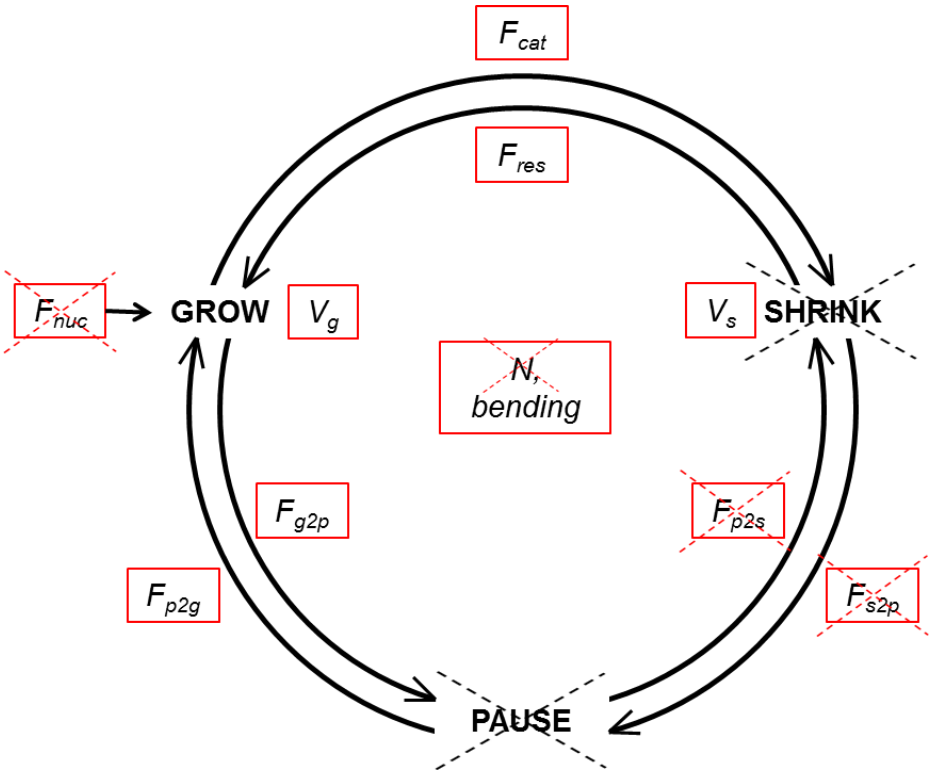

Figure 8. Microtubule dynamics parameters from plusTipTracker. Microtubules transit between the 3 phases shown in black capitals, with frequencies denoted by *F*. Nucleation frequency (F_{nuc}), microtubule number (*N*) and microtubule bending (*bending*) also affect organisation of the network. As with any labelled +Tip protein, plusTipTracker can only infer the characteristics of shrinkage and pausing (indicated by dashed black crosses), and thus, nothing can be said of the transitions between these states (indicated by dashed red crosses).

Growth and shrinkage rates are immediately obtainable; however, transition frequencies are estimated based upon the number of occurrences of a given transition, and the time spent in the phase it transits from:

$$F_{trans} = N_{trans}/t_{phase}, \quad (1)$$

where F_{trans} and N_{trans} are the frequency and total occurrences of a transition, respectively, and t_{phase} is the time spent in the phase that the transition moves away from. With the plusTipTracker data, as with any data set based on observation of +TIPs, where direct information concerning microtubule behaviour is only available for the growth phase, the estimation is subject to potential bias. This is because, e.g. both catastrophes that result in

extinction of the microtubule and those that are followed by rescue or a transition to the paused state, only catastrophes that are followed by a rescue event can be detected, where the +TIP protein re-labels the now growing end. This is in contrast to live recordings of labelled microtubules, where all phases can be observed directly, but it is not as easy to discriminate individual microtubules.

Thus, the catastrophe events that lead to extinction are lost; the catastrophe events that are followed by a transition to a pause event have two possible fates: either they will be lost, if the paused microtubule undergoes another catastrophe and then goes extinct, or they may be detected, if the pause event is followed by a rescue, or subsequent catastrophes and pauses are followed at some point by a rescue event. In the latter case, the shrinkage to pause and potential pause to shrinkage transitions, F_{s2p} and F_{p2s}, respectively, are never detected, and at the level of the plusTipTracker analysis, all that is recorded is one catastrophe event, a shrinkage rate with inaccuracy affected by the length of any pausing events, and one rescue event. Therefore, the estimated catastrophe frequency is affected by the rescue frequency, since it is rescue events that allow us to infer shrinkage and the preceding catastrophe, and so any estimate of catastrophe frequency based on this type of data is likely to be an underestimate.

While the estimation of catastrophe frequency is subject to inaccuracy because of inability to observe the true number of events, in theory, every rescue event should be observable. However, the estimate of rescue frequency is affected by a related problem: while for catastrophe, we can be fairly confident that we know the total time in the growth phase that we substitute into eq. 1, for F_{res}, we do not know the total time in the shrinking phase. Assuming that every rescue event is detected, i.e., the preceding growth and shrinkage phases were observed and inferred, respectively, estimates of rescue frequency based on these data are likely to be overestimates.

The same arguments apply to the growth to pause, and the reverse, transition, F_{g2p} and F_{p2g}, respectively, where, here, F_{p2g} estimation suffers from the same problems as those in estimating F_{cat}, and F_{p2g} is affected by similar problems for estimating F_{res}.

Therefore, when calculating transition frequency estimates with eq. 1, when based on this type of data, these caveats must be kept in mind. A means of addressing the discrepancies between catastrophe and rescue (or grow to pause and pause to grow) frequency estimates, i.e., the tendency to underestimate the former, and overestimate the latter, is to use only the growth or shrinkage times preceding the catastrophe (or grow to pause) or rescue (or pause to grow). In absolute terms, these estimates are still inaccurate, because the times of growth or shrinkage in eq. 1 will not the total time; rather, just the time of a subset of tracks, and estimates of both transition frequencies will be liable to overestimation. However, in relative terms, the transition frequencies are now more comparable, since the catastrophe frequency is based now only on the time preceding it, as is the estimate of rescue frequency. Indeed, these types of estimates may be more valid for calculations of drift (see below), etc. Both types of estimate will be calculated and presented in the results.

Transition frequencies calculated according to eq. 1 can be used to obtain a probability distribution for the transition in question, as long as it is assumed that the probability of that transition is the same through the lifetime of a microtubule (see the next chapter for a thorough discussion of this). However, it is also possible, if the distribution of microtubule lifetimes prior to a particular transition is considered, to obtain such a probability distribution directly. In this case, rather than making assumptions about the type of distribution describing the lifetimes before transition, we could fit a distribution to the lifetimes. Such an approach is potentially possible with the methods outlined in the previous sub-section. However, as reported in the results section below, there were not enough data recorded for such an analysis.

b. Track and edge relative orientation

The relative orientation of track segments, i.e. the difference in orientation between segments, was found by first calculating orientations based on the x- and y-coordinates of tracks, and then finding the absolute difference between adjacent segments. The relative orientation between a track and its nearest edge was found in a similar manner.

For generation of the "straight" track data, tracks were split where a relative orientation was greater than a given threshold. To avoid extensive data manipulation, the co-ordinate matrices were not altered, i.e., upon track splitting, the compound track remains the same, but the start and end frame references change in the sub-track matrix. Relative orientations are only valid for growth tracks, so velocities, lifetimes and distances of only growing tracks are re-calculated. Entries in the new sub-track matrix that are only one frame long are removed.

Unfortunately, splitting tracks in this manner means they can no longer be linked to pausing and shrinking tracks, and thus, the straight data is intended purely as a means of ascertaining whether the growth properties of tracks with low relative orientations differ to the original growth properties.

Fitting of probability distributions to the relative orientation data was conducted in Matlab, making use of the interactive distribution-fitting tool, "dfittool". Visual analysis in the interactive tool was used to determine that all available parametric distributions excluding the generalised pareto and exponential were not good fits; subsequent analyses of these distributions are reported in the results. The non-parametric kernel-based approach was also used: here, to obtain a relatively smooth probability distribution, the empirical data is smoothed by a kernel with a given "bandwidth"; the bandwidth value can be set or determined according to which produces the best fit; here, the latter approach was used. A higher bandwidth produces a smoother function, but potentially at the expense of worse representation of the empirical data.

C. RESULTS

I. Track orientation

a. Straight vs. bendy tracks

The aim of this section is to characterise the "orientation behaviour" of microtubules, i.e. essentially to answer the question: how bendy are growing microtubules? This question is applied to both experimental conditions, all tracks, and inner and outer areas. After post-processing of data obtained from plusTipTracker (see methodology), the total numbers of tracks analysed here were 16,205 and 14,548 in the control condition, for original and "straight" tracks, respectively, and 15,155 and 13,341 in the Rac1-inhibited condition for original and "straight" tracks respectively.

Figure 9 shows histograms of the relative orientation between adjacent segments of tracks for all tracks, and tracks from outer and inner areas. Here, the data for each experimental condition has been pooled. Evident in the histograms in figure 9 is the fact that a higher proportion of relative orientations are lower for control data, and in the Rac1-inhibited cells, there is a greater proportion of larger relative orientations. This is true for all areas, so control tracks are generally straighter than Rac1-inhibited tracks.

There is an increase, in both experimental conditions in all areas, in proportions of relative orientations from about 120° to 180°. This is unusual, since these are very large angles for a microtubule to subtend in a short length segment. For example, an average growth of 12.67 μm min^{-1} over a frame length of 2.5 s, gives a distance of ~0.5 μm. Of course this distance, which is the direct route between two points of growth, may not truly represent the length of the microtubule in question, since the microtubule can bend, and does not have to go directly between the two points. Therefore, if we assume that any two orientations in a track define 3 points on a circle joined by two chords of length 0.5 μm, the radius of this circle is the radius of curvature required of a microtubule to pass through these points. A relative orientation of 120° would require a radius of curvature of ~0.3 μm, half the value at which microtubules have been observed to break (Waterman-Storer and Salmon, 1997). Faster-growing microtubules require a lower radius of curvature for any given relative orientation, e.g., a growth speed of 20 μm min^{-1} giving a distance of ~0.8 μm, could pass through the same 3 points with a radius of curvature of ~0.5 μm. Incidentally, these large relative orientations are greater than the threshold value specified in plusTipTracker. The source of this apparent error is unclear.

Do overly deviating tracks influence microtubule dynamics? An extensive presentation of the dynamics results is given in the next sub-section; however, efforts were made here to address this question by splitting tracks (see methodology) at points where the relative orientation was above a threshold of 60°. This value was chosen because, although the relative orientation that satisfies the constraints discussed in the paragraph above at the average speed of 12.67 μm min^{-1} is approximately 30°, the above discussion is very much an approximate account of relative orientation constraints, and moreover, although much of the data is below 30°, still a lot of the data would be discarded, and the intermediate relative

orientations between 30° and 60° may represent true trajectories. The original and "straight" data are compared in figure 10 and tables I-III.

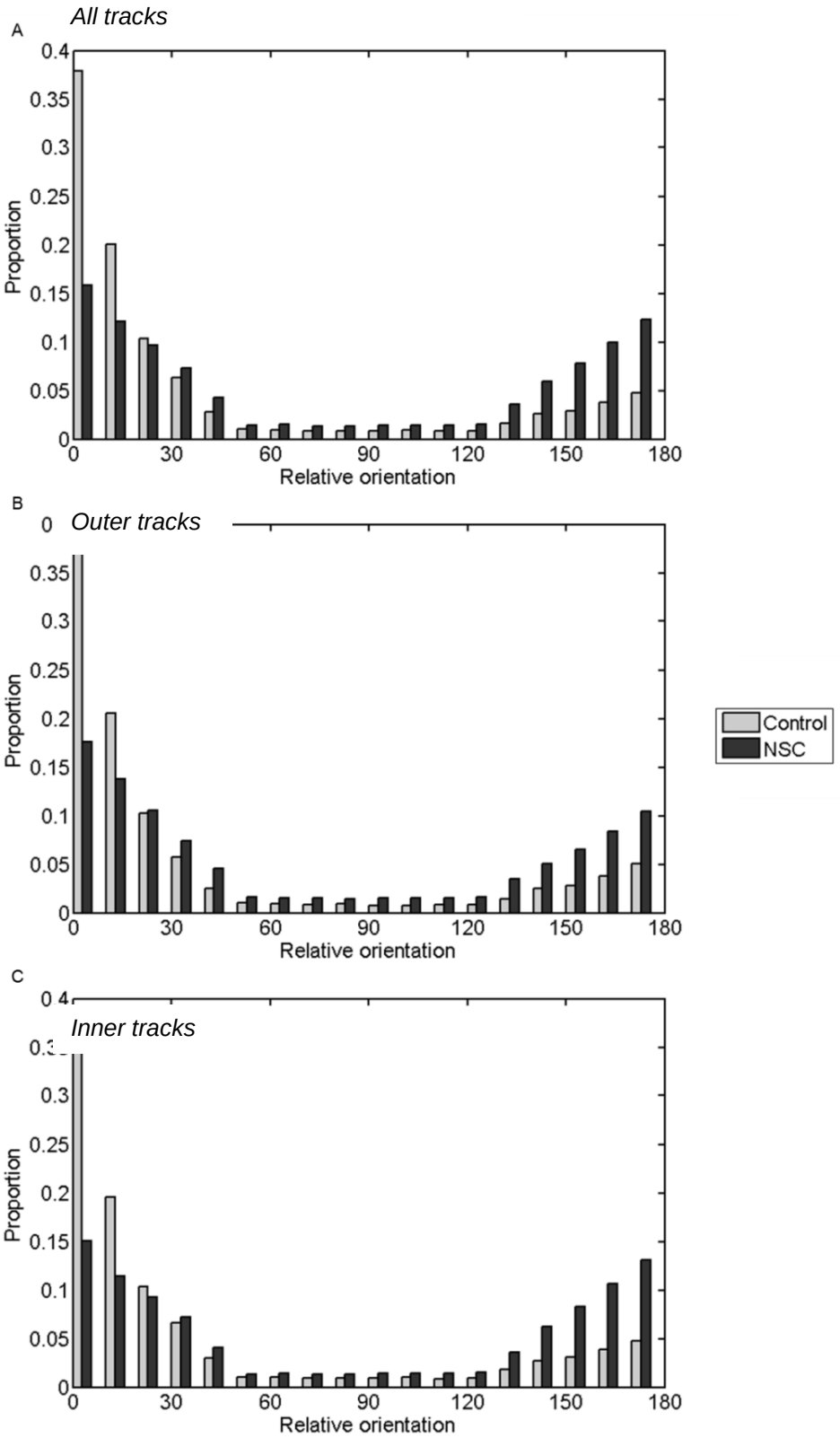

Figure 9. Histograms of relative orientation. The proportion of all data is given for differences between adjacent track segments, in bins of 10°, for all (A), outer (B) and inner (C) control and Rac1-inhibited (NSC) tracks.

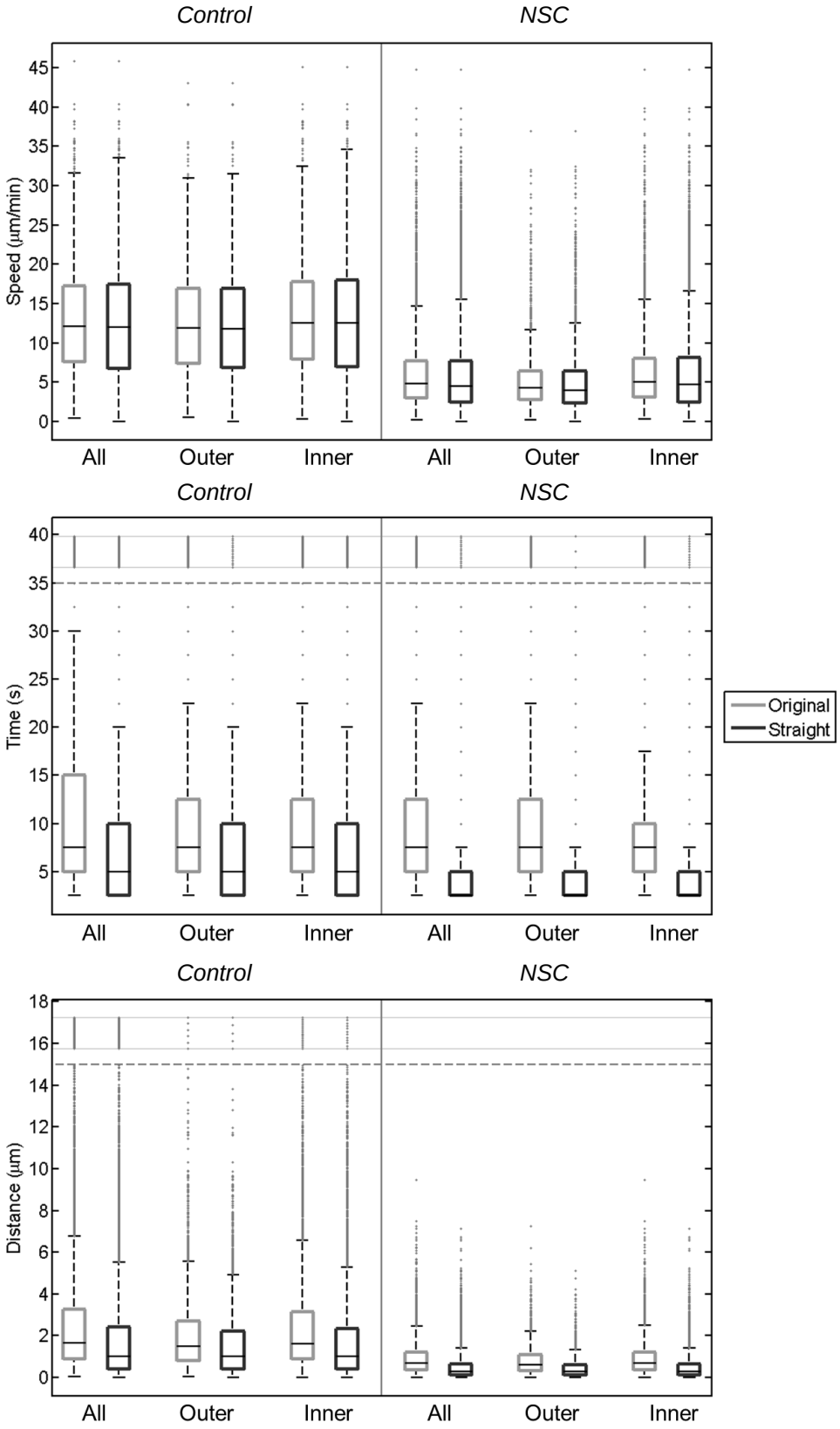

Figure 10. Track characteristics in original and straight data. Growth speed, time and distance are shown for original and "straight" data for both control (left panels) and Rac1-inhibited (NSC, right panels) cells. Lines are median values, boxes extend to 25th and 75th percentiles (q1 and q3, respectively), whiskers to q1 – 1.5(q3 – q1) q3 + 1.5(q3 – q1).

Table I. Growth speed of original and straight tracks. Median values and the inter-quartile range (IQR) for each area in each experimental condition (control and NSC), before (original) and after splitting of overly deviating tracks (straight), are shown.

	All		**Outer**		**Inner**	
	Original	Straight	Original	Straight	Original	Straight
Control						
Median	12.09	11.98	11.89	11.78	12.57	12.50
IQR	9.61	10.72	9.51	10.03	9.92	11.04
NSC						
Median	4.80	4.50	4.26	4.00	5.00	4.70
IQR	4.65	5.22	3.59	4.06	4.98	5.66

Table II. Growth time of original and straight tracks. Median values and the inter-quartile range (IQR) for each area in each experimental condition, before (original) and after splitting of overly deviating tracks (straight), are shown.

	All		**Outer**		**Inner**	
	Original	Straight	Original	Straight	Original	Straight
Control						
Median	7.50	5.00	7.50	5.00	7.50	5.00
IQR	10.00	7.50	7.50	7.50	7.50	7.50
NSC						
Median	7.50	2.50	7.50	2.50	7.50	2.50
IQR	7.50	2.50	7.50	2.50	5.00	2.50

Table III. Growth distance of original and straight tracks. Median values and the inter-quartile range (IQR) for each area in each experimental condition, before (original) and after splitting of overly deviating tracks (straight), are shown.

	All		**Outer**		**Inner**	
	Original	Straight	Original	Straight	Original	Straight
Control						
Median	1.65	1.02	1.50	1.00	1.60	1.01
IQR	2.36	2.05	1.90	1.80	2.27	1.96
NSC						
Median	0.69	0.28	0.60	0.28	0.70	0.28
IQR	0.84	0.51	0.76	0.48	0.85	0.51

As figure 10 and tables I-III show, there is a consistent decrease in median values for growth speed, time and distance in the straight tracks compared to the original tracks. This is true for both experimental conditions. As is the case with the original data, the straight data was not normally distributed (Chi-squared test, $p < 0.05$). The differences between the original and straight data were significant for time and distance (Wilcoxon rank sum test, $p < 0.01$).

Therefore, tracks with lower intra-segment relative orientation grow more slowly, for less time and distance, than tracks with greater intra-segment relative orientation. The decrease in time and distance was expected due to the splitting of tracks between segments with high relative orientation. The decrease in average speed must result from exclusion from the straight data of faster parts of tracks; exclusion can result either from the splitting, whereby the portion of the track between two frames that have now been put into different tracks is no longer considered, or from removal of serial segments that have high relative orientation.

As the straight growth tracks cannot be linked with tracks allocated to other phases, nothing can be said of the characteristics of pausing and shrinkage in straight tracks. Additionally, the trajectories of pausing and shrinkage tracks are of course inferred from flanking growth tracks, so it does not make a great deal of sense to commit these phases to the same kind of analysis as above.

b. Orientation distribution

To quantitatively describe the relative orientation of each experimental condition and intracellular area, selected probability distributions were fit to the data. To avoid overtly complex probability models, only relative orientation data up to 60° were considered. Also, it was found that all completely straight adjacent segments (i.e. 0° relative orientation) were attributable to those tracks that were originally allocated as pausing tracks but re-assigned to growing tracks (see methodology for plusTipTracker data description) by plusTipTracker; thus, all zero relative orientation data were removed.

For each experimental condition or area, the proportions of relative orientations in bins of 5° were found; this type of data is analogous to a probability density function. These data are shown in figures 11 and 12 for control and Rac1-inhibited conditions, respectively. In finding an appropriate probability distribution, visual inspection of the probability density distributions, which decreased rapidly and then levelled off with increasing relative orientation, suggested that an exponential distribution might be a good representative model. Further analysis (see methods) suggested that a generalised Pareto distribution may also be an appropriate fit. Random numbers ($n = 20{,}000$) taken from these distributions were plotted as proportions over the probability densities (figs. 11 & 12 Ai & Bi), or in cumulative distributions (figs. 11 & 12 Aii & Bii). Although in many cases, both of these distributions appeared to the fit the data quite well, they were both found to be significantly different from the empirical data in all cases (2-sample Kolmogorov-Smirnov test, $p < 0.05$).

Other standard distributions also did not fit the data well (methods), and so a non-parametric, smoothing kernel-based approach was adopted (again, see methods for details). Bandwidth values for the best-fitting distributions are shown in table IV. The kernel probability

distribution fits are also shown in figures 11Ci-ii and 12Ci-ii. Visual inspection of these distributions suggests that they provide better fits of the data, and indeed, they were significantly similar to the data in every case (2-sample Kolmogorov-Smirnov test, $p > 0.05$).

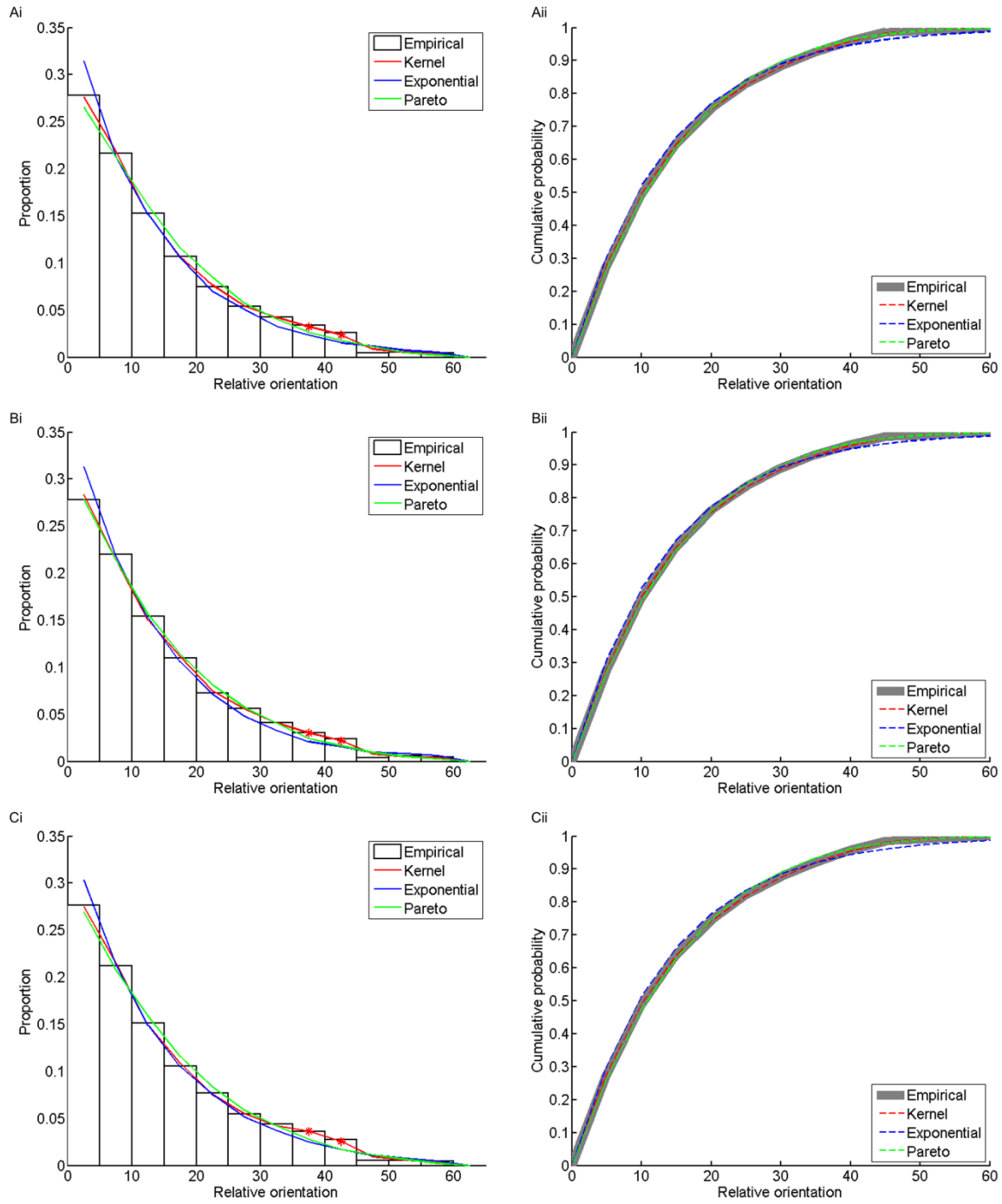

Figure 11. Control proportions and cumulative distribution functions. For all tracks (A) and outer (B) and inner (C) areas, empirical proportions sampled distributions (i) and empirical and modelled cumulative distribution functions (ii) are shown.

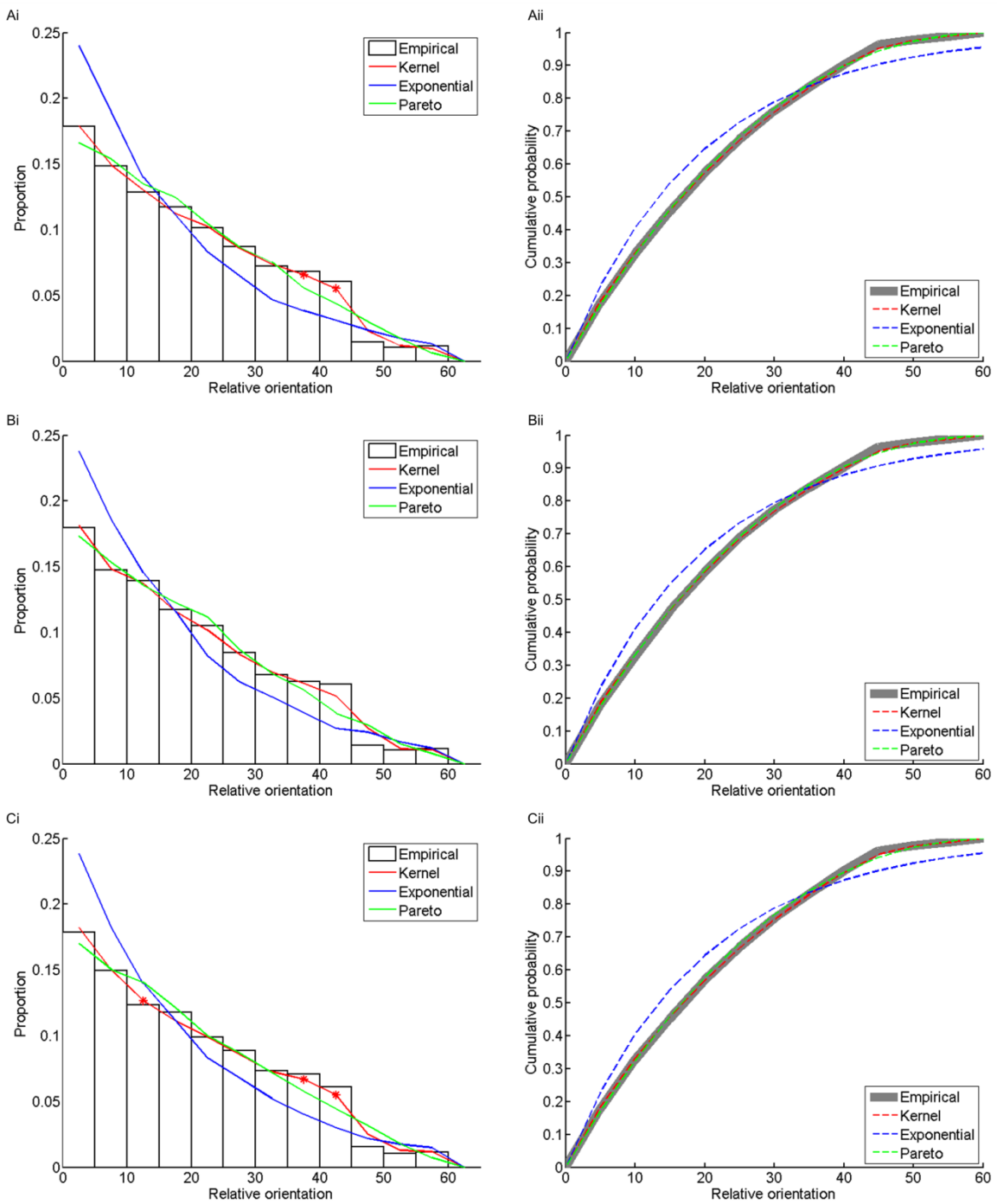

Figure 12. Rac1-inhibited proportions and cumulative distribution functions. For all tracks (A) and outer (B) and inner (C) areas, empirical proportions sampled distributions (i) and empirical and modelled cumulative distribution functions (ii) are shown.

Table IV. Bandwidth values for kernel-based probability distributions. Values for control and Rac1-inhibited (NSC) conditions for each area, so determined by best fitting.

Condition	All	Outer	Inner
Control	0.186	0.232	0.206
NSC	0.232	0.284	0.255

It makes sense to test only the relative orientations of control and Rac1-inhibited tracks in inner and all tracks groups; these are not normally distributed (Kolmogorov-Smirnov test, $p < 0.05$), and differ significantly (2-sample Kolmogorov-Smirnov test, $p < 0.001$). The proportions of relative orientations in bins of 5° show that there is little difference (fig. 13) between intracellular areas: the relative orientation data are not significantly different between areas (2-sample Kolmogorov-Smirnov test, $p > 0.05$).

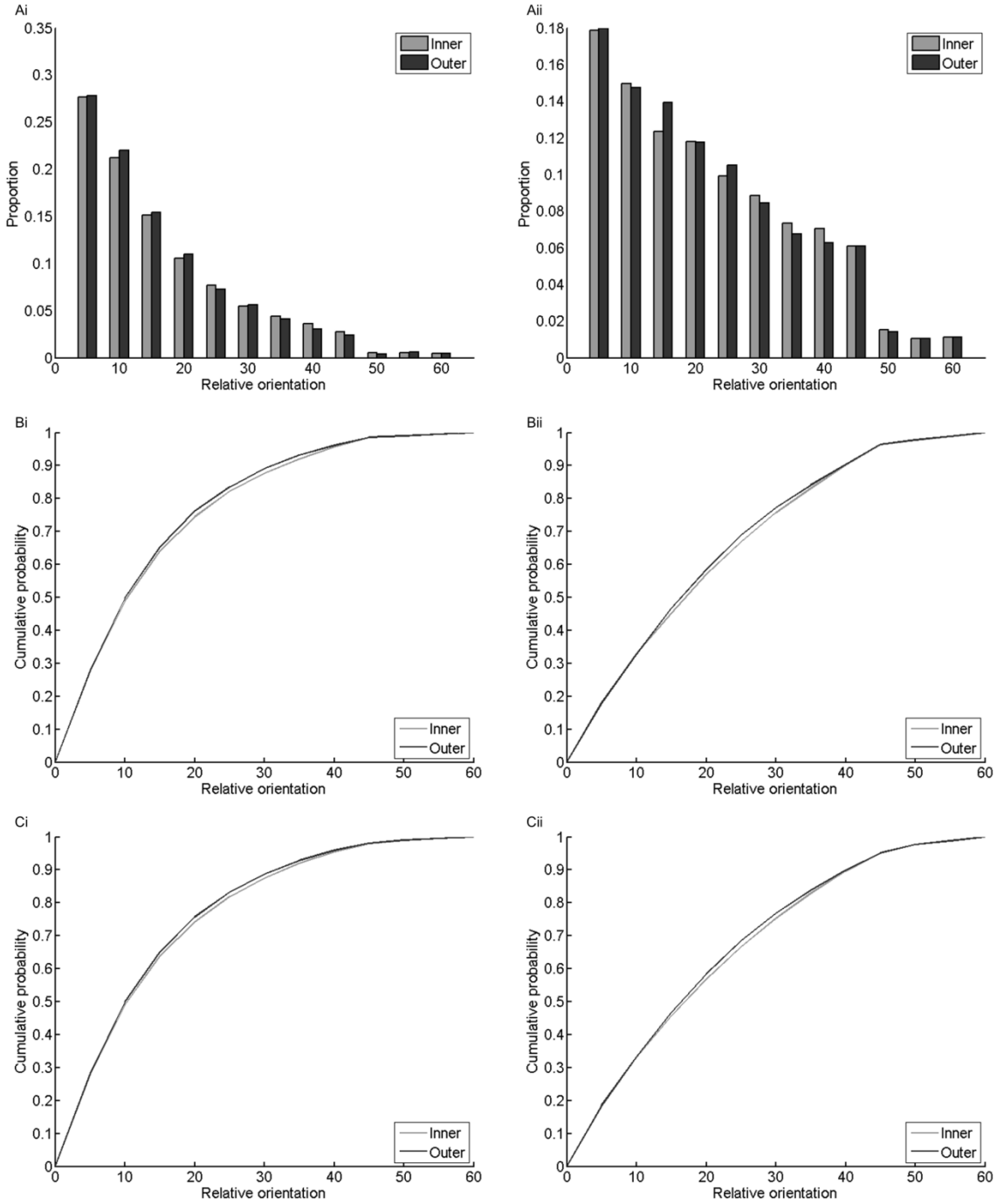

Figure 13. Proportions and cumulative distribution functions by area. For control (i) and Rac1-inhibited (ii) conditions, the proportions (A), empirical (B) and modelled (C) cumulative distribution functions are shown for outer and inner areas.

c. Cortical approach orientation

In this section, the orientation of comet tracks relative to the cell edges is considered. As with the previous analyses of orientation, tracks were split according to the relative orientation between adjacent segments. Since these tracks are close to the cell edge, a greater allowance was made for microtubule bending, and the threshold was set at 90°.

First of all, the edge-relative orientation as a function of the distance between a comet and the edge is considered. Here, the depth of each outer area was normalised so as to allow pooling of the data for each condition; thus, a value of 1 is the farthest point from the edge, and 0 is right upon the edge. The distribution of comets was found for discrete groups: distance was split into 10 groups of size 0.1 – "normalised groups", and relative orientation was split into 18 groups of size 10°. For each of these groups, the number of comets, or rather, instances of a comet (i.e. the appearance of a comet in one frame) was found, and normalised to the maximum count.

Heat maps of the comet counts are shown in figure 14A & B for control and Rac1-inhibited, respectively. Here we see that the greatest number of comets occurs at approximately 0°, i.e. parallel to the edge. In the control condition, this maximum is shifted closer to the edge relative to the other condition. There are more comets in both conditions on the positive orientation side, indicating that more microtubules do grow toward the edge rather than away from it, and again, in the control condition, these higher values are shifted closer to the edge relative to the other condition.

Another way of representing the data is to express the counts relative to the maximum value in each discrete distance bin. This reveals the distribution of comets at each distance (fig. 14 C & D). In this case, the heat maps differ to a greater extent; we see that at greater distances in the control condition, there are the highest numbers of comets at high positive angles, indicating that microtubules grow predominantly perpendicular to the edge up until around the 0.5 distance mark. In the Rac1-inhibited condition, however, although there are more comets at high positive orientations at greater distances than negative orientations, the maxima occur closer to the 0° mark, indicating that in this condition, microtubules tend to grow predominantly parallel to the edge even at greater distances.

Finding the resultant relative direction at each discrete distance supports the conclusions made above (fig. 15A). Here, the resultant direction of control comets relative to the edge is towards the cell edge more than in the Rac1-inhibited condition, and this difference is marked for the first 5 distance groups, i.e. 0.5 – 1.0 in normalised distance.

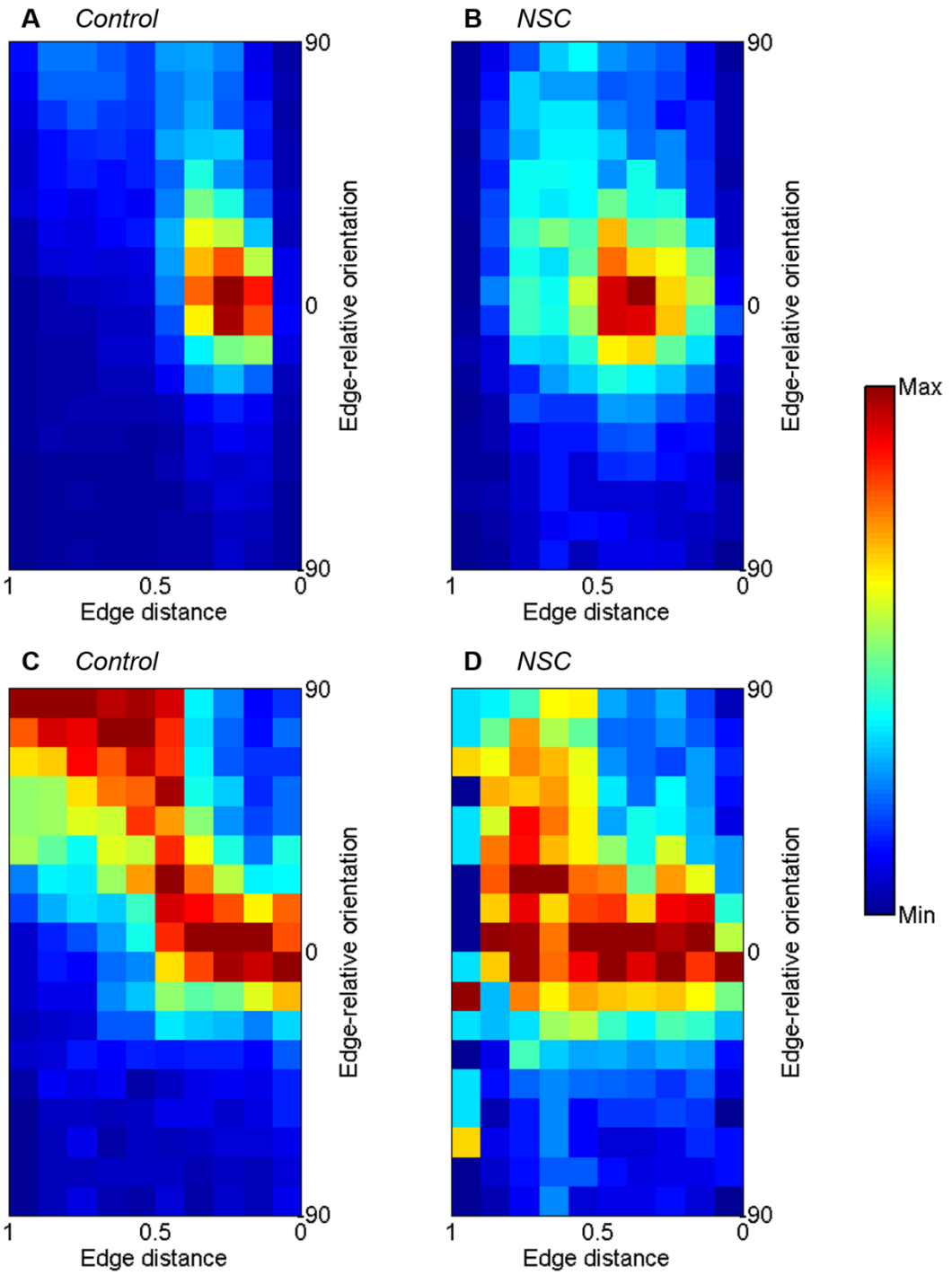

Figure 14. Heat maps of comet orientation relative to cell edge (previous page). Colours indicate the numbers of comets relative to the maximum (refer to colour bar) for all orientation and distance bins (A & B, for control and Rac1-inhibited conditions respectively), and for each distance bin (C & D, for control and Rac1-inhibited conditions respectively), i.e. the top row colours depend on the ratio of comets in a given bin compared to the bin with the highest number of comets overall, while the bottom row colours depend only on ratios compared to the bin with highest number of comets in a given distance bin. The concentration of "hot" colours around 0° in D indicates that Rac1-inhibited cells take shallower approach angles that control comets (C).

Forgetting the distance groups and taking the proportion of comets in each orientation group, there is a higher proportion of comets with edge-relative orientations in the region of 90°-60° than in the Rac1-inhibited group (fig. 15B). For many of the other orientation groups, proportions are similar between the conditions; however, the proportion of comets in the control condition that are oriented at -90° to -30° is much less than in the other condition.

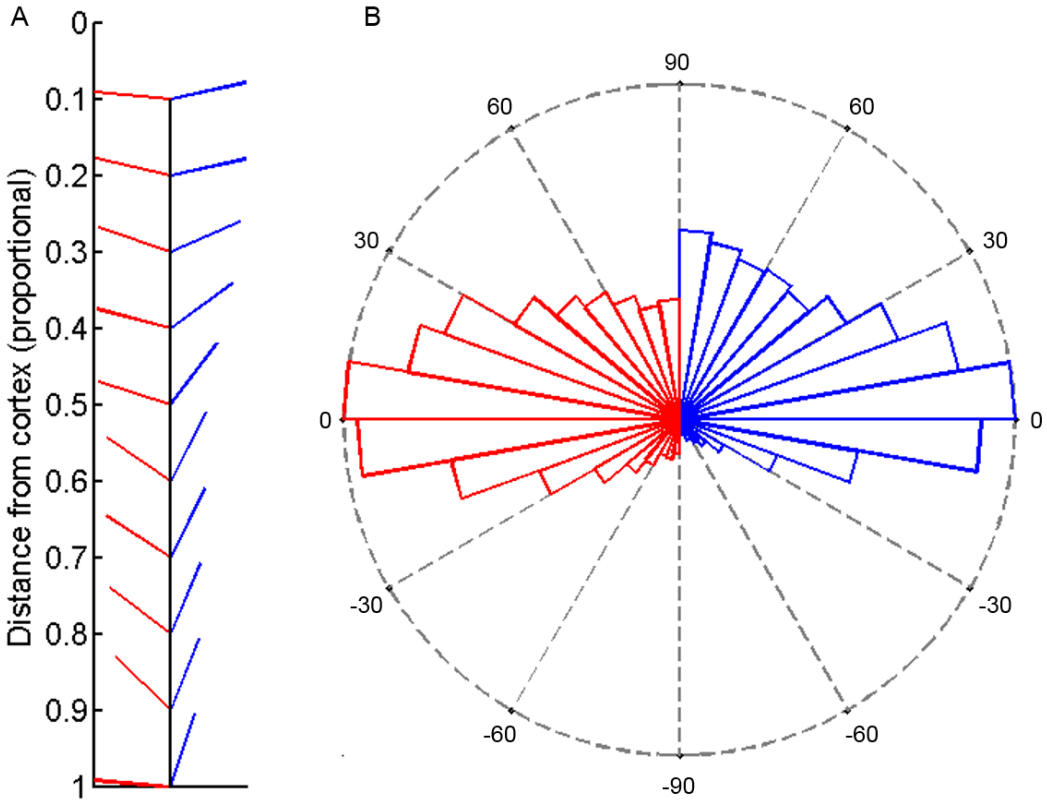

Figure 15. Resultant edge-relative comet orientations. The resultant direction at each distance bin, from 1 to 0 in bins of size 0.1, for control (blue) and Rac1-inhibited (red) conditions (A), and the proportion of comets in each direction bin for control (blue) and Rac1-inhibited (red) (B). Units in B are degrees.

Histograms of the edge-relative orientation for all edge distances, and for the closest and farthest 5 bins, demonstrate further the differences and similarities between treatments seen in the preceding figures (fig. 16). Here, for all edge distances, proportions of comets are similar between conditions apart from the high positive relative orientations (fig. 16A), whereas for the furthest distances (bins 1 – 0.5), the conditions have an entirely different distribution (fig. 16B), and in the closest distances (bins 0.5 – 0), the conditions again have similar distributions, perhaps more so than for all distances (fig. 16C). Despite the similarities in some cases, the differences in edge-relative orientations were significant (Wilcoxon rank sum test, $p < 0.001$), after establishing non-normality (Chi-squared test, $p < 0.05$). Therefore, control condition microtubules generally grow at greater angles relative to

the cell edge, and this difference is accentuated at the farthest distance away from the cell edge, within the outer areas.

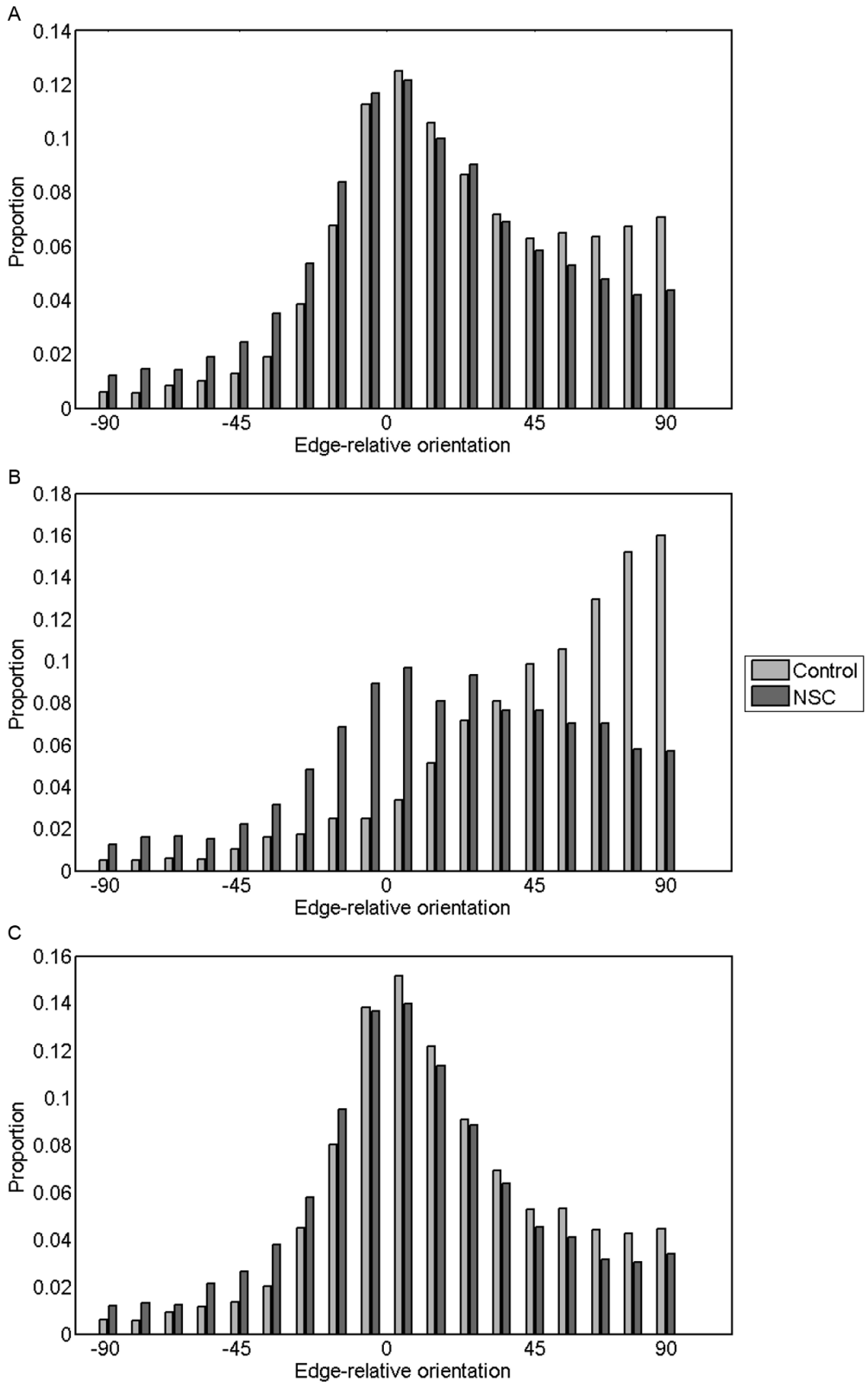

Figure 16. Edge-relative comet orientation histograms. The relative orientation of comets for each experimental condition, for all edge distances (A), the farthest 5 distance bins (B) and the closest 5 bins (C).

Another means of quantifying the edge-relative comet orientation is to take the proportion of comet tracks that point toward the cell edge; this measure is similar to the radiality measure discussed above. Figure 17 shows the cumulative sums of the proportions of comets in each orientation bin of size 10°. Here, the steeper slopes indicate greater accumulation of tracks, and thus, a higher propotion. Thus, the Rac1-inhibited condition has a greater proportion between -90° and approximately -30°, while the steeper slope in the control condition above 45° indicates that there are a higher proportion of tracks there. The radiality, based on varying levels of threshold edge-relative orientations, is shown in table V. This shows that the control treatment has consistently higher radiality scores than the Rac1-inhibited condition.

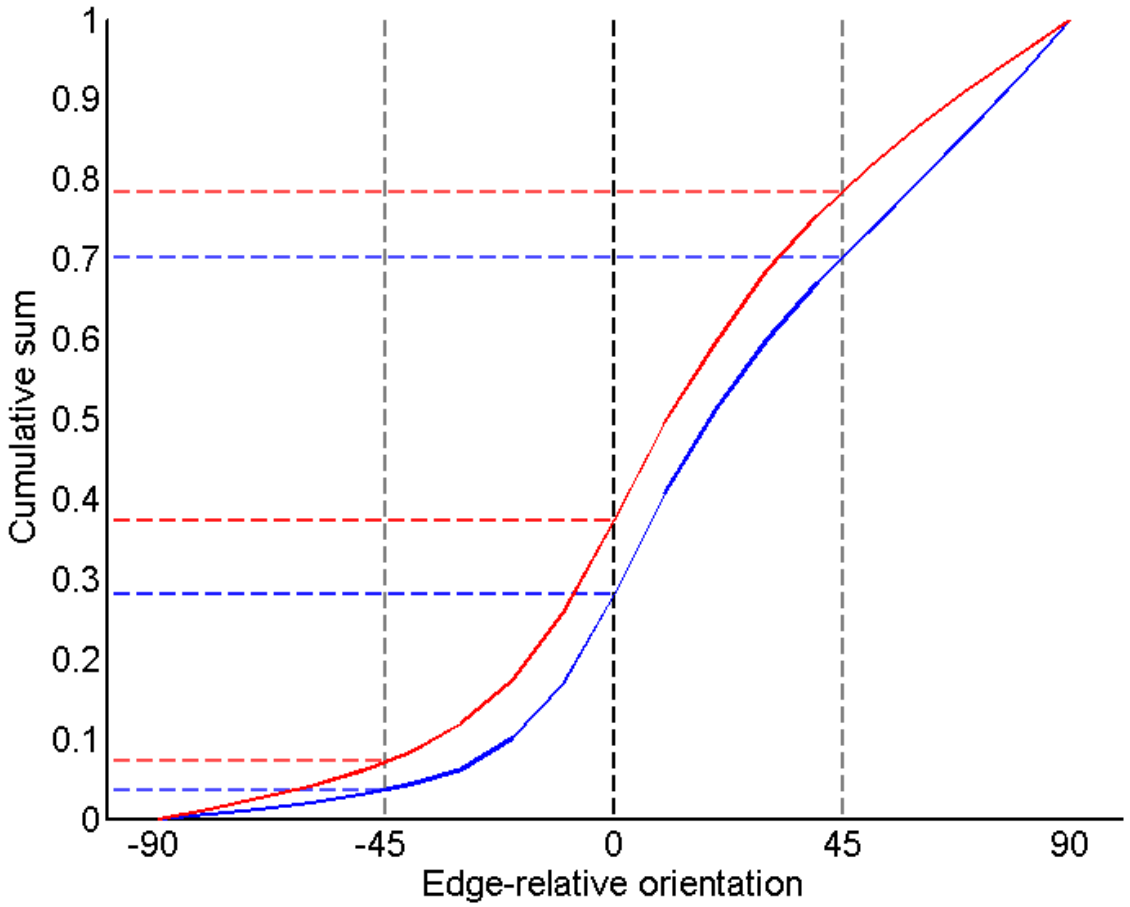

Figure 17. Cumulative sums of edge-relative orientation. Shown for control (blue) and Rac1-inhibited (red). Dashed lines correspond to thresholds shown in table V.

Table V. Radiality of outer area comets. Proportions of comets oriented relative to the cell edge above threshold values, θ, are shown for control and Rac1-inhibited (NSC) conditions.

	Proportion	
Edge-relative orientation	Control	NSC
θ > -45°	0.9505	0.9034
θ > 0°	0.7189	0.6261
θ > 45°	0.2350	0.1574

II. Microtubule dynamics

a. Whole-cell microtubule properties

In this section, microtubule properties over the whole cell are considered. Although in the previous section, the orientation data showed that a small proportion of the tracks appear to deviate by a rather great extent, there is no thorough means of dealing with these overly-deviating tracks when it comes to the analysis of microtubule dynamics. Since shrinking and pausing phases are inferred between episodes of growth, splitting tracks according to relative orientation criteria effectively disconnects these tracks, and the pausing and shrinking phases are lost. Therefore, the subsequent analysis is based on all of the data.

First, the speeds, times and distances for each microtubule phase are considered. The data for all similar areas were pooled, i.e. for each treatment, all data for the inner tracks were put together, as were those for the outer tracks, and all tracks. The mean values for each treatment (i.e. using the pooled data) are shown in table VI and figure 18. All data sets were found to be non-normally distributed (Chi-squared test, $p < 0.01$). Note that, despite this non-normality, the mean values are reported because the mean is reported in the literature. Growth speed, time and distance and pause time (see terms list) were significantly decreased in the Rac1-inhibited condition (Wilcoxon rank sum test, $p < 0.01$).

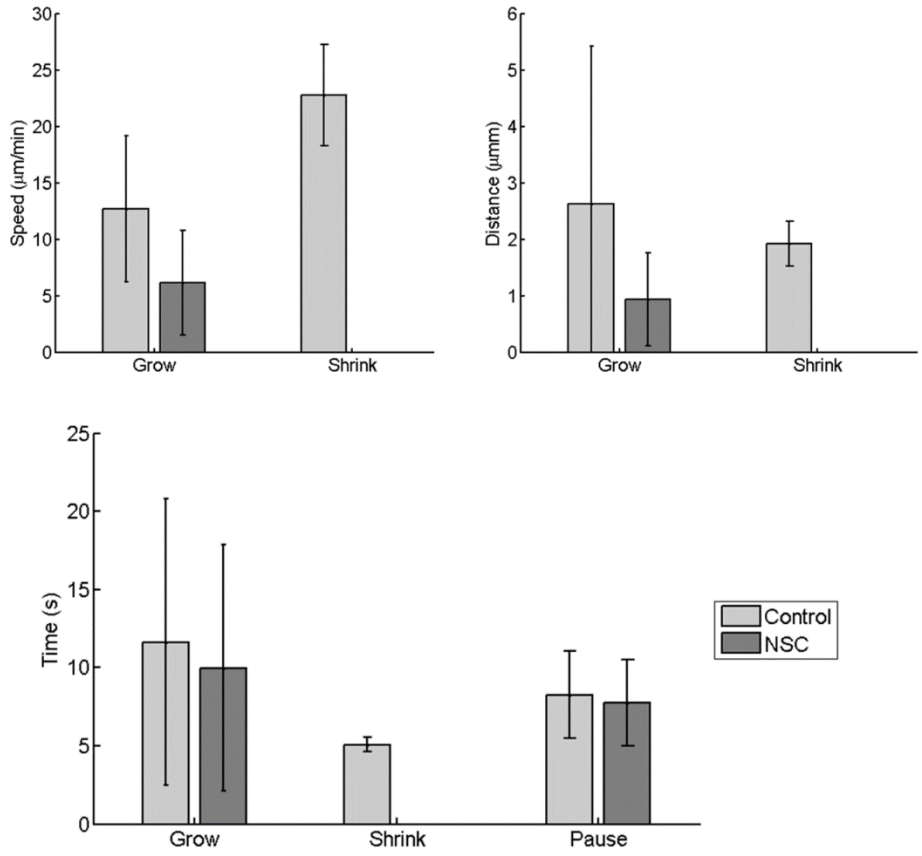

Figure 18. Average values of speed, distance and time for pooled data. All tracks data were used to calculate mean values for applicable phases for control and Rac1-inhibited (NSC) cells. Error bars are standard deviation.

Table VI. Average values of speed, distance and time for pooled data. The mean values, for applicable phases, of data from all tracks for control and Rac1-inhibited (NSC) cells, ± the standard deviation. Units are μm min^{-1} (speed), s (time) and μm (distance).

	Control	**NSC**
Grow		
Speed	12.67 ± 6.47	6.12 ± 4.64
Time	11.63 ± 9.18	9.98 ± 7.87
Distance	2.63 ± 2.80	0.93 ± 0.82
Shrink		
Speed	22.76 ± 4.50	-
Time	5.08 ± 0.46	-
Distance	1.93 ± 0.40	-
Pause		
Time	8.26 ± 2.78	7.77 ± 2.76

b. Microtubule properties by area

The same properties, for each area in both experimental conditions, are shown in table VII and figure 19. The all track data is repeated for ease of comparison with the inner and outer track data. The difference between experimental conditions found in the all track data is also evident in the area data, where the values for similar areas are all greater in the control condition than those for the Rac1-inhibited condition.

Comparing within-treatment values, in the control condition, the inner area growth speed, distance and time are all greater than in the outer area, as is the pausing time, while the speed of shrinkage is greater in the outer area, and although shrinkage time is reduced in the outer area, the distance is narrowly greater there. For the Rac1-inhibited data, we see that growth speed and distance are greater for the inner area, while growth time is greater for the outer area. As in the control cells, pause time is greater in the inner area.

The results presented in table VII were subject to statistical testing. Upon tests for normality, all data sets were either found to be non-normal (Chi-squared test, $p < 0.05$) or had too few entries (the shrinkage data sets for control cells) to conduct a proper normality test. The collected data, i.e., all areas for each experimental condition for a single measure, e.g., growth time (except shrinkage data, which was not assessed for Rac1-inhibited cells) was then non-parametrically tested for significant differences. The data for growth speed, time and distance, and pause time were found to have a significant difference (Kruskal-Wallis test, $p < 0.05$), while none of the shrinkage properties were found to be significantly different (Kruskal-Wallis test, $p > 0.05$). Next, intra-data comparisons were conducted for the growth and pause data; these were: 1. all tracks, control vs. Rac1-inhibited, 2. outer tracks, control vs. Rac1-inhibited, 3. inner tracks, control vs. Rac1-inhibited, 4. control cells, inner vs. outer tracks, and 5. Rac1-inhibited cells, inner vs. outer tracks.

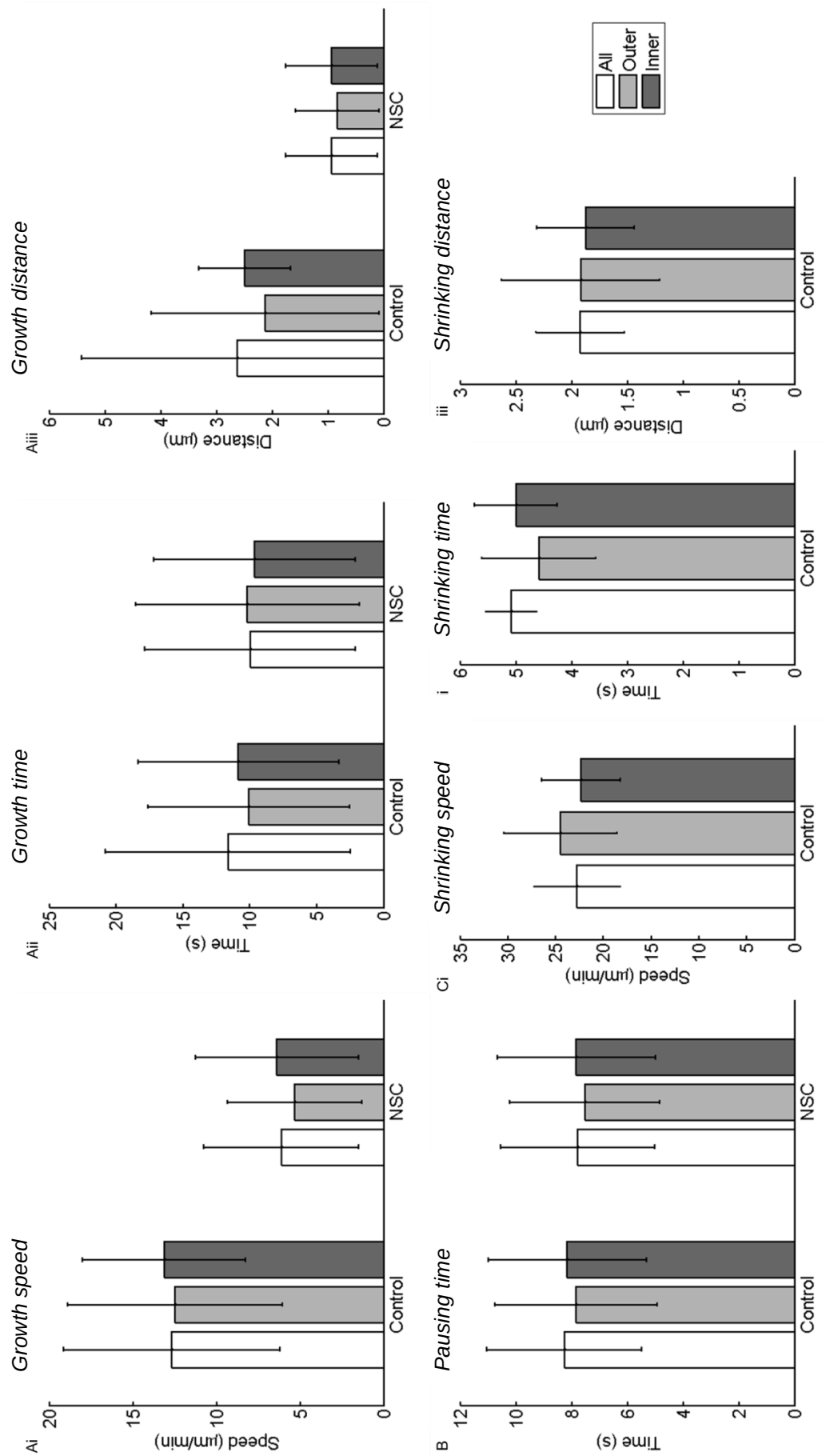

Figure 19. Average growth, shrinkage and pausing properties in cell areas. For both control cells and Rac1-inhibited cells, the average growth speed (Ai), time (Aii) and distance (Aii) is shown for each area ("all", "outer" and "inner"). Pausing time for all areas in each treatment is also shown (B), while shrinkage speed, time and distance is shown only for control cells (Ci-iii). Values are ± the standard deviation.

Table VII. Average area values of speed, distance and time. The average values, ± the standard deviation are shown for growing, shrinking and pausing tracks for each cell area for control and Rac1-inhibited (NSC) cells. Units are μm min^{-1} (speed), s (time) and μm (distance).

	Control			**NSC**		
	All	Outer	Inner	All	Outer	Inner
Grow						
Speed	12.67 ± 6.47	12.46 ± 6.43	13.13 ± 6.68	6.12 ± 4.64	5.32 ± 4.00	6.37 ± 4.86
Time	11.63 ± 9.18	10.10 ± 7.55	10.86 ± 8.37	9.98 ± 7.87	10.19 ± 8.36	9.65 ± 7.52
Distance	2.63 ± 2.80	2.13 ± 2.04	2.49 ± 2.54	0.93 ± 0.82	0.83 ± 0.75	0.94 ± 0.82
Shrink						
Speed	22.76 ± 4.50	24.46 ± 5.91	22.34 ± 4.12	-	-	-
Time	5.08 ± 0.46	4.58 ± 1.02	5.00 ± 0.74	-	-	-
Distance	1.93 ± 0.40	1.92 ± 0.71	1.87 ± 0.44	-	-	-
Pause						
Time	8.26 ± 2.78	7.84 ± 2.91	8.16 ± 2.86	7.77 ± 2.76	7.53 ± 2.68	7.83 ± 2.83

To limit the chance of falsely detecting a significant result, the level taken for significance was adjusted according to the Bonferroni method. Here, the original p value for the collected data is divided by the number of intra-data comparisons, thus $p = 0.05/5 = 0.01$. In the first three comparisons, i.e. those between similar areas of different experimental conditions, all data were found to be significantly different (Wilcoxon rank sum test, $p < 0.01$) apart from growth time for outer areas, and pause time for outer and inner areas (Wilcoxon rank sum test, $p > 0.01$). Thus, in general, growth properties are significantly greater in control versus Rac1-inhibited cells, while pause time is only significantly elevated in the all track data.

For the within-treatment comparisons, in the control cells, inner and outer tracks were found to be significantly different from one another in all growth properties (Wilcoxon rank sum test, $p < 0.01$), while pause time was not significantly different (Wilcoxon rank sum test, $p > 0.01$). Therefore, all growth properties are significantly greater in inner areas in control cells, while pause time is not. In the Rac1-inhibited cells, growth speed and distance were significantly different (Wilcoxon rank sum test, $p < 0.01$), while growth and pause time were not (Wilcoxon rank sum test, $p > 0.01$). Thus, Rac1-inhibited cells, though they exhibit significantly lower growth speeds and distances, show the same relationship between growth speed and distance (significant) and pause (not significant) time between inner and outer areas as control cells, with greater values for the inner area. The opposite is true for growth time, however, which is greater for outer areas in Rac1-inhibited cells, but not significantly so. These statistical results are summarised in table VIII.

Table VIII. Summary of significance tests on comparisons of areas. Similar areas ("all", "outer" and "inner") are compared between treatments ("control vs. NSC") and inner areas are compared with outer areas within each treatment ("within treatment"). A tick indicates significance at the level given by the Bonferroni correction (original significance: $p < 0.05$), while a cross indicates a non-significant result.

	Control vs. NSC			*Within treatment* **Inner vs. outer**	
	All	Outer	Inner	Control	NSC
Grow					
Speed	✓	✓	✓	✓	✓
Time	✓	x	✓	✓	x
Distance	✓	✓	✓	✓	✓
Pause					
Time	✓	x	x	x	x

The data can also be considered in terms of percentages of the total time or distance of track observation. These are shown in table IX. Here, we see that in inner areas in control and Rac1-inhibited cells, growth accounts for proportionately more time than in outer areas, and there is a proportionately longer time in pause in outer areas than in inner areas for both control and Rac1-inhibited cells. Inner areas have twice the percentage of observation time in shrinking than outer areas. In proportion to all track data, in control and Rac1-inhibited cells, inner and outer areas have an increased and decreased percentage, respectively, time in growth, and a decreased and increased percentage, respectively, time in pausing. The data for distance percentage hold little information for the Rac1-inhibited cells, while for control cells, inner areas have greater percentage distance in shrinking than outer areas, and decreased percentage in growth. These data are summarised in figure 20.

Table IX. Percentages of total time and distance in applicable phases. The percentages of total time or distance for each treatment, in each area, are shown.

	Control			**NSC**		
	All	Outer	Inner	All	Outer	Inner
% time						
Growing	91.11	90.72	91.29	95.31	94.87	95.47
Shrinking	0.12	0.07	0.13	0.00	0.00	0.00
Pausing	8.78	9.21	8.58	4.69	5.13	4.53
% distance						
Growing	99.78	99.85	99.76	100.00	100.00	100.00
Shrinking	0.22	0.15	0.24	0.00	0.00	0.00

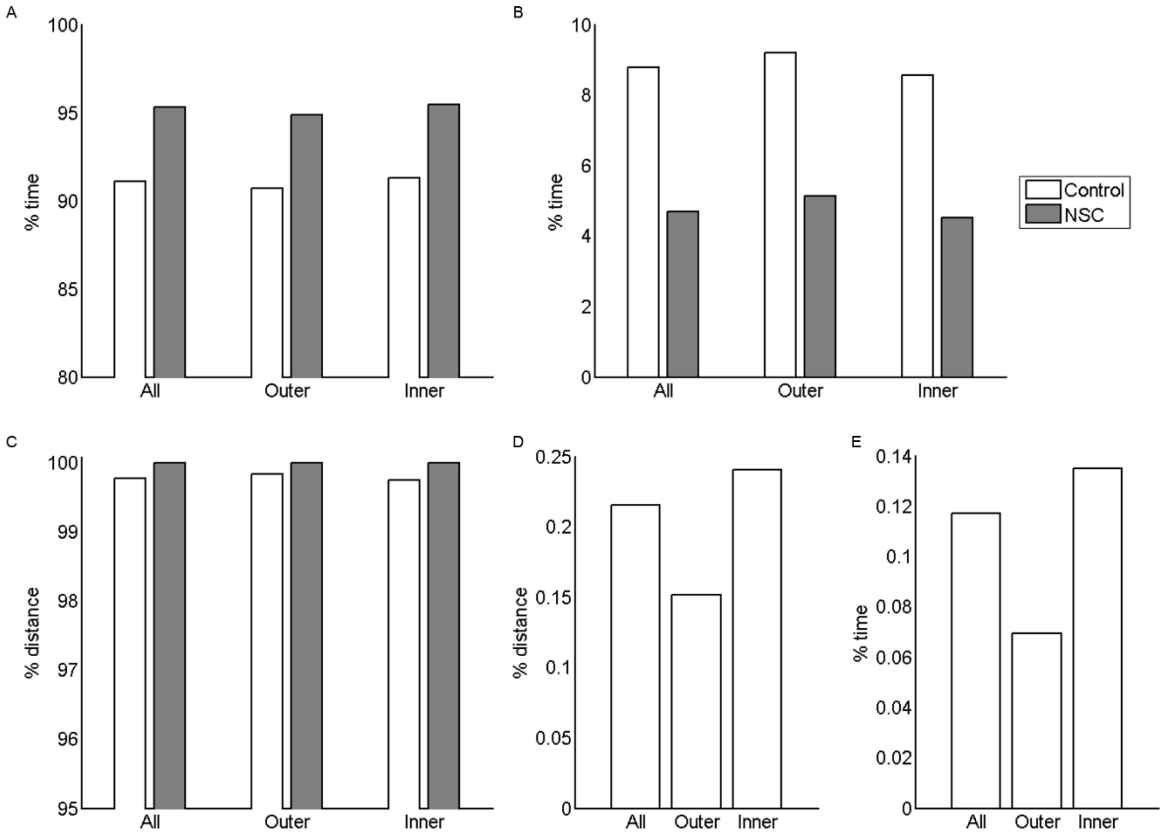

Figure 20. Percentage times and distances in applicable phases. For each area in each condition, the percentage times in growth (A) and in pause (B), and percentage distance in growth (C) are shown. For the shrinking phase, only control data are applicable, for which the percentage distance and time (D & E) are shown.

c. Estimating dynamics parameters

As figure 8 showed, the parameters available for estimation based on the data obtained with plusTipTracker are limited to transition frequencies from growth to pausing and shrinkage and back again, the rate of growth and an inferred rate of shrinkage. Thus, because we cannot directly observe shrinkage and pausing with this method, we cannot know the values of the transition frequencies between these states. See the methodological details in the previous sub-section for a discussion of the inherent biases in making estimations of transitions frequencies based on data obtained with observation of a +Tip proteins.

The two estimates based on the "biased" and corrected" approaches (again, see methodology) of the transition frequencies are shown in table X, along with growth and shrinkage rates and numbers of pausing and shrinking tracks. The calculations of dynamics are based on pooled data for each condition. The growth and shrinkage rates are as presented above, as are the numbers of tracks; they are shown again here for the completeness of dynamics parameters and to show the numbers involved in making the transition frequency calculations according to eq. 1.

Table X. Dynamics parameters. For each area in control and Rac1-inhibited (NSC) conditions, the mean and median (as indicated) phase speeds, transition frequencies and numbers of pausing and shrinking events are shown. Where the biased and corrected values differ, there are two values for a transition frequency (in the order indicated); otherwise, just one value is shown. See terms list for definitions of terms.

	Control			**NSC**		
	All	Outer	Inner	All	Outer	Inner
V_g						
Mean	12.67	12.46	13.13	6.12	5.32	6.37
Median	12.09	11.89	12.57	4.80	4.26	5.00
V_s						
Mean	22.76	24.46	22.34	-	-	-
Median	22.59	25.63	22.59	-	-	-
F_{cat}						
Biased	0.02	0.01	0.02	0.00	0.00	0.00
Corrected	5.45	5.33	6.62			
F_{res}						
Biased	11.80	13.09	12.00	0.00	0.00	0.00
Corrected						
F_{g2p}						
Biased	0.70	0.78	0.69	0.38	0.43	0.36
Corrected	4.96	6.07	5.32	6.37	5.89	6.82
F_{p2g}						
Biased	7.26	7.66	7.35	7.72	7.97	7.67
Corrected						
Number pause	1383	466	935	605	192	414
Number shrink	30	6	24	0	0	0

Since there were no shrinkage events detected in the Rac1-inhibited cells, F_{cat} and F_{res} in these cells is zero, which, as was touched upon above, is likely to be inaccurate since microtubules without these dynamics would be unusual, given that the "dynamicity" of microtubules in cells is highly documented. In the control condition, F_{cat} is increased in the inner area relative to the outer area. This is true for the biased and corrected methods. F_{res} decreases in the inner area relative to the outer area. In the control condition, both F_{g2p} and F_{p2g} decrease in the inner area relative to the outer area, while in the Rac1-inhibited condition, this is true only for F_{p2g} and the biased calculation of F_{g2p}; the corrected F_{g2p} is increased in the inner area. Thus, there is a disagreement between the two methods here.

Comparing experimental conditions, there is a greater corrected F_{g2p} in the Rac1-inhibited condition for all and inner areas, but not for outer areas, while the biased F_{g2p} is lower for each area in the Rac1-inhibited condition. So, again, there is disagreement between the two types of calculation. Values for F_{p2g} are greater in the Rac1-inhibited condition, for all areas,

and both conditions show a similar small decrease in inner areas relative to outer areas for this transition frequency.

To clarify the relationships between outer and inner transition frequencies, we can consider the ratios between them; these are shown in table XI. Here, in the control condition, only F_{cat} is smaller in the outer areas relative to inner areas, by both methods; all other transition frequencies are greater in the outer area relative to the inner. For the Rac1-inhibited condition, only the corrected value of F_{g2p} is smaller in the outer area relative to the inner area; here, the disagreement between methods described for Rac1-inhibited F_{g2p} is more clearly seen, since the biased value indicates that there is a greater value for this transition frequency in outer areas relative to inner areas.

Table XI. Ratios of transition frequencies in outer to inner areas for pooled data. For pooled control and Rac1-inhibited (NSC) condition data, the ratios of outer:inner for the indicated transition frequencies are shown. Thus, a value greater than one indicates an increase in the outer area relative to the inner area, and values below one: *vice versa*.

	Control		**NSC**	
	Biased	Corrected	Biased	Corrected
F_{cat}	0.56	0.81	-	-
F_{res}	1.09	1.09	-	-
F_{g2p}	1.13	1.14	1.18	0.86
F_{p2g}	1.04	1.04	1.04	1.04

The ratios of F_{g2p} in outer to inner areas in both experimental conditions are identical to the precision shown, while the biased values for the F_{p2g} outer to inner area ratio is greater in the Rac1-inhibited condition, but the corrected value ratio is smaller than the control condition. Therefore, in general, outer areas exhibit greater tendency to undergo a transition in all cases but catastrophe, and, according to the corrected method, in growth to pausing transitions in the Rac1-inhibited condition.

Next, we can consider the ratio of "opposing" transition frequencies within areas. Here, the two transition frequencies that move to and from two given phases are compared with one another (table XII). In this case, we have the pairs of F_{cat} and F_{res}, and F_{g2p} and F_{p2g}. In finding these ratios, the corrected values were used, since, as discussed in the methodology, these are more comparable, not only in terms of magnitude but also in the methods of their calculation.

Table XII. Transition frequency ratios in pooled data. For both control and Rac1-inhibited (NSC) conditions, the indicated ratios are given, using "corrected" frequencies.

	Control			**NSC**		
	All	Outer	Inner	All	Outer	Inner
F_{cat}:F_{res}	0.46	0.41	0.55	-	-	-
F_{g2p}:F_{p2g}	0.68	0.79	0.72	0.83	0.74	0.89

The trend here is smaller values for those transition frequencies that move away from the growing phase, compared to those that move toward the growing phase. Although this trend is also present in the Rac1-inhibited condition, the ratios are greater for the all track and inner area data, indicating that in these groups, there is an increased tendency toward growth to pause transitions than in similar groups in the control condition.

Finally, the dynamics of the different areas and different treatments are summarised qualitatively in figure 21. Presentation in this way helps understand where the differences between areas and treatments lie. The most obvious difference is that, since no shrinkage events were detected in the Rac1-inhibited condition, there are zero values for catastrophe and rescue frequencies, and for shrinkage speed. If these are accurate and not due to false negatives, then we can expect the Rac1-inhibited condition to have microtubules that are much more prone to growth.

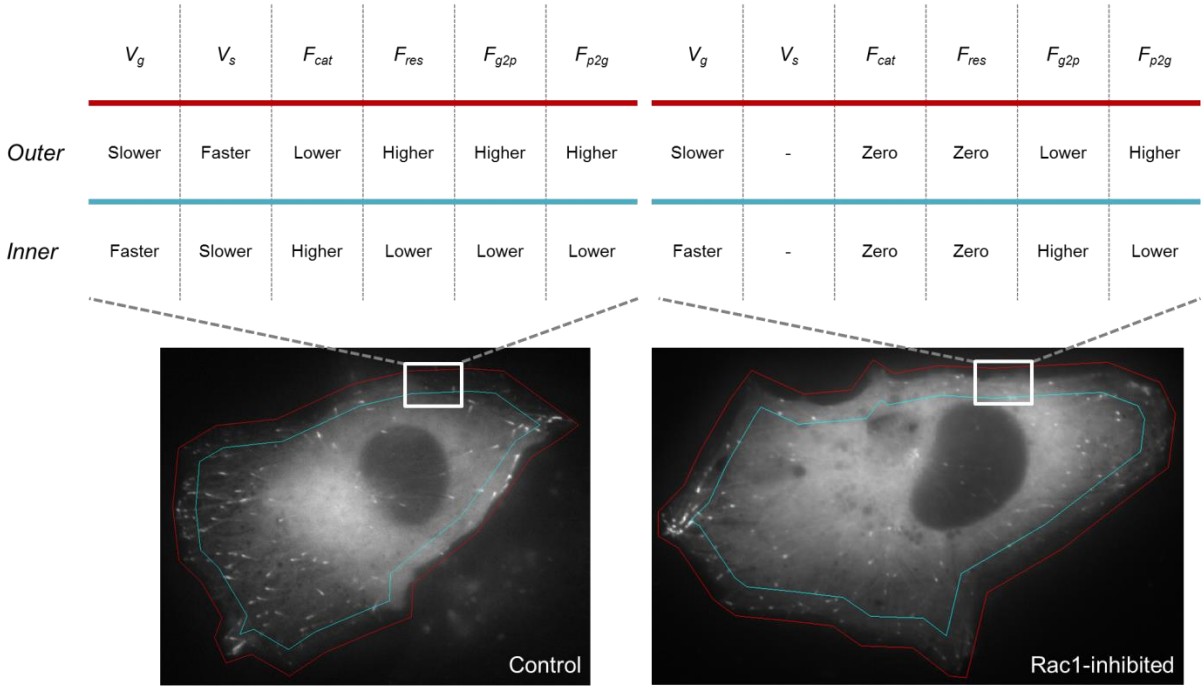

Figure 21. Summary of microtubule dynamics within inner and outer areas, between experimental conditions. Qualitative descriptions are given as to the relationship between dynamics parameters in each area.

Apart from these differences, the only other qualitative difference between the cell areas in the two treatments is for F_{g2p}; here, there is a higher frequency in the outer area compared to the inner in the control condition, but the opposite is true in the Rac1-inhibited condition. Added to this the fact that F_{p2g} is higher in outer areas compared to inner areas in the Rac1-inhibited condition, we can expect that microtubule growth in the outer areas of this condition dominates more than in the outer areas in the control condition.

D. DISCUSSION

I. Microtubule characteristics in unperturbed and Rac1-inhibited cells

a. Microtubule dynamics throughout the cell

Tracking of a labelled microtubule +TIP protein CLIP-170 has allowed measurement of certain microtubule characteristics, including times, distances, and speeds in the different microtubule phases. Conducting this analysis in control and Rac1-inhibited cells has permitted comparison of the dynamics in these different conditions.

In the control treatment, microtubules were found to grow faster than in the Rac1-inhibited treatment, and microtubules spent more time and covered more distance in this phase in the control condition too. In accordance with the disagreement between microtubule organisation in Rac1-inhibited cells from the Mogensen lab and in the presence of DN-Rac1, the dynamics also differ relative to the respective controls. In Wittmann et al. (2003), DN-Rac1 actually elevated microtubule growth speed slightly, whereas here, inhibition of Rac1 was found to decrease growth speed by over half. In addition, Nishimura et al. (2012) found that DN-Rac1 increased growth speed, but in agreement with the results here, they found that DN-Rac1 decreased time spent in growth. An analysis of dynamics with all means of interfering with Rac1 function is necessary to clarify the differences between these studies.

The dynamics reported are based on two different calculations: one that used total growth and (inferred) shrinkage times, the biased method, and one that used only the times in each phase that preceded a given transition; the corrected method. The corrected method was used in comparisons of transition frequencies between conditions and subcellular areas because it is possible to find values for all transition frequencies based on this method, and therefore compare them. Thus, there is of course an element of inaccuracy and doubt here, but this is true of all dynamics measurements. For example, Shelden and Wadsworth (1993) demonstrated that microtubule dynamics measurements vary with the time interval between film frames. As Applegate et al. (2011) suggest, the dynamics measured with plusTipTracker have their own set of confounding factors.

Unusually, there were no shrinkage events detected in the Rac1-inhibited condition in this study, although the efficacy of this is doubtful, and the potential interference with tracking of overly-deviating microtubule tracks aside, there are three possible scenarios to explain this unlikely result: 1) both F_{cat} and F_{res} are not zero but very low, hindering their detection, 2) F_{cat} is low and F_{res} is high, and shrinking events are missed as a result of infrequent transitions to and frequent transitions from the state, and 3) F_{cat} is high and F_{res} is low, and shrinking events are missed because they are rarely rescued but result in extinction instead. Distinguishing between these scenarios could be achieved by recording labelled microtubule dynamics, rather than using a +TIP protein, or alternatively, modelling could be used. The next two chapters address the latter approach.

Values for transitions between pausing and shrinking states were not obtainable with the methods employed here. Estimating values for F_{p2s} and F_{s2p} by comparing microtubule network properties will also be topics in the next two chapters.

b. Microtubule dynamics in subcellular areas

In this study, the development of tools to semi-automatically segment cells into inner and outer areas, and to allocate tracks to these areas, has allowed further comparison of microtubule dynamics between the subcellular areas and experimental conditions.

Using just the corrected dynamics values, in the control condition, V_g was decreased and V_s increased in outer areas relative to inner areas; F_{cat} was lower and F_{res} was higher in outer areas, and F_{g2p} was high and F_{p2g} was slightly higher in outer areas. In the Rac1-inhibited condition, V_g was also decreased in outer areas relative to inner areas, as was F_{g2p}; F_{p2g}, however, was higher in outer areas. Are these dynamics sufficient to explain the organisations seen in each condition? Also, do the differences between conditions explain the differences in organisation? These are difficult questions to answer, and as with exploration of the undetermined parameters, discussed above, they will be addressed in the next two chapters, which make use of comparisons of the results here with previously-reported microtubule dynamics (chapter 5), and modelling too (chapters 4 and 5).

However, the results do suggest possible mechanisms. Considering the phase time percentages now, microtubules spend more time in pause in the control condition, and within this condition, this time is greater in outer areas. In addition, microtubules grow more slowly in control outer areas, and spend less time in shrinkage. Perhaps the higher occurrence of pausing is indicative of, or indeed a mechanism of, capture of microtubules at the cortex. Indeed, higher incidence of pausing at the cell periphery has been reported (Mimori-Kiyosue et al., 2005).

Interestingly, the relationship between outer and inner areas for time spent in growth and pausing is maintained in the Rac1-inhibited condition, except here, there is an increase in growth time compared to the control condition. Perhaps the increase in percentage time in growth in the Rac1-inhibited condition is again a manifestation, a cause or a consequence, of defective cortical capture.

Since the dynamics parameters are based only on a subset of times in growth and shrinkage phases, correspondence between them and the phase times, both absolute and as percentages, should not be assumed. This is explored further in chapter 5. The fact that in the control condition, F_{g2p} is higher in the outer area, but in the Rac1-inhibited condition, it is lower in the outer area, taken with the phase time percentages, suggests that there is a fundamental difference in tendency to pause between microtubules of each condition.

A potentially interfering factor in this analysis is that the dynamics measurements were made with GFP-labelled CLIP-170. As CLIP-170 is a +Tip protein and is involved in microtubule-cortex interaction through interaction at its C-terminus and N-terminus with microtubules and IQGAP, respectively, labelling CLIP-170 with GFP could interfere with these interactions

and confuse the conclusions made above. Moreover, if microtubules are stabilised at the cortex, these would not be observed using this methodology. Further work might address this by combining methods of measuring microtubule dynamics.

c. Microtubule bending

The analysis of adjacent segment relative orientation revealed that in some cases, microtubule tracks created by plusTipTracker were potentially unrealistically deviating. Since it was not possible to locate the source of allowance of these overly-deviating tracks within plusTipTracker, the issue of these bending tracks could not be addressed earlier than the point at which comets are linked into tracks. As a result, the analysis of microtubule dynamics had to include these highly-bending tracks. The extent to which these influenced the dynamics measurements is difficult to evaluate, for example, we saw that there were significant differences in microtubule dynamics between straight and bendy tracks. However, in favour of the notion that these tracks would have a small rather than large effect, the proportion of tracks that were bendy was low, and furthermore, it should be noted that most of these tracks were not consistently high in relative orientation, rather, they contained one or a few segments that were deviating and thus, by the criteria set, required splitting.

d. Microtubule orientation relative to the cell edge

The orientations of microtubule tracks relative to the periphery of the cell were also assessed. These results indicated that microtubules in Rac1-inhibited cells grow at shallower angles, and even away from the cortex, to a greater extent than control microtubules. This is consistent with the appearance of Rac1-inhibited cells, since, as was described, they have relatively low radiality. The mechanisms of radiality are addressed further in the next two chapters.

II. Microtubule organisation

a. Organisation as a systems property

Clearly, there are differences in the organisation of unperturbed and Rac1-inhibited microtubule networks. Similarly, there are differences between the dynamics of microtubules in unperturbed and Rac1-inhibited cells. Moreover, there is not just one simple difference between the conditions, belying the possibility of an easily-identifiable mechanism to link microtubule dynamics and their organisation; this is a common feature of systems, where the outcome is difficult to predict from the components.

To elaborate, this study has established that Rac1-inhibited microtubules grow more slowly, bend to a greater extent, and take shallower angles relative to the cell edge. Furthermore, there are probably differences in microtubule shrinkage rate, and F_{cat} and F_{res}; the results found zero values for the latter two, and, by extension, a non-existent shrinkage rate. As has been discussed, these values are unlikely, and a number of scenarios have been posited for these results. In any event, there are differences in the organisation of cells subject to these experimental conditions: to what extent can differences in their dynamics explain this?

These results hint at possible mechanisms for the differences in organisation of the microtubule array between control and Rac1-inhibited conditions: microtubules may grow more slowly in the Rac1-inhibited condition, but do not transition to the shrinking phase and thus grow more persistently than in the control condition. Moreover, in outer areas, this persistence is increased since microtubules transition to the pausing phase less here, relative to inner areas. However, recall from chapter 2 that in some cases, for example where microtubule growth is guided by some mechanism, persistent growth might make for a better cortical targeting strategy. Of course, this analysis is based on zero shrinking events in the Rac1-inhbited condition, limiting its validity. The zero F_{cat} and F_{res} notwithstanding, the difference in conditions in the frequency of their transitions to and from pausing might contribute to the differences in organisation.

b. Mechanisms of organisation

Here, the inhibition of Rac1 was used as a model for disrupted microtubule-cortex interaction, based on previous results in migratory cells (Fukata et al., 2002), and on the disorganised microtubule phenotype seen upon Rac1 inhibition in the Mogensen laboratory, where microtubules oriented at predominantly parallel angles relative to the cell border suggested interference with microtubule-cortex interactions. The data presented here suggest that Rac1 does indeed function to promote perpendicular microtubule-cortex targeting: microtubules in Rac1-inhibited cells grow at shallow angles relative to the cortex in comparison to control cells.

It should be kept in mind, however, that microtubule dynamics were altered in inner areas as well as outer areas of the cell in the Rac1-inhibited cells. In inner areas, Rac1-inhibited microtubules spent a higher percentage of the time in growth relative to inner control areas, but actually covered under half the distance of control microtubules due to the slower growth rate in this condition. Furthermore, Rac1-inhibited tracks had greater relative orientation, indicating more bendy microtubules, or perhaps aberrant guidance of microtubules, throughout the cell. These differences that are not outer area-specific are important; they suggest that Rac1 inhibition affects not only microtubule dynamics at regions of the cortex where junctions are located, but elsewhere too.

Although undifferentiated ARPE-19 cells are quite flat in culture, and Rac1 is localised to cell junctions which are at the borders of the cell (when viewing from above or below with a microscope), a potential explanation for the altered dynamics in inner areas might be that Rac1 is involved in microtubule-cortex interactions elsewhere in the cell, and not just at the junctions. However, there were significant differences between growth speed and distance between Rac1-inhibited areas, where microtubules grow more slowly and for shorter distances, but for longer times (this was not a significant difference); perhaps the mechanism lies here. In support of this, control outer microtubules spend less time growing than inner areas, the opposite of Rac1-inhibited outer microtubules. Also, control outer microtubules spend less time in absolute and in percentage terms than Rac1-inhibited outer microtubules, although this difference was not significant.

In summary, microtubule dynamics in unperturbed and Rac1-inhibited cells have been measured in inner and outer areas of cells, with a view to explaining how microtubule dynamics contribute to radiality. To what extent can the estimated dynamics parameters account for the differences in organisation between the two conditions? It is difficult to attribute with complete certainty any organisational difference to the differences in dynamics, but it is clear that there are differences between the two experimental conditions that could lead to the differences in organisation. Ultimately, these mechanisms will be better understood if they are subject to rigorous analysis with a model; this is the focus of the next two chapters.

E. APPENDIX: MATERIALS AND METHODS

Cell culture, drug treatment and transfection

Human retinal pigment epithelial cells (ARPE-19) cells were maintained at 37° in 5% CO_2. Cells were cultured in DMEM/F12, containing 5 mM Hepes and 2.5 mM L-glutamine, supplemented with 5% FBS.

Rac1 inhibition experiments were performed by treating cells with 250 μM NSC 23766 for 24 hours.

For CLIP-170 transfection, 2 μg of CLIP-170-GFP was delivered using JetPrime (Polyplus).

Microscopy

After plating and growing to confluence, transfected cells were imaged using a Zeiss Axiovert 200M (widefield).

REFERENCES

Abal, M., M. Piel, V. Bouckson-Castaing, M. Mogensen, J.B. Sibarita, and M. Bornens. 2002. Microtubule release from the centrosome in migrating cells. *The Journal of cell biology*. 159:731-737.

Applegate, K.T., S. Besson, A. Matov, M.H. Bagonis, K. Jaqaman, and G. Danuser. 2011. plusTipTracker: Quantitative image analysis software for the measurement of microtubule dynamics. *Journal of structural biology*. 176:168-184.

Bacallao, R., C. Antony, C. Dotti, E. Karsenti, E.H. Stelzer, and K. Simons. 1989. The subcellular organization of Madin-Darby canine kidney cells during the formation of a polarized epithelium. *The Journal of cell biology*. 109:2817-2832.

Bashour, A.M., A.T. Fullerton, M.J. Hart, and G.S. Bloom. 1997. IQGAP1, a Rac- and Cdc42-binding protein, directly binds and cross-links microfilaments. *The Journal of cell biology*. 137:1555-1566.

Bellett, G., J.M. Carter, J. Keynton, D. Goldspink, C. James, D.K. Moss, and M.M. Mogensen. 2009. Microtubule plus-end and minus-end capture at adherens junctions is involved in the assembly of apico-basal arrays in polarised epithelial cells. *Cell motility and the cytoskeleton*. 66:893-908.

Bouckson-Castaing, V., M. Moudjou, D.J. Ferguson, S. Mucklow, Y. Belkaid, G. Milon, and P.R. Crocker. 1996. Molecular characterisation of ninein, a new coiled-coil protein of the centrosome. *Journal of cell science*. 109 (Pt 1):179-190.

Brunner, D. 2002. How to grab a microtubule on the move. *Developmental cell*. 3:2-4.

Brunner, D., and P. Nurse. 2000. CLIP170-like tip1p spatially organizes microtubular dynamics in fission yeast. *Cell*. 102:695-704.

Dammermann, A., and A. Merdes. 2002. Assembly of centrosomal proteins and microtubule organization depends on PCM-1. *The Journal of cell biology*. 159:255-266.

Delgehyr, N., J. Sillibourne, and M. Bornens. 2005. Microtubule nucleation and anchoring at the centrosome are independent processes linked by ninein function. *Journal of cell science*. 118:1565-1575.

Eden, S., R. Rohatgi, A.V. Podtelejnikov, M. Mann, and M.W. Kirschner. 2002. Mechanism of regulation of WAVE1-induced actin nucleation by Rac1 and Nck. *Nature*. 418:790-793.

Fukata, M., T. Watanabe, J. Noritake, M. Nakagawa, M. Yamaga, S. Kuroda, Y. Matsuura, A. Iwamatsu, F. Perez, and K. Kaibuchi. 2002. Rac1 and Cdc42 capture microtubules through IQGAP1 and CLIP-170. *Cell*. 109:873-885.

Gundersen, G.G., E.R. Gomes, and Y. Wen. 2004. Cortical control of microtubule stability and polarization. *Current opinion in cell biology*. 16:106-112.

Hall, A. 2012. Rho family GTPases. *Biochemical Society transactions*. 40:1378-1382.

Hart, M.J., M.G. Callow, B. Souza, and P. Polakis. 1996. IQGAP1, a calmodulin-binding protein with a rasGAP-related domain, is a potential effector for cdc42Hs. *The EMBO journal*. 15:2997-3005.

Hill, T.L. 1985. Theoretical problems related to the attachment of microtubules to kinetochores. *Proceedings of the National Academy of Sciences of the United States of America*. 82:4404-4408.

Holy, T.E., M. Dogterom, B. Yurke, and S. Leibler. 1997. Assembly and positioning of microtubule asters in microfabricated chambers. *Proceedings of the National Academy of Sciences of the United States of America*. 94:6228-6231.

Holy, T.E., and S. Leibler. 1994. Dynamic instability of microtubules as an efficient way to search in space. *Proceedings of the National Academy of Sciences of the United States of America*. 91:5682-5685.

Komarova, Y.A., I.A. Vorobjev, and G.G. Borisy. 2002. Life cycle of MTs: persistent growth in the cell interior, asymmetric transition frequencies and effects of the cell boundary. *Journal of cell science*. 115:3527-3539.

Kuroda, S., M. Fukata, K. Kobayashi, M. Nakafuku, N. Nomura, A. Iwamatsu, and K. Kaibuchi. 1996. Identification of IQGAP as a putative target for the small GTPases, Cdc42 and Rac1. *The Journal of biological chemistry*. 271:23363-23367.

Laan, L., N. Pavin, J. Husson, G. Romet-Lemonne, M. van Duijn, M.P. Lopez, R.D. Vale, F. Julicher, S.L. Reck-Peterson, and M. Dogterom. 2012. Cortical dynein controls microtubule dynamics to generate pulling forces that position microtubule asters. *Cell*. 148:502-514.

Meng, W., Y. Mushika, T. Ichii, and M. Takeichi. 2008. Anchorage of microtubule minus ends to adherens junctions regulates epithelial cell-cell contacts. *Cell*. 135:948-959.

Mimori-Kiyosue, Y., I. Grigoriev, G. Lansbergen, H. Sasaki, C. Matsui, F. Severin, N. Galjart, F. Grosveld, I. Vorobjev, S. Tsukita, and A. Akhmanova. 2005. CLASP1 and CLASP2 bind to EB1 and regulate microtubule plus-end dynamics at the cell cortex. *The Journal of cell biology*. 168:141-153.

Mogensen, M.M. 1999. Microtubule release and capture in epithelial cells. *Biology of the cell / under the auspices of the European Cell Biology Organization*. 91:331-341.

Mogensen, M.M., A. Malik, M. Piel, V. Bouckson-Castaing, and M. Bornens. 2000. Microtubule minus-end anchorage at centrosomal and non-centrosomal sites: the role of ninein. *Journal of cell science*. 113 (Pt 17):3013-3023.

Moss, D.K., G. Bellett, J.M. Carter, M. Liovic, J. Keynton, A.R. Prescott, E.B. Lane, and M.M. Mogensen. 2007. Ninein is released from the centrosome and moves bi-directionally along microtubules. *Journal of cell science*. 120:3064-3074.

Nishimura, Y., K. Applegate, M.W. Davidson, G. Danuser, and C.M. Waterman. 2012. Automated screening of microtubule growth dynamics identifies MARK2 as a regulator of leading edge microtubules downstream of Rac1 in migrating cells. *PloS one*. 7:e41413.

Perez, F., G.S. Diamantopoulos, R. Stalder, and T.E. Kreis. 1999. CLIP-170 highlights growing microtubule ends in vivo. *Cell*. 96:517-527.

Picone, R., X. Ren, K.D. Ivanovitch, J.D. Clarke, R.A. McKendry, and B. Baum. 2010. A polarised population of dynamic microtubules mediates homeostatic length control in animal cells. *PLoS biology*. 8:e1000542.

Ridley, A.J. 2001. Rho GTPases and cell migration. *Journal of cell science*. 114:2713-2722.

Ridley, A.J., and A. Hall. 1992. The small GTP-binding protein rho regulates the assembly of focal adhesions and actin stress fibers in response to growth factors. *Cell*. 70:389-399.

Ridley, A.J., H.F. Paterson, C.L. Johnston, D. Diekmann, and A. Hall. 1992. The small GTP-binding protein rac regulates growth factor-induced membrane ruffling. *Cell*. 70:401-410.

Shelden, E., and P. Wadsworth. 1993. Observation and quantification of individual microtubule behavior in vivo: microtubule dynamics are cell-type specific. *The Journal of cell biology*. 120:935-945.

Stillwell, E.E., J. Zhou, and H.C. Joshi. 2004. Human ninein is a centrosomal autoantigen recognized by CREST patient sera and plays a regulatory role in microtubule nucleation. *Cell cycle (Georgetown, Tex.)*. 3:923-930.

Sugioka, K., and H. Sawa. 2012. Formation and functions of asymmetric microtubule organization in polarized cells. *Current opinion in cell biology*. 24:517-525.

van der Vaart, B., W.E. van Riel, H. Doodhi, J.T. Kevenaar, E.A. Katrukha, L. Gumy, B.P. Bouchet, I. Grigoriev, S.A. Spangler, K.L. Yu, P.S. Wulf, J. Wu, G. Lansbergen, E.Y. van Battum, R.J. Pasterkamp, Y. Mimori-Kiyosue, J. Demmers, N. Olieric, I.V. Maly, C.C. Hoogenraad, and A. Akhmanova. 2013. CFEOM1-associated kinesin KIF21A is a cortical microtubule growth inhibitor. *Developmental cell*. 27:145-160.

Waterman-Storer, C.M., and E.D. Salmon. 1997. Actomyosin-based retrograde flow of microtubules in the lamella of migrating epithelial cells influences microtubule dynamic instability and turnover and is associated with microtubule breakage and treadmilling. *The Journal of cell biology*. 139:417-434.

Weissbach, L., J. Settleman, M.F. Kalady, A.J. Snijders, A.E. Murthy, Y.X. Yan, and A. Bernards. 1994. Identification of a human rasGAP-related protein containing calmodulin-binding motifs. *The Journal of biological chemistry*. 269:20517-20521.

Wittmann, T., G.M. Bokoch, and C.M. Waterman-Storer. 2003. Regulation of leading edge microtubule and actin dynamics downstream of Rac1. *The Journal of cell biology*. 161:845-851.

Wollman, R., E.N. Cytrynbaum, J.T. Jones, T. Meyer, J.M. Scholey, and A. Mogilner. 2005. Efficient chromosome capture requires a bias in the 'search-and-capture' process during mitotic-spindle assembly. *Current biology : CB*. 15:828-832.

Chapter 4

Modelling microtubules and radiality

A. A MODEL FOR RADIALITY

I. Generation of radiality

a. Mechanisms of radiality

Previously in this thesis, the generation and maintenance of radiality, i.e. perpendicular microtubule-cortex relative orientation, has been discussed. We saw in chapter 3 that an otherwise radial array is perturbed upon inhibition of Rac1, and that this is accompanied by a change in microtubule dynamics. Indeed, radiality is a common feature of microtubule arrays in undifferentiated cells, the large proportion of which exhibit the classic radial array microtubule organisation.

Generally, implicit in discussions of microtubule organisation, in radial arrays and also in other types of organisation, is the assumption that microtubule dynamics are modulated in some way at the periphery of the cell in order to generate radiality. Yet, few studies have addressed this either by experimental or theoretical means. Exceptions include Komarova et al. (2002), who found that microtubules grow persistently in central regions of the cell, but undergo a change in dynamics upon reaching the periphery that gives rise to a tendency to shrink more. van der Vaart et al. (2013) have also addressed the generation of radiality, finding that a growth inhibitor located at the cortex contributes to radiality.

The differences between inner and outer area dynamics were assessed in chapter 3; there, differences were found between inner and outer areas within both control and Rac1-inhibited cells, and also between experimental conditions. However, it is difficult to assign organisational differences to differences in dynamics, and modelling can help. In this and the next chapter, the basic mechanisms of radiality are first addressed, the focus of this chapter, and then in the next chapter, the results of the previous chapter are considered in terms of generation of radiality.

b. Addressing radiality with a model

The aim of this chapter is to elucidate the ways in which radiality is generated. I take a modelling approach here, simplifying the system to a 1-dimensional problem wherein the contribution of different sets of dynamics in inner and outer areas to radiality is assessed by the competence of these dynamics in accurately attaining the target length, i.e. the distance to the border of the cell.

II. Why model?

a. Rationale

The purpose of a model is to serve almost as a formal thought experiment; one specifies the framework of the model: the parameters, i.e. the components of the system, their relationship to one another, and the values they will take. By doing this, we can test our ideas rigorously;

unlike a qualitative, or conceptual model, whereby we might display our thoughts of how a system works in the form of a diagram, a quantitative model allows us to actually assess whether these thoughts make sense. For example, in this chapter, we will ask: can these two sets of dynamics, one for an inner area and one for an outer area, produce a proper radial array? It would be difficult to answer this with an experiment, and thus a model is a complementary tool; we know enough about microtubule dynamics to create a model of the phenomenon, and use it to test our ideas on how radiality is generated. In the succeeding sub-sections, I will briefly outline some more of the nuances of modelling, and review previous models of microtubule dynamics.

b. Modelling as a tool

In chapter 2, we saw that microtubule dynamic instability is used and modified in cells to give rise to various types of organisation, depending on the requirements of the cell. In trying to define the relationships between microtubule dynamics and organisation, researchers have used predominantly microscopic imaging and modelling. Continual progress in microscopy and elegant experimental manipulations (e.g. Schek et al. (2007)) have permitted ever-more detailed descriptions of microtubule behaviour, and various image processing algorithms (e.g. Applegate et al. (2011)) have made dynamics measurements more accessible. With these advances, modelling has become ever more useful, complementing traditional (although modelling has been around for a long time, e.g. the model by Hodgkin and Huxley (1952) of action potential propagation, which is over 60 years old, it is generally not practised by the majority of investigators) means of experimentation by testing the findings of those experiments within the stringent confines of mathematical language.

c. The modelling process

As in imaging, modelling approaches have been varied, ranging from fine-grain models at the level of the tubulin heterodimer, to coarse-grain and phenomenological models based on approximations of whole-microtubule behaviour, and even population-level features (for a good short review, see Karsenti et al. (2006)). The diversity of approaches reflects an important point: that one model for one set of experiments may be valid, but it may not be applicable to another set; models must be created with experiments and applications decided upon *a priori*. One model may turn out to be applicable to another set of experiments, but we should not assume that it will be; we are not aiming for a universal model (for the time being): as Mogilner et al. (2012) put it, there is no modelling "Road to Valhalla", i.e. it may be better to switch between types and scopes of models, rather than dedicate heroic effort toward making a "whole-cell" model. Indeed, as the oft-cited observation that "all models are wrong, but some are useful" (Box and Draper, 1987) is true, so it is also true that some models are more useful for one application than another. Thus, part of a good modelling study is to identify the type and scope of the model that is most appropriate.

To identify the relevant scope and type of model, one must match the model to the data that is available; the information obtained from experiments must be able to act as inputs to the model. Furthermore, the outputs of the model should be comparable in some way to the reality; in essence, the model and experiments must be compatible. This dialogue works even

better when some perturbation can be made, in both model and experiment. In this way, one can test mechanisms suspected to be in operation in reality with the model.

So, why model? Modelling is a useful tool to help understand biology, by the fact that models can help test our interpretations of experiments, and also suggest new ones. However, in order to make the most of a model, we must choose how we go about constructing it carefully. This chapter addresses both the appropriate construction of a model and its use to answer a real biological question; this is elaborated on in the next sub-section.

III. Survey of microtubule models

a. Modelling methods

The means of creating and using a model are no different in studies of microtubules, indeed, in all biology, to those methods used elsewhere in science. As was briefly mentioned, all models require that their workings be specified explicitly, and this specification usually comes in mathematical form. It is the exact mathematical form the specifications take that determines the type of model, which in turn affects the information that is compatible with the model and the subsequent analysis of the model.

The most basic distinction one can make is between models that are deterministic or stochastic. The former type of model is based on differential equations; these can be so-called ordinary differential equations (ODE), or partial differential equations (PDE). ODEs simply express the change of a variable, usually over time, as a function of the variable, whereas PDEs include not only the change of a variable in time, but also space. Parameters in these types of models will usually be rate constants of reactions. Generally, one will have a system of ODEs or PDEs, meaning that there will be one equation per variable in the system; variables might be, e.g. concentrations of the molecules in a particular system. The analysis of a model based on ODEs and PDEs centres on finding solutions to the system of equations: by solving a system of ODEs, e.g. one can find the variation in concentrations of the components of the system over time. A clear advantage of PDEs over ODEs is that, because space is represented in a PDE, one can include, e.g. variations in concentration in space; however, PDEs are more difficult to solve.

Deterministic models are so-called because, given the same parameters, the result will always be the same. This is not the case with stochastic models, which are probabilistic in nature. For example, a deterministic model might specify the rate of change of a variable as a function of its concentration, perhaps also the concentration of another variable, and a rate constant. In a stochastic model, the change of the same variable will be the result of the probability that it will undergo a reaction; the probability will have a distribution obtained from some empirical data, or some prior knowledge of the mechanisms that underlie the particular reaction. Because stochastic models are based on probabilities, there is uncertainty in the way in which the system will progress: there can be more than one outcome, unlike deterministic models.

Stochastic models can be approached in a number of ways. Generally, the different approaches refer to the way in which the model is “simulated”. Simulation simply means the

advancement of the model through time; probabilities are assessed either at discrete time steps, as in a so-called "Monte Carlo" simulation, while finding the time to the next change in the system is an approach sometimes referred to as "Gillespie" simulation.

Other types of models are used in biology, such as Boolean and agent-based models, but discussions of these are beyond the scope of this chapter. For an excellent introduction to the various modelling approaches available to a biologist and examples of how they have been used, see Mogilner et al. (2012).

b. Microtubule problems addressed with models

Generally, microtubule models fall into two groups. There are those models that address the mechanism of dynamic instability, and there are those that consider how dynamic instability affects microtubule population organisation. Models created to understand the mechanisms of dynamic instability are generally based on information regarding tubulin dimers: rate constants of association and disassociation, etc., whereas models focussed on understanding how dynamic instability relates to array organisation are usually based on information on whole-microtubule dynamics: growth and shrinking speeds, transitions frequencies, etc.

Consequently, microtubule models generally accede to the principle of an appropriate level of abstraction; it would be unnecessary to use tubulin biochemical data in a model of microtubule population dynamics, while a model of dynamic instability based solely on growth rates and transition frequencies would tell us nothing new about dynamic instability. Often, the properties that "emerge" from a given level, e.g. growth/shrinkage rates and transition frequencies that emerge from the biochemistry of tubulin, can be used in a model that seeks to explain phenomena at a higher level; thus, the growth and shrinkage rates and transition frequencies will be applicable for a model with the goal of understanding microtubule array organisation.

The first applications of modelling to microtubule-oriented problems were carried out in order to explain the existence of discrete phases of microtubule polymerisation. Since it had become evident that a population of microtubules could consist of individuals in different phases at the same time (Mitchison and Kirschner, 1984a; Mitchison and Kirschner, 1984b), which was contrary to established theory on polymer dynamics (Oosawa and Asakura, 1975) because of the coupling between polymerisation and GTP (or ATP) hydrolysis, Hill and Carlier (1983) and Hill and Chen (1984) sought to better-understand the processes of these phase changes with a model. Their model is stochastic and based at the level of tubulin units in a polymer with unit width (i.e. analogous to modelling a single protofilament). Each unit is GTP- or GDP-bound, and the probabilities of changing nucleotide state are calculated based on rate constants derived from experimental data; GDP-bound units cannot go back to GTP-bound, and upon each iteration of the model, the nucleotide state of each GTP-bound unit is tested for change by comparing a uniform random number against the probability of changing (Chen and Hill, 1983). They found that when they did not average results over large times (Hill and Carlier, 1983), the modelled microtubules exhibited discrete states whereby all units were GDP-bound or GTP-bound (Hill and Chen, 1984), supporting the

experimental findings of Mitchison and Kirschner (1984a) and Mitchison and Kirschner (1984b).

Many more studies dedicated to furthering understanding of dynamic instability with modelling have since appeared, some combining deterministic and stochastic approaches (Ranjith et al., 2009), while others combining mechanical modelling of the microtubule plus end with a stochastic approach (VanBuren et al., 2005). An interesting, more abstract take on the mechanism of just catastrophe is provided by Brun et al. (2009). These authors use a stochastic model of a set of protofilaments where catastrophe occurs if a given number N of terminal tubulin units in one protofilament become GDP-bound and that protofilament does not encounter a GTP-bound unit in an adjacent protofilament as it shrinks, and they find that $N = 2$ best reproduces experimental results. Of course, since this model is more abstract, i.e. it is phenomenological, it is more difficult to interpret the result. Brun et al. (2009) suggest that it might reflect dependencies of catastrophe on mechanical properties of the microtubule in addition to kinetic processes.

Moving on to models that consider microtubule dynamics and organisation, these started with the work of Verde et al. (1992) and Dogterom and Leibler (1993). In this case, microtubule dynamics are no longer considered in terms of associations and disassociation of tubulin units and hydrolysis of GTP; instead, they are modelled purely in terms of transition frequencies and growth and shrinkage rates. Such models are often described as "mesoscopic" or "phenomenological". As with the mechanistic models of dynamic instability, they are amenable to deterministic and stochastic analysis.

Stochastic simulations have been used to investigate the efficiency of proposed "search and capture" mechanisms, for a general target (Holy and Leibler, 1994), and in the location of chromosomes by microtubules (Wollman et al., 2005). In Wollman et al. (2005), the authors found that a spatial bias in catastrophe frequency was required for microtubules to locate chromosomes in observed times. Meanwhile, a deterministic approach was taken by Green et al. (2005) to find the average length of microtubules, given experimentally determined phase transitions and growth rates. Here, the authors perturbed the function of APC and measured dynamics with EB1. To find the mean length, they had to derive solutions for their set of ODEs; assuming steady-state allowed them to do this.

One study notable for being an exception to the trend of microtubule population models being based on a phenomenological treatment of microtubule dynamics is that of Gregoretti et al. (2006). In this study, the authors explore the effects of limited tubulin concentration and limited space in which to grow, with the aims of establishing principles of microtubule growth "in a cell-like environment". The model is similar to that of Hill and Chen (1984), in that it is stochastic and that tubulin units are modelled, with given probabilities of association and disassociation, but instead of just one microtubule, many microtubules are modelled, and there is a finite amount of free tubulin in solution. Of course, they also specify concentration dependence in these rates. There is also a finite microtubule length, intended to mimic the effects of growing against the boundaries of the cell.

Because the authors of this study update the free tubulin concentration upon each iteration of the simulation, they can explore the interplay between confined growth and tubulin concentration. They find that, with permissive model parameters, microtubules grow persistently in the cell interior, and generally only exhibit catastrophe at the cell border. This behaviour has been documented in real cells by Komarova et al. (2002), and Gregoretti et al. (2006) suggest that this behaviour arises because the increase in catastrophe that would not occur if there were no cell borders serves to increase the soluble tubulin to a level similar to that which would occur for higher total tubulin concentrations (again with no border). Thus, their results can be interpreted thus: boundaries act to effectively increase the total tubulin pool, in terms of microtubule behaviour, and this is why microtubules often grow persistently against cell borders.

IV. A rationale for modelling in this chapter

a. Setting the problem

The above discussion and review makes it clear that it is good practice in any modelling study to set the problem that the model is to address before the type of model and other particulars can be decided. This and the next chapter address two closely related problems: the mechanisms of generation of radiality, addressed here, and the role of Rac1 in microtubule organisation, addressed in chapter 5. The problems are related by the fact that one phenotype of Rac1 inhibition is loss of radiality; thus, as the general problem of establishing radiality is addressed with a model here, in the next chapter, the mechanism behind loss of radiality upon inhibition of Rac1 can be considered. Therefore, the model must be made to address the general mechanisms of radiality.

b. Model reasoning

A point previously made by van der Vaart et al. (2013) is that, as microtubules are flexible and can bend upon growing into a barrier, then when a growing microtubule reaches the cell cortex, there is no reason to expect that it should stop growing there and be oriented perpendicularly to the edge of the cell; it could indeed bend, and continue to grow unimpeded. Therefore, there must be one or more mechanisms by which microtubule growth is halted at the cortex.

So, following this rationale, radiality ensues from a process or processes by which microtubules are accurately targeted to the correct length. One way in which this could occur is a change in microtubule dynamics at the cell periphery, and there are also likely to be other, non-exclusive ways in which microtubule properties are modulated so that a target length, and thus radiality, can be achieved. For example, work from Gardner et al. (2011) has shown that microtubule catastrophe can be regulated so that it is a multi-step process, conferring a lower chance of catastrophe upon younger microtubules. This type of mechanism could be used to tune microtubule length, creating areas of the cell, toward the periphery, where catastrophe frequencies are elevated relative to the rest of the cell (Gardner et al., 2013). Moreover, a more basic mechanism could be capture and stabilisation of microtubules at the cortex; in this case, a captured microtubule would be withdrawn from the dynamic pool of microtubules and remain fixed in length. The discussion of selective

stabilisation in chapter 2 makes it clear that such events are possible. Notably, such microtubules would not be detected by the methods used in chapter 3.

The true situation is likely to be a balance of these factors; the microtubule-inherent and cortex-mediated dynamics changes can both contribute to tuning of microtubule length to a target magnitude, while, although contributing to radiality themselves, these mechanisms will also contribute to cortical capture, by virtue of fine-tuning microtubule length and thus allowing a plus end to remain, on average, in the same place.

Here, I investigate the cortex-mediated dynamics changes that are posited to contribute to the generation of radiality. Because radiality follows from accurate tuning of microtubule length to a target magnitude, then a simplified model is justified. In this model, a microtubule grows in one dimension, i.e. it is straight, and is subject to two sets of dynamics. The first set is that of the inner area, and up to a given length that specifies the start of the cell periphery, these are the relevant dynamics. Once the periphery length has been exceeded, the second dynamics set, that of the outer area, is employed. The aim of using this model is to establish which combinations of dynamics produce accurate microtubule length targeting, and thus, radiality.

B. METHODOLOGY

I. Abstract measures of microtubule dynamics

a. The purpose of abstract measures

Where there are a number of parameters in a system, reducing the complexity of the system by some form of abstraction can be helpful for comparing sets of parameters. This applies to microtubule dynamics, where, even in the two-state model, there are four parameters, and it is difficult to compare different sets of these four values. These abstract measures include microtubule drift, average length, length randomness, and phase proportions. Below, I discuss each of these measures in more detail. These measures use shorthand notation for the dynamics parameters, so please refer to the terms list for definitions.

b. Microtubule drift

Microtubule drift, first employed by Verde et al. (1992) and Dogterom and Leibler (1993), is based on the treatment of microtubule dynamics as a one-dimensional random walk. A random walk, where in one dimension, the walker takes one step per unit time along a line, usually has equal probability of going in either direction. However, they can be biased, and in this case, have a drift term that indicates the direction and extent of the bias by its sign and magnitude, respectively (fig. 1). Thus, the tendency of a microtubule to grow or shrink, and how quickly it does either, are indicated by the drift; a positive value indicates continual growth, while a negative value indicates shrinking on average. Verde et al. (1992) and Dogterom and Leibler (1993) find the drift, *V*, in terms of the dynamics parameters:

$$V = \frac{V_g F_{res} - V_s F_{cat}}{F_{res} + F_{cat}}, \quad (1).$$

Where drift is positive, there is "unbounded" growth, and where drift is negative, "bounded" growth (Dogterom and Leibler, 1993). When the drift is zero, there is neither net growth nor shrinking. In unbounded growth, the average microtubule length (see below) is not defined; microtubules grow indefinitely, and therefore the average length increases indefinitely. To recap, the dynamics parameters are shown in the diagram in figure 2.

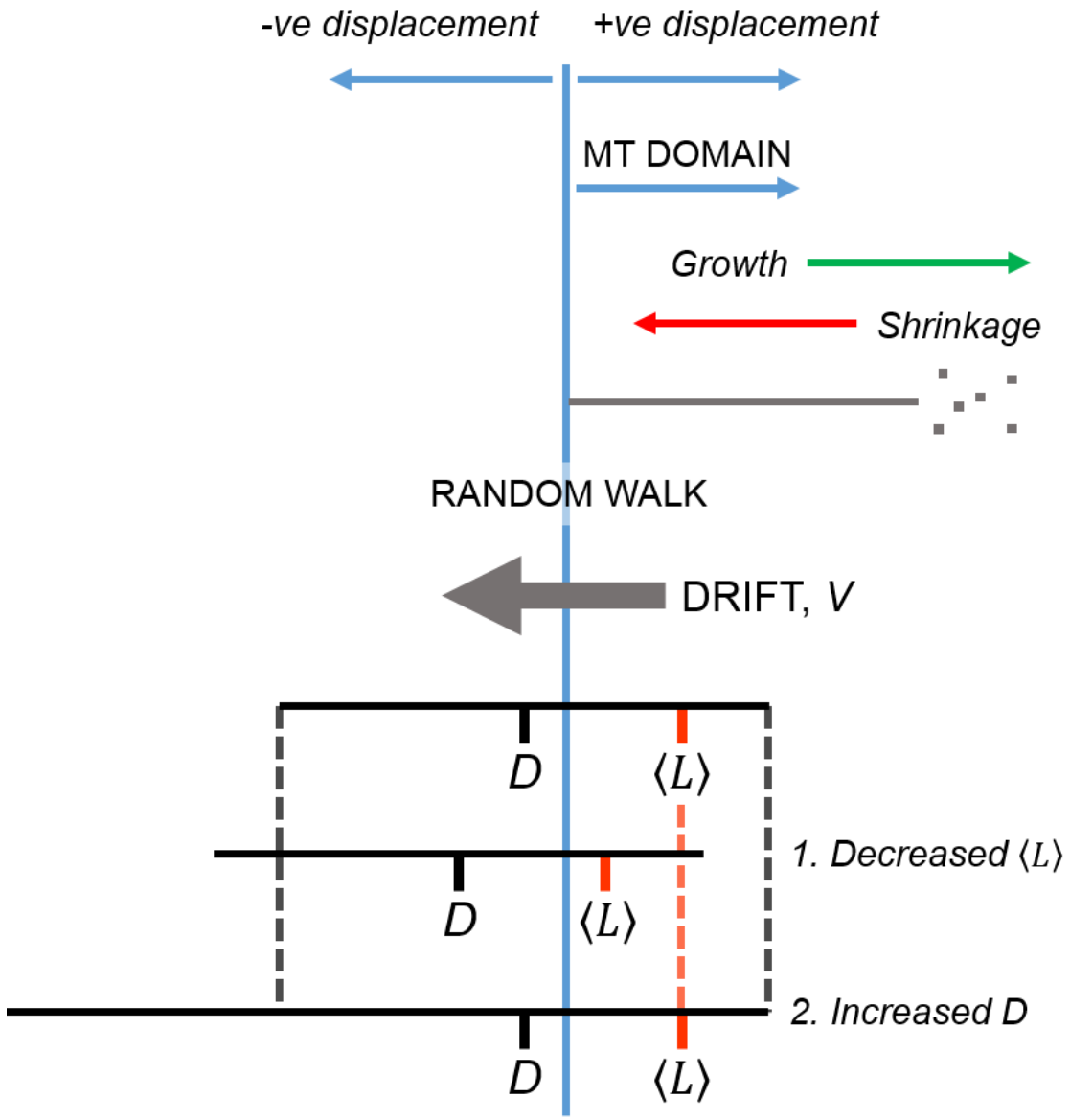

Figure 1. Random walk analogy of microtubule dynamics. Microtubule dynamics can be treated as a biased one-dimensional random walk, whereby the drift, *V*, indicates the directional bias of the random walk. If *V* is negative, then the average length $\langle L \rangle$ is defined. The diffusion coefficient, *D*, indicates the extent to which lengths will vary. Note that discrepancies between the theory and microtubule properties can arise because the random walk can take on both positive and negative displacement, whereas microtubules only have positive displacement (i.e. their length). In case 1, decreasing $\langle L \rangle$ with constant *D* will give greater (i.e. more negative) *V*, and empirical measures of variation in length will be expected to decrease. In case 2, increasing *D* with constant $\langle L \rangle$ will also give greater (again, more negative) *V*, and empirical measures of length variation will be expected to increase, but will be limited by the fact that an increased D and V mean more of the random walk will be obscured in negative displacement.

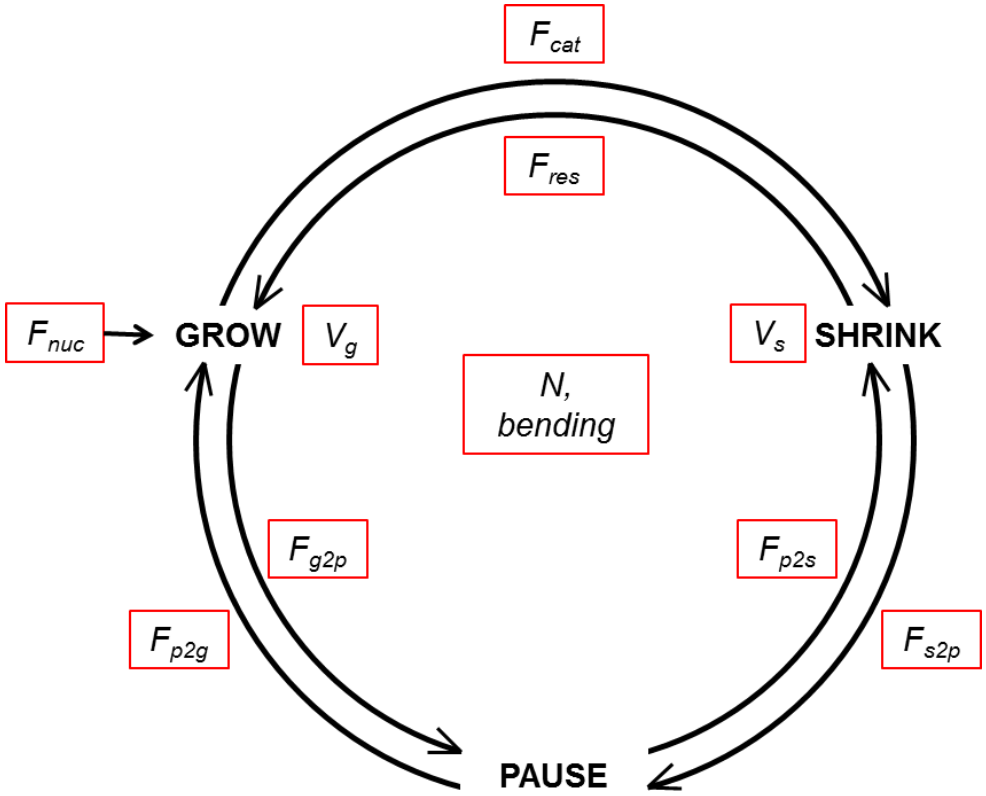

Figure 2. Microtubule model parameters. Microtubules can transition between 3 states (grow, pause and shrink) with given frequencies (boxes next to arrows; see text for details on notation). Nucleation creates new microtubules in the growth state with a given frequency (F_{nuc}), while there is also a total number of microtubules in the system (N) and microtubules have some kind of orientation behaviour (bending). Microtubules in the growth state grow with rate V_g, and those in the shrinking state shrink with rate V_s. Red boxes denote parameters

How does V respond to the dynamics parameters? Increasing V_s or F_{cat} means that a microtubule will be more prone to shrinkage, and increasing V_g or F_{res} will push the balance toward growth; this is fairly intuitive. Note that V is sensitive to the absolute difference between V_g and V_s, and the ratio of F_{cat}:F_{res}. Thus, increasing F_{cat} and F_{res}, but maintaining F_{cat}:F_{res} will produce the same values of V. Another feature of the drift is that it is, of course, bounded by V_g and V_s: a microtubule cannot grow more quickly than V_g, and cannot shrink faster than V_s. The units of drift are those of velocity: μm min^{-1}.

In the three-state case, the random walk analogy is not strictly valid anymore, since by definition, a random walker takes a step at each time increment. With no allowance for remaining in one place, the random walk is not technically applicable. However, there is a threshold value, V_t determined by Green et al. (2005) and Allard et al. (2010):

$$V_t = V_s\left(F_{g2p}F_{p2s} + F_{cat}F_{p2g} + F_{cat}F_{p2s}\right) - V_g\left(F_{p2g}F_{res} + F_{p2g}F_{s2p} + F_{p2s}F_{res}\right), \quad (2a),$$

which, like equation 1, indicates the direction and extent of bias by its sign and magnitude. Arranged as it is, equation 2a indicates infinite and finite growth with negative and positive

values respectively, vice versa to the two-state V in equation 2. Thus, the equation can be re-arranged so that the sign of V_t indicates a similar result to the two-state case:

$$V_t = V_g\left(F_{p2g}F_{res} + F_{p2g}F_{s2p} + F_{p2s}F_{res}\right) - V_s\left(F_{g2p}F_{p2s} + F_{cat}F_{p2g} + F_{cat}F_{p2s}\right), \quad (2b).$$

This threshold quantity, unlike V, is not bound by V_g and V_s, which can hinder making inferences about a set of dynamics based on it. Instead, it can be put in a form similar to V:

$$V_3 = \frac{V_g\left(F_{p2g}F_{res} + F_{p2g}F_{s2p} + F_{p2s}F_{res}\right) - V_s\left(F_{g2p}F_{p2s} + F_{cat}F_{p2g} + F_{cat}F_{p2s}\right)}{\left(F_{p2g}F_{res} + F_{p2g}F_{s2p} + F_{p2s}F_{res}\right) + \left(F_{g2p}F_{p2s} + F_{cat}F_{p2g} + F_{cat}F_{p2s}\right)}, \quad (3).$$

So, as with V, we can make V_3 bound by V_g and V_s if we divide by the sum of the terms that multiply V_g and V_s. As stated, the random walk analogy for the three-state has limited applicability. Indeed, V_3 is not responsive to increased pause time percentage (see below), i.e. a proxy for the percentage of time spent in the pausing state, since a set of dynamics that have a predicted pausing time of 0.96% has the same drift as another set of dynamics with 0.04% predicted pausing time percentage. However, the particular dynamics sets referred to have equal transitions from the pausing state, and the transitions to the pausing state are also equal; in this case, the balance, so to speak, of the growth and shrinking phases is equal.

Although V_3 does not accurately reflect the percentage of time spent in pause, it does respond to the balance between growth and shrinkage: changing the ratio F_{p2g}:F_{p2s} changes the value of V_3, as does changing the ratio F_{g2p}:F_{s2p}. This is a manifestation of the complex systems nature of microtubule dynamics: by changing the flux of microtubules towards or away from pause or in the direction of growth or shrinkage, the drift, V_3, will change. Thus, V_3 is still of some use, but it must be used with caution; presumably, the sign of V_3 is still valid as an indicator of the direction of drift in three states, but the magnitude must be modulated by the pausing proportion; thus, taking V_3 with pausing proportion should indicate to what extent V_3 is valid.

In either case, the drift is intended as a metric for understanding the effect of a combination of dynamics parameters; in many cases, it is not exact. Indeed, it accurately describes the growth of a microtubule that at no point shrinks to extinction (Verde et al., 1992), and this is a manifestation of the discrepancy between theory and reality highlighted in figure 1. Furthermore, where sets of dynamics parameters that produce negative drift are concerned, microtubules are only persistent in this case because of re-nucleation (Verde et al., 1992). If there were no re-nucleation in a microtubule population with negative drift, we would not observe any microtubules.

c. Average length

The average length of the microtubule population is defined only in cases where the drift is negative. This is intuitive since a microtubule population with positive drift will continue to grow indefinitely, and the average length increases continually too. As with drift, Verde et al. (1992) and Dogterom and Leibler (1993) have found the average length in terms of the dynamics parameters:

$$\langle L \rangle = \frac{V_s V_g}{V_s F_{cat} - V_g F_{res}}, \quad (4),$$

where $\langle L \rangle$ is the average length. In the three-state case, Green et al. (2005) and Allard et al. (2010) have derived the appropriate equation for the mean length:

$$\langle L \rangle = \frac{V_g V_s (F_{p2g} + F_{p2s})}{V_s \left(F_{g2p} F_{p2s} + F_{cat} F_{p2g} + F_{cat} F_{p2s}\right) - V_g (F_{p2g} F_{res} + F_{p2g} F_{s2p} + F_{p2s} F_{res})}, \quad (5).$$

In both cases, the distribution of lengths decreases exponentially. It is important to note that the mean equation ignores nucleation and microtubules with zero length. Thus, if an empirical microtubule average length is to be compared directly with a theoretical prediction, the mean length must be calculated for only those microtubules with non-zero length. However, $\langle L \rangle$ is best used as a theoretical indicator of microtubule growth properties

d. Length randomness

The next measure to consider is that of the tendency of a microtubule, or indeed a population of microtubules, to fluctuate about the average length. There are a few related ways of quantifying this. Firstly, continuing with the random walk analogy, Mirny and Needleman (2010) use the effective diffusion coefficient, *D*, as a measure of the extent to which the length of a microtubule will fluctuate. The use of the diffusion coefficient comes from the similarities between a random walk and diffusion; here, *D* indicates the extent to which we can expect lengths to deviate from the average. It is an indirect measure of velocity, in that it indicates how quickly a diffusible object (in this case, this is the plus end of the microtubule) will explore space, and it has units of $\mu m^2\ min^{-1}$. Mirny and Needleman (2010) find *D* in terms of the dynamic parameters:

$$D = \frac{V_g V_s}{F_{res} + F_{cat}}, \quad (6).$$

This interpretation of the randomness of microtubule growth is good for its ease of understanding. We can see from equation 6 that the randomness is simply a ratio between the product of the growth and shrinkage rates and the sum of the transition frequencies. Increasing V_g or V_s, or decreasing the transitions between them, increases the randomness of lengths. This is because, as microtubules will transit between phases less frequently, or if they grow or shrink more quickly, they will be able to undergo larger unchecked excursions of growth or shrinkage than if F_{res} or F_{cat} were greater, or if V_g or V_s were smaller.

Note that, as with the drift, the diffusion coefficient is not intended to give an exact measure of microtubule length randomness; rather, its magnitude indicates how much we can expect length to vary, and indeed, a dynamics set with a larger *D* will have a wider spread of microtubule lengths than another set with a smaller *D*. The reason that it is not exact is because a random walker can go in both directions; the displacement can be negative, whereas a microtubule will not have a negative length (fig. 1). Thus, *D* is not accurate, but it is a good theoretical measure of the spread of microtubule lengths.

One other point of note is the case where one of the transitions is zero. If F_{cat} is zero, then D is not appropriate, because, as all microtubules initiate in the growing state, there will be no transitions to the shrinking phase, and there will be no deviation in lengths: the dynamics are essentially deterministic in this case; all microtubules will be the same. If F_{res} is zero, D is still valid.

Related to the concept of the diffusion coefficient of a given set of dynamics is the total displacement of a microtubule over a given time. This type of measure is similar to the mean-squared displacement, commonly employed in random walk theory. The mean-squared displacement actually depends on the diffusion coefficient:

$$\langle x^2 \rangle = 2Dt, \quad (7),$$

where $\langle x^2 \rangle$ is the mean-squared displacement, and t is time. This relationship is quite intuitive, since the diffusion coefficient quantifies how much space a diffusive particle will explore, the average displacement would be dependent on this and time; the 2 at the beginning of the right-hand-side is a constant that depends on dimensionality (for one dimension, the constant is 2).

The mean-squared displacement, at least in the standard form in equation 7, is again not an exact measure of microtubule dynamics due to the same issue discussed above, i.e. that this is a relationship based on a true random walk, not microtubule dynamics. However, there are two related concepts: first is one that is quite often employed in the literature and is generally referred to as dynamicity (e.g. Rusan et al. (2001)), and the second is the range of microtubule lengths.

Dynamicity is the total length change per unit time as a result of growth and shrinkage, and can be used as a measure of microtubule length randomness, the rationale being that microtubules that change length more quickly are more random. The calculation for dynamicity is similar to the mean-squared displacement because it involves making growth and shrinking episodes of the same sign by squaring; generally, dynamicity is not reported in units of $\mu m^2\ min^{-1}$, just $\mu m\ min^{-1}$, therefore the sum of the square root of the square of the growth and shrinking distances is used:

$$d = \sum \sqrt{x^2}, \quad (8),$$

where d is dynamicity, and x is the displacement of a microtubule plus end. The dynamicity is not exactly comparable to the mean-squared displacement of the diffusion coefficient because for high values of D, one must have low transition frequencies, and although such a dynamics set could also give rise to high dynamicity values, a dynamics set with high transition frequencies could also lead to high dynamicity. Dynamicity is still a useful measure, however, and it is also a good indicator of the time spent in pause, where a low dynamicity would indicate long times in pause.

The second measure related to the mean-squared displacement and D is the length range. Although difficult to measure *in vivo*, such a measure could be used in conjunction with the modelling in this chapter. The rationale behind this measure being an indicator of length

randomness is quite simple: dynamics sets that have greater *D* should have a larger range in length, because microtubules will be more prone to undergo significant episodes of growth and shrinkage. The last two measures discussed here are more heuristic than the preceding measures that are backed by theory, and below, the theoretical measure *D* will be used more often to compare dynamics; however, for empirical comparison of simulations, both dynamicity and length range will be used.

e. Drift, average length and diffusion coefficient relationship

The three theoretical measures introduced above are united by the relationship:

$$|V| = \frac{D}{\langle L \rangle}, \quad (9),$$

where $|V|$ indicates the modulus (the absolute value) of the drift. Note that, since the average length, $\langle L \rangle$, is only valid when there is negative drift, as *V* becomes more negative, the average length is shorter, while a larger diffusion coefficient, *D*, will increase the average length for similar values of *V*. These relationships provide a quite basic insight to the workings of a microtubule population: in the bounded growth regime, the average length is a balance of the randomness of length and the drift that is working to shorten microtubules, so larger randomness in length can effectively work to overcome the bounds of a negative drift, making average length larger. Likewise, when length randomness is small compared to the drift, the drift dominates, and average length is reduced.

f. Phase time percentages

Another useful set of measures is the expected proportion of time spent in each phase:

$$T_g = \frac{F_{res}F_{p2g} + F_{res}F_{p2s} + F_{p2g}F_{s2p}}{\sum T_{phase}}, \quad (10a),$$

$$T_s = \frac{F_{cat}F_{p2s} + F_{cat}F_{p2g} + F_{p2s}F_{g2p}}{\sum T_{phase}}, \quad (10b),$$

$$T_p = \frac{F_{g2p}F_{s2p} + F_{g2p}F_{res} + F_{s2p}F_{cat}}{\sum T_{phase}}, \quad (10c),$$

where T_g, T_s and T_p are the percentages of time in growing, shrinking and pausing, respectively, and T_{phase} denotes the total of the numerators in the three equations. The numerators in the formulae for T_g and T_s are actually used in the calculation of the three-state drift, where they are multiplied by V_g and V_s, respectively. The above formulae, rather than giving an absolute number for phase times, which would depend on the time of observation, give the percentages of time spent in each phase. Only the three-state equations are given, since in two states, the drift is a good measure of the balance between the two phases. Therefore, this measure is particularly useful as an indicator of the prominence of the pausing state in any dynamics set.

As with many of the other measures discussed, these phase proportions are not exact in all cases. One of the main complicating factors that affects the accuracy of these measures is

extinction and re-nucleation. Nucleation is not taken into account in any of the measures so far discussed, and in this case, by removing shrinking microtubules and substituting them, at some point, by growing microtubules, this process especially affects T_g and T_s, making them greater and lower, respectively, than predicted. T_p is not affected on the same scale as T_g and T_s by nucleation, but the extent to which it is affected will depend on the relative sizes of transitions to and from the pausing phase. Knowing this, we can see that the accuracy of the phase proportions will be increased for greater average lengths, where nucleation should have less of an affect by allowing more representative times in growth and shrinkage, and the accuracy should also be increased for dynamics sets that are not as random in length, since it is these fluctuations (fig. 1), specifically those in shrinking, that lead to extinction and re-nucleation.

II. Modelling approach

a. Outline

This section is essentially the methodology section, describing the workings of the model. Having reviewed previous instances of use of modelling in microtubule biology, and formulated the question that is to be addressed in this chapter, I now summarise the requirements of a model that will be used to investigate these problems, and set forth how it will be implemented.

The model is phenomenological, at the level of individual microtubules, their behaviour described by the transition frequencies and growth and shrink rates obtained with light or fluorescence microscopy of microtubules in real cells, and not by association/dissociation reaction rates for tubulin, generally obtained *in vitro*. This level of abstraction is chosen since it is effectively just below that in which we are interested, the organisation of the microtubule population. Previous models have shown that specifying tubulin interactions, modelling at the level below that chosen here, produces the features of dynamic instability at our level (Gregoretti et al., 2006). To model at a lower level here would be to introduce unnecessary model complexity.

In the model, there will be an inner and outer area, each with its own set of dynamics. Furthermore, the model will be implemented in two- and three-state versions; thus, depending on this, there are four or eight parameters to describe the dynamics within each area. Nucleation is instant, i.e. as soon as a microtubule is extinct, it grows again in the next iteration; this is justifiable because it is the mechanisms of microtubule radiality that are of interest, not the balance of microtubule numbers, or polymer level. Although the model is based on individual microtubule dynamics, the abstract parameters just described will be used extensively too, so as to aid in understanding the effect of changing various parameters. Employing these measures as a read-out for the effect of combinations of dynamics parameters also assists in comparisons of inner and outer area dynamics.

Microtubule models at this level of abstraction are amenable to stochastic and deterministic approaches. In fact, the average length calculation described in the previous section is based on deterministic considerations of microtubules at this level. Here, I implement a stochastic, Monte-Carlo type approach, the methodology for which is described below. First, the model

is introduced, then the parameters and implementation are specified. A diagram of the model is shown in figure 3.

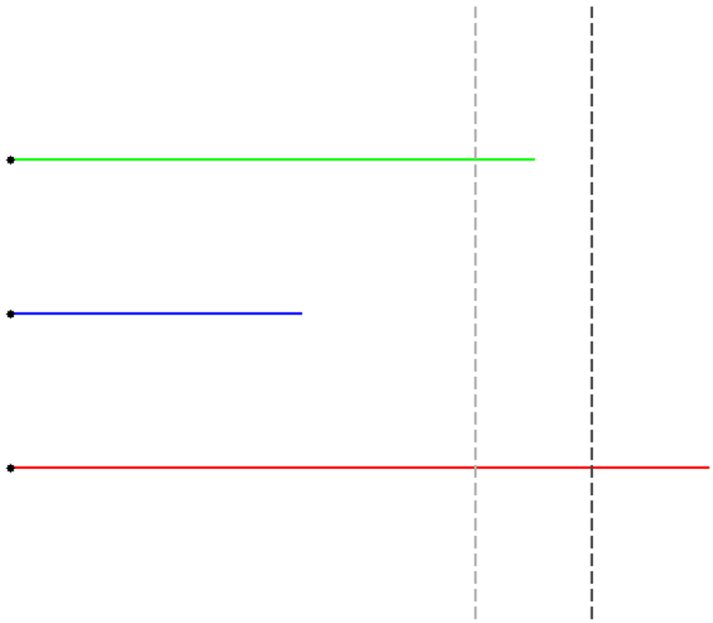

Figure 3. Microtubule model. In the model, the inner and outer boundaries are marked by light and dark grey dashed lines, respectively. Microtubules are modelled in 1-dimension; they do not bend, and are subject to inner dynamics (blue microtubule) and outer dynamics (green microtubule), and can also grow past the outer border (red microtubule). The microtubules have differing levels of accuracy; the green microtubule has accurately targeted the outer area, while the blue and red microtubule are inaccurate.

b. Model details

The model is designed specifically to investigate the mechanism of accurately regulating microtubule length in order to produce proper cortical targeting. It will answer the question: what are the combinations of dynamics in inner and outer areas that target microtubules to the outer area? Microtubules here are straight, and all grow in one dimension (fig. 3). Since the model is one-dimensional, the inner and outer areas are represented by lengths: when a microtubule reaches a given length, it obeys outer dynamics, and before that, inner dynamics.

As the model is intended to answer the question of outer area, or cortical, targeting, there is no maximum length imposed, and microtubules are free to grow past the outer boundary. This is because we want to know here how inner and outer dynamics can combine to produce microtubules of the appropriate length.

c. Dynamics parameters

Microtubule dynamic instability can be defined by either four or eight parameters, depending on whether a two- or three-state model is used. The former case neglects the pause phase, and here, both dynamics models will be used (fig. 2).

III. Implementation

a. Parameter values

It is very well having the growth and shrink rates expressed in μm min^{-1} or μm s^{-1}, since, if we assume that growth and shrinkage is uniform with microtubule length, i.e., that there is no length-dependence in these rates, then the increase in length over unit time is simply proportional to the time. According to the specifications set out in section BII, we can use these values as our growth and shrink rates, and scale them according to the time step in the simulation, more of which is discussed below. However, the situation is not so clear-cut with the phase transitions. Commonly, the frequency of a particular transition is calculated by dividing the number of occurrences of that transition by the total time spent in the phase that the transition leaves (e.g. Rusan et al. (2001)):

$$F_{trans} = N_{trans}/t_{phase}, \quad (11).$$

For example, to calculate the frequency of catastrophe, F_{cat}, the number of catastrophes is divided by the total time spent in the growing phase, t_g. Depending on the units, we may have transition frequency expressed in s^{-1} or min^{-1}; the latter is more common. Refer to section BII in chapter 3 for a discussion of the various ways of calculating transition frequencies.

Our model specification requires that we have some kind of probability for each transition that determines what a microtubule will do at each time step. Since these transitions are recorded as frequencies based on long observation times of many microtubules, with units min^{-1} or s^{-1}, how do they fit into a simulation? To answer this, we need to cover some of the basics of probability, and this is discussed in the next section.

b. On probability

Thus far, we have established that our qualitative model specifications regarding transition frequency do not immediately correspond to measurements that are commonly reported. The problem is this: given that an accurate simulation of microtubule dynamics will require a time step on the order of a second or smaller, how do we handle the transition frequencies reported in the literature so that we have meaningful probabilities in the simulation? Here, I cover some of the relevant aspects of probability theory with the aim of making the quantitative features of the model the best approximation of reality that is possible.

Probability theory, in what is known as the "frequentist" approach, states that, as we observe a process, or repeat an experiment, the longer or the more times for which we do this, the frequency of an observed event approaches the probability of that event (Ross, 2006). To illustrate, a common example is rolling two dice. The "sample space" is the various combinations of numbers on the dice, and each of these is said to be an "event". The sum of the probabilities of each event is 1; it is never more than one. The more times we roll the dice, the frequency with which these combinations occur approaches their probability; this is often described as the "relative frequency". In this case, the relative frequencies of the events should all be equal at $^1/_{36}$, assuming fair dice. So, in our case, the longer we watch

microtubules for, the frequency of transitions is a truer representation of microtubule behaviour.

However, this still does not solve the problem of how to model a transition probability; yes, we have a relative transition frequency, but can we just scale this frequency with time step? Firstly, is it appropriate to say, for example, that a transition frequency of 10 min^{-1} is the same as 5 every 30 seconds? And, given this frequency, is it appropriate to suppose that we can expect a transition every 6 seconds? It makes intuitive sense that this is the case, but this is still not a probability, since it is greater than 1, and we know that a probability cannot be so. Of course, it could be easy to make this mistake when using a smaller time step that reduces the relative frequency to a value smaller than 1.

To obtain probabilities of microtubule phase transitions, we require some kind of probability model, but what is a probability model, and which would be appropriate for microtubule transitions? A probability model is simply the way in which we expect a variable, in this case transition frequency, to behave probabilistically. As we might expect given the frequentist interpretation of probability, such a model is based on the results of a number of experiments; it has a distribution, and can tell us the probability of a given event occurring.

So what is the appropriate probability model for microtubule transitions? Rather than an average number for each transition frequency, the distribution of transition time would indicate what type of model would be appropriate. Unfortunately, very few have addressed this question empirically; pioneering work from Odde et al. (1995) is a notable exception.

Previous modelling work does not make the problem much clearer: methodological details being somewhat scarce, some have treated transition probabilities as uniform random numbers between 0 and 1, others use an "exponential random number" for transition probability, while perhaps the clearest account of microtubule modelling method at this scale comes from Gardner and Odde (2010). In this case, the authors describe how they find the transition probability using the cumulative exponential function:

$$p = 1 - e^{-\mu\tau}, \quad (12),$$

where p is a transition probability, μ is the exponential parameter, and τ is the time step of the simulation. In this case, μ is the observed frequency of the transition in question, measured as described above. However, these authors did not state the reasons for their methodology, and thus leave us still without a full understanding of transition probabilities.

Fortunately, the situation can be clarified by taking an alternative approach. Instead of basing a probability model on empirical observation, i.e., on population data, it can be based on what is known, or at least, what is assumed, about the process in question at the individual, small-time scale. With regard to microtubule catastrophe and rescue (and transitions to and from pause), the consensus is that the probability of a transition is the same regardless of microtubule age, length, etc. Thus, given a length of time, the probability that a transition will occur in that window is the same as the probability in the next time window, and the window after that, and so on. Recent *in vitro* work (Gardner et al., 2011), and that work

mentioned above from (Odde et al., 1995), has suggested that the situation may not be as simple as this, but we will continue with it for now, the reason for this becoming clear later.

There is a probability model that applies to this problem. Firstly, bearing in mind that we are assuming a constant chance of an event, in this case a transition occurring, per time increment, we will set the problem. The task is to record the time for each event; that is, upon starting the experiment, the clock starts, and upon an occurrence of an event, we reset the clock, and start counting again. This is a form of what is known as a counting process, known as a "Poisson" process.

The premises of a Poisson process are that the number of events counted in any given interval of time are independent of the number of events occurring in another time interval; this is called "independent increments", and furthermore, that the numbers, *n*, of events in any given time interval, *t*, are Poisson distributed (Ross, 2006). These premises essentially state that the Poisson process is stochastic; each event is independent of other events. Given that we are assuming that the probability of a transition occurring within any given time window is the same as that of another equivalent time window, we can model the counting of transitions as a Poisson process. Forgetting time for a moment, the Poisson distribution, with rate parameter λ, is thus:

$$p(i) = P\{x = i\} = e^{-\lambda}\frac{\lambda^i}{i!}, \quad i = 0, 1 \ldots, \quad (13),$$

where *x* is the random variable, and *i* is any of the integer values *x* may take. The rate parameter λ must be greater than zero. In our case, *x* would be the number of events of a given transition, and thus, the Poisson distribution would give the probability of counting a given number, *i*, of those transitions.

Of course, from a modelling perspective, the quantity that is really of interest here is not the probability of a given number of events occurring, but the time before each transition, i.e. the time between events. The inverse of the time between events gives the frequency; this is the same as dividing the number of events by the total time of observation, the common method of calculating transition frequencies. The problem of finding the probability of times between events in a Poisson process is known as the "inter-arrival" time problem; in other words: given that we are counting events that obey a Poisson process, what is the distribution of the times that we wait for each event?

If we say that the time between the n^{th} and $n\text{-}1^{th}$ events is T_n (if it is the first event, T_1 is the time before the first event) then T_n, for all values of *n*, gives the distribution of inter-arrival times (Ross, 2006). What is the distribution? Starting with the first event, T_1, we can say that the event occurs only if no events have occurred prior to it, in the time interval [0,*t*], where *t* is the length of time just before T_1 occurs (square brackets denote $0 \leq x \geq t$). Thus, we want to know the probability that T_1 is greater than *t*, i.e. $P\{T_1 > t\}$. Taking time into account in the Poisson process just involves the time interval, t, multiplying the rate parameter λ (Ross, 2006).

$$P\{T_1 > t\} = P\{N(t) = 0\} = e^{-\lambda t}\frac{(\lambda t)^0}{0!},$$

$$P\{N(t) = 0\} = e^{-\lambda t}, \quad (14),$$

where $P\{N(t) = 0\}$ is just restating the question; it simply means the probability of events occurring in time *t*, *N(t)*, being zero. $e^{-\lambda t}$ is an exponential distribution; thus, the distribution of times, T_1, before the first event, is exponential. How are the times between the first and second events distributed? In this case, for the second event to occur, the first event must already have occurred. If we denote the time at which the first event occurred as *s*, and the time elapsed from the first event just up to the occurrence of the second event as *t*, the probability for the second inter-arrival time is a conditional probability; we ask: what is the probability that T_2 is greater than *t*, given that T_1 occurred at time *s*, i.e. $P\{T_2 > t \mid T_1 = s\}$, where $\mid$ denotes the condition that $T_1 = s$, thus:

$$P\{T_2 > t | T_1 = s\} = P\{0\ events\ in\ (s, s+t] | T_1 = s\},$$

$$= P\{0\ events\ in\ (s, s+t]\},$$

$$= e^{-\lambda t}\frac{(\lambda t)^0}{0!},$$

$$= e^{-\lambda t}, \quad (14)$$

where, as above, a square bracket indicates a closed interval and a circular bracket indicates an open interval, i.e. $(s, s + t] = s < x \geq t$. The conditional statement in the first line can be discounted because of independent increments as described above: the probability of events occurring in any interval is independent of the probability of events occurring in other intervals, thus, the problem is reduced to finding the probability that the numbers of events occurring within a given time interval is equal to zero; the same problem as with T_1. Therefore, T_2 follows the same exponential distribution as T_1, and this is true for any T_n, n = 1,2, …

Thus, a Poisson process, where an event has an equal (and independent) chance of occurrence every time increment, gives rise to an exponential distribution of so-called inter-arrival times. We can verify this experimentally. Figure 4 shows the distribution of inter-arrival times for an event with rate parameter λ of 0.1 every time increment, *t*, of one. The probability and time increment are academic here; the point is that this process, whatever the probability or waiting time, produces a distribution with this shape. An exponential distribution can be fitted to the inter-arrival times, and indeed, random data shown in figure 4 that are generated from the fitted exponential distribution are not significantly different from the original data (2-sample Kolmogorov-Smirnov test, $p > 0.05$).

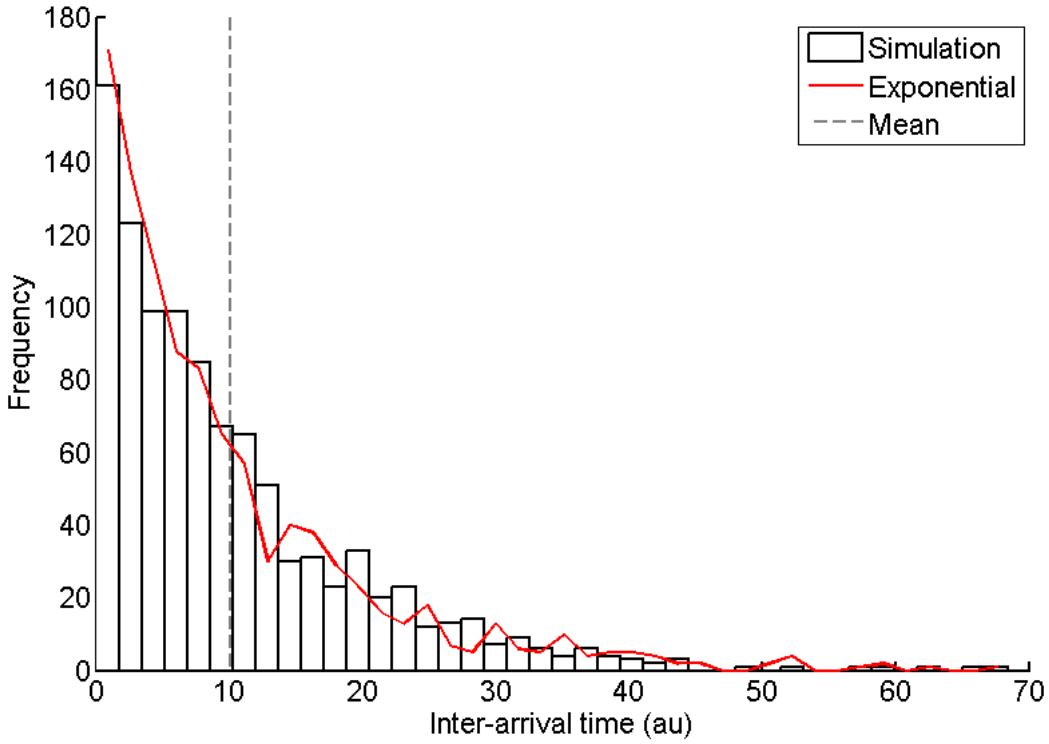

Figure 4. Inter-arrival times in a Poisson process. The simulated data, which are the inter-arrival times between an event occurring with equal chance per time step, are closely matched by random numbers generated from the expected distribution; the mean of the distribution is also shown (refer to legend)

How does this bear on our initial problem of finding transition probabilities, given their frequencies? The exponential distribution has a very helpful property in this regard. The expected value, or mean, of the distribution is equal to $1/\lambda$; figure 4 shows the mean value of the inter-arrival times. Here, the rate λ is 0.1; thus we would expect the mean to be $1/0.1 = 10$, and indeed, the experimental mean is close to this value at 10.06. Therefore, the average value of the inter-arrival times is the inverse of the rate parameter of the Poisson process that gives rise to those times. This is the underlying assumption in calculation of microtubule transition frequencies, which are taken as the inverse of the observed frequency of transitions. Therefore, since the rate parameters of microtubule phases transitions are easily calculated, we can find the probability of a transition occurring in a given time step using the exponential distribution. Specifically, the exponential cumulative distribution probability function is used:

$$F(a) = 1 - e^{-\lambda a}, \quad a \geq 0, \quad (15).$$

The cumulative distribution function gives the probability of finding a value in the exponential distribution with rate parameter λ that is less than or equal to the value of a. In this case, the variable a is a length of time; we substitute for a the time step of the simulation, and ask: what is the probability of the time before a transition being less than or equal to the time step? Although this is exactly what we are asking, the question is more intuitively stated

thus: over this length of time, what is the probability of observing a transition? Thus, all transition frequencies will be treated this way in the model.

c. Simulation

As the model is a stochastic model, it will be simulated with all microtubules in the model being updated at each iteration. The time of the simulation is updated according to a discrete time step of 0.1 seconds. Therefore, at each advance of 0.1 seconds, all microtubules will be tested for a phase transition, and their lengths updated accordingly. To get a good appreciation of the effects of the two areas, simulations will be run with two area, the "two-area" model, and with only one set of dynamics, in an "area-free" model.

d. Microtubule dynamics

In the model, each microtubule has a state, a length, and a "region". The region property is simply a logical for whether the plus end of the microtubule is located in the inner (false) or outer (true) area. For a quicker simulation, the microtubule dynamics are implemented in parallel: thus, states, lengths and regions are stored in column vectors of length N, where N is the total number of microtubules in the model.

The model simulation begins with all microtubules in the "extinct" state, having zero length, and, of course, being in the inner area. All minus ends are located at the centrosome, the location of which is specified in 2-dimensional Cartesian co-ordinates. For simplicity, the location of the centrosome is kept at (0, 0), and microtubules grow in the positive x-direction, i.e. to the right. At each iteration, it is determined whether a microtubule will undergo a phase transition or not. The particular phase transitions possible depend of course on the state of the microtubule. Thus, those in growth can either undergo catastrophe or growth to pause, or stay in growth, and so on for the other states. As discussed, all transition frequencies are assumed to be constant, and thus the probability of each phase transition is obtained using the exponential cumulative distribution function with the appropriate rate (i.e. the particular transition frequency) and time step (0.1 seconds).

In order to determine whether a transition will occur, a uniform random number between zero and one is generated using the Matlab command "rand". This number is compared to the transition probability: if it is less than the transition probability, the transition occurs, and if it is greater than the probability, the transition does not occur. This is a standard method of simulating probabilities, and is documented for microtubules in Gardner and Odde (2010) (note that, in this paper, it is stated that the probability must be less than the uniform random number for a transition to occur, but this is erroneous, and a correction is in the process of being submitted at time of writing, D. Odde, *pers. comm.*).

In the three-state model, there are two potential transitions available, and so the probabilities for each transition must use discrete intervals between zero and one. This is handled by assigning one transition value between zero and its probability, and the other transition values between the probability of the first transition and its probability added to the probability of the first transition. For example, for the pause state, a transition to growth might occur with probability 0.2, and a transition to shrinking might occur with probability 0.1; the transition

to growth will occur if the uniform random number x lies on the interval $0 < x \geq 0.2$, and the transition to shrinking will occur if the uniform random number x lies on the interval $0.2 < x \geq 0.2 + 0.1 = 0.3$. It does not matter which way around this is done; the transitions will still occur with the appropriate probability.

Once it has been determined whether a transition will occur, the state of the microtubule is updated if necessary, as is the length. If the microtubule is to grow, then it is assumed that the growth rate is constant; thus the length added is the growth length in a minute multiplied by the time step. At a time step of 0.1 seconds, this is a small increment of growth. The same principles are applied to the shrinking rate if the microtubule is to shrink

C. PARAMETER VALUES

I. Dynamics combinations

a. Two-state dynamics

As is discussed in the results below, the drift and average length were varied in initial simulation of the model so as to investigate cortical targeting accuracy. The change in drift here was implemented by changing the F_{cat}:F_{res} ratio. However, the diffusion coefficient, D, which indicates the randomness in microtubule lengths, was required to remain constant so as not to bias the results in any way, for example, changing the F_{cat}: F_{res} ratio by increasing F_{cat} while holding F_{res} constant changes not only the drift and average length, but also D. This effect arises because D is sensitive to the sum of the transition frequencies. Therefore, the concept of a target transition frequency sum was introduced: in each dynamics combination, the sum of F_{cat} and F_{res} is the same, so D is constant. For full details of the dynamics values, see the appendix tables (section F). All dynamics parameter values were chosen with reference to values reported in the literature; these are documented further in chapter 5.

In the second set of experiments, only outer dynamics were varied, and inner dynamics remained at high positive drift. Two more dynamics sets were created; here, in set 4, the diffusion coefficient was held constant while the theoretical average length was varied, and in set 5, the theoretical average length was held constant while the diffusion coefficient was varied. In each set, the drift varied with the parameter that was being varied for that set. Again, for details of the dynamics, see the appendix tables (section F).

b. Three-state dynamics

In these experiments, there were 5 dynamics sets, and as with the second set of experiments in two states, only outer dynamics were changed; inner dynamics remained at high and positive drift. Within each set, the abstract parameters were held constant, and the pausing time percentage was varied. Between sets, drift and average length were varied; for values, see the appendix tables.

D. RESULTS

I. Two-state dynamics

a. Model efficacy

Firstly, the two-state version of the model was tested. The area-free and two-area simulations were both examined, and both types of simulation reproduced the specified dynamics well. In the area-free simulation, results were similar, with good agreement between the specified and observed transition frequencies indicated by high correlation coefficients. In fact, the Pearson's linear correlation coefficients here were all 1.00 for each dynamics set (from hereon, all correlations will be Pearson's linear). The specified and observed transition frequencies in the area-free and two-area simulations are plotted in figures 5 and 6, respectively. In the two-area simulation, the correlation between the specified and observed transition frequencies in both areas in the first simulation type was also high (table I).

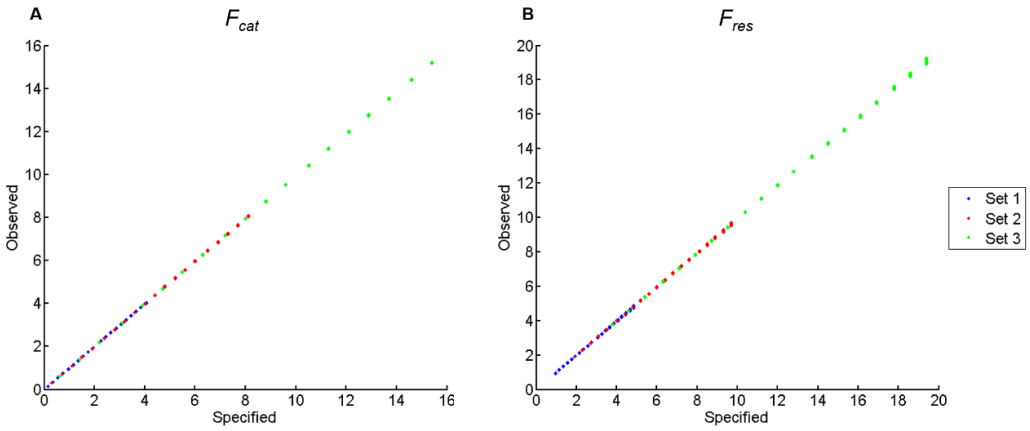

Figure 5. Specified and observed transition frequencies for 2-state model 1 in area-free simulations. The specified and observed values are plotted for F_{cat} (A) and F_{res} (B) for each dynamics set (refer to legend). Transition frequency units are min^{-1}.

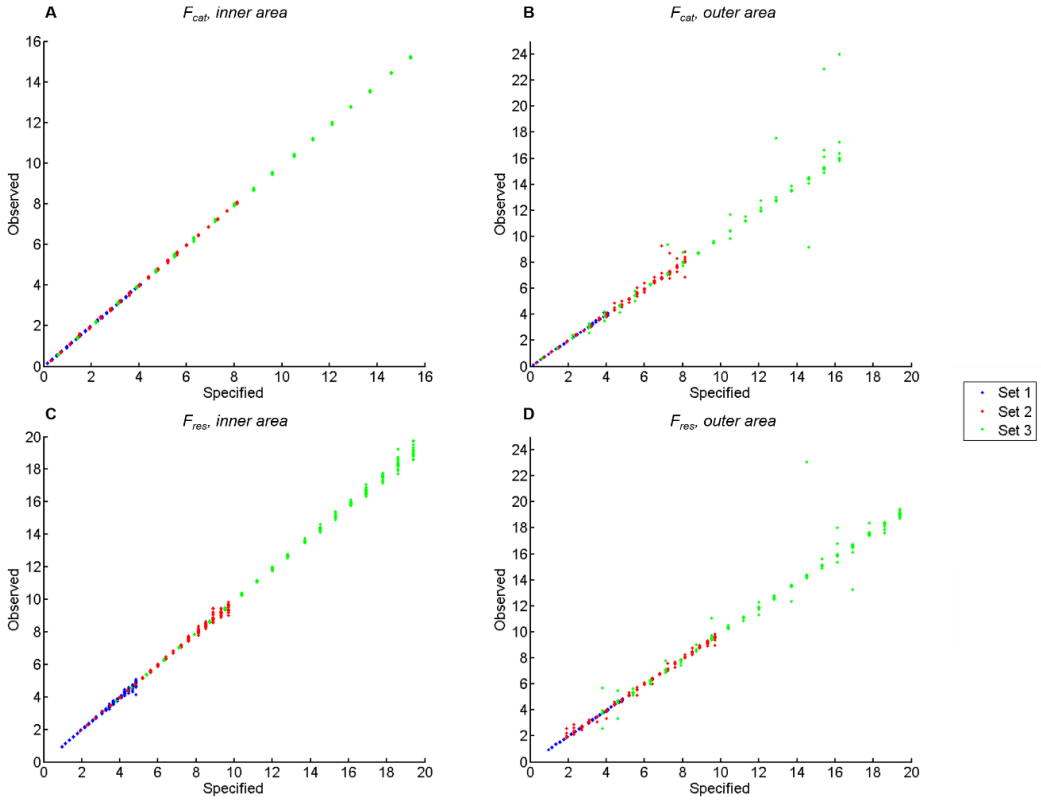

Figure 6. Specified and observed transition frequencies for 2-state model 1 in two-area simulations. The specified and observed values are plotted for F_{cat} in the inner (A) and outer (B) areas and for F_{res} in the inner (C) and outer (D) areas, for each dynamics set (refer to legend). Transition frequency units are min^{-1}.

Table I. Correlation between specified and observed transition frequencies in the two-area simulation. The correlation coefficient for each transition frequency in each area, for each dynamics set, is shown.

	Inner area		Outer area	
Set	F_{cat}	F_{res}	F_{cat}	F_{res}
1	1.00	1.00	1.00	1.00
2	1.00	1.00	1.00	1.00
3	1.00	0.99	1.00	0.99

b. Population measures

Where in the previous section, both two-area and area-free simulations were used to test the model efficacy, here, only the area-free simulations are used. This is because simulating a single set of dynamics simplifies the complexity of the system a great deal, and it is easier to determine if a given set of dynamics reproduce theoretical predictions. Recall that the aim of these sections, where simulated and theoretical population measures are compared, is not to test model efficacy; rather, it is to establish the population properties of a given set of dynamics, and to understand whether theory agrees with these.

Firstly, to investigate how the average microtubule length varied in response to changing dynamics parameters, the observed length was found by averaging microtubule lengths over

the final 10 minutes of a 60-minute simulation for each dynamics set. The observed lengths are plotted against the theoretical length in figure 7. For all but the greatest of the theoretical lengths in each set, the observed lengths are similar to their predicted counterparts; the relationship falls off somewhat at the largest predicted value, with the observed value lower than predicted. Nevertheless, the predicted and observed lengths are very well-correlated (table II), indicating that the dynamics sets behave as predicted. Furthermore, the mean-squared error between the predicted and observed lengths is fairly low, and if the predicted and observed lengths at the smallest magnitude negative drift are omitted, the mean-squared error is very low (table II), indicating that the dynamics produce the expected theoretical population characteristics.

Note that increasing the simulation time has little effect on the average length, so explanations of the discrepancy between the predicted and observed average lengths at the smallest negative drift that are based on the population not yet having reached steady state are unlikely. Moreover, at the lowest negative drift, theory suggests that the population should shrink less on average, thus presumably reaching a steady state sooner than those with greater negative drift. However, since the lengths are exponentially distributed, to achieve a large average length, some individual microtubules would need to be very long; the fact that some microtubules may not yet have reached these large lengths may contribute to the lower average. In any case, in the subsequent section, these drift values are found to produce low accuracy, and longer simulation time would worsen this accuracy by allowing an increase in $\langle L \rangle$. Thus, it is not relevant to accuracy, and is not considered further in this section.

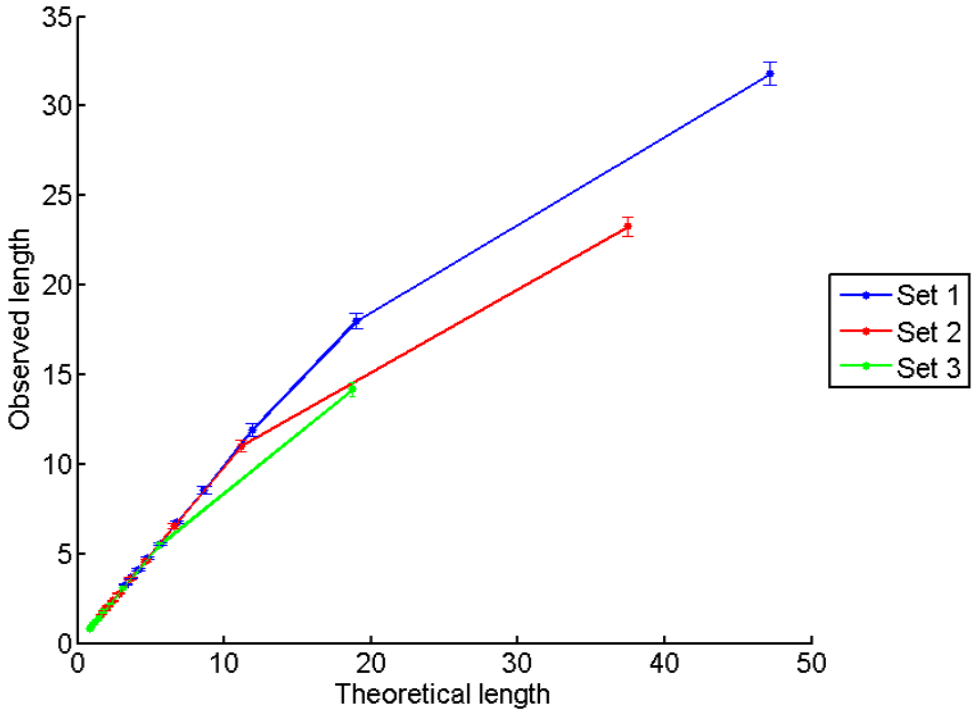

Figure 7. Theoretical and observed length in area-free model 1, two-state. The theoretical average length, $\langle L \rangle$, is plotted against the observed average length for each dynamics set (refer to legend). Length units are μm.

Next, the diffusion coefficient was considered. In dynamics sets 1-3, the diffusion coefficient is held constant within each set, but it varies between sets; in set 1, it is 33 $\mu m^2\ min^{-1}$; in set 2, it is 16.5 $\mu m^2\ min^{-1}$, while in set 3, it is 8.25 $\mu m^2\ min^{-1}$ (appendix). Recall that these are not exact measures, but they do indicate that the expected length randomness should be similar within sets, and be twice as large in set 1 as in set 2, and again twice as large in set 2 as in set 3. The diffusion coefficient as it is defined by theory (see chapter 4) is not a measurable property, and so as a measure of length randomness, the average of the range in length over the final 10 minutes of the simulation was taken for each negative drift value in each set (table III).

The first premise of the theory that the randomness should remain similar within each dynamics set is not supported by the data. Within each dynamics set, the average range in length decreases with increasingly large negative drift. The reason for this lies in the inconsistencies between the random walk model and real microtubule biology (fig. 1), which were discussed in chapter 4. Because microtubules cannot take on negative length, those dynamics sets that have large negative drift, and thus a small average length, are likely to be suppressed in terms of length randomness when compared to theory, because the theory allows for the random walker to have negative displacement. Therefore, where there are small average lengths, the deviation in lengths is more limited than at large average lengths, explaining the decrease in length range as negative drift becomes larger.

Table II. Predicted and observed average lengths for dynamics sets 1-3. For each set, the predicted and observed lengths are shown (units μm) for increasing large values of negative drift. The correlation and mean-squared error (MSE), the latter with and without the values for the smallest negative drift, are also shown.

Drift (negative)	**Set 1**		**Set 2**		**Set 3**	
	Predicted	Observed	Predicted	Observed	Predicted	Observed
Low	47.14	31.81 ± 0.63	37.50	23.26 ± 0.55	18.75	14.18 ± 0.42
	18.97	17.99 ± 0.41	11.15	11.02 ± 0.33	5.57	5.49 ± 0.11
	11.87	11.90 ± 0.34	6.55	6.54 ± 0.14	3.11	3.08 ± 0.06
Increasing drift	8.64	8.57 ± 0.21	4.63	4.62 ± 0.08	2.24	2.22 ± 0.03
	6.79	6.78 ± 0.09	3.59	3.59 ± 0.07	1.74	1.73 ± 0.02
	5.59	5.56 ± 0.09	2.80	2.79 ± 0.03	1.43	1.42 ± 0.01
	4.76	4.76 ± 0.08	2.38	2.37 ± 0.03	1.21	1.20 ± 0.01
	4.14	4.11 ± 0.06	2.07	2.07 ± 0.02	1.03	1.03 ± 0.01
	3.66	3.66 ± 0.04	1.83	1.83 ± 0.01	0.91	0.91 ± 0.01
High	3.28	3.26 ± 0.04	1.64	1.63 ± 0.01	0.82	0.82 ± 0.00
Correlation	0.99		0.98		1.00	
MSE						
With lowest drift	23.59		20.27		2.09	
Without lowest drift	0.11		0.00		0.00	

Although the first premise of the diffusion analogy to microtubule dynamics is not met, the second, stating that lengths should be progressively less random moving from set 1 to 3, is supported by the results. The ratios of the ranges at each negative drift value are shown in table III. As with the average length, the ratios between length ranges are remarkably similar to that predicted by theory, roughly at 2, apart from those for the smallest negative drift, where the ratio is smaller. This relationship is clearly visible in figure 8.

The fact that the range ratio at the smallest negative drift is not as large as expected provides an explanation for the average lengths in this case not being as large as predicted. Here, the lengths being not as random as predicted suggests that they have not explored space to the extent required to achieve the predicted average length.

Table III. Ranges of microtubule lengths and their ratios in dynamics sets 1-3. For increasingly large negative values of drift, the average range in length (units, μm) for each dynamics set is shown. Also shown are the ratios between sets 1 and 2 (1:2) and 2 and 3 (2:3).

Drift (negative)	Range			Range ratio	
	Set 1	Set 2	Set 3	1:2	2:3
Low	166.21	121.38	78.43	1.37	1.55
	123.86	75.99	41.69	1.63	1.82
	86.71	47.40	22.38	1.83	2.12
Increasing drift	65.30	34.01	17.24	1.92	1.97
	49.26	26.35	13.19	1.87	2.00
	40.92	20.67	10.65	1.98	1.94
	37.21	17.85	8.87	2.08	2.01
	30.42	15.78	7.63	1.93	2.07
	27.20	13.62	6.74	2.00	2.02
High	24.05	12.15	6.20	1.98	1.96

To further explore the relationships between the dynamics parameterisations and empirical measures of microtubule properties, the dynamicity was also found for sets 1-3 and the length range and dynamicity was found for dynamics sets 4-5. Using both of these measures as indicators of variation in length will allow further comparison of the theory with reality, and also establish the utility of the measures. The dynamicity for sets 1-3 is plotted with the length range in figure 8, and the length range and dynamicity for sets 4-5 is plotted in figure 9. Note that D is fixed in set 4, and $\langle L \rangle$ is fixed in set 5.

The results in figures 8-9 are consistent with the assessment of the correspondence of the theory and reality given in figure 1. There, it was suggested that increased theoretical length should produce greater values of empirical measures of variation in length. As figure 8 shows, this is the case for length range, and also for dynamicity. The fact that dynamicity levels of for all dynamics sets 1-3 as a function of theoretical length is explained by the theory in that increasing theoretical average length should not increase dynamicity *per se*, but move the random walk space further into positive displacement, and thus allow microtubules to reach levels of dynamicity that more accurately reflect the diffusion coefficient. Because the magnitude of drift increases with decreasing theoretical average length, the dynamicity and length range are small at large negative drift, and increase as drift approaches zero (fig. 8). The theory is also supported by the fact that the sets are ordered in both length range and dynamicity by their diffusion coefficients; with the greatest diffusion coefficient having the greatest values of these measures.

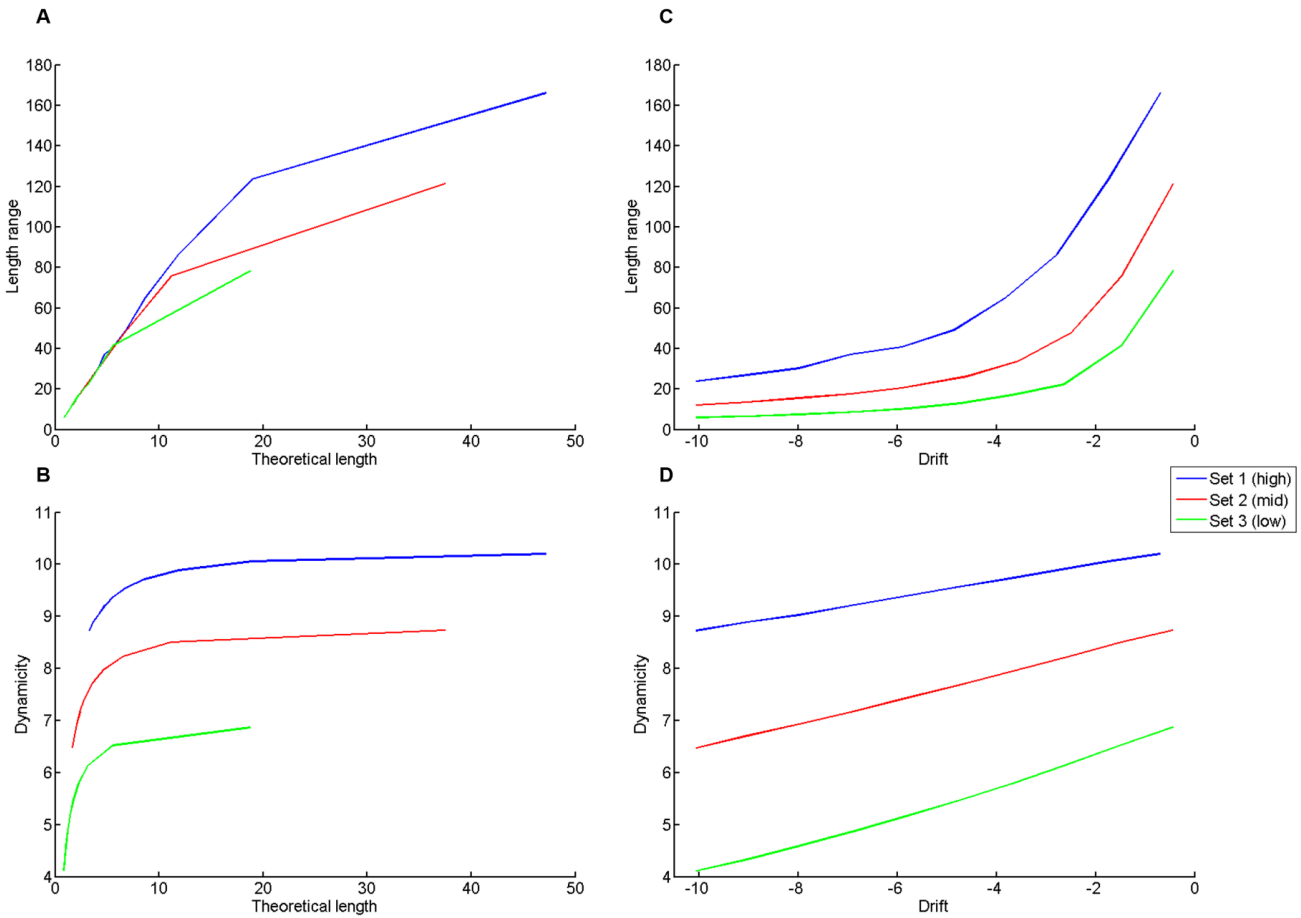

Figure 8. Length range and dynamicity in dynamics sets 1-3, area-free simulations. The length range and dynamicity are plotted as a function of theoretical average length (A and B, respectively), and of drift (C and D, respectively), for each dynamics set (refer to legend). Length and theoretical average length units are μm; dynamicity and drift units are μm min^{-1}. Increased theoretical length produces greater variation in length, while smaller-magnitude drift gives greater length variation.

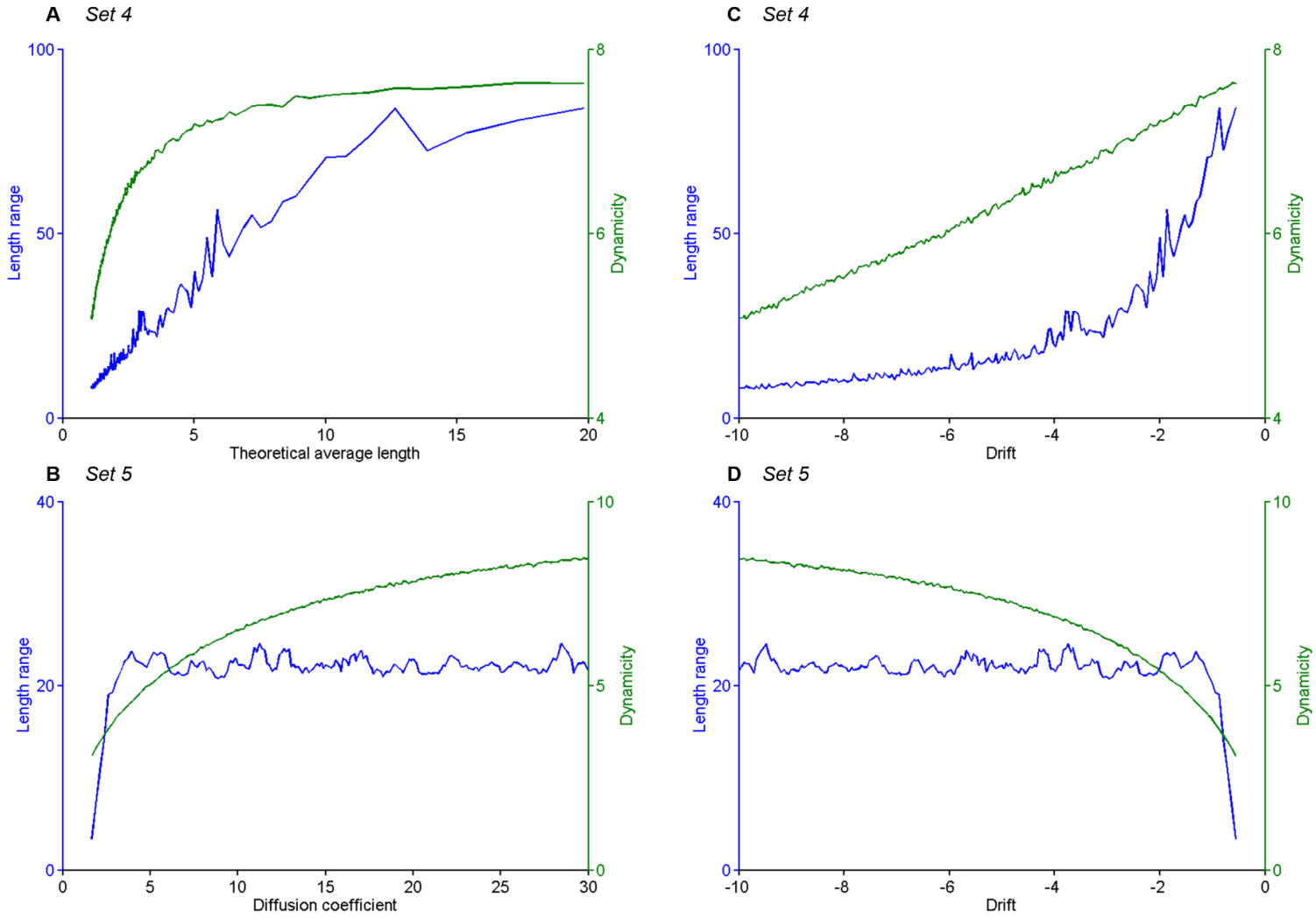

Figure 9. Length range and dynamicity in dynamics sets 4 and 5, area-free simulations. Length range and dynamicity are plotted against the theoretical average length for set 4 (A) and the diffusion coefficient for set 5 (B), then both are plotted against drift for set 4 (C) and set 5 (D). Length and theoretical average length units are μm; dynamicity and drift units are μm min^{-1}.

Dynamics set 4, in which the theoretical average length is varied while D is held constant, behaves in a similar manner to dynamics sets 1-3, which also had varying $\langle L \rangle$ (fig. 9A). Dynamicity and length range both increase with increasing theoretical average length, with the dynamicity levelling off as in sets 1-3. The dynamicity and length range also display a similar relationship with drift to sets 1-3 (fig. 9C).

In set 5, the situation is different, because here, D varies and $\langle L \rangle$ is fixed. However, it is still consistent with the assessment of the theory in figure 1. Here we see that an increase in the diffusion coefficient brings about an increase in dynamicity and also initially in length range; the latter quickly levels off and remains at similar levels for increasing D. Because theoretical average length is fixed here, an increase in D is limited in its effect on length range, because as D increases, the drift becomes larger (negative), and more of the random walk space becomes inaccessible to a microtubule, being moved into negative displacement. This can explain the steep rise and quick levelling of the length range. The rate of increase of dynamicity is also slowed as D becomes greater, and this is also for the same reason that length range cannot increase; however, the effect is more marked for length range because re-nucleation serves to decrease the length range, but has less of an effect on dynamicity. Because the magnitude of drift increases with increasing D, dynamicity is high for large negative drift, and length range undergoes a sharp decrease as drift approaches zero.

To summarise this section, the results indicate that the dynamics sets produce the expected population characteristics in general, with some interesting population properties emerging from the differences between the theoretical treatment and microtubule biology. Firstly, average length behaves as expected, but the variation in length, rather than being absolute, depends on the theoretical diffusion coefficient (because set 1 is still more random than sets 2 and 3), but also on the average length, or indeed the drift (because high negative drift and small average length is less random than low negative drift and large average length). Moreover, we have seen from sets 4 and 5 that for similar drift values, microtubule growth properties can be quite different. Next, the applicability of these dynamics sets for cortical targeting is assessed.

c. Cortical targeting in two states

In the first instance, the effects of combinations of inner and outer dynamics in two states on the accuracy of cortical targeting are considered. The first question addressed with the model was: what are the effects of particular combinations of inner and outer area dynamics on the accuracy of cortical targeting? Dynamics sets 1-3 were assessed first, for which only the theoretical average length was chosen to vary with drift, and to control for the potential effects of a changing diffusion coefficient with decreasing drift and average length, the dynamics sets were created in a way so that the diffusion coefficient remained constant (see section C).

The three dynamics sets have drift from -10.06 μm min^{-1} to 10.22 μm min^{-1}. The drift between these extremes is evenly spaced, and in total there are 20 dynamics combinations. Each of these is assigned to an area, giving $20^2 = 400$ simulations, and over 3 dynamics sets, 1,200. The diffusion coefficient, though fixed in each dynamics set, was changed for each: in

set 1, it was 33 $\mu m^2 min^{-1}$; set 2, 16.5 $\mu m^2 min^{-1}$, and set 3, 8.25 $\mu m^2 min^{-1}$. The drift and theoretical average length varied within sets, but between the sets, because the diffusion coefficients had different values, these theoretical average lengths differed. Thus, in set 1, the theoretical average lengths (once in negative drift) ranged from 47.14 μm to 3.28 μm; in set 2, from 37.50 μm to 1.64 μm, and in set 3, from 18.75 μm to 0.82 μm.

Each simulation was run for 50 simulation minutes before results were recorded; first, the accuracy of each dynamics combination was found. The measure of accuracy used here is simply the proportion of microtubule plus ends within the target cortical area. Thus, the accuracy was measured starting from 50 minutes, and average over the final 10 minutes of simulation time. As there were two sets of dynamics operating in these simulations, one for each area, and thus two drift values per simulation, the accuracy for each dynamics set is plotted as a surface, where the accuracy determines the height, or z co-ordinate, and x and y are the inner and outer drift, respectively (fig. 10).

The plots in figure 10 show that, while accuracy depends on the drift in both areas, the sign of the outer area drift is a major influence on accuracy; where there is positive outer area drift, accuracy is always low regardless of inner area drift. It is evident that to achieve good levels of accuracy, the negative outer area drift is best combined with positive inner area drift; however, compared to outer area drift, the accuracy does not fall off so steeply as inner area drift decreases, indicating that the accuracy is tolerant to negative inner drift values to a greater extent than it is to positive outer drift. Thus, the first conclusion here is that positive inner drift and negative outer drift produce the greatest accuracy in cortical targeting.

These observations can be reconciled with the average lengths in each dynamics set (fig. 11), because average length is effectively an indicator of accuracy. Again plotted as a surface with area drifts on the x- and y- axes, we can see that average length increases with increasing drift in both areas, but that the effect is more marked with increases in outer area drift. We can also see that at drift combinations that gave the greatest accuracy, the average length is close to the target area distance, indicated by the red shading. The average length here is actually just below the target length in set 3, but above it in set 1, consistent the accuracy results.

Interestingly, the plots in figures 11 reveal that the low accuracy at large negative inner drift and large positive outer drift arises for fundamentally different reasons in different sets. In sets 2 and 3, the average length is low at these drift combinations, indicating that the low accuracy here is due to microtubules not reaching the target area, while in set 1, the average length at these drift combinations is large, indicating that the low accuracy here is due to microtubules overshooting the target area. Therefore, although these dynamics sets have similar accuracy results for those drift combinations, the differences between them in their diffusion coefficient and theoretical average length mean that these similarities are reached via different mechanisms.

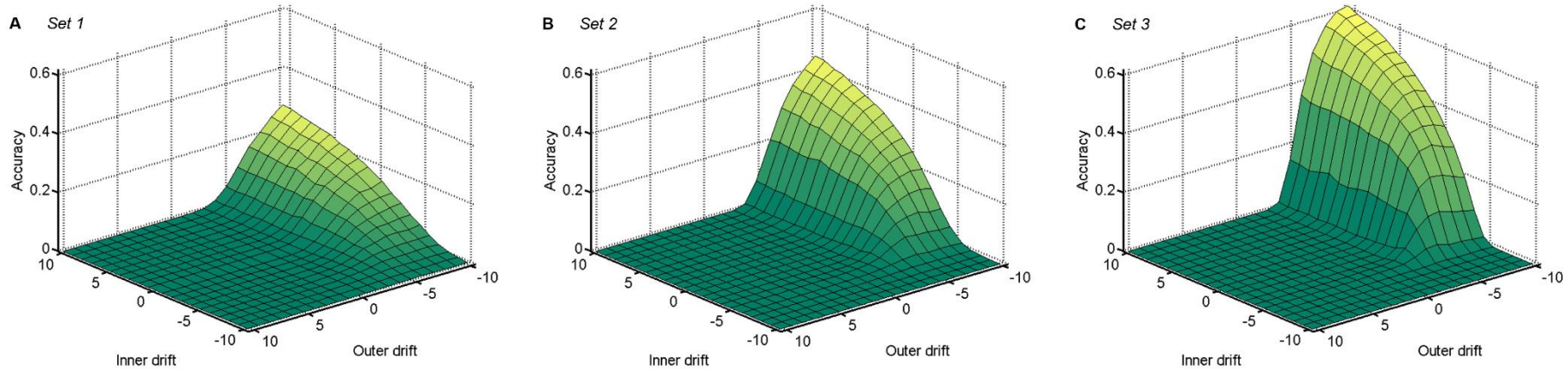

Figure 10. Area drift and accuracy of cortical targeting. The accuracy, i.e. the proportion of plus ends within the outer area is plotted as a function of inner and outer drift, for each dynamics set (A-C). Drift units are μm min^{-1}.

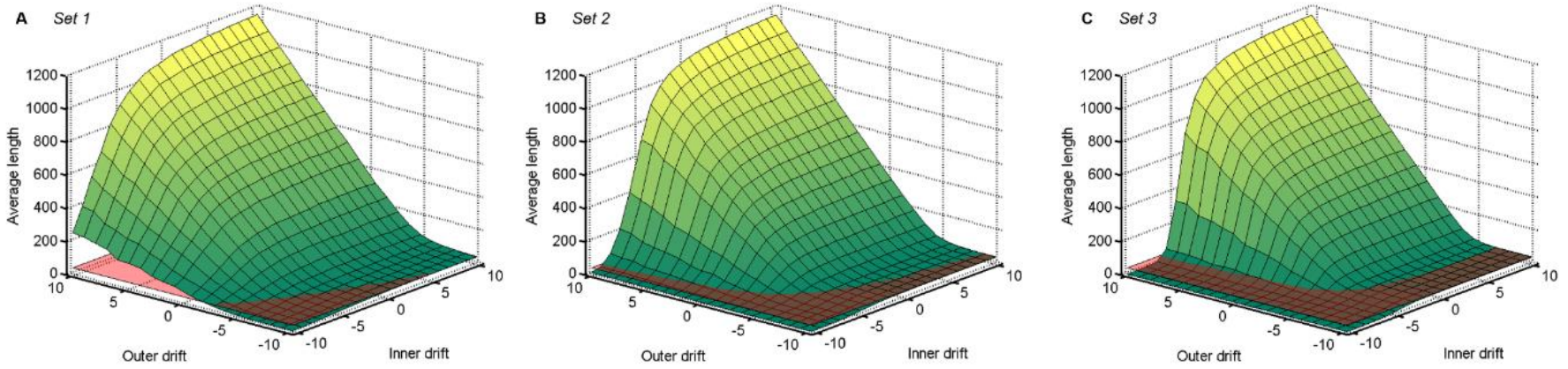

Figure 11. Area drift and average microtubule length. The average length (units, μm) plotted as a function of area drift, for each dynamics set (A-C). The target length, here taken as the distance to the outer border, is indicated by red shading. Drift units are μm min^{-1}.

It is also interesting to note that, although negative drift in the outer area generally produces accurate cortical targeting when combined with large positive inner drift, this is not always the case. At small negative outer drift, accuracy is low, and this is true regardless of the sign of the inner drift (fig. 10). Considering the average lengths as a function of area drift, we can see that the average length at these drift combinations is very large in comparison to the target length, only reducing when the inner drift reach values of around -5 μm min^{-1}. Thus, the small magnitude of the outer drift cannot balance the tendency toward growth of the inner area; indeed, the average lengths at these low magnitude, albeit negative, outer area drift values are on the order of tens of microns (appendix), thus it appears that there is a point at which the negative drift in the outer area becomes too small to allow accurate cortical targeting.

To demonstrate the effect of drift combinations on microtubule lengths, two example histograms are plotted in figure 12. Here we see that for the drift combination that produced the greatest accuracy in each dynamics set, i.e. maximum inner drift, minimum outer drift, the lengths, on the order of tens of microns, are distributed around the target length (fig. 12A), while in a drift combination that gives low accuracy, i.e. maximum inner and outer drift, the lengths, now on the order of thousands of microns, are distributed a long way from the target length (fig. 12B), which now appears more as a thin line than an area, far to the left of the histogram.

One of the most striking features of the plots in figure 10 is the fact that accuracy increases as the dynamics sets change: set 3 has the greatest accuracy, and set 1 the worst. Thus, for similar values of drift, the dynamics combinations in set 3 will generally give more accurate cortical targeting than those in sets 1 or 2. Recall that the differences between these dynamics sets is in their diffusion coefficients: set 1 has the greatest *D*, and set 3 the lowest *D*. Note also that within each dynamics set, since *D* remains constant while the drift changes, the theoretical average length, $\langle L \rangle$, must also change. The difference in accuracy between the sets must therefore arise from these differences.

To clarify the issue, the accuracy of dynamics sets 1-3 is plotted in figure 13 as a function of $\langle L \rangle$ for two inner drift values: 10.22 μm min^{-1}, the maximum, and 5.02 μm min^{-1}, and mid-range value for positive drift. Here, we see that contrary to the impression of the surface plots, dynamics set 1 actually produces the greatest accuracy for any given $\langle L \rangle$. Indeed, the reason that sets 2 and 3 produce greater accuracy is because they attain smaller $\langle L \rangle$ than set 1. Therefore, we can conclude that although similar area drift combinations produce good accuracy between the dynamics sets, the magnitude of this effect of drift is affected by the theoretical average length. This is of course a manifestation of the relationship in equation 9:

$$|V| = \frac{D}{\langle L \rangle}, \quad (9),$$

so for similar drift values, a decrease in *D* must be accompanied by a decrease in $\langle L \rangle$, explaining the results; setting drift equal between the dynamics sets while reducing *D* means that sets with smaller *D* will have smaller $\langle L \rangle$. To conclude, drift *per se* is not an absolute determinant of accuracy, and for any negative drift value, decreasing both D and $\langle L \rangle$ will give

greater accuracy. Or indeed, ⟨*L*⟩ *per se* is not an absolute determinant of accuracy, since, for any given ⟨*L*⟩, a greater *D*, and thus drift, will give greater accuracy.

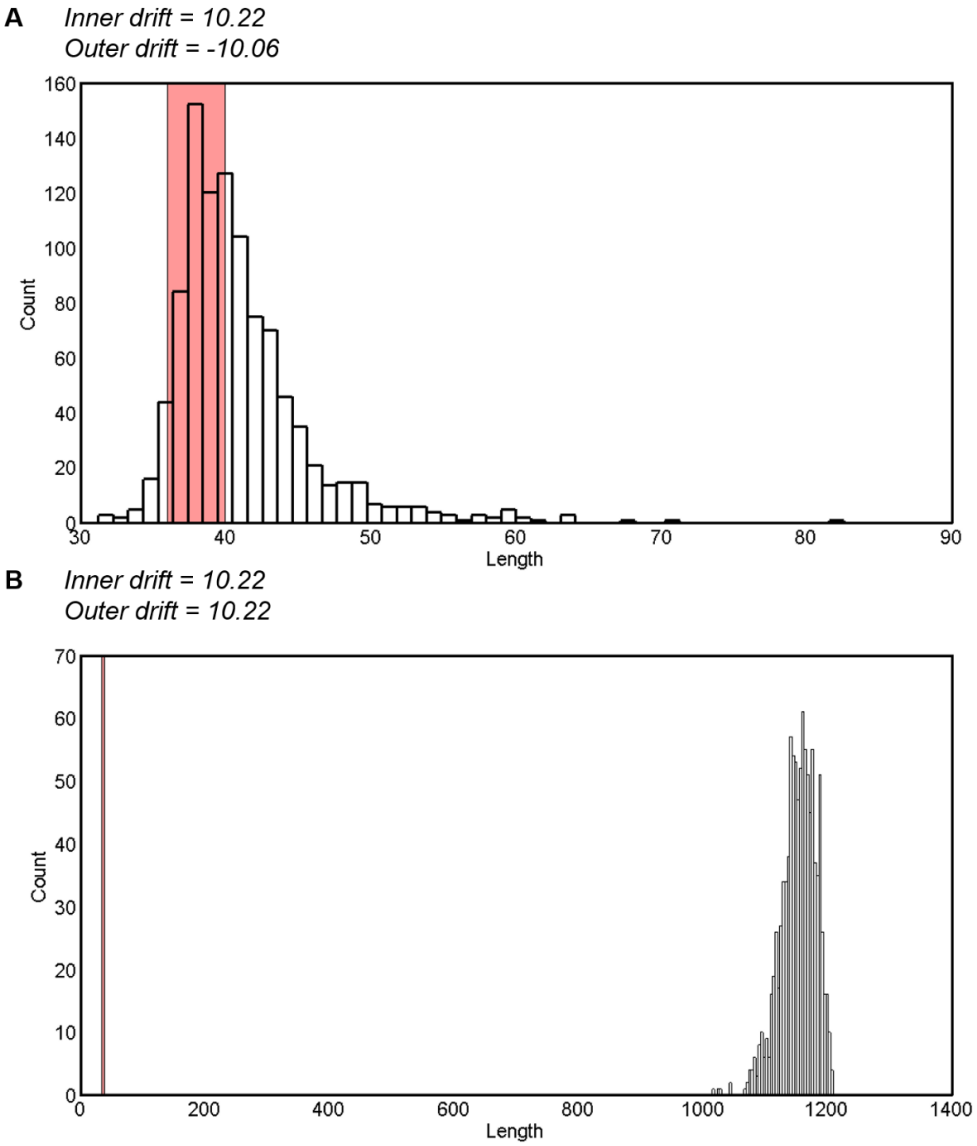

Figure 12. Example histograms of microtubule lengths. In the maximum inner drift, minimum outer drift combination (A), lengths are distributed around the target area (indicated by red shading), while for maximum drift in both areas (B), lengths are distributed far from the target area. Length units are μm.

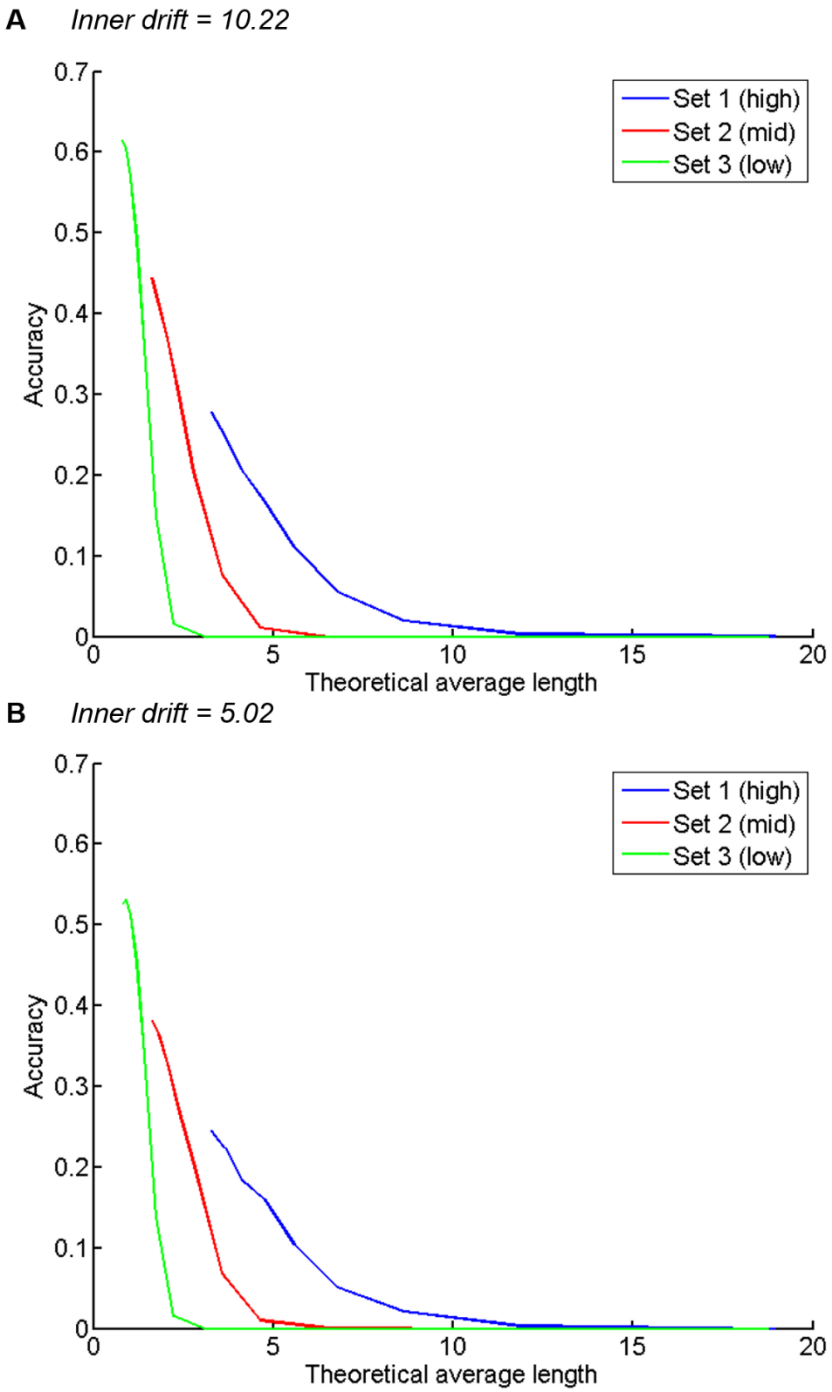

Figure 13. Accuracy and theoretical average length in the outer area, dynamics sets 1-3. Accuracy is plotted against theoretical average length for an inner drift of 10.22 μm min^{-1} (A) and 5.02 μm min^{-1} (B) for each dynamics set (refer to legend). Theoretical average length units are μm.

Note that increases in accuracy as a result of decreasing $\langle L \rangle$ is relevant only to the outer area; in the inner area, the situation is apparently reversed. Here, for any given $\langle L \rangle$, a smaller D, and thus smaller (a small negative) drift, will give greater accuracy here, as the plots in figure 14 demonstrate; because D is smaller in set 3 compared to sets 1 and 2, and again smaller in 2 than in 1, for each $\langle L \rangle$, the drift is smaller in set 3 than in sets 2 or 1, and accuracy is greater.

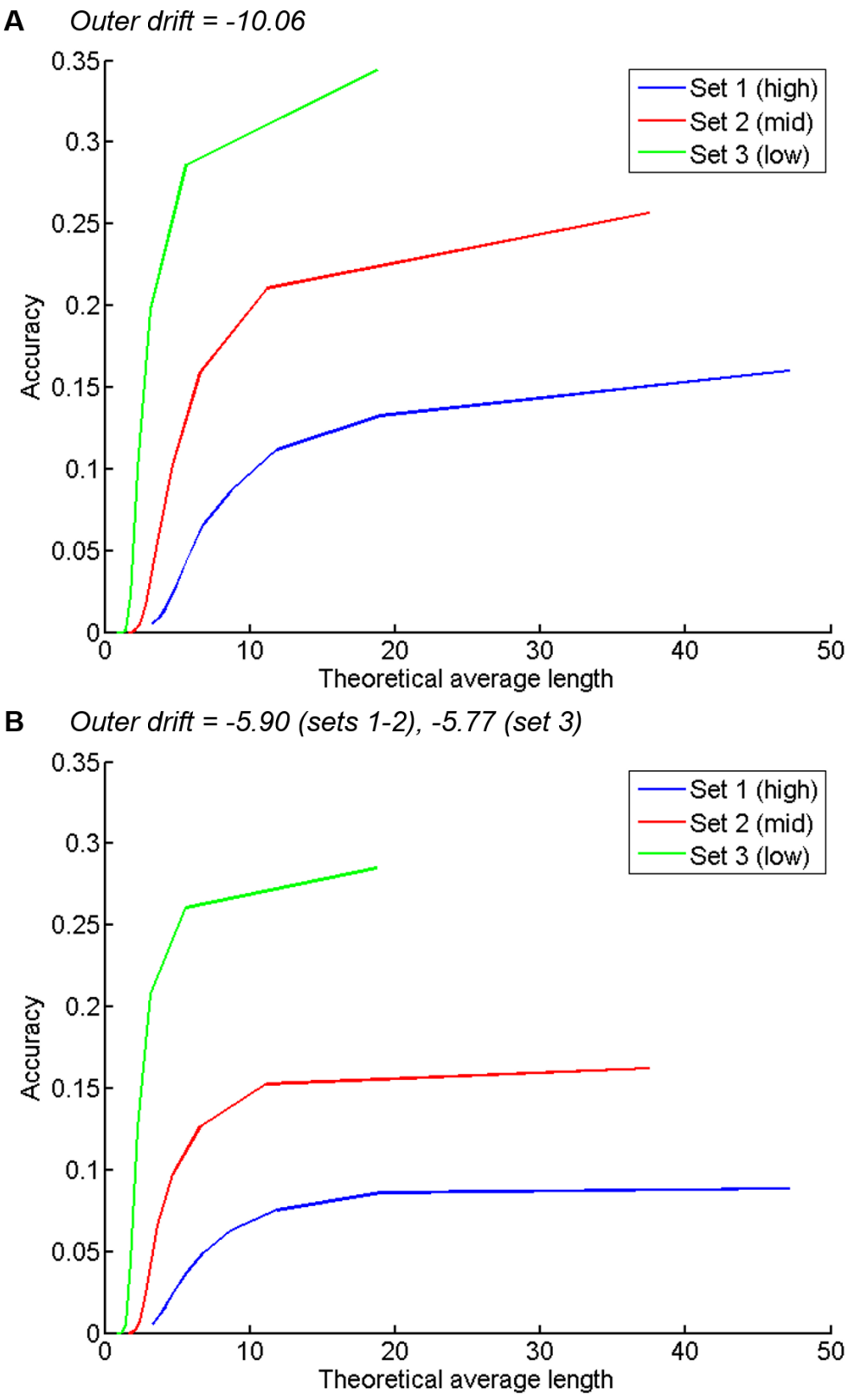

Figure 14. Accuracy and theoretical average length in the inner area, dynamics sets 1-3. Accuracy is plotted against theoretical average length for an outer drift of -10.06 μm min^{-1} (A) and -5.90 (sets 1-2) and -5.77 (set 3) μm min^{-1} (B) for each dynamics set (refer to legend). Theoretical average length units are μm.

These results lead to a rationale for accurate cortical targeting: we can say that for good accuracy in targeting microtubule plus ends to an area, positive drift in the inner area combined with negative drift in the target area produce the best results, whatever the theoretical average length or diffusion coefficient of the particular dynamics sets. Secondary to this, combinations of negative drift in both areas can produce good accuracy in targeting, as long as the negative inner drift is not too great. Within these both-area-negative-drift combinations, inner area dynamics sets that have a greater theoretical average length for any drift value in the inner area will produce greater accuracy. Least successful in cortical targeting are the combinations that involve positive drift in the outer area, regardless of the sign or magnitude of drift in the inner area, though in some cases the mechanisms leading to poor accuracy are different.

This cortical targeting rationale is displayed diagrammatically in figure 15. It provides a convenient means of thinking about cortical targeting in terms of area drift. Indeed, the success of cortical targeting, i.e. accuracy, can be considered in terms of "drift space", whereby the combinations of drift in each area are split into discrete regions based on their sign (fig. 15). Thus, drift combinations in region 4 of drift space will tend to produce accurate cortical targeting, while drift combinations in region 1 will be poor at cortical targeting.

Note that this is a general framework, and only indicates potential for successful targeting; the discussion of low accuracy at small negative drift in the outer area serves as one example where these general rules do not hold. Moreover, the actual accuracy cannot be determined from the drift space, since it is clear that, although drift combinations are major determinants of accuracy in cortical targeting, the theoretical average length and diffusion coefficient modulate this relationship. However, it does serve as a heuristic guide as to the plausibility of any given dynamics combinations as means of accurate cortical targeting.

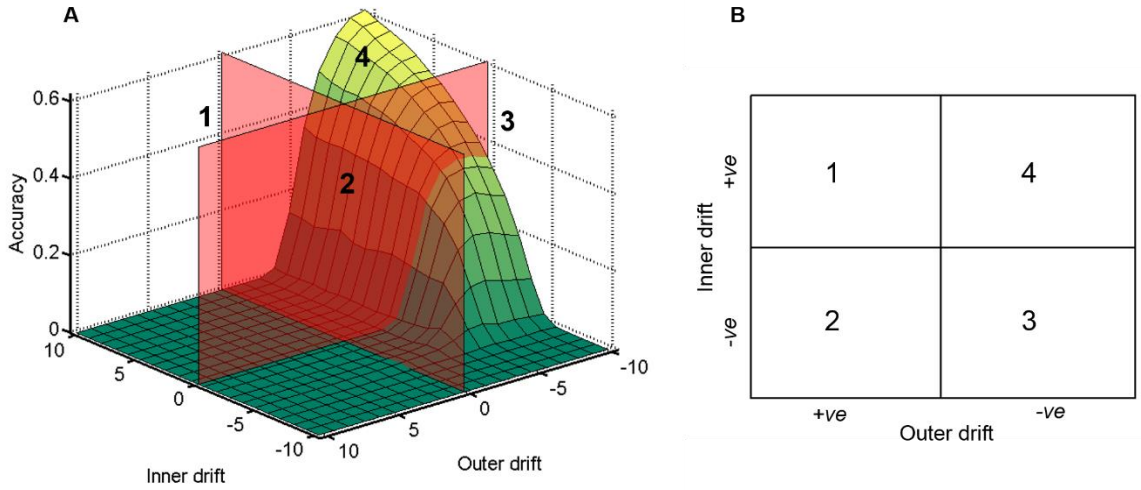

Figure 15. Accuracy and "drift space". The combinations of drift in each area can be split into discrete regions based on the signs of the drift (A & B). Quadrants 1 and 2, where outer drift is positive with either negative or positive inner drift (B) have low potential for accurate cortical targeting (A), while quadrant 3, with negative outer and inner drift (B) has better accuracy

potential (A), and quadrant 4, with negative outer and positive inner drift (B) has the best accuracy potential. Units in A for drift are μm min^{-1}.

With it being apparent that the best combinations of drift for accurate cortical targeting in model 1 are positive inner drift and negative outer drift, dynamics sets that satisfied this condition were used to investigate further the effect of changing the theoretical average length and diffusion coefficient in the outer area. Two dynamics sets, 4 and 5, are used here, each with the same single set of dynamics parameters for the inner area, specified so as to give high positive drift, at 12 μm min^{-1}. Thus, any variation in accuracy in dynamics sets 4 and 5 will be due to the variation in outer area dynamics, simplifying the problem. The outer area dynamics in sets 4 and 5 are specified so that they both vary in drift, but so that set 4 varies in average length with a fixed diffusion coefficient, while set 5 has a variable diffusion coefficient, but a fixed average length. Therefore, these dynamics sets will allow further exploration of how the theoretical average length and diffusion coefficient affect the accuracy of cortical targeting.

The results, shown in figure 16, demonstrate that both the average length and diffusion coefficient affect the accuracy of cortical targeting, and that each one of the parameters can indeed remain fixed while the other varies and with it determines accuracy (fig. 16A & B). In set 4, where the theoretical average length was varied and the diffusion coefficient held constant, the accuracy is very low as length decreases from the maximum, until around 4 μm, where the accuracy increases steeply with decreasing average length (fig. 16A & C). This makes intuitive sense, since we might expect that low average lengths in a target area will yield more plus ends within that area, and it is also consistent with the previous results.

Note that the theoretical average length below which accuracy starts to rise is on the order of the size of the target area (4 μm), which could lead to the conclusion that theoretical average length must be smaller than or equal to the dimension of the target area; however, the previous results showed that, although theoretical average length yield greater accuracy when it is smaller, in the high *D* dynamics set (set 1), accuracy began to increase before 4 μm was reached.

The results are not so intuitive in dynamics set 5, where the accuracy increases with an increasing diffusion coefficient (fig. 16B & C). Although this is consistent with the previous results, where dynamics sets with greater *D* (i.e. set 1) produced greater accuracy for any given theoretical average length, the more explicit result shown in figure 16 raises the question of how a greater *D*, which should indicate greater randomness in length, leads to greater accuracy.

The result can again be explained by reference to equation 9, which shows that as *D* increases, so must the magnitude of the drift, $|V|$. Since we are considering a negative drift regime in the outer area, the larger *D* produces a larger negative drift in the outer area, which we have seen contributes to greater accuracy. Because negative drift indicates dominance of shrinkage over growth, *D* in this instance indicates the extent to which microtubules will undergo large excursions, which will generally be in the shrinking state. Thus, increased

accuracy as *D* increases results from microtubules being more likely to undergo larger episodes of shrinkage.

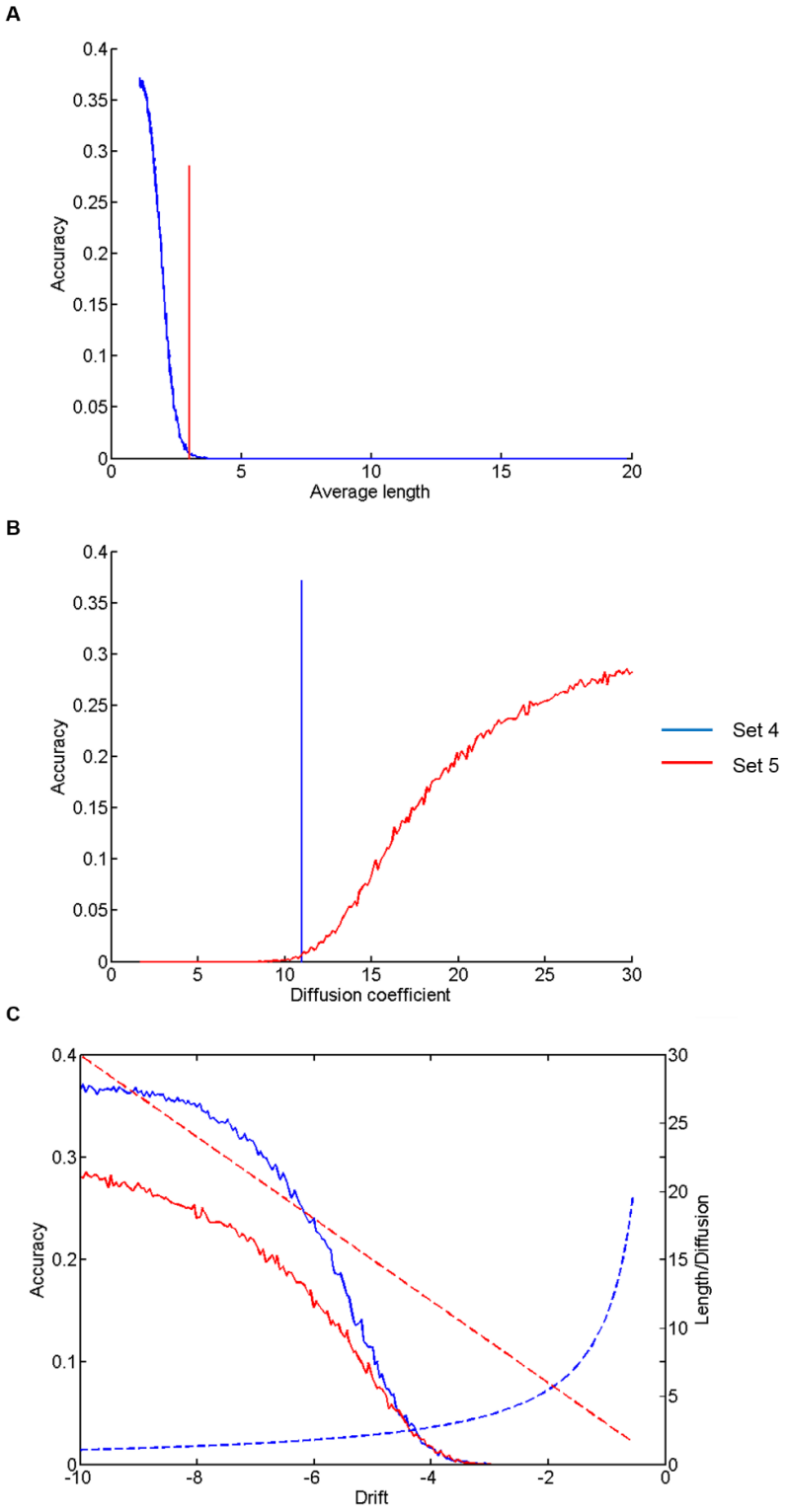

Figure 16. Accuracy, average length, diffusion coefficient and drift in dynamics sets 4-5. Accuracy is plotted as a function of average length (A; length units, μm), diffusion coefficient (B; diffusion units, $\mu m^2\ min^{-1}$) and drift (C; drift units, $\mu m\ min^{-1}$) for each dynamics set (see legend). In C, the average length and diffusion coefficient are also plotted as a function of drift (dotted lines, right y-axis; units as in A and B).

Are there common microtubule properties behind the accurate targeting at low $\langle L \rangle$ and high D? The previous experiments have already established that good accuracy is essentially an indicator of an average length around the target area, so other properties were investigated. The range of microtubule lengths and microtubule dynamicity were determined for each dynamics set. Where the length range reveals the extent to which microtubule lengths vary, the dynamicity indicates the extent to which microtubules change their length.

In set 4, with decreasing $\langle L \rangle$, the length range at first stays relatively constant, and then decreases quite rapidly. The dynamicity in set 4 behaves differently with decreasing $\langle L \rangle$; it also decreases at first but then increases at smaller $\langle L \rangle$ (fig 17A). In set 5, as the diffusion coefficient increases, so does the dynamicity (fig. 17B). The length range behaves differently here, at first increasing with the diffusion coefficient and then decreasing. Thus, dynamicity in set 4 and length range in set 5 both have a qualitative switch in their relationship with either decreasing $\langle L \rangle$ or increasing D, respectively.

This qualitative reversal in length range and dynamicity is brought about by the systems effects of decreasing drift in the outer area with a constant positive drift in the inner area. For comparison, the area-free simulations in the previous sub-section showed that length range and dynamicity increase with increasing theoretical average length in set 4, with the dynamicity levelling off, and so both measures increase as drift approaches zero. In set 5, the dynamicity and length range also increased, but the latter only very steeply and quickly, after which it remained relatively constant with increasing diffusion coefficient. Thus, set 4 reproduces the area-free behaviour for length range but not dynamicity, and set 5 mimics the area-free simulations for dynamicity but not for length range.

However, the area-free behaviours are reproduced for some of the changes in either $\langle L \rangle$ or D; at large $\langle L \rangle$, dynamicity is similar in these simulations for set 4 as it was in the area-free simulations, while in set 5, at small D, length range is similar here to the area-free simulations. The fact that both changes in the relationships occur at similar outer area drift values suggests that they are a consequence of the systems nature of these simulations; as microtubules in the outer area experience dynamics sets that cause them to shrink more, they will be returned to the inner area, upon which they will experience dynamics sets that cause them to grow more, and they will return to the outer area. Thus, the length range reduces, but the dynamicity increases; as outer negative drift becomes large, microtubules range less in length but cover greater distance. It is interesting that this common mechanism, which produces good accuracy, is manifest purely from the combinations of area dynamics, and indeed, causes deviations from the microtubule growth behaviour that would otherwise occur.

To conclude, in two-state dynamics, the combination of drift in the two areas is a vital determinant of accuracy, and this arises from a common mechanism of reducing length range while total distance covered increases, regardless of whether theoretical average length or the diffusion coefficient is varied to bring about changes in drift. Having elucidated the mechanisms behind accurate targeting of microtubules in two-state dynamics regimes, the influence of the third state will be considered next.

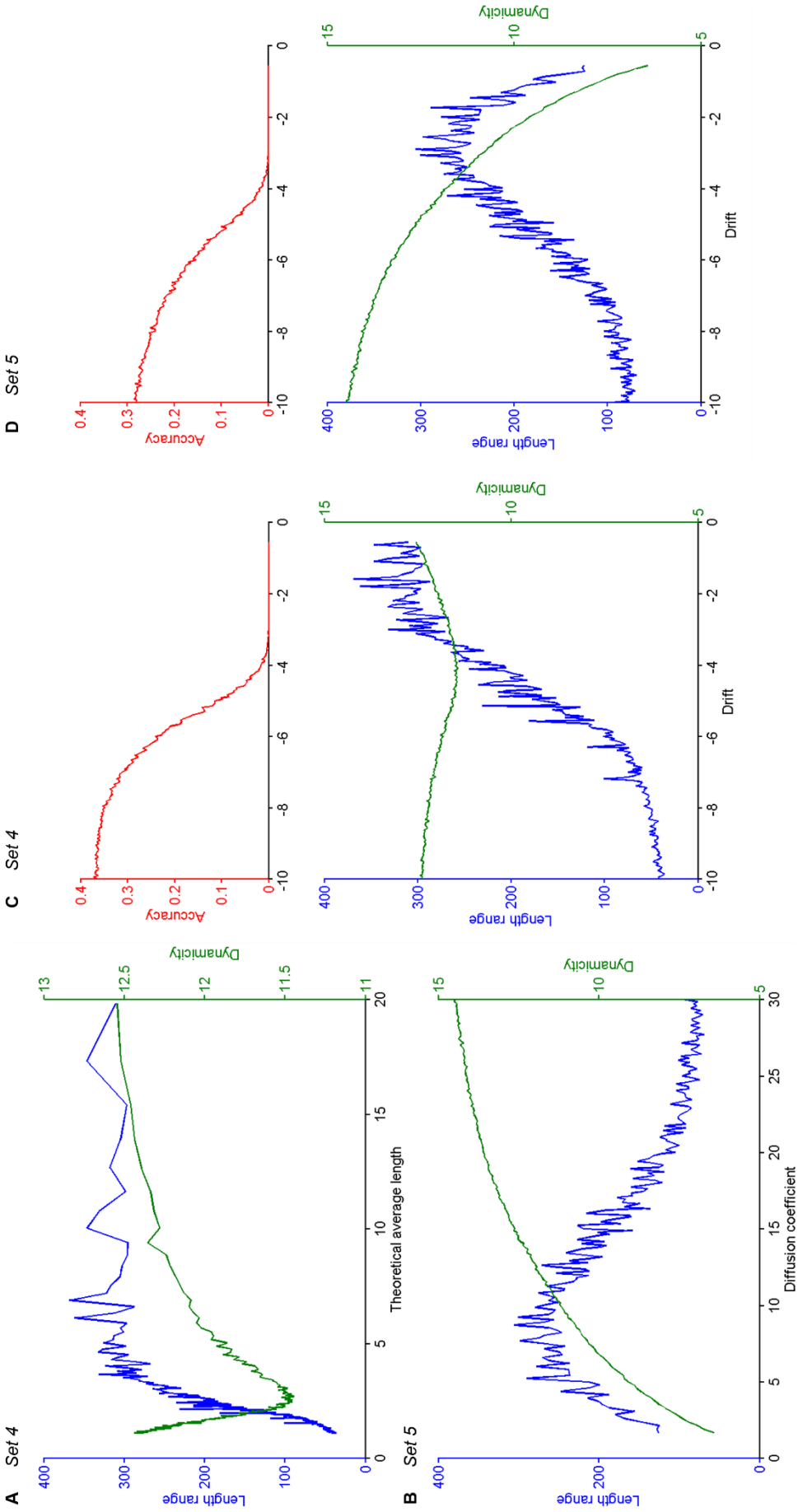

Figure 17. Length range and dynamicity in dynamics sets 4-5. In both dynamics sets 4 and 5, length range and dynamicity vary with theoretical average length (A, set 4) and diffusion coefficient (B, set 5). Length range and dynamicity also vary with outer area drift, as does the cortical targeting accuracy (C and D). Units are: length range, μm; dynamicity and drift, μm min^{-1}; diffusion coefficient, $μm^2$ min^{-1}.

II. Three-state dynamics

a. Model efficacy

In the simulations of three-state model 1, only two transition frequencies were varied within each dynamics set; these were F_{p2g} and F_{p2s}. The purpose of varying just these transition frequencies was so that the time percentage for the pausing phase varied, but other system properties did not. Therefore, to establish the efficacy of model in three-state simulations, the correlation between specified and observed F_{p2g} and F_{p2s} will be a useful measure, and the mean-squared error for all observed transition frequencies will also be used to test that these were close to their specified values.

The correlation coefficients for F_{p2g} and F_{p2s} for each dynamics set were high (table IV), in both the area-free and two-area simulations. These correlations are easy to see in the plots in figure 18. For all transition frequencies, the mean-squared error was low (table V-VI). These results indicate that the 3-state version of model 1 reproduced the specified behaviour well.

Table IV. Correlation coefficients for varied transitions frequencies in dynamics sets 6-10. The correlation between specified and observed transition frequencies in both simulations types is shown.

Set	F_{p2g}		F_{p2s}	
	Area-free	*Two-area*	*Area-free*	*Two-area*
6	1.00	1.00	1.00	1.00
7	1.00	1.00	1.00	1.00
8	1.00	1.00	1.00	1.00
9	1.00	1.00	1.00	1.00
10	1.00	1.00	1.00	1.00

Table V. Mean-squared error for transition frequencies in dynamics sets 6-10, area-free simulations. The error between specified and observed transition frequencies is shown.

Set	F_{cat}	F_{res}	F_{g2p}	F_{p2g}	F_{s2p}	F_{p2s}
6	0.01	0.01	0.00	0.00	0.00	0.00
7	0.01	0.01	0.00	0.00	0.00	0.00
8	0.01	0.00	0.00	0.00	0.00	0.00
9	0.02	0.00	0.00	0.00	0.00	0.00
10	0.04	0.00	0.00	0.00	0.00	0.00

Table VI. Mean-squared error for transition frequencies in dynamics sets 6-10, two-area simulations. The error between specified and observed transition frequencies is shown.

Set	F_{cat}		F_{res}		F_{g2p}		F_{p2g}		F_{s2p}		F_{p2s}	
	In	Out	In	Out	In	Out	In	Out	In	Out	In	Out
6	0.00	0.01	0.00	0.01	0.00	0.00	0.00	0.01	0.00	0.00	0.00	0.00
7	0.00	0.01	0.00	0.01	0.00	0.00	0.00	0.00	0.00	0.00	0.00	0.00
8	0.00	0.01	0.00	0.00	0.00	0.00	0.00	0.00	0.00	0.00	0.00	0.00
9	0.00	0.02	0.00	0.00	0.00	0.00	0.00	0.00	0.00	0.00	0.00	0.00
10	0.00	0.04	0.00	0.00	0.00	0.00	0.00	0.00	0.00	0.00	0.00	0.00

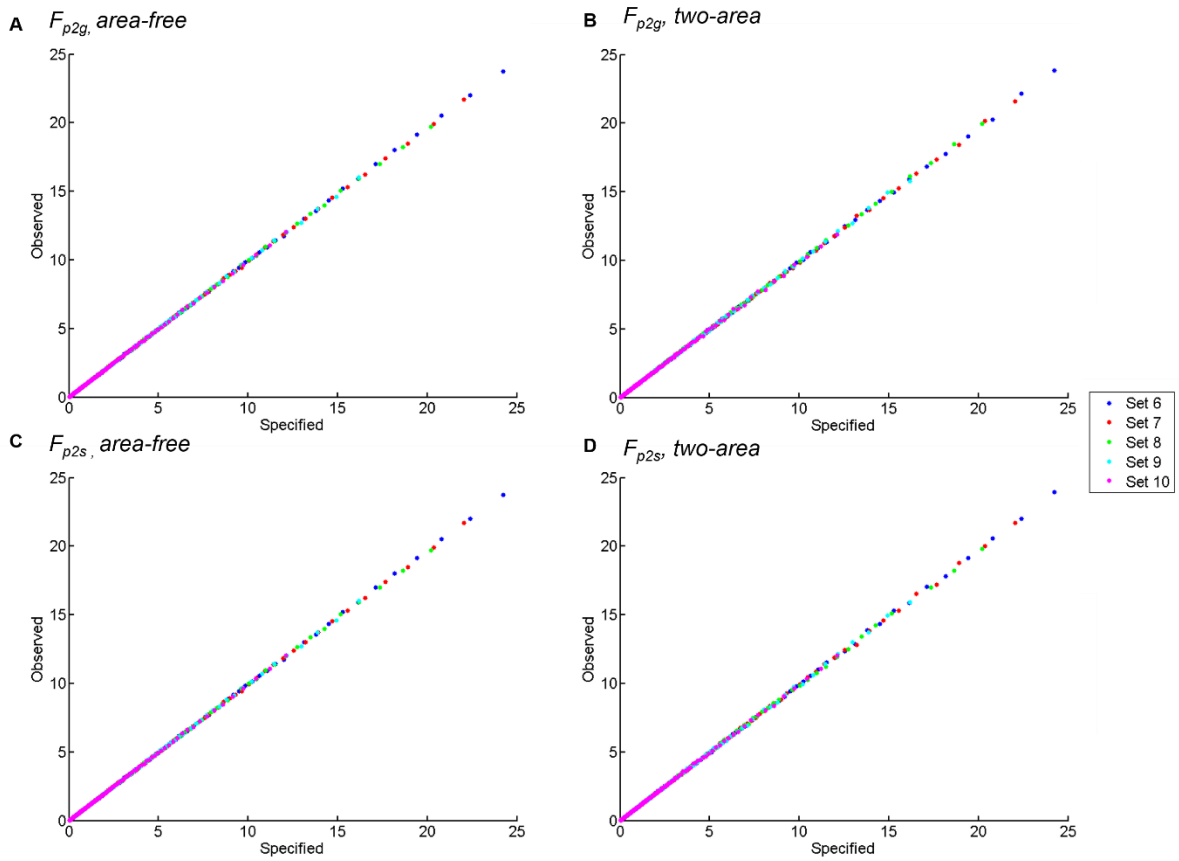

Figure 18. Specified and observed transition frequencies for dynamics sets 6-10 in area-free and two-area simulations. The observed transition frequencies, as indicated, for area-free (A, C) and two-area (B, D) simulations are plotted against the specified values for each dynamics set (refer to legend). Transition frequency units are min^{-1}.

b. Population measures

Next, certain population properties of model 1 in 3 states are considered. As with the two-state version of model 1, these measures are conducted on the area-free simulations only; similar measures will be considered for the two-area simulation in the subsequent section. Firstly, although dynamics sets 6-10 were created so that the pause time percentage varied while drift, length and the diffusion coefficient were fixed within each, the percentage time in pause is strictly a population parameter, and is a predicted feature of the simulations. The same is true of the predicted time percentages in the other phases. Indeed, it is possible that the observed times deviate from the predicted values due to certain systems properties, one of which is favouring of the growth phase due to re-nucleation. Since the effect of this process is marked at shorter average lengths, deviation of the phase times may well differ here, where the average length ranges from 3.84 μm to 0.92 μm.

The observed phase time percentages are plotted in figure 19. In each of the individual set plots (fig. 19A-E), the pausing time percentage is evidently behaves as expected, since there is an essentially linear relationship between the predicted and observed values. This linear relationship is not as strong as we go through the dynamics sets; thus, since the average length decreases with the dynamics sets, there is evidence of the aforementioned deviation from expected phase time percentages at short average lengths. Indeed, this trend is more marked for the other phases; observed growth time percentage becomes greater than predicted as the average length decreases, and the opposite is true of shrinking time percentage. Again, this is consistent with the predictions made above. Comparing the phase times between dynamics sets (fig. 19F-H), these effects are clearer. Therefore, although predicted phase times do differ from the observed phase times, we can understand why, and moreover, the observed pause time deviates from the predicted values less than the other phases, and it is pause time percentage that we are particularly interested in here. Also, there is good correlation between the predicted and observed phase time percentages (table VII).

Table VII. Correlation between predicted and observed phase time percentages for dynamics sets 6-10, area-free simulation. For each dynamics set, the correlation between predicted and observed phase time percentages is shown.

Dynamics set	Pause	Grow	Shrink
6	1.00	1.00	1.00
7	1.00	1.00	1.00
8	1.00	1.00	1.00
9	1.00	1.00	1.00
10	1.00	1.00	1.00

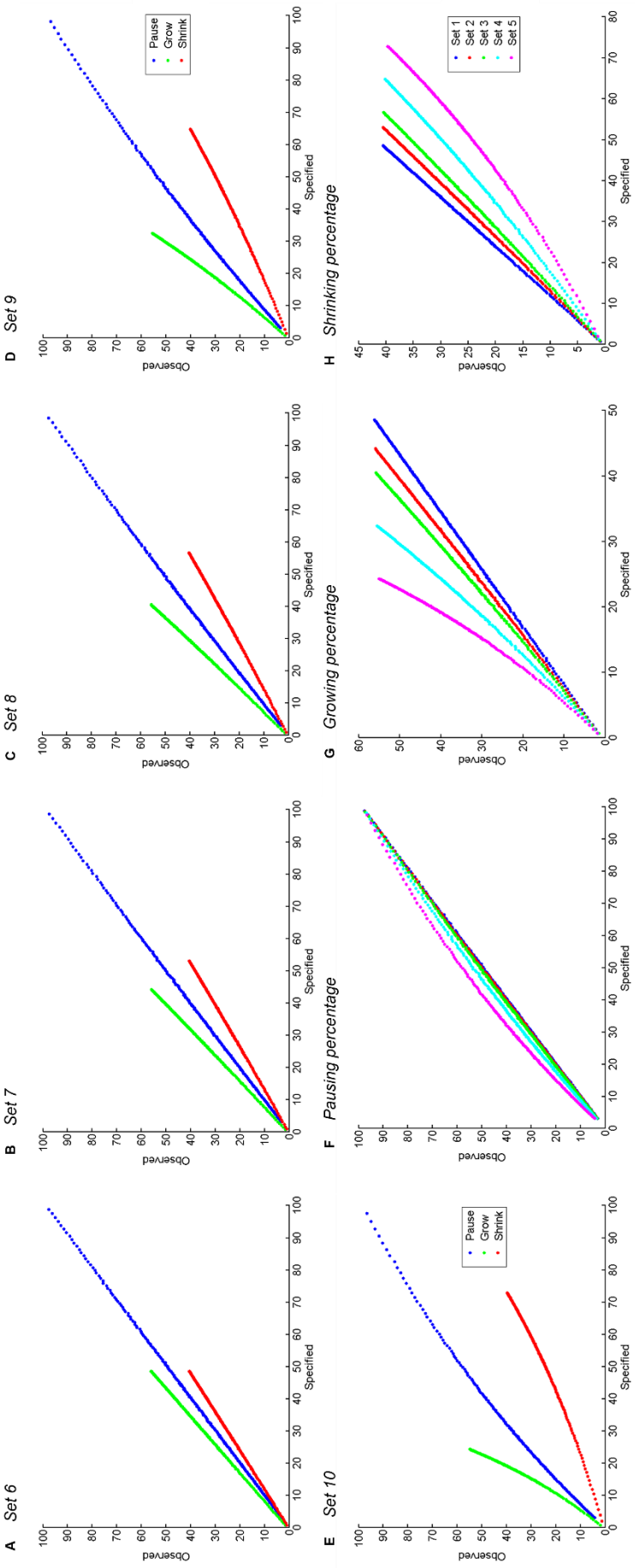

Figure 19. Specified and observed phase time percentages for dynamics sets 6-10, area-free simulations. The observed phase time percentages for each dynamics set (A-E, as indicated) are plotted against the predicted values for each phase (refer to legend), and the observed phase time percentages for each phase (F-H, as indicated) are plotted against predicted values for each dynamics set (refer to legend).

Previously in the two-state version of model 1, the length range was found to decrease with larger outer area negative drift and this was concurrent with increased cortical targeting accuracy. Therefore, the length range in the three-state version of model 1 was found as a function of pausing time percentage. In general, the pausing time percentage has little effect on the length range (fig. 20), but in dynamics set 6, and to a certain extent dynamics set 7, the length range does fall as pausing time percentage reaches its greatest values (fig. 20). Note also that although pausing time percentage has little effect on the length range within each dynamics set, the length range is consistently different between the dynamics sets. Since when *D* is fixed in the two-state version of model 1, length range was found to decrease with more negative values of drift, it is likely that the decreasing (i.e. more negative) drift from set 6 to set 10 is the source of these differences in length range. Added to this is the differences between sets in average length; this decreases concomitantly with drift from set 6 to set 10, and a shorter average length combined with a larger negative drift will produce smaller length ranges, as we have seen previously.

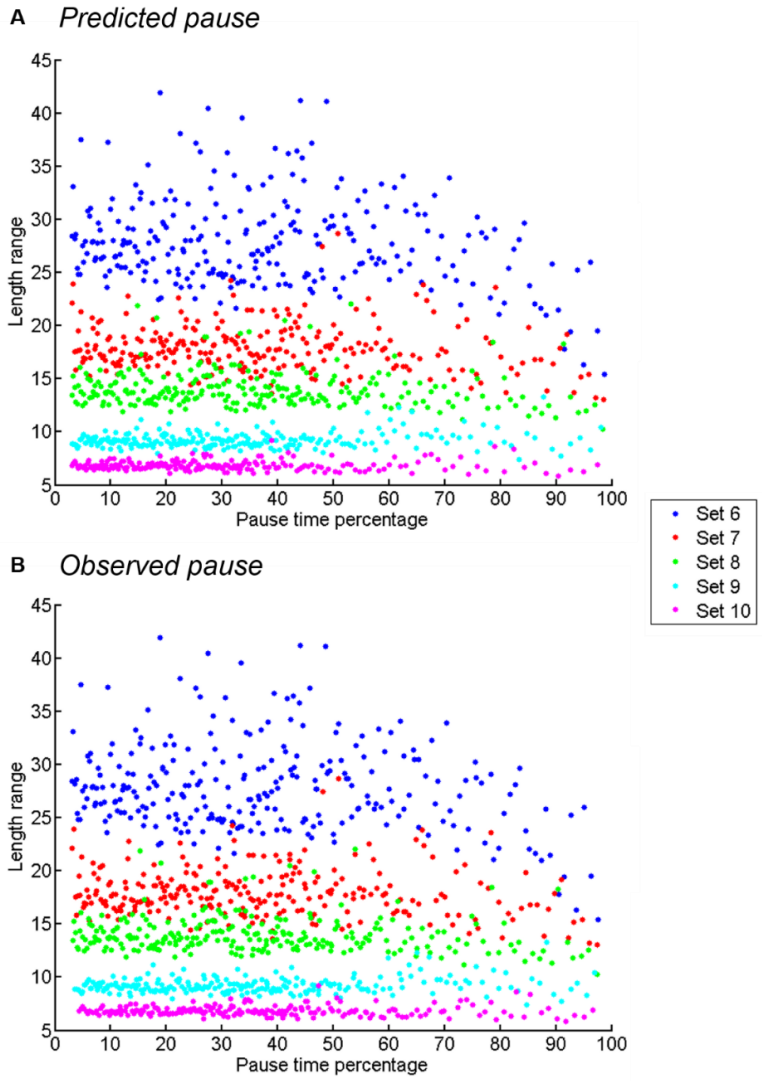

Figure 20. Length range and pausing time percentage in dynamics sets 6-10, area-free simulations. The length range is plotted against predicted (A) and observed (B) pause time percentage for each dynamics set (refer to legend). Length range units are μm.

Finally, the average length in the area-free, three-state version of model 1 was determined for each dynamics set. As average length was held constant within each dynamics set, the mean-squared error for the observed average lengths against the specified average length was found. The result of this are shown in table VIII. The low mean-squared error for each dynamics set indicates that the predicted average length is similar to the observed average length in the area-free simulations.

Table VIII. The mean-squared error average length in area-free simulations of dynamics sets 6-10. For each dynamics set, the mean-squared error (MSE) for the difference between observed and theoretical average length is shown.

Dynamics set	MSE
6	0.04
7	0.01
8	0.00
9	0.00
10	0.00

c. Cortical targeting in three states

Having introduced the third microtubule state into the two-area simulations, the immediate matter is verification of the observed pausing time percentages; are they similar to the specified pausing percentage times, or does the system change this property? Figure 21 shows a plot of the specified and observed pausing time percentages for dynamics sets 6-10. The specified and observed pausing time percentage for these two-area simulations was highly positively correlated as in the area-free simulations, at 1.00 for all dynamics sets.

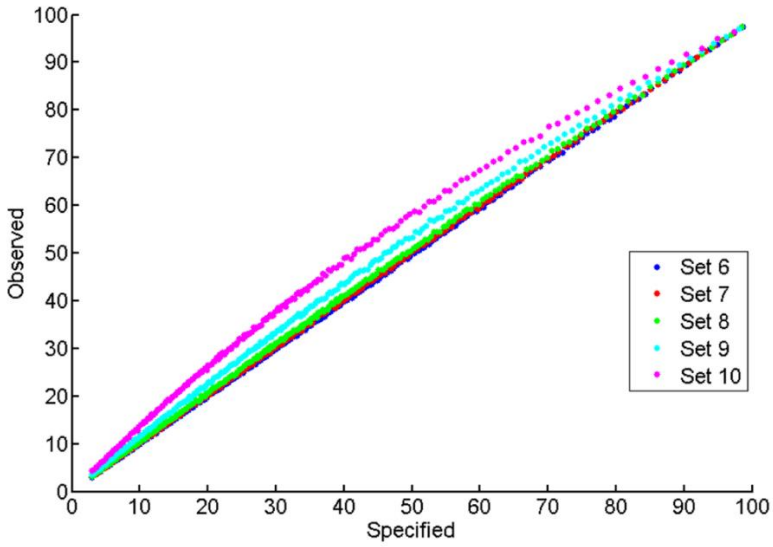

Figure 21. Specified and observed pausing time percentage in two-area simulations of dynamics sets 6-10. For each set (refer to legend), the specified and observed pausing time percentages are plotted.

Having verified that there are no emergent systems processes whereby the observed and specified pausing time percentages differ, the next issue is whether pause time percentage affects the accuracy of cortical targeting. The results are plotted in figure 22. The accuracy of cortical targeting is clearly affected by pausing time percentage; in all dynamics sets, accuracy increases with pausing time percentage, and this increase becomes greater with large pausing time percentages (fig. 22A). Given the introduction of drift space in the two-state model 1 earlier, and the finding that increasing negative drift in the outer area produces better accuracy, it is not surprising that, although accuracy responds to pausing time percentage in a similar fashion between dynamics sets, the absolute level of accuracy changes between these sets, which of course differ in their outer area drift values. Thus, it is useful to consider accuracy as a function of both outer area drift and pausing time percentage (fig. 22B). Plotted as a surface, we can see that accuracy is most responsive to increases in pausing time percentage when outer area drift is more negative. Therefore, we can conclude that increasing pausing time percentage increases accuracy, but the extent to which it does so is modulated by the magnitude of the outer area negative drift.

It is interesting to note that, although the effect of pausing time percentage is modulated by outer area drift, introducing the third state into the simulations produces greater accuracy at smaller negative drift compared to the two-state model. Set 6 represents the smallest outer area drift value here, and the most comparable dynamics set used in the two-state model is set 3. At similar outer area drift and average length values, accuracy was almost zero in set 3, whereas in set 6, it is greater than 0.2. Note that the inner area drift in dynamics set 3 was slightly lower than in set 6, 10.22 μm min^{-1} at the maximum, and this may have a small effect on the accuracy there.

What is the mechanism by which increases in pausing time percentage increase accuracy? To investigate, various microtubule growth characteristics were analysed. In the two-state simulations, it was found that larger negative drift in the outer area, when combined with positive inner drift, resulted in decreased length range and increased dynamicity, regardless of whether the changes in outer drift was brought about by changing theoretical average length or the diffusion coefficient. Thus, the length range and dynamicity were investigated for sets 6-10. In the area-free simulations, it was found that increased pausing time percentage had little effect on the length range until large T_p was reached, upon which length range decreased in the sets with small negative drift (i.e. sets 6 and 7). Here, the moving average of the length range was taken so that the results were easier to interpret; this and the dynamicity are plotted against the specified T_p in figure 23. As with the area-free simulations, the length range remains relatively constant for a large portion of T_p, but as T_p becomes large, the length range decreases quickly. In this case, this rapid decrease in length range at high T_p occurs in all dynamics sets. The dynamicity decreases with increasing T_p; this follows simple reasoning that larger proportions of time spent in the pausing phase should give rise to lower absolute change in length.

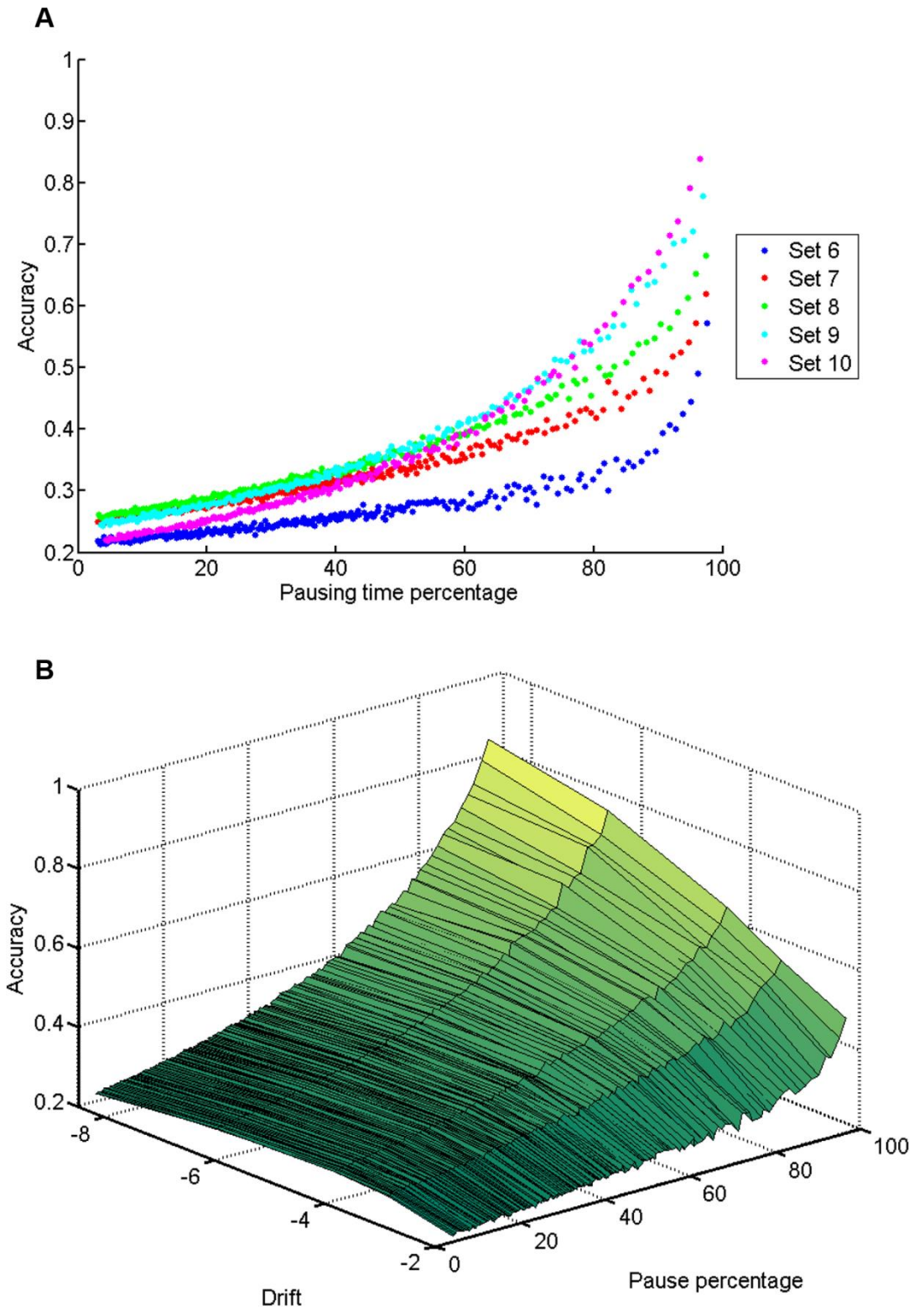

Figure 22. Accuracy in three-state simulations of model 1, dynamics sets 6-10. The accuracy is plotted against pausing time percentage (A) for each dynamics set (refer to legend), and as a surface against drift (essentially going through dynamics sets 6-10 with increasing drift magnitude) and pausing time percentage (B). Drift units are μm min^{-1}.

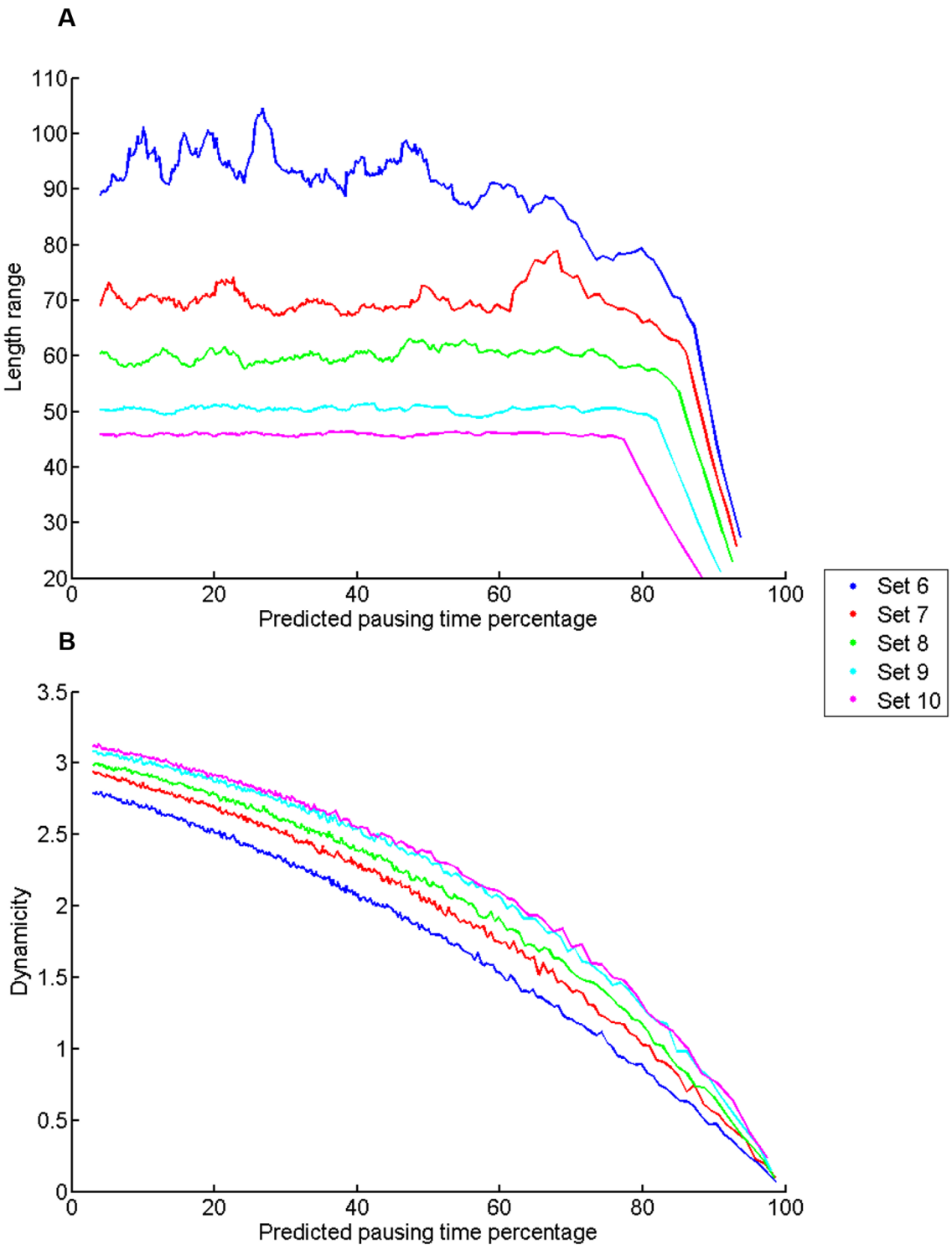

Figure 23. Length range and dynamicity for predicted pausing time percentages in dynamics set 6-10. For each dynamics set (see legend), the length range (A) and dynamicity (B) are plotted for the specified pausing time percentages. Length range units are μm; dynamicity units are μm min^{-1}.

Previously, it was found that both length range and dynamicity increase with theoretical average length in area-free two-state simulations, but that in two-area, two-state simulations at low $\langle L \rangle$, the trend was reversed and dynamicity decreased with increasing $\langle L \rangle$. Since $\langle L \rangle$ was varied between dynamics sets here, the length range and dynamicity were determined for each dynamics set, i.e. as functions of $\langle L \rangle$. The averages of the length range and dynamicity for each set, i.e. over the variable T_p, are shown in figure 24A & C, while the averages over discrete 20% portions of T_p are shown in figure 24B & D. Here, we see that the relationship between length range and $\langle L \rangle$ found in two-state simulations still holds here (fig. 24A), and that as T_p becomes large, the length range increases with $\langle L \rangle$ at a slower rate (fig. 24B). Thus, for any given $\langle L \rangle$, increasing T_p to very high values makes length range smaller. Dynamicity also decreases, albeit slowly, with increasing $\langle L \rangle$, consistent with the earlier findings. As with the length range, increasing T_p decreases dynamicity for any given $\langle L \rangle$, but here, the effect is more marked than for length range.

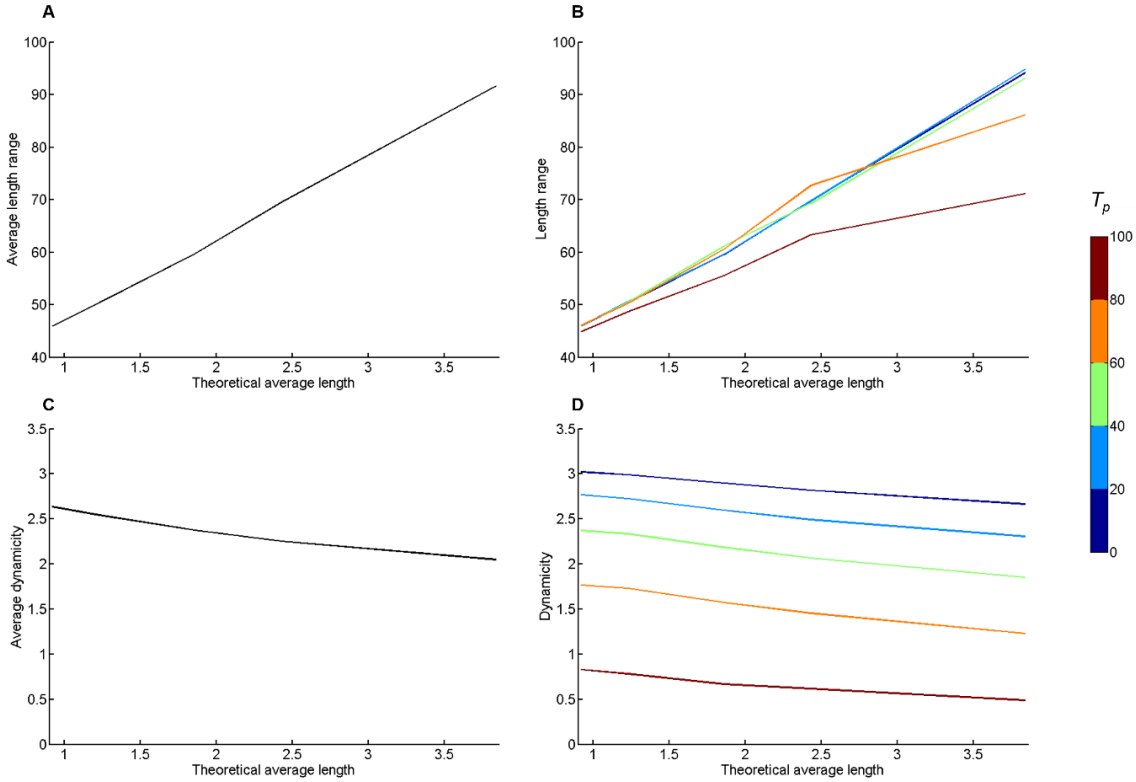

Figure 24. Length range and dynamicity as functions of theoretical average length, dynamics sets 6-10. Theoretical average length varies between sets 6-10, with set 6 having the largest value, and set 10, the smallest. Thus, length range and dynamicity are plotted as functions of these theoretical average lengths: the average values are shown in A and C, and the averages of discrete intervals of T_p (see colour bar) are shown in B and D. Length range and theoretical average length units are μm; dynamicity units are μm min^{-1}.

As each dynamics set has a constant drift value, the length range and dynamicity can be plotted as against outer area drift (fig. 25). Since drift becomes smaller with increasing $\langle L \rangle$, the length range and dynamicity behave in a similar manner here, both for average (fig. 25B) and discrete T_p averages (fig. 25C); accuracy is quite consistent relative to the two-state model (fig. 25A).

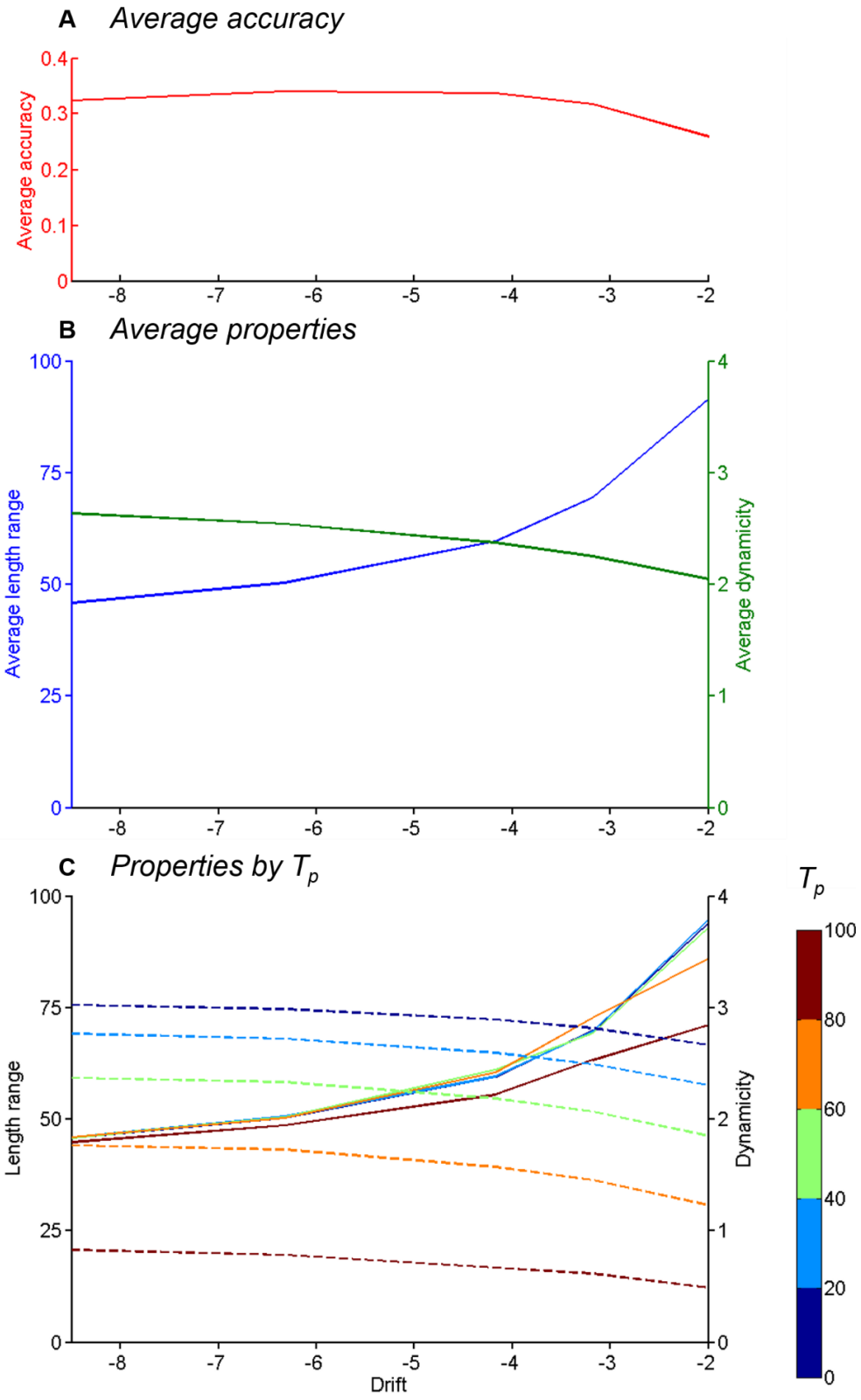

Figure 25. Length range, dynamicity and accuracy as functions of drift for dynamics sets 6-10. Each dynamics set has one drift value, for which the average accuracy (A), the average length range and dynamicity (B), and the length range and dynamicity averaged over discrete Tp (see colour bar) (C), are shown. Length range units are μm; dynamicity and drift units are μm min^{-1}.

Finally, the fact that on average, accuracy does not increase with larger negative outer drift warrants a discussion of the response of accuracy to changing drift and T_p. Firstly, notice that the average accuracy in figure 25A is actually lower at the largest negative drift compared to the intermediate negative drifts. However, the first set of results showed that accuracy is greatest at the largest negative drift. The situation can be clarified by considering in a bit more detail how accuracy responds to the combinations of drift and T_p. In figure 26A, the accuracy is plotted with drift, colour-coded for T_p. Note that the range in accuracy values increases with larger negative drift; these are plotted in figure 26B. The low accuracy values for small T_p evidently lower the average accuracy in figure 25A.

What is the link between a small T_p and non-increasing accuracy with larger negative drift? Firstly, it is relevant that the introduction of pausing elevates accuracy for lower negative drift values, regardless of the value of T_p; in two-state simulations, accuracy was always very low at outer drift value of -2 μm min^{-1}, whereas here it is greater than 0.2 μm min^{-1}; this was discussed above. Secondly, and more fundamentally, introduction of pausing means that dynamicity does not vary to the same extent with drift as it does in the two-state simulations. Thus, T_p modulates dynamicity almost independently of drift; there is a small decrease in dynamicity as drift approaches zero, as discussed.

However, the introduction of pausing does not alter length range to the same extent as it does dynamicity; here, it still increases as drift approaches zero. This means that for small negative drift regimes where the length range is large, the reduction in dynamicity afforded by increases in T_p has a small effect, as large T_p values do yield greater accuracy here, but this effect is not as great as when length range is small at large negative drift values. Here, reducing dynamicity by increasing T_p can have a stronger effect because the length range is not limiting; it is small. This explains the increase in accuracy range as negative drift becomes larger.

These results suggest that in the two-state case, the increase in dynamicity with decreasing length range seen in dynamics set 4 is limiting further increases in accuracy. Similarly, in the two-state dynamics set 5 where D varied and dynamicity increased with increasing D and larger negative drift, i.e. dynamicity was effectively "forced", length range reduced and accuracy increased; in two states, accuracy is achieved by decreasing length range but there is concomitant increase in dynamicity. In three states, these are (almost) uncoupled, allowing greater accuracy by reducing dynamicity at low length ranges.

To conclude this section, the findings presented above demonstrate that the systems behaviour found in the two-state model is still applicable in general; greater accuracy is associated with a decrease in length range and a very slight increase in dynamicity, but that pausing contributes to greater accuracy by permitting decreases in dynamicity that would otherwise be unattainable. As with two states, pausing effectively focusses plus ends to the target area, but without concomitant increases in dynamicity. This means higher accuracy is attainable at smaller outer negative drift than in two-states, and for any drift value, larger T_p means more accurate targeting.

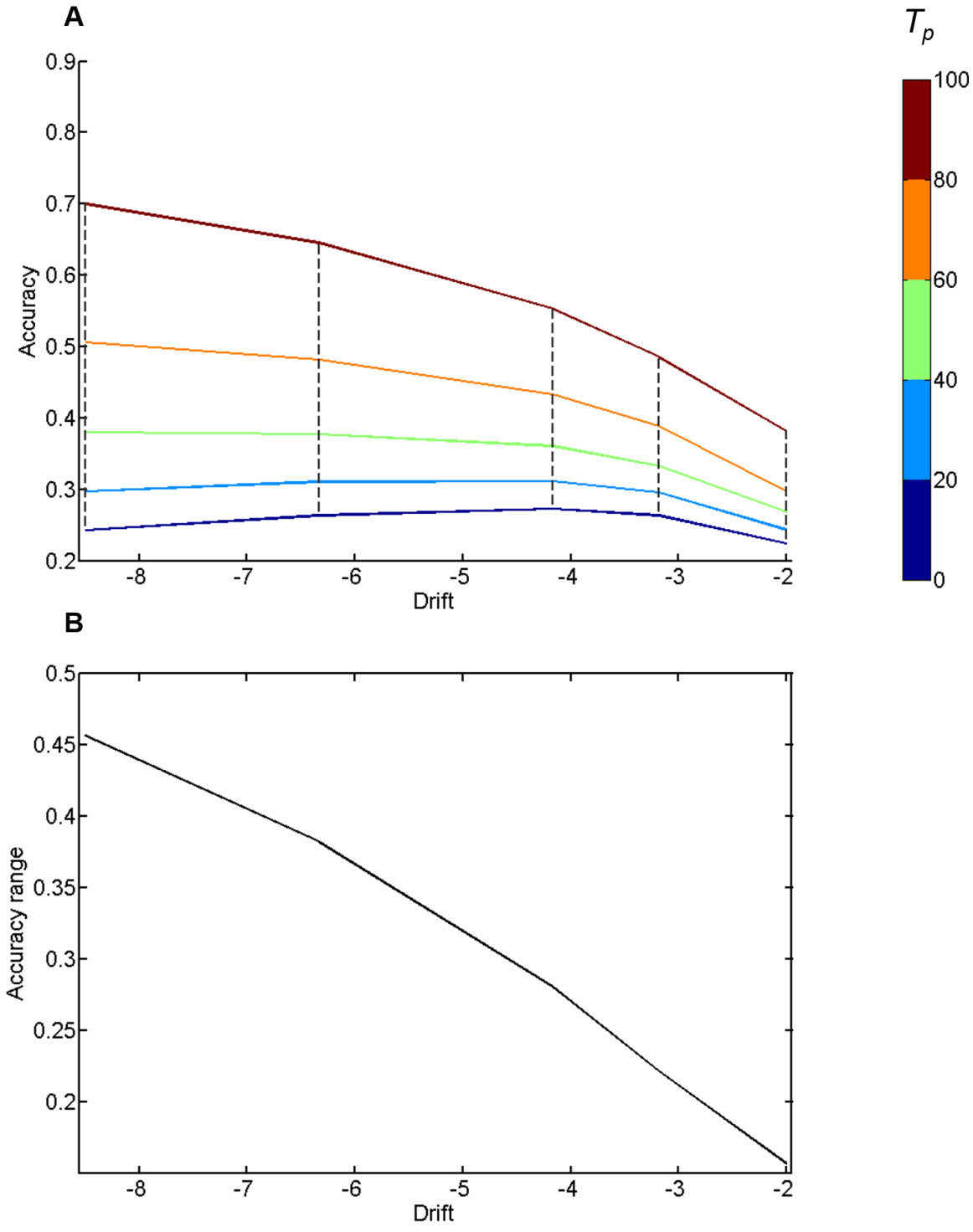

Figure 26. Accuracy and accuracy range with drift, dynamics sets 6-10. The average accuracy for discrete pausing time percentage groups is shown as a function of drift (A), and the range of the accuracy values, indicated by the dashed grey lines in A, is shown in B. Drift units are μm min^{-1}.

E. DISCUSSION

I. Mechanisms of radiality

a. Evaluation of investigation rationale

In this chapter, the general principles of accurate cortical targeting have been deduced by coarsening the model of microtubule dynamics into just three parameters: drift, V, diffusion coefficient, D, and theoretical average length, $\langle L \rangle$ (though note that only two are ever needed because they are related by eq. 4). Therefore, even though in the model, the full complement of dynamics parameters were specified, i.e. V_g, V_s, F_{cat} and F_{res} in two states, and the transitions to and from the pausing state added to these to make eight parameters for the three state case, considering the area dynamics in terms of these parameters borrowed from the theory of random walks helped to elucidate the characteristics of area dynamics regimes that will give rise to accurate targeting of microtubules to the cortex.

Here, the framework for the modelling, where one-dimensional microtubules grew in two areas with particular dynamics regimes, followed from the rationale that radiality must necessarily follow from control of microtubule length, and that one mechanism to do this is cell periphery-specific changes in microtubule dynamics relative to the more central areas of the cell. Indeed, it was postulated at the beginning of this chapter that this may not be an exclusive mechanism for radiality, and that other processes, particularly microtubule-intrinsic length control and cortical capture of microtubules, would contribute to radiality.

b. General principles of accurate cortical targeting

In the first simulations of the model in two state (sets 1-3), it is interesting to note that the effect of $\langle L \rangle$ is opposite between the areas: in outer areas, decreases in $\langle L \rangle$ produce more accurate targeting, while in inner areas, increases in $\langle L \rangle$ give better accuracy. How can this be rationalised? In inner areas in a negative drift regime, a greater $\langle L \rangle$ will mean that microtubules will be more likely to reach the target area, whereas in outer areas, lower $\langle L \rangle$ will be beneficial by the fact that microtubules will effectively be contained better within the target area, giving greater accuracy.

The effect of D is less intuitive compared to $\langle L \rangle$, since increases in D, essentially an indicator of the randomness of microtubule lengths, produce better cortical targeting. How can this be? As discussed in the results, we can rationalise this by the fact that in a negative drift regime, larger D means larger negative drift, and thus the randomness, as such, is better thought of as an increased tendency for microtubules to undergo large excursions in the shrinking phase. Of course, in a two-area model, once the microtubules have shrunk sufficiently, they will experience the dynamics allocated to the inner area. Therefore, when inner area dynamics permit, i.e. when they have large and positive drift, large D in the outer area and high accuracy is reasonable.

The switching back and forth between areas that must arise when outer area dynamics produce large negative drift and the inner area dynamics have large positive drift is indicated by the increase in dynamicity as outer area negative drift got larger in sets 4 and 5; this is

especially true of set 4, where *D* was fixed, because in area-free simulations, the trend in dynamicity went against this, decreasing with larger negative drift.

When pausing in the outer area was introduced into the simulations, it increased accuracy when it was increased in the outer area. We saw that for large negative outer area drift, T_p had more of a modulatory effect than at small negative outer area drift, suggesting that at these drift combinations (i.e. large negative outer, large positive inner), dynamicity was limiting, whereas at small negative outer, large positive inner drift, the smaller modulatory role of pausing suggests that here, length range may be the limiting factor.

These observations can be condensed into a unifying theory of cortical targeting: that the accuracy of any targeting strategy depends on the extent to which the inner area promotes transit of microtubules to the outer area, and the extent to which the outer area maintains these microtubules, or, failing that, returns them to the inner area.

c. General principles compared to measured dynamics

In the cell, it is generally assumed that where there is negative drift, the system is maintained by a complementary nucleation rate, and where there is positive drift, the confines of the cell somehow act to limit this tendency toward growth; very few studies have considered this experimentally, although Komarova et al. (2002), Mimori-Kiyosue et al. (2005) and Komarova et al. (2009) are good exceptions.

In those studies, microtubule dynamics were found to be different near the cell periphery compared to more central areas of the cell. In summary, the dynamics at the cell periphery differed in such a way that at the periphery, microtubules were found to be in negative drift (Komarova et al., 2002), have increased incidence of transitions between states (Komarova et al., 2009; Komarova et al., 2002; Mimori-Kiyosue et al., 2005), and increased incidence of pausing (Mimori-Kiyosue et al., 2005). These experimental findings are all consistent with the results of the modelling in this chapter, and thus, the "general mechanisms" outlined above may be able to account for good cortical targeting in some cases, without the need for subsequent capture to be invoked to produce better accuracy.

Whether these indeed are general mechanisms *in vivo* and cells do not rely on the contribution of other mechanisms, such as the cortical capture and stabilisation of microtubules, will require further experiments that address differences in microtubule dynamics between central and peripheral areas.

d. Future experiments

As discussed earlier in the chapter, the hallmark of a good model is that it will not only test our notions of reality, it will also hint at possible future experiments. What can the model suggest for future experiments? The fact that, in a low or no-pausing dynamics regime, good accuracy in cortical targeting is concomitant with increased dynamicity, indicates that microtubules need not necessarily be less dynamic as they approach the cell periphery. Indeed, as some studies posit an increase in rescue (e.g. Komarova et al. (2009)) at or near the cell periphery, repeated cycles of growth, collision with the cell border, shrinkage, and subsequent rescue may well increase dynamicity relative to other areas of the cell. Therefore,

a future experiment might address dynamicity and the extent of radiality. Doing such an experiment in conjunction with interfering with the function of various MAPs and potential cortical stabilising factors, which were discussed in chapter 2, would be interesting.

Other experiments might include an assessment of cortical stabilisation. Indeed, although there have been many good studies of selective stabilisation, it would be interesting to further characterise dynamics at the periphery and stabilisation. For example, we might characterise microtubule dynamics at the same time as implementation of an assay of selective stabilisation, and thus obtain cortical selective stabilisation as a function of microtubule dynamics. Such an experiment could be conducted in conjunction with a certain model extension described below.

II. Modelling for radiality

a. Model evaluation

In the discussion of the modelling process near the beginning of this chapter, the point was made that models are best when designed for specific purposes with particular complementary experiments. Here, the model was designed with the methodology of chapter 3 in mind; there, microtubule dynamics were measured in central and peripheral areas of the cell; here, microtubules were modelled with two sets of dynamics: one for inner areas and one for outer areas. The complementary experiments are examined in a bit more detail in the next chapter; the purpose here was to really understand what makes for a good microtubule cortical targeting strategy, and indeed, this has been possible with the simple one-dimensional model that was used. Of course, the model can be extended, and thus be more complex, and this is discussed below. However, models need not be complex for the sake of complexity, and the model used here was appropriate for the questions at hand.

b. Comparison with other models

Theoretically, Gregoretti et al. (2006) and Vorobjev and Maly (2008) have given attention to the effects of a boundary on microtubule dynamics. The former study found that microtubule dynamics could be modulated by the effect of increasing soluble tubulin concentration at the cell periphery upon growth being limited by a barrier. To elaborate, as microtubules grew against the cell border, their subsequent transition to the shrinking phase lead to an increase in soluble tubulin concentration, and thus an elevated rescue frequency (which was concentration-dependent in their model), and thus, microtubules grew again and appropriate length was achieved. This makes for an appealing self-organising mechanism, and is not exclusive; it is compatible with the mechanisms discussed here and also with cortical capture.

The model of Vorobjev and Maly (2008) found that if microtubule length was limited, for example by a cell boundary, then positive drift dynamics could produce a radial array. Without bending microtubules, this makes sense, since microtubules will grow persistently up to a target length, and then stop. If capture is immediate, then this positive drift could be the maximum (i.e. the growth rate) and microtubules would form a radial array. In some ways, the model here builds upon that work by allowing microtubules to continue to grow

past a target length, and asking what the appropriate dynamics parameters are if they are to be accurately targeted to that length.

Finally, in a similar model in a predominantly experimental paper, van der Vaart et al. (2013) addressed how microtubule growth might be regulated at the cell periphery. They found that the increased rescue frequency found at the cell periphery required a decrease in microtubule growth rate if the microtubules were to be radially-organised. Since decreases in growth rate would cause decreases in drift, their findings are consistent with those presented here, and again, increased rescue can also be explained if dynamics in the inner area are in positive drift.

c. Model extensions

An obvious extension to the model that has not been addressed here is inner area pausing. The reason it was omitted here is because its effects on accuracy of cortical targeting are evaluated in the next chapter; however, as we will see, this is only for dynamics regimes in quadrant 3 of drift space. Therefore, one part of the two-area model to be implemented in the future is inner area pausing in dynamics regimes located in quadrant 4 of drift space.

Note that, although this model was designed to investigate the potential for cell periphery-specific modulation of microtubule dynamcis, it may also be applicable as a very coarse model of microtubule-intrinsic length control. Indeed, although the term intrinsic is used here to indicate mechanisms distinct from those based on cortex-located processes, this intrinsic length control can be modulated by microtubule-extrinsic agents, for example various kinesins (Gardner et al., 2011). Thus, discrete areas of dynamics could be applied to test age- or length-dependent microtubule dynamics modulation.

Further extensions to the model could include an investigation of the effect of microtubule length control as investigated here on the rate of microtubule capture. To elaborate, a simple hypothesis that extends from the idea that a number of processes contribute to radiality is that accurate cortical targeting, as determined by the modelling here, contributes to radiality by making microtubules available to capture. In this view, a microtubule that is more accurately targeted to the cortical area will by definition spend more time in that area; capturing a microtubule should proceed more successfully if the microtubule is near the capture site more often, as it would be if it is more accurately targeted. Thus, a model whereby microtubules are captured with a given frequency and are subsequently stabilised and removed from the dynamic pool of microtubules, would be applicable for this type of problem. Such a model is not a significant extension from that used here.

Related to the evaluation of the model given above, it is apparent that in future modelling studies, including cell dimensions may be applicable; indeed, it is likely that the mechanisms postulated to contribute to radiality above, and probably many others, are tuned so that they are applicable to cell dimensions. As discussed, it is apparent that the inner-outer changes in dynamics here may not, in many cases, be comprehensive for radiality. Therefore, we could expect a cell system whereby the cortex mediated dynamics play a role in the generation of radiality, but that this is a role in a large ensemble of other processes that are tuned by the cell to produce appropriate microtubule dynamics, and thus length, and subsequent radiality.

Such tuning might include concentrations of various molecules that contribute to the microtubule-intrinsic mechanisms, and localisation of cortical molecules for modulation of dynamics and also capture and subsequent stabilisation of microtubules.

To conclude, in this chapter, the general mechanisms for accurate cortical targeting have been characterised, and abstraction of the many dynamics parameters into just a few parameters has helped in doing this. The modelling should inform future studies of cortical microtubule behaviour, and there are also a number of extensions to the model that will be interesting to explore. In the next chapter, the model is carried forward and we revisit the dynamics measurements made in the previous chapter, and together with modelling of dynamics sets similar to those of chapter 3, a small survey of literature-reported microtubule dynamics is conducted so as to be able to better understand where the measured dynamics and the dynamics sets used in this chapter relate to dynamics recorded by other researchers.

F. APPENDICES

I. Two-state dynamics

Table IX. Dynamics set 1. Dynamics parameters, V_g, V_s, F_{cat} and F_{res} are shown, together with the F_{cat}:F_{res} ratio, and abstract measures theoretical average length, $\langle L \rangle$, drift, V, and diffusion coefficient, D. Units: V_g, V_s, V, μm min^{-1}, F_{cat}, F_{res}, min^{-1}, $\langle L \rangle$, μm, and D, μm^2 min^{-1}. Each row was assigned in turn to one of the model areas.

V_g	V_s	F_{cat}	F_{res}	F_{cat}:F_{res}	$\langle L \rangle$	V	D
11	15	0.15	4.85	0.03	-	10.22	33
11	15	0.35	4.65	0.08	-	9.18	33
11	15	0.55	4.45	0.12	-	8.14	33
11	15	0.75	4.25	0.18	-	7.10	33
11	15	0.95	4.05	0.23	-	6.06	33
11	15	1.15	3.85	0.30	-	5.02	33
11	15	1.35	3.65	0.37	-	3.98	33
11	15	1.55	3.45	0.45	-	2.94	33
11	15	1.75	3.25	0.54	-	1.90	33
11	15	1.95	3.05	0.64	-	0.86	33
11	15	2.25	2.75	0.82	47.14	-0.70	33
11	15	2.45	2.55	0.96	18.97	-1.74	33
11	15	2.65	2.35	1.13	11.87	-2.78	33
11	15	2.85	2.15	1.33	8.64	-3.82	33
11	15	3.05	1.95	1.56	6.79	-4.86	33
11	15	3.25	1.75	1.86	5.59	-5.90	33
11	15	3.45	1.55	2.23	4.76	-6.94	33
11	15	3.65	1.35	2.70	4.14	-7.98	33
11	15	3.85	1.15	3.35	3.66	-9.02	33
11	15	4.05	0.95	4.26	3.28	-10.06	33

Table X. Dynamics set 2. Dynamics parameters, V_g, V_s, F_{cat} and F_{res} are shown, together with the F_{cat}:F_{res} ratio, and abstract measures theoretical average length, $\langle L \rangle$, drift, V, and diffusion coefficient, D. Units: V_g, V_s, V, μm min^{-1}, F_{cat}, F_{res}, min^{-1}, $\langle L \rangle$, μm, and D, μm^2 min^{-1}. Each row was assigned in turn to one of the model areas.

V_g	V_s	F_{cat}	F_{res}	F_{cat}:F_{res}	$\langle L \rangle$	V	D
11	15	0.3	9.7	0.03	-	10.22	16.5
11	15	0.7	9.3	0.08	-	9.18	16.5
11	15	1.1	8.9	0.12	-	8.14	16.5
11	15	1.5	8.5	0.18	-	7.10	16.5
11	15	1.9	8.1	0.23	-	6.06	16.5
11	15	2.4	7.6	0.32	-	4.76	16.5
11	15	2.8	7.2	0.39	-	3.72	16.5
11	15	3.2	6.8	0.47	-	2.68	16.5
11	15	3.6	6.4	0.56	-	1.64	16.5
11	15	4	6	0.67	-	0.60	16.5
11	15	4.4	5.6	0.79	37.50	-0.44	16.5
11	15	4.8	5.2	0.92	11.15	-1.48	16.5
11	15	5.2	4.8	1.08	6.55	-2.52	16.5
11	15	5.6	4.4	1.27	4.63	-3.56	16.5
11	15	6	4	1.50	3.59	-4.60	16.5
11	15	6.5	3.5	1.86	2.80	-5.90	16.5
11	15	6.9	3.1	2.23	2.38	-6.94	16.5
11	15	7.3	2.7	2.70	2.07	-7.98	16.5
11	15	7.7	2.3	3.35	1.83	-9.02	16.5
11	15	8.1	1.9	4.26	1.64	-10.06	16.5

Table XI. Dynamics set 3. Dynamics parameters, V_g, V_s, F_{cat} and F_{res} are shown, together with the F_{cat}:F_{res} ratio, and abstract measures theoretical average length, $\langle L \rangle$, drift, V, and diffusion coefficient, D. Units: V_g, V_s, V, μm min^{-1}, F_{cat}, F_{res}, min^{-1}, $\langle L \rangle$, μm, and D, μm^2 min^{-1}. Each row was assigned in turn to one of the model areas.

V_g	V_s	F_{cat}	F_{res}	F_{cat}:F_{res}	$\langle L \rangle$	V	D
11	15	0.6	19.4	0.03	-	10.22	8.25
11	15	1.4	18.6	0.08	-	9.18	8.25
11	15	2.2	17.8	0.12	-	8.14	8.25
11	15	3.1	16.9	0.18	-	6.97	8.25
11	15	3.9	16.1	0.24	-	5.93	8.25
11	15	4.7	15.3	0.31	-	4.89	8.25
11	15	5.5	14.5	0.38	-	3.85	8.25
11	15	6.3	13.7	0.46	-	2.81	8.25
11	15	7.2	12.8	0.56	-	1.64	8.25
11	15	8	12	0.67	-	0.60	8.25
11	15	8.8	11.2	0.79	18.75	-0.44	8.25
11	15	9.6	10.4	0.92	5.57	-1.48	8.25
11	15	10.5	9.5	1.11	3.11	-2.65	8.25
11	15	11.3	8.7	1.30	2.24	-3.69	8.25
11	15	12.1	7.9	1.53	1.74	-4.73	8.25
11	15	12.9	7.1	1.82	1.43	-5.77	8.25
11	15	13.7	6.3	2.17	1.21	-6.81	8.25
11	15	14.6	5.4	2.70	1.03	-7.98	8.25
11	15	15.4	4.6	3.35	0.91	-9.02	8.25
11	15	16.2	3.8	4.26	0.82	-10.06	8.25

Table XII. Dynamics set 4. Dynamics parameters, V_g, V_s, F_{cat} and F_{res} are shown, together with the abstract measures theoretical average length, $\langle L \rangle$, drift, V, and diffusion coefficient, D. Units: V_g, V_s, V, μm min^{-1}, F_{cat}, F_{res}, min^{-1}, $\langle L \rangle$, μm, and D, μm^2 min^{-1}. Here, the single dynamics set for the inner area is shown, and the outer area parameters are summarised.

V_g	V_s	F_{cat}	F_{res}	$\langle L \rangle$	V	D
Inner						
12	15	0	5	-	12	36
Outer						
11	15	6.67 *to* 12.12	8.33 *to* 2.88	19.8 *to* 1.1	-0.56 *to* -10	11

Table XIII. Dynamics set 5. Dynamics parameters, V_g, V_s, F_{cat} and F_{res} are shown, together with the abstract measures theoretical average length, $\langle L \rangle$, drift, V, and diffusion coefficient, D. Units: V_g, V_s, V, μm min^{-1}, F_{cat}, F_{res}, min^{-1}, $\langle L \rangle$, μm, and D, μm^2 min^{-1}. Here, the single dynamics set for the inner area is shown, and the outer area parameters are summarised.

V_g	V_s	F_{cat}	F_{res}	$\langle L \rangle$	V	D
Inner						
12	15	0	5	-	12	36
Outer						
11	15	44 *to* 4.44	55 *to* 1.06	3	-0.56 *to* -10	1.67 *to* 30

II. Three-state dynamics

Table XIV. Dynamics set 6. Dynamics parameters, V_g, V_s, F_{cat} to F_{p2s} are shown, together with the abstract measures theoretical average length, $\langle L \rangle$, drift, V, diffusion coefficient, D and pausing time percentage, T_p. Units: V_g, V_s, V, μm min^{-1}, all transition frequencies, min^{-1}, $\langle L \rangle$, μm, and D, μm^2 min^{-1}. Here, the single dynamics set for the inner area is shown, and the outer area parameters are summarised.

V_g	V_s	F_{cat}	F_{res}	F_{g2p}	F_{p2g}	F_{s2p}	F_{p2s}	V	$\langle L \rangle$	D	T_p
Inner											
12	15	0	5	0	0	0	0	12	-	-	0
Outer											
11	15	10	10	1.50	0.01 *to* 24.25	1.50	0.01 *to* 24.25	-2.00	3.84	7.67	98.68 *to* 3.00

Table XV. Dynamics set 7. Dynamics parameters, V_g, V_s, F_{cat} to F_{p2s} are shown, together with the abstract measures theoretical average length, $\langle L \rangle$, drift, V, diffusion coefficient, D and pausing time percentage, T_p. Units: V_g, V_s, V, μm min^{-1}, all transition frequencies, min^{-1}, $\langle L \rangle$, μm, and D, μm^2 min^{-1}. Here, the single dynamics set for the inner area is shown, and the outer area parameters are summarised.

V_g	V_s	F_{cat}	F_{res}	F_{g2p}	F_{p2g}	F_{s2p}	F_{p2s}	V	$\langle L \rangle$	D	T_p
Inner											
12	15	0	5	0	0	0	0	12	-	-	0
Outer											
11	15	10.91	9.09	1.50	0.01 *to* 22.04	1.50	0.01 *to* 22.04	-3.18	2.43	7.67	98.55 *to* 3.00

Table XVI. Dynamics set 8. Dynamics parameters, V_g, V_s, F_{cat} to F_{p2s} are shown, together with the abstract measures theoretical average length, $\langle L \rangle$, drift, V, diffusion coefficient, D and pausing time percentage, T_p. Units: V_g, V_s, V, μm min^{-1}, all transition frequencies, min^{-1}, $\langle L \rangle$, μm, and D, μm^2 min^{-1}. Here, the single dynamics set for the inner area is shown, and the outer area parameters are summarised.

V_g	V_s	F_{cat}	F_{res}	F_{g2p}	F_{p2g}	F_{s2p}	F_{p2s}	V	$\langle L \rangle$	D	T_p
Inner											
12	15	0	5	0	0	0	0	12	-	-	0
Outer											
11	15	11.67	8.33	1.50	0.01 *to* 20.20	1.50	0.01 *to* 20.20	-4.17	1.86	7.67	98.42 *to* 3.00

Table XVII. Dynamics set 9. Dynamics parameters, V_g, V_s, F_{cat} to F_{p2s} are shown, together with the abstract measures theoretical average length, $\langle L \rangle$, drift, V, diffusion coefficient, D and pausing time percentage, T_p. Units: V_g, V_s, V, μm min^{-1}, all transition frequencies, min^{-1}, $\langle L \rangle$, μm, and D, μm^2 min^{-1}. Here, the single dynamics set for the inner area is shown, and the outer area parameters are summarised.

V_g	V_s	F_{cat}	F_{res}	F_{g2p}	F_{p2g}	F_{s2p}	F_{p2s}	V	$\langle L \rangle$	D	T_p
Inner											
12	15	0	5	0	0	0	0	12	-	-	0
Outer											
11	15	13.33	6.67	1.50	0.01 *to* 16.16	1.50	0.01 *to* 16.16	-6.33	1.23	7.67	98.04 *to* 3.00

Table XVIII. Dynamics set 10. Dynamics parameters, V_g, V_s, F_{cat} to F_{p2s} are shown, together with the abstract measures theoretical average length, $\langle L \rangle$, drift, V, diffusion coefficient, D and pausing time percentage, T_p. Units: V_g, V_s, V, μm min^{-1}, all transition frequencies, min^{-1}, $\langle L \rangle$, μm, and D, μm^2 min^{-1}. Here, the single dynamics set for the inner area is shown, and the outer area parameters are summarised.

V_g	V_s	F_{cat}	F_{res}	F_{g2p}	F_{p2g}	F_{s2p}	F_{p2s}	V	$\langle L \rangle$	D	T_p
Inner											
12	15	0	5	0	0	0	0	12	-	-	0
Outer											
11	15	15	5	1.50	0.01 *to* 12.12	1.50	0.01 *to* 12.12	-8.50	0.92	7.67	97.40 *to* 3.00

REFERENCES

Allard, J.F., G.O. Wasteneys, and E.N. Cytrynbaum. 2010. Mechanisms of self-organization of cortical microtubules in plants revealed by computational simulations. *Molecular biology of the cell*. 21:278-286.

Applegate, K.T., S. Besson, A. Matov, M.H. Bagonis, K. Jaqaman, and G. Danuser. 2011. plusTipTracker: Quantitative image analysis software for the measurement of microtubule dynamics. *Journal of structural biology*. 176:168-184.

Box, G.E.P., and N.R. Draper. 1987. Empirical model-building and response surfaces. Wiley.

Brun, L., B. Rupp, J.J. Ward, and F. Nedelec. 2009. A theory of microtubule catastrophes and their regulation. *Proceedings of the National Academy of Sciences of the United States of America*. 106:21173-21178.

Chen, Y., and T.L. Hill. 1983. Use of Monte Carlo calculations in the study of microtubule subunit kinetics. *Proceedings of the National Academy of Sciences of the United States of America*. 80:7520-7523.

Dogterom, M., and S. Leibler. 1993. Physical aspects of the growth and regulation of microtubule structures. *Physical review letters*. 70:1347-1350.

Gardner, M.K., and D.J. Odde. 2010. Stochastic simulation and graphic visualization of mitotic processes. *Methods (San Diego, Calif.)*. 51:251-256.

Gardner, M.K., M. Zanic, C. Gell, V. Bormuth, and J. Howard. 2011. Depolymerizing kinesins Kip3 and MCAK shape cellular microtubule architecture by differential control of catastrophe. *Cell*. 147:1092-1103.

Gardner, M.K., M. Zanic, and J. Howard. 2013. Microtubule catastrophe and rescue. *Current opinion in cell biology*. 25:14-22.

Green, R.A., R. Wollman, and K.B. Kaplan. 2005. APC and EB1 function together in mitosis to regulate spindle dynamics and chromosome alignment. *Molecular biology of the cell*. 16:4609-4622.

Gregoretti, I.V., G. Margolin, M.S. Alber, and H.V. Goodson. 2006. Insights into cytoskeletal behavior from computational modeling of dynamic microtubules in a cell-like environment. *Journal of cell science*. 119:4781-4788.

Hill, T.L., and M.F. Carlier. 1983. Steady-state theory of the interference of GTP hydrolysis in the mechanism of microtubule assembly. *Proceedings of the National Academy of Sciences of the United States of America*. 80:7234-7238.

Hill, T.L., and Y. Chen. 1984. Phase changes at the end of a microtubule with a GTP cap. *Proceedings of the National Academy of Sciences of the United States of America*. 81:5772-5776.

Hodgkin, A.L., and A.F. Huxley. 1952. A quantitative description of membrane current and its application to conduction and excitation in nerve. *The Journal of physiology*. 117:500-544.

Holy, T.E., and S. Leibler. 1994. Dynamic instability of microtubules as an efficient way to search in space. *Proceedings of the National Academy of Sciences of the United States of America*. 91:5682-5685.

Karsenti, E., F. Nedelec, and T. Surrey. 2006. Modelling microtubule patterns. *Nature cell biology*. 8:1204-1211.

Komarova, Y., C.O. De Groot, I. Grigoriev, S.M. Gouveia, E.L. Munteanu, J.M. Schober, S. Honnappa, R.M. Buey, C.C. Hoogenraad, M. Dogterom, G.G. Borisy, M.O. Steinmetz, and A. Akhmanova. 2009. Mammalian end binding proteins control persistent microtubule growth. *The Journal of cell biology*. 184:691-706.

Komarova, Y.A., I.A. Vorobjev, and G.G. Borisy. 2002. Life cycle of MTs: persistent growth in the cell interior, asymmetric transition frequencies and effects of the cell boundary. *Journal of cell science*. 115:3527-3539.

Mimori-Kiyosue, Y., I. Grigoriev, G. Lansbergen, H. Sasaki, C. Matsui, F. Severin, N. Galjart, F. Grosveld, I. Vorobjev, S. Tsukita, and A. Akhmanova. 2005. CLASP1 and CLASP2 bind to EB1 and regulate microtubule plus-end dynamics at the cell cortex. *The Journal of cell biology*. 168:141-153.

Mirny, L.A., and D.J. Needleman. 2010. Quantitative characterization of filament dynamics by single-molecule lifetime measurements. *Methods in cell biology*. 95:583-600.

Mitchison, T., and M. Kirschner. 1984a. Dynamic instability of microtubule growth. *Nature*. 312:237-242.

Mitchison, T., and M. Kirschner. 1984b. Microtubule assembly nucleated by isolated centrosomes. *Nature*. 312:232-237.

Mogilner, A., J. Allard, and R. Wollman. 2012. Cell polarity: quantitative modeling as a tool in cell biology. *Science (New York, N.Y.)*. 336:175-179.

Odde, D.J., L. Cassimeris, and H.M. Buettner. 1995. Kinetics of microtubule catastrophe assessed by probabilistic analysis. *Biophysical journal*. 69:796-802.

Oosawa, F., and S. Asakura. 1975. Thermodynamics of the polymerization of protein. Academic Press.

Ranjith, P., D. Lacoste, K. Mallick, and J.F. Joanny. 2009. Nonequilibrium self-assembly of a filament coupled to ATP/GTP hydrolysis. *Biophysical journal*. 96:2146-2159.

Ross, S.M. 2006. Introduction to Probability Models. Elsevier Science.

Rusan, N.M., C.J. Fagerstrom, A.M. Yvon, and P. Wadsworth. 2001. Cell cycle-dependent changes in microtubule dynamics in living cells expressing green fluorescent protein-alpha tubulin. *Molecular biology of the cell*. 12:971-980.

Schek, H.T., 3rd, M.K. Gardner, J. Cheng, D.J. Odde, and A.J. Hunt. 2007. Microtubule assembly dynamics at the nanoscale. *Current biology : CB*. 17:1445-1455.

van der Vaart, B., W.E. van Riel, H. Doodhi, J.T. Kevenaar, E.A. Katrukha, L. Gumy, B.P. Bouchet, I. Grigoriev, S.A. Spangler, K.L. Yu, P.S. Wulf, J. Wu, G. Lansbergen, E.Y. van Battum, R.J. Pasterkamp, Y. Mimori-Kiyosue, J. Demmers, N. Olieric, I.V. Maly, C.C. Hoogenraad, and A. Akhmanova. 2013. CFEOM1-associated kinesin KIF21A is a cortical microtubule growth inhibitor. *Developmental cell*. 27:145-160.

VanBuren, V., L. Cassimeris, and D.J. Odde. 2005. Mechanochemical model of microtubule structure and self-assembly kinetics. *Biophysical journal*. 89:2911-2926.

Verde, F., M. Dogterom, E. Stelzer, E. Karsenti, and S. Leibler. 1992. Control of microtubule dynamics and length by cyclin A- and cyclin B-dependent kinases in Xenopus egg extracts. *The Journal of cell biology*. 118:1097-1108.

Vorobjev, I.A., and I.V. Maly. 2008. Microtubule length and dynamics: Boundary effect and properties of extended radial array. *Cell Tiss. Biol.* 2:272-281.

Wollman, R., E.N. Cytrynbaum, J.T. Jones, T. Meyer, J.M. Scholey, and A. Mogilner. 2005. Efficient chromosome capture requires a bias in the 'search-and-capture' process during mitotic-spindle assembly. *Current biology : CB*. 15:828-832.

Chapter 5

Comparing and modelling microtubule dynamics

A. INTRODUCTION

I. Chapter aims

The first aim of this chapter is to put the results of chapter 3 into context by comparing them with previously reported measurements of microtubule dynamics. This will reveal the extent to which the dynamics reported in chapter 3 differ or are similar to other measurements of dynamics, and it will also indicate the degree to which microtubule dynamics differ across various cell lines, types, etc. In order to be able to compare sets of microtubule dynamics, the abstract measures used in the previous chapter are again employed to reduce the complexity of the task and to allow an understanding of how changing certain dynamics parameters, or the relationships between them, influence the population-level characteristics of the network.

In the discussion at the end of chapter 3, it was apparent that in many cases, the results suggest mechanisms to explain the organisation, and in the systems view of microtubule organisation proposed in that chapter, those results would indeed be taken as the components of the system, from which the organisation emerges. However, another fact in evidence in that discussion was that it is difficult to truly establish those results as causes of the organisation seen. Therefore, the second aim of this chapter is to begin to establish a rationale for explaining the maintenance of organisation in the radial array. This will be carried out in light of the survey and comparison of microtubule dynamics and the modelling results from the previous chapter. Indeed, the aim is to identify common principles between the surveyed dynamics and those reported in the chapter 3, in the hope that these might be the important components of the radial array system. This is then carried forward into the second part of this chapter, where the proposals are evaluated with the model used in chapter 4.

B. METHODOLOGY

I. Survey of dynamics

Literature searches were carried out using standard databases. To limit the extent of the survey, firstly, only reports of microtubule dynamics *in vivo* were kept, and secondly, of those, only reports of dynamics in animal cells were retained. In every case, the values for dynamics parameters were obtained from the report, and all measurements were adjusted so that they were in similar units. This last step was taken so that values were more easily compared. Where there were more than one instance of a set of dynamics, even if some of the measurements were the same between sets, two entries were made into the results table. Examples where this type of thing occurred include repeated experiments, and different cell lines, etc. Average values reported in the literature are not always explicitly stated as being the mean average; it is assumed here that this is the case. Only the average values were surveyed here; no efforts were made to obtain information as to the distribution of speeds, times, etc. Thus, there are no ± standard deviations/standard errors in the results table.

II. Modelling of measured dynamics

The model used in chapter 4 is used again here, so refer to the methodology of that chapter for a detailed discussion of the model and issues pertaining to it. In this chapter, different dynamics sets were used; the tables documenting them are in the appendix, and here, a brief description of the rationale for the choice of parameters is given.

In light of the location in drift space of the measured dynamics from chapter 3, presented below in the results, the dynamics combinations here were chosen so as to be able to investigate how the abstract parameterisations affected accuracy when imposed on a dynamics background from quadrant 3 of drift space. Thus, where quadrant 4 of drift space was investigated in the majority of the previous chapter, in this chapter, dynamics sets produce area dynamics combinations that are in quadrant 3 of drift space, i.e. negative inner and outer drift.

As stated, the aim was to investigate the effect of changing the parameterisations of dynamics, including T_p. To this end, there were three "principal" dynamics sets, and three variations on each principal set. To avoid confusion when comparing these dynamics sets with the sets from the previous chapter, these 3 sets of 3 dynamics sets are numbered from 11-19. The defining feature of a principal set is the drift of the inner area; the principal dynamics sets have inner area drifts of -0.56 μm min^{-1} (sets 11, 14 and 17), -2.00 μm min^{-1} (sets 12, 15 and 18), and -4.17 μm min^{-1} (sets 13, 16 and 19). The variation between the sets with similar inner area drift is the outer area drift: these are: -10.06 μm min^{-1} (sets 11-13), -5.38 μm min^{-1} (sets 14-16) and -0.96 μm min^{-1} (sets 17-19).

Within each of these sets, there are subsets that have different $\langle L \rangle$ and D, and within each of these subsets, there are 5 sets with T_p values of 10, 20, 40, 60 and 80. In sets 11 and 12, and the corresponding sets with similar inner area drift, there are four subsets. In these, $\langle L \rangle$ is described qualitatively: there is a "high", "equal", "mid" and "low" value, and since drift is fixed within each set, D varies with $\langle L \rangle$; small $\langle L \rangle$, small D. The qualitative values, or rather, relative $\langle L \rangle$, indicate the value of $\langle L \rangle$ in relation to the target length. So, the high $\langle L \rangle$ is greater than the average length, equal $\langle L \rangle$ is around the target length, mid $\langle L \rangle$ is just under half the target length, and low $\langle L \rangle$ is approximately half of the mid value. For the actual values of $\langle L \rangle$, see the appendix tables (section E).

In the sets with the largest magnitude inner area drift (sets 13, 16 and 19), the high $\langle L \rangle$ is not achievable, since the large negative drift prevents reaching such values of $\langle L \rangle$; therefore, in those sets, there are only 3 subsets, with relative $\langle L \rangle$ of equal, mid and low. Note that even for the equal relative $\langle L \rangle$ in sets 13, 16 and 19, the value of $\langle L \rangle$ is not as great as for sets 11-12 and their corresponding sets (i.e, 14-15, and 17-18).

Recall that for each subset, there are 5 different values of T_p; thus, for the four-subset sets, there are 20 parameter combinations, and for the three-subset sets, 15. In examination of results, it is probably easiest to forget which set each dynamics combination comes from, and rather, bear in mind that each relevant parameter has been systematically varied; to place too

much emphasis on where each sub-set lies in terms of drift space and accuracy will only cause confusion.

C. RESULTS

I. Dynamics survey

Values for dynamics parameters were obtained from the literature and sorted according to magnitude (table I). For ease of comparison, the dynamics parameters found in chapter 3 are also in table I, highlighted. Reports of transitions to and from pausing are scarce, and are discussed in the text rather than entered into table I. Dynamics parameters definitions can be found in the terms list.

Table I. Values for dynamics parameters in the literature. Mean **v**alues for each parameter of microtubule dynamics are shown, sorted by increasing magnitude. Refer to key below table for details of notation. Highlighted values are results of previous chapter; the mean value for V_g and V_s is shown.

Parameter	Value	Cell/system	Methodology	Reference
Growth rate,	3.6	F, 1	Microinjection	1
	4.5 τ1	E, 2	Microinjection	8
V_g	4.9	E, 2	DIC	7
μm min^{-1}	5.32	E, 7	GFP-CLIP-170	NSC, outer
	6.37	E, 7	GFP-CLIP-170	NSC, inner
	6.8 τ2	E, 2	Microinjection	8
	7.05 †	X	Added tubulin	5
	7.2	E, 2	DIC	2
	7.9	E, 2	DIC	4
	9.2	F, 1	Microinjection	7
	9.3	X	Added tubulin	3
	11.5	E, 5	Microinjection	9
	11.5	E, 5	Stable GFP	9
	11.9	E, 3	Microinjection	6
	12.46	E, 7	GFP-CLIP-170	Ctrl, outer
	13.13	E, 7	GFP-CLIP-170	Ctrl, inner
	15.8	EI, 6	Microinjection, enucleation	10
	16.5	EI, 6	GFP-CLIP-170	10
	17.8	EI, 6	Microinjection, photobleach	10
	18.3	EI, 6	GFP-CLIP-170, enucleation	10
	18.5	EI, 6	Microinjection	11
	19.7	F, 4	Microinjection	6
	21.2 ‡	F, 4	Microinjection	6
	24.3	EI, 6	YFP-CLIP-170	11

Table I contd.

Parameter	Value	Cell/system	Methodology	Reference
Shrink rate, V_s μm min^{-1}	5.2	E, 2	Microinjection	8
	7.6	E, 2	Microinjection	8
	9.35 †	X	Added tubulin	5
	12.4	F, 1	Microinjection	7
	12.8	X	Added tubulin	3
	13.1	E, 5	Stable GFP	9
	14.3	E, 2	DIC	7
	14.8	E, 5	Microinjection	9
	17.3	E, 2	DIC	2
	19.8	E, 3	Microinjection	6
	21.1 ‡	F, 4	Microinjection	6
	22.34	E, 7	GFP-CLIP-170	Ctrl, inner
	24.46	E, 7	GFP-CLIP-170	Ctrl, outer
	28.8	El, 6	Microinjection	10
	30	El, 6	YFP-CLIP-170, microinjection	11
	32.2	F, 4	Microinjection	6
Catastrophe frequency, F_{cat} min^{-1}	0	E, 7	GFP-CLIP-170	NSC
	0.2	El, 6	Microinjection	12
	0.3 *φ1	El, 6	Microinjection, photobleach, enucleation	10
	0.3	El, 6	YFP-CLIP-170	11
	0.6 *ξ1	X	Added tubulin	3
	0.61	E, 2	Microinjection	8
	0.66 *ξ2	X	Added tubulin	5
	0.72 *ξ2	X	Added tubulin	5
	0.84 *	E, 2	DIC	2
	0.96 *	E, 2	DIC	7
	1.57	E, 2	Microinjection	8
	1.6 *	E, 5	Stable GFP	9
	1.9 *ξ1	X	Added tubulin	3
	1.91 *‡	F, 4	Microinjection	6
	1.98 *	F, 1	Microinjection	7
	2.1 *	E, 5	Microinjection	9
	3.246 *	E, 3	Microinjection	6
	3.636 *	F, 4	Microinjection	6
	4.8 *φ2	El, 6	Microinjection, photobleach, enucleation	10
	5.33	E, 7	GFP-CLIP-170	Ctrl, outer
	6.62	E, 7	GFP-CLIP-170	Ctrl, inner

Table I contd.

Parameter	Value	Cell/system	Methodology	Reference
Rescue frequency, F_{res} min^{-1}	0	E, 7	GFP-CLIP-170	NSC
	0.5 *ξ1	X	Added tubulin	3
	0.96 *ξ1	X	Added tubulin	3
	0.96 *ξ2	X	Added tubulin	5
	1.2 *ξ2	X	Added tubulin	5
	2.31	E, 2	Microinjection	8
	2.59	E, 2	Microinjection	8
	2.6 *	E, 2	DIC	2
	3.12 *	E, 2	DIC	7
	6 *	F, 1	Microinjection	7
	7.2 *	El, 6	Microinjection	10
	7.794 *	F, 4	Microinjection	6
	8.22 *‡	F, 4	Microinjection	6
	10	El, 6	YFP-CLIP-170, microinjection	11
	10.5 *	E, 5	Stable GFP	9
	11.77 *	E, 3	Microinjection	6
	12.00	E, 7	GFP-CLIP-170	Ctrl, inner
	13.09	E, 7	GFP-CLIP-170	Ctrl, outer

General key:
‡ = stable microtubule population
† = my average of experiment repeats
* = frequency recalculated to min^{-1}
ξ = Minimum and maximum values from experiment repeats (numbers denote experiments)
“ = “as above”
τ = Values for microtubules perpendicular (τ1) and parallel (τ2) to cell edge
φ = Values for cell interior (φ1) and periphery (φ2)

“Cell/system” key:
E: epithelial cell
F: fibroblast cell
X: *Xenopus* extract
El: epithelial-like

1: African Green Monkey (*Cercopithecus aethiops*) kidney (BSC1)
2: Newt (*Taricha granulosa*) lung
3: Rat Kangaroo (*Potorous tridactylis*) kidney (PtK1)
4: Chinese Hamster (*Cricetulus griseus*) ovary (CHO)
5: Pig (*Sus scrofa*) kidney (LLCPK-1)
6: Chinese Hamster (*Cricetulus griseus*) ovary sub-clone (CHO-K1)
7: Human retinal pigment epithelium (ARPE-19)

Table references:

1. Schulze and Kirschner (1986)
2. Cassimeris et al. (1988)
3. Belmont et al. (1990)
4. Hayden et al. (1990)
5. Verde et al. (1992)
6. Shelden and Wadsworth (1993)
7. Vasquez et al. (1997)
8. Waterman-Storer and Salmon (1997)
9. Rusan et al. (2001)
10. Komarova et al. (2002)
11. Komarova et al. (2009)

The values in the control condition for V_g, at 12.46 μm min^{-1} (mean) and 11.89 μm min^{-1} (median) for outer areas, and 13.13 μm min^{-1} (mean) and 12.57 μm min^{-1} (median) for inner areas, are comparable to those reported in the literature, being positioned approximately at the median position and above within the data. The Rac1-inhibited V_g is low in comparison; at 5.32 μm min^{-1} (mean) and 4.26 μm min^{-1} (median) for outer areas, and 6.37 μm min^{-1} (mean) and 5.00 μm min^{-1} (median) for inner areas, it is closest to the values reported for microtubules in Newt lung epithelial cells that were measured throughout the cell (4.9 μm min^{-1}) (Vasquez et al., 1997) or just for those growing perpendicular to the cell edge (4.5 μm min^{-1}) or parallel (6.8 μm min^{-1}) (Waterman-Storer and Salmon, 1997).

V_s for the Rac1-inhibition is not comparable to any reported in the literature; it is undefined in this condition. As was discussed in chapter 3, it is not probable that there really are no shrinking events in the Rac1-inhibited condition, and the effect of introducing shrinking episodes in the dynamics set for the Rac1-inhibited condition is explored below. However, in the control condition, values for V_s, at 24.46 μm min^{-1} (mean) and 25.63 μm min^{-1} (median) for outer areas and 22.34 μm min^{-1} (mean) and 22.59 μm min^{-1} (median) for inner areas, are toward the high end of reported values, with only shrinkage speeds in the Chinese Hamster ovary (CHO) cell line, between 28.8 μm min^{-1} (Komarova et al., 2002) and 32.2 μm min^{-1} (Shelden and Wadsworth, 1993) exceeding them.

The zero values for F_{cat} and F_{res} in the Rac1-inhibited condition are of course the lowest of all; no other zero values have been reported. The lowest values in the literature for F_{cat} are for microtubules in the inner areas of cells, at 0.2 min^{-1} (Komarova et al., 2009) and 0.3 min^{-1} (Komarova et al., 2009; Komarova et al., 2002). The lowest values in the literature for F_{res} are found in the *Xenopus* extract system; these range from 0.5 min^{-1} (Belmont et al., 1990) to 1.2 min^{-1} (Verde et al., 1992). Therefore, very low values of F_{cat} and F_{res} have been reported, but none so low as those found in the Rac1-inihibited condition. As mentioned, it may be that F_{cat} and F_{res} are not truly zero, and could indeed be just very low as in the *Xenopus* studies, and the low frequencies, combined with higher relative orientation between track segments, has hindered detection of shrinking events, and thus catastrophe and rescue, in plusTipTracker. Alternatively, these transitions could have values heavily in favour of one over the other; this is explored further below.

In the control condition, the values for F_{cat}, at 5.33 min^{-1} and 6.62 min^{-1} for outer and inner areas, respectively, and F_{res}, at 13.09 min^{-1} and 12.00 min^{-1} for outer and inner areas, respectively, are higher than any of those reported in the literature. As discussed in the methodology section, the "corrected" values (those which are quoted above) are likely to be an overestimate; however, these values will have to be used from a practical standpoint, because "biased" values for F_{res} (and also F_{p2g}) are the same as the corrected values. Moreover, it is likely that the biased values are an underestimate, so both figures have limitations.

Mimori-Kiyosue et al. (2005) have measured transitions to and from pausing in central and peripheral regions of the cell. The results of that study and the values determined for the transition frequencies F_{g2p} and F_{p2g} in chapter 3, i.e. the two that are obtainable with plusTipTracker, are shown in table II.

Table II. Transitions to and from pause compared. The dynamics measured in chapter 3 are compared to those of another study, (Mimori-Kiyosue et al., 2005).

Transition min^{-1}	**Chapter 3**				**Mimori-Kiyosue et al. (2005)**	
	Control		NSC			
	Outer	*Inner*	*Outer*	*Inner*	*Outer*	*Inner*
F_{g2p}	6.07	5.32	5.89	6.82	24.1	14.3
F_{p2g}	7.66	7.35	7.97	7.67	0.960	3.20
F_{s2p}	-	-	-	-	16.5	12.8
F_{p2s}	-	-	-	-	1.56	2.28

Comparing these transition frequencies, we see that those estimated for F_{g2p} by Mimori-Kiyosue et al. (2005) are large relative to those determined in chapter 3, for both areas in both conditions. The trend between areas is the same between that study and the control condition, however, with the outer area F_{g2p} being greater than that of the inner area; this is not the case for the Rac1-inhibited condition. For F_{p2g}, the values in Mimori-Kiyosue et al. (2005) are much more different between outer and inner areas compared to the values of chapter 3. In fact, the relationship between areas is reversed here for both conditions in the chapter 3 dynamics compared to Mimori-Kiyosue et al. (2005), with F_{p2g} being greater for the outer area in chapter 3 dynamics.

The values for F_{s2p} and F_{p2s} could not be determined with the methodology of chapter 3; however, for Mimori-Kiyosue et al. (2005), table II shows that F_{s2p} is elevated in outer areas relative to inner areas, and F_{p2s} is decreased in outer areas relative to inner areas. These area relationships preserve the relationships between areas for F_{g2p} and F_{p2s} reported by Mimori-Kiyosue et al. (2005): the transitions to pause are larger in outer areas compared to inner areas, and also greater than the transitions away from pause in the outer areas, which are both smaller for outer areas compared to inner areas.

II. Population measures

a. Two-state drift, average length and diffusion coefficient

To make comparison of microtubule dynamics easier, the drift, average length and diffusion coefficient were found for the dynamics sets reported in table I. In addition to these, as was done in chapter 3, the F_{cat}:F_{res} ratio can also be considered as an easy means of establishing the balance between the two. In order to compare the dynamics measured in the previous chapter with the literature, the two-state versions of the drift, average length and diffusion coefficient were calculated for these dynamics.

To compare literature dynamics with the Rac1-inhibited condition, where no catastrophes or rescues were detected, some values had to be specified for these transitions, and also for the shrinkage rate. Commonly, as table I shows, the shrinkage rate, V_s, is greater than the growth rate, V_g, and so, in this case, values for V_s were specified for each area in the Rac1-inhibited condition that gave the same V_g:V_s ratio of the same area in the control condition. Thus, in the Rac1-inhibited condition, V_s for outer areas was 9.18 μm min^{-1} and 8.99 μm min^{-1} for inner areas. These values are used for this condition hereafter. The three possibilities proposed for the values F_{cat} and F_{res} in this condition were encapsulated in three parameter sets (table III), where both are equal and low, and then each is alternately much greater than the other. Here, values were chosen that gave F_{cat}:F_{res} ratios of 0.1 (low F_{cat}, parameter set 2) and 10 (high F_{cat}, parameter set 3).

Table III. Values for F_{cat} and F_{res} in the Rac1-inhibited condition. Three different sets of values for these transition frequencies are tested.

Parameter set	F_{cat} min^{-1}	F_{res} min^{-1}	F_{cat}:F_{res}
A	0.1	0.1	1
B	1	10	0.1
C	10	1	10

The F_{cat} and F_{res} ratio, drift, average length and diffusion coefficient are presented in table IV. Predominantly, drift values are positive in the surveyed dynamics, indicating that in the majority of cases, microtubules are in the unbounded growth regime, continually increasing their length. In the cell, this presumably means that microtubules grow to the periphery of the cell, and then undergo some sort of cortex-mediated behaviour as modelled in the previous chapter, since we rarely observe microtubules that simply continue growing along the cortex; the role of Rac1 in this behaviour is of course a theme of this and other chapters.

On the matter of cortex-specific behaviour, the outer area in the control condition has greater positive drift than the control inner area, at 1.03 μm min^{-1} to 0.07 μm min^{-1}, which is perhaps contrary to what might be expected if it were the case that microtubule dynamics are modulated at the cell periphery to effectively stop microtubules and contribute to radiality, as the model in the previous chapter suggested would be required. The fact that this is a two-state simplification of a three-state dynamic set might bear upon this problem, and is

investigated in the next sub-section. With regard to area differences in the Rac1-inhibited condition, there is in fact much-reduced difference between areas relative to the control condition. This is true for the three dynamics sets (tables III-IV), so is probably not due to domination of the population measures by one particular dynamics parameter. Again, the role of simplification of this parameter set to two states is not clear.

Although the drift is sensitive to all of the two-state dynamics parameters, the role of the F_{cat}:F_{res} ratio in its contribution to drift is particularly well-demonstrated in table IV. Indeed, the drift increases from its most negative value of -7.96 μm min^{-1} in the outer area of the Rac1-inhibited condition (parameter set 3) at an F_{cat}:F_{res} ratio of 10, up to its maximum value of 22.72 μm min^{-1} in the inner areas of Chinese hamster ovary sub-clone cells (CHO-K1) (Komarova et al., 2009), at an F_{cat}:F_{res} ratio of 0.03; between these, the increases in drift and F_{cat}:F_{res} ratio are generally associated. Further evidence of the significant contribution of the F_{cat}:F_{res} ratio to drift is seen in the Rac1-inhibited parameter sets. The largest ratio (parameter set 3) provides the most negative drift, the intermediate ratio (set 1) a greater drift, and the smallest ratio (set 2) a positive drift.

Note that average length does not always increase with increasing drift. Certainly, the relationship between average length, drift and diffusion coefficient as discussed in chapter 4, is in evidence in table IV. For example, in the dynamics sets reported for the *Xenopus* extract (Belmont et al., 1990), we see that the average lengths do not increase with increasing drift; instead, of the three reported dynamics sets, the set with the intermediate drift has the greatest average length. This is reconciled by considering the diffusion coefficient; it is greatest for this intermediate set, at 123.77 μm^2 min^{-1} compared to 59.83 μm^2 min^{-1} (lowest drift) and 80.14 μm^2 min^{-1} (greatest drift), so the average length is greater as a result. What contributes to the increased length randomness in this particular case? Inspection of the dynamics parameters indicates that the set with the largest diffusion coefficient also has the greatest shrinkage rate, and although it has the lowest growth rate, it also has the lowest F_{cat} and joint-lowest F_{res}; the large V_s and small F_{cat} and F_{res} produce the greater D. The effect of lower transition frequencies on D is further illustrated by the Rac1-inhibited dynamics parameter sets; the lowest F_{cat} and F_{res} values (set 1) produce the greatest D.

Table IV. Dynamics parameters from literature survey with drift and average length. For studies surveyed previously (indicated by same number as in table I; see table references), the dynamics parameters are shown again, with the F_{cat}:F_{res} ratio also shown, along with the drift and average length. Positive drifts have undefined average lengths, indicated by a hyphen.

Study	V_g μm min^{-1}	V_s μm min^{-1}	F_{cat} min^{-1}	F_{res} min^{-1}	F_{cat}:F_{res}	Average length μm	Drift μm min^{-1}	Diffusion coefficient μm^2 min^{-1}
NSC outer 3	4.26	9.18	10	1	10.00	0.45	-7.96	3.56
NSC inner 3	5	8.99	10	1	10.00	0.53	-7.71	4.08
3	11.1	15.2	1.86	0.96	1.94	9.58	-6.25	59.83
3	8.5	16.6	0.6	0.54	1.11	26.28	-4.71	123.77
3	8.6	12.3	0.78	0.54	1.44	21.37	-3.75	80.14
NSC outer 1	4.26	9.18	0.1	0.1	1.00	79.46	-2.46	195.59
NSC inner 1	5	8.99	0.1	0.1	1.00	112.72	-1.99	224.64
10	17.8	28.8	4.8	7.2	0.67	50.86	-0.84	42.72
Ctrl inner	12.57	22.59	6.62	12.00	0.55	-	0.07	-
7	4.9	14.3	0.96	3.12	0.31	-	0.38	-
8	4.5	5.2	1.57	2.31	0.68	-	0.58	-
5	6.5	9.3	0.72	1.2	0.60	-	0.58	-
5	7.6	9.4	0.66	0.96	0.69	-	0.67	-
Ctrl outer	11.89	25.63	5.33	13.09	0.41	-	1.03	-
2	7.2	17.3	0.84	2.6	0.32	-	1.22	-
NSC outer 2	4.26	9.18	1	10	0.10	-	3.04	-
6	19.7	32.2	3.636	7.794	0.47	-	3.19	-
NSC inner 2	5	8.99	1	10	0.10	-	3.73	-
7	9.2	12.4	1.98	6	0.33	-	3.84	-
8	6.8	7.6	0.61	2.59	0.24	-	4.06	-
6	11.9	19.8	3.246	11.77	0.28	-	5.05	-
9	11.5	14.8	2.1	12.2	0.17	-	7.64	-

Table IV contd.

Study	V_g μm min^{-1}	V_s μm min^{-1}	F_{cat} min^{-1}	F_{res} min^{-1}	F_{cat}:F_{res}	Average length μm	Drift μm min^{-1}	Diffusion coefficient μm^2 min^{-1}
9	11.5	13.1	1.6	10.5	0.15	-	8.25	-
6	21.2	21.1	1.91	8.22	0.23	-	13.22	-
10	17.8	28.8	0.3	7.2	0.04	-	15.94	-
11	18.5	30	0.2	10	0.02	-	17.55	-
11	24.3	30	0.3	10	0.03	-	22.72	-

Table references:

2. Cassimeris et al. (1988)
3. Belmont et al. (1990)
5. Verde et al. (1992)
6. Shelden and Wadsworth (1993)
7. Vasquez et al. (1997)
8. Waterman-Storer and Salmon (1997)
9. Rusan et al. (2001)
10. Komarova et al. (2002)
11. Komarova et al. (2009)

b. Three-state drift, average length and diffusion coefficient

Calculation of the three-state drift and average length requires that we have values for F_{s2p} and F_{p2s}, which were not obtainable with plusTipTracker. Earlier, the values for transitions to and from pause from another study were shown (Mimori-Kiyosue et al., 2005). Those values, for Fg2p and Fp2g, were found to be larger than those determined in chapter 3. It is difficult to estimate values for undetermined transition frequencies, however, pause time percentage, introduced in the previous chapter, can be compared between chapter 3 dynamics and literature-reported values. Therefore, by comparing the percentage time spent in pause and the other phases in the experiments to the times given in the literature, we can estimate values for these transition frequencies.

To elaborate, we can consider how the transition frequencies affect the times spent in the different phases. A diagram of this framework is shown in figure 1. Here, by comparing the proportion of time spent in each phase, we arrive at an idea of what values F_{s2p} and F_{p2s} might take. This rationale makes the assumption that pause time proportion will be similar between the experiments in the previous chapter and those being compared from the literature, which may not be valid in every case. However, this means of estimating values for the remaining dynamics parameters should at least provide an idea of how these transitions between the pausing and shrinking state affect the phase proportions, and also how these transition frequencies affect the population measures (investigated later).

In this view, we now consider the transition frequencies in relation to the phase time percentages. Note that these percentages, as the name suggests, refer to the total percentage of time spent in a phase, and not the average absolute time in a phase; the two measures can be very different. They are calculated according to equations in chapter 4. Each transition frequency appears twice in figure 1; each serves to increase one phase time and decrease another. Those which are unknown in the current situation have antagonistic effects on the time in shrinkage and in pause.

The phase time percentage values reported in the literature, along with the values found in the experiments of chapter 3, are shown in table V. Microtubules in both experimental conditions consistently spent less time in pause than previously reported pause times. The same is true for the time spent in the shrinking phase, while the growth phase proportion is over two-times greater than the average of literature values.

What do these differences mean for the dynamics parameters found with plusTipTracker in the chapter 3? Three questions become apparent; first of all, two related questions are: 1) is the discrepancy between phase proportions real? And 2) if so, what is the source of this discrepancy? The third question asks: what values must F_{s2p} and F_{p2s} take to correct these discrepancies?

Focussing on the first two questions, it is plausible that there is overestimation of time spent in the growth phase using plusTipTracker, because, as was touched upon in chapter 3, catastrophes are only recorded if they are followed by a rescue event, and growth to pause

events are only recorded if they are followed by a pause to grow event. Thus, we overestimate time in the growth phase, and underestimate shrinking and pausing time.

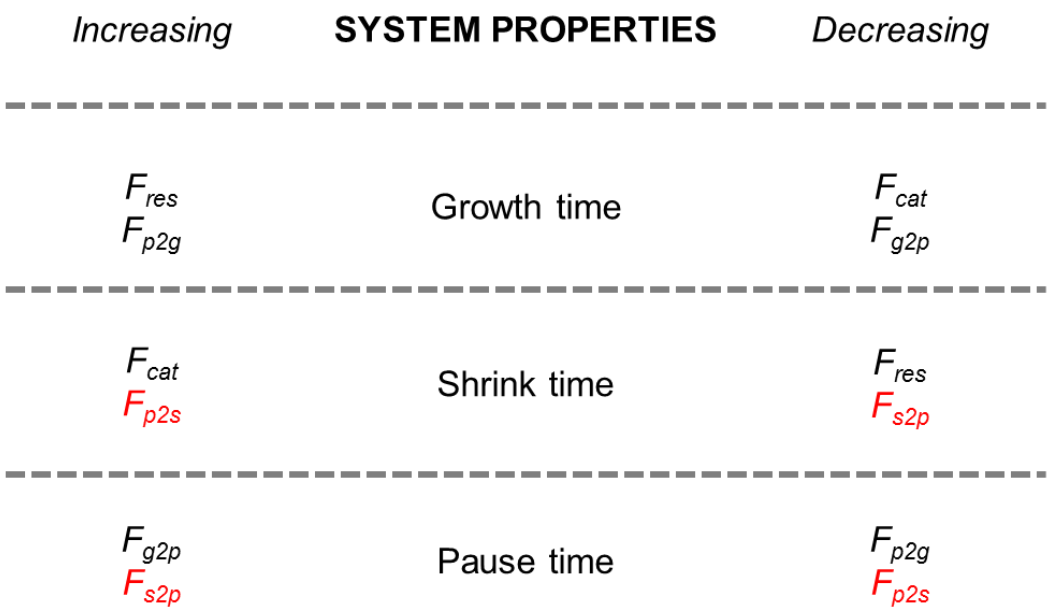

Figure 1. Diagram of relationship between transition frequencies and phase times. Phase time can be considered a "system property", emerging from the combination of transition frequencies, which either act to increase or decrease certain phase times. Transition frequencies shown in red are those that are unknown.

Table V. Phase time percentages for experimental and literature microtubule dynamics. The experimentally-determined and literature-reported proportions for each phase are shown.

Study	Grow	Shrink	Pause
Experimental			
Control outer	90.72	0.07	9.21
Control inner	91.29	0.13	8.58
NSC outer	94.87	0	5.13
NSC inner	95.47	0	4.53
Surveyed			
6	-	-	46.3
8	35.7	24.2	40.1
8	75.6	17.7	6.7
9	16.7	12.8	70.5
9	15	11.5	73.5
Average of surveyed	**36.35**	**19.92**	**43.72**

Table references:

6. Shelden and Wadsworth (1993)
8. Waterman-Storer and Salmon (1997)
9. Rusan et al. (2001)

However, it is also true that the calculation of the "corrected" transition frequencies is based only on the times in the growing phase where an event subsequently occurred. The estimation of transition frequencies is based only upon portions of the total time in a given phase. For transitions between growth and shrinkage, we use the time in growth preceding a catastrophe or the time in shrinkage preceding a rescue. For transitions between growth and pause, we use the time in growth preceding a growth to pause transition, or the time in pause preceding a pause to growth transition. Since these calculations are based only on intervals of the total phase times, it is likely that they are overestimated.

The fact that the dynamics parameters are calculated using only a portion of the time in growth, which is also only a portion of the time in that phase, and thus only a portion of the growth phase proportion reported in table V, complicates the issue. This is because it is likely that the measured proportion of time in growth will not correspond to the same measure calculated according to equations 10a-c, which are based on the dynamics parameters. Thus, although the discrepancy is real by the fact that there is a difference between the experimentally-measured value and those reported in the literature, it is likely that this value has been overestimated by the particular experimental methodology; this is the probable source of the discrepancy. Calculating the phase proportions by equations 10a-c will elucidate the matter, but the third question above, the matter of the choice of values for F_{p2s} and F_{s2p}, must be answered before this is done; a number of rationales are employed:

1. F_{s2p} and F_{p2s} are equal, and are small compared to other transition frequencies.
2. F_{s2p} and F_{p2s} are equal, and are of similar magnitude to other transition frequencies.
3. F_{s2p} and F_{p2s} are equal, and are large compared to other transition frequencies.
4. F_{s2p} and F_{p2s} take values equal to the transitions that go towards the phase that they leave, from the phase that they do not go towards; thus, $F_{s2p} = F_{cat}$, and $F_{p2s} = F_{g2p}$.
5. F_{s2p} and F_{p2s} take values equal to the transitions that go away from the phase they also go away from; thus, $F_{s2p} = F_{res}$, and $F_{p2s} = F_{p2g}$.
6. F_{s2p} and F_{p2s} take values equal to the transitions that go away from the phase they go to, to the phase they do not come from; thus, $F_{s2p} = F_{p2g}$, and $F_{p2s} = F_{res}$.

The different dynamics regimes produced following the rationales above are chosen so as to be able to study the effects of the systems nature of the microtubule dynamics sets. In this respect, it is important to bear in mind the relative values of the transition frequencies; it is this that drives the systemic nature of microtubule dynamics sets. Evidence of this is seen below.

In table VI, the predicted phase time percentages for the control condition are reported. These values are quite different to the measured phase proportions, and more similar to those reported in the literature. However, T_g is still larger and T_p smaller than the literature-reported average phase proportions. T_s, however, is now much more similar to the literature values; indeed, there is a dramatic increase in T_s when calculated according to equation 10b in comparison to the measured value. As a result of this increase, T_s is now actually generally greater than the average of the literature values, with the exception of the outer area dynamics in regime 5.

Because each transition frequency affects more than one system property (fig. 1) and these effectively emerge from the combination of transition frequencies, it is difficult to predict how changes in the transition frequencies will affect the phase time percentages. This is borne out by the fact that increasing and equal values of F_{s2p} and F_{p2s} produce increased time in shrinkage, and decreased time in pause. Why do increased and equal transitions to different phases not produce increased time in both? It is a manifestation of system dynamics: the differences in the other transition frequencies mean that similar increases between F_{s2p} and F_{p2s} will not have the same effect on the phases which they go towards.

It is also difficult to predict how changing F_{p2s} and F_{s2p} will affect the population properties. The drift and theoretical length are also given in table VI, and here, we can see that over the first 3 regimes, where F_{s2p} and F_{p2s} are equal but increase relative to the other transition frequencies, there is a decrease in the drift values for both areas. This being so, the theoretical average length also reduces. Interestingly, there is a qualitative change in the relationship between outer and inner areas as values of F_{s2p} and F_{p2s} increase in the first 3 regimes: first, the drift in outer areas is greater than inner areas, and is even unbounded where the inner area is bounded. The relationship remains the same at intermediate values of F_{s2p} and F_{p2s}, although the outer area is also now bounded, while in regime 3, the drift in the outer area is now less than that of the inner area, and the theoretical length is also. This is an example of how the system dynamics can produce effects that would be difficult to predict.

An important related note here is that the values for the undetermined transition frequencies have been kept the same here, so as just to study the effect of changing their value on the abstract measures. In the second part of this chapter, the effect of changing pausing time percentage in the inner area is investigated.

In the regimes where F_{s2p} and F_{p2s} use values of other transition frequencies, we see that regime 4 produces negative drift for both areas, but the theoretical length for the inner area is very large. This occurs without a large change in the phase times relative to the outer area; indeed, T_g is less in regime 4 for the inner area than the outer area. Regime 5 gives positive drift for both areas, with increased T_g in the outer area relative to the inner area, and regime 6 produces the greatest negative drift for both areas. Consequently, the theoretical lengths are the shortest here, too. In the outer area in regime 6, this large negative drift occurs with the highest growth phase time; however, there is also the lowest pause time percentage here, and indeed, regime 6 has the two greatest shrinking phase time percentages.

Incidentally, the data in table VI demonstrate the point made earlier that changing just F_{s2p} and F_{p2s} has the biggest effect on T_s and T_p, and little effect on T_g; changing these transition frequencies influences the times spent in T_s and T_p directly, but only influence T_g indirectly

Table VI. Phase proportions, drift and average length for the control experimental condition. For each dynamics regime, 1-6, discussed in the text, the values of F_{s2p} and F_{p2s} are shown with the population measures average length, drift and phase proportions. The experimentally-measured phase proportions, the average length and drift of the two-state treatment of the control condition dynamics and the averages of the literature-reported phase proportions are also shown for comparison.

Regime	Area	F_{s2p} min $^{-1}$	F_{p2s} min $^{-1}$	Average length μm	Drift μm min^{-1}	T_g	T_s	T_p
1	Outer	2.00	2.00	-	0.27	46.08	20.68	33.24
	Inner	2.00	2.00	61.07	-0.22	44.19	25.26	30.55
2	Outer	6.00	6.00	32.78	-0.38	46.65	22.67	30.68
	Inner	6.00	6.00	25.36	-0.46	44.41	26.15	29.45
3	Outer	18.00	18.00	11.63	-0.93	47.17	24.49	28.34
	Inner	18.00	18.00	15.40	-0.67	44.59	26.93	28.48
4	Outer	5.33	6.07	21.18	-0.60	46.85	23.37	29.78
	Inner	6.62	5.32	317.39	-0.04	44.04	24.61	31.35
5	Outer	13.09	7.66	-	0.68	45.74	19.49	34.77
	Inner	12.00	7.35	-	0.61	43.51	22.43	34.06
6	Outer	7.66	13.09	6.70	-1.81	48.07	27.66	24.27
	Inner	7.35	12.00	7.44	-1.54	45.45	30.48	24.07
Experimental *3-state*	**Outer**	-	-	-	-	**90.72**	**0.07**	**9.21**
	Inner	-	-	-	-	**91.29**	**0.13**	**8.58**
Theoretical *2-state*	**Outer**	-	-	-	**1.03**	-	-	-
	Inner	-	-	-	**0.07**	-	-	-
Survey average	-	-	-	-	-	**36.35**	**19.92**	**43.72**

Analysis like this helps to assess both the implications of the measured dynamics parameters, but it also helps to choose appropriate values for undetermined parameters. In table VI, there are some instances of combinations of parameters that produce theoretical lengths that would appear quite short, when compared to the dimensions of a cell; this is true for regime 6. The issue of theoretical average length in the inner area is addressed in the second part of this chapter. There are other cases where the theoretical average length is either undefined, due to unbounded growth, or the theoretical average length is very great. However, unbounded growth is often reported in the literature, as table IV showed, and an ever-growing microtubule array is usually posited to be "contained" by the cell.

The fact that, in a few cases, the outer area drift is larger than the inner area, suggests that these parameter values may not be appropriate for good cortical targeting in light of the results from the previous chapter. Furthermore, the phase time percentages, although different to the average of the surveyed data, are in the range of the values surveyed. As mentioned, the effect of pausing in the inner area is investigated later; in the previous chapter, we saw that greater pausing time percentage in the outer area produced better accuracy; at the values in table VI, accuracy increased relatively modestly (the largest increases in accuracy were at mch higher values of T_p).

Next, we must explore the parameters in the Rac1-inhibited condition. Recall that there are three proposed possibilities to account for the zero shrinking events in this condition: A) F_{cat} and F_{res} are both very small; B) F_{cat} is small relative to F_{res}, and C) F_{cat} is large relative to F_{res}. These possibilities can be assessed with similar means as those used for the control condition. First, using the same system of choosing F_{s2p} and F_{p2s} as in the control condition, the drift, theoretical length and phase times were found for the three different sets of values for F_{cat} and F_{res} (tables VII-IX).

In all cases in the Rac1-inhibited set A, drift is negative. In this set, while drift is relatively constant for A1-3, the theoretical average length decreases, and phase time percentages remain relatively similar between areas. However, in sets 4 and 5, the drift has much greater magnitude in both areas, and theoretical average length is small. In set 6, drift is at its smallest magnitude for both areas, and the difference between the area drifts is greatest here. In all case in the Rac1-inhibited set B, drift is positive, and thus the theoretical average length is undefined. In these sets, growth would be unbounded, and in light of the results from the previous chapter, we could expect very low accuracy in cortical targeting here. Thus, it is unlikely that these parameter values, where F_{res} is much greater than F_{cat}, are realistic. In Rac1-inhibited set C, again, drift is negative as in set A for all areas. However, theoretical average length is very low for all sets, as is T_g in comparison to some of the values in Rac1-inhibited A.

Table VII. Phase proportions, drift and average length for the Rac1-inhibited experimental condition, low F_{cat}, low F_{res} regime. For each F_{s2p} and F_{p2s} dynamics regime, 1-6, discussed in the text, the values of F_{s2p} and F_{p2s} are shown with the population measures average length, drift and phase proportions. The experimentally-measured phase proportions, the average length and drift of the two-state treatment of the Rac1-inhibited condition dynamics and the averages of the literature-reported phase proportions are also shown for comparison.

$F_{cat} = 0.1\ min^{-1}$; $F_{res} = 0.1\ min^{-1}$

Regime	Area	F_{s2p} min^{-1}	F_{p2s} min^{-1}	Average length µm	Drift µm min^{-1}	T_g	T_s	T_p
1	Outer	2.00	2.00	8.63	-1.52	40.06	30.22	29.73
	Inner	2.00	2.00	8.74	-1.61	35.89	32.15	31.96
2	Outer	6.00	6.00	4.28	-1.49	40.18	29.99	29.82
	Inner	6.00	6.00	4.29	-1.60	35.93	32.07	32.00
3	Outer	18.00	18.00	2.71	-1.47	40.23	29.92	29.86
	Inner	18.00	18.00	2.73	-1.59	35.95	32.04	32.02
4	Outer	1.00	5.89	1.68	-8.42	5.53	91.45	3.01
	Inner	1.00	6.82	1.55	-8.37	4.30	93.04	2.67
5	Outer	10.00	7.97	1.43	-8.55	4.59	93.13	2.28
	Inner	10.00	7.67	1.46	-8.41	4.00	93.61	2.39
6	Outer	7.97	5.89	9.89	-0.54	43.47	24.16	32.37
	Inner	7.67	6.82	5.02	-1.20	37.21	29.61	33.18
Experimental *3-state*	**Outer**	-	-	-	-	**94.87**	**0**	**5.13**
	Inner	-	-	-	-	**95.47**	**0**	**4.53**
Theoretical *2-state*	**Outer**	-	-	**79.46**	**-2.46**	-	-	-
	Inner	-	-	**112.72**	**-1.99**	-	-	-
Survey average	-	-	-	-	-	**36.35**	**19.92**	**43.72**

Table VIII. Phase proportions, drift and average length for the Rac1-inhibited experimental condition, low F_{cat}, high F_{res} regime. For each F_{s2p} and F_{p2s} dynamics regime, 1-6, discussed in the text, the values of F_{s2p} and F_{p2s} are shown with the population measures average length, drift and phase proportions. The experimentally-measured phase proportions, the average length and drift of the two-state treatment of the Rac1-inhibited condition dynamics and the averages of the literature-reported phase proportions are also shown for comparison.

$F_{cat} = 1\ min^{-1}$; $F_{res} = 10\ min^{-1}$

Regime	Area	F_{s2p} min^{-1}	F_{p2s} min^{-1}	Average length µm	Drift µm min^{-1}	T_g	T_s	T_p
1	Outer	2.00	2.00	-	2.13	55.05	10.35	34.60
	Inner	2.00	2.00	-	2.59	51.12	10.63	38.25
2	Outer	6.00	6.00	-	1.46	55.63	14.63	29.74
	Inner	6.00	6.00	-	1.78	51.85	15.49	32.66
3	Outer	18.00	18.00	-	0.94	56.14	18.38	25.47
	Inner	18.00	18.00	-	1.18	52.48	19.73	27.78
4	Outer	1.00	5.89	-	0.92	56.18	18.61	25.22
	Inner	1.00	6.82	-	1.01	52.68	21.06	26.25
5	Outer	10.00	7.97	-	1.46	55.63	14.63	29.74
	Inner	10.00	7.67	-	1.82	51.81	15.23	32.96
6	Outer	7.97	5.89	-	1.66	55.45	13.32	31.23
	Inner	7.67	6.82	-	1.78	51.85	15.53	32.62
Experimental *3-state*	**Outer**	-	-	-	-	**94.87**	**0**	**5.13**
	Inner	-	-	-	-	**95.47**	**0**	**4.53**
Theoretical *2-state*	**Outer**	-	-	-	**3.04**	-	-	-
	Inner	-	-	-	**3.73**	-	-	-
Survey average	-	-	-	-	-	**36.35**	**19.92**	**43.72**

Table IX. Phase proportions, drift and average length for the Rac1-inhibited experimental condition, high F_{cat}, low F_{res} regime. For each F_{s2p} and F_{p2s} dynamics regime, 1-6, discussed in the text, the values of F_{s2p} and F_{p2s} are shown with the population measures average length, drift and phase proportions. The experimentally-measured phase proportions, the average length and drift of the two-state treatment of the Rac1-inhibited condition dynamics and the averages of the literature-reported phase proportions are also shown for comparison.

$F_{cat} = 10\ min^{-1}$; $F_{res} = 1\ min^{-1}$

Regime	Area	F_{s2p} min^{-1}	F_{p2s} min^{-1}	Average length µm	Drift µm min^{-1}	T_g	T_s	T_p
1	Outer	2.00	2.00	0.43	-6.65	14.80	63.68	21.52
	Inner	2.00	2.00	0.50	-6.40	14.23	62.76	23.01
2	Outer	6.00	6.00	0.41	-5.68	18.28	51.78	29.94
	Inner	6.00	6.00	0.47	-5.47	17.30	51.48	31.22
3	Outer	18.00	18.00	0.39	-4.93	20.49	44.22	35.29
	Inner	18.00	18.00	0.45	-4.77	19.20	44.50	36.30
4	Outer	1.00	5.89	0.45	-4.47	21.68	40.15	38.18
	Inner	1.00	6.82	0.52	-4.47	19.93	41.83	38.25
5	Outer	10.00	7.97	0.35	-7.79	9.49	81.87	8.64
	Inner	10.00	7.67	0.40	-7.58	9.12	81.51	9.37
6	Outer	7.97	5.89	0.43	-5.03	20.19	45.22	34.59
	Inner	7.67	6.82	0.48	-5.11	18.30	47.79	33.91
Experimental *3-state*	**Outer**	-	-	-	-	**94.87**	**0**	**5.13**
	Inner	-	-	-	-	**95.47**	**0**	**4.53**
Theoretical *2-state*	**Outer**	-	-	-	**3.04**	-	-	-
	Inner	-	-	-	**3.73**	-	-	-
Survey average	-	-	-	-	-	**36.35**	**19.92**	**43.72**

Thus far, the dynamics obtained in chapter 3 have been compared to some of the dynamics reported in the literature, and various values have been proposed for the undetermined parameters based on these comparisons. Examination of how these parameters alter the abstract population measures for the measured dynamics sets has demonstrated that there is not a great difference between inner and outer areas, which, according to the previous chapter, is requisite for accurate cortical targeting. However, in chapter 3, the differences in microtubule organisation between unperturbed and Rac1-inhibited cells was presented, and there clearly is a difference in radiality between these microtubule networks. Aberrant modulation of microtubule dynamics at the cell periphery was put forward as a potential cause for this, but so far, it has been difficult to attribute the differences in organisation to any of the differences in dynamics between treatments and between areas within treatments. To better understand how the dynamics measured in chapter 3 affect cortical targeting accuracy, the rest of this chapter returns to a model.

III. A model of measured dynamics

a. Cortical targeting with measured dynamics

In the previous chapter, we saw that drift space is a large part of attaining good accuracy (fig. 2), and within quadrant 4 of drift space, where outer drift is negative and inner drift is positive, the two drift regimes combine to reduce the range in microtubule length, and this is concurrent with an increase in dynamicity. When pausing is introduced into the outer area with these dynamics combinations, the length range reduces as in the two-state simulations, but dynamicity is also reduced, and greater accuracy over the two state dynamics regimes is achieved.

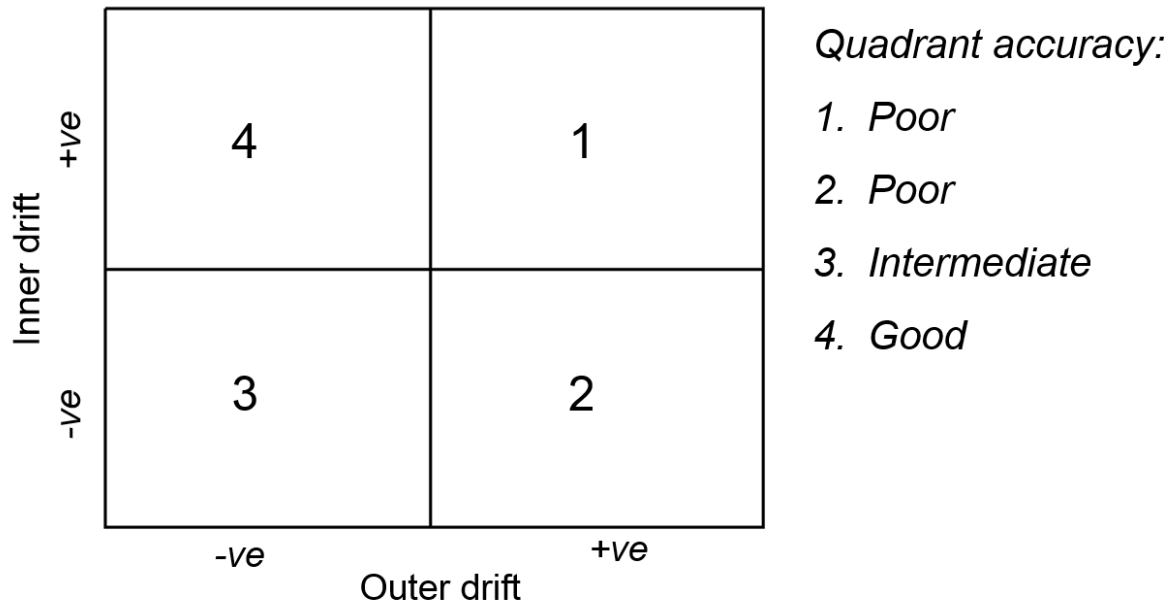

Figure 2. Drift space recap. Drift space is the combination of inner and outer drift, with numbered quadrants defining the particular combination. In chapter 4, the accuracy potential of each quadrant was determined.

In this section, the relevance of the findings with the model from chapter 4 to the dynamics measured in chapter 3 is considered. Firstly, in the control condition, the dynamics combinations that were specified in table VI earlier, where various values for the transitions to and from the pausing state where specified, are plotted in drift space in figure (3A). Similarly, the Rac1-inhibited condition dynamics (tables VII-IX) are plotted in drift space in figure (3B-D). The experimental dynamics for both the control and Rac1-inhibited condition are located in either quadrant 1 or 3 of drift space, with the exception of set 1 in the control condition, which is in quadrant 2. As discussed, quadrants 1 and 2 yield little or no accuracy in cortical targeting at all; however, quadrant 3 of drift space can produce increased levels of accuracy relative to quadrant 1; thus, dynamics combinations in quadrant 3 are investigated further here.

Although quadrant 3 was investigated in the first set of experiments, the effect of pausing in the inner area was not. If the applicability of experimentally-measured dynamics for cortical targeting are to be assessed, then an investigation of the effect of pausing in the inner area is necessary. However, the situation is complicated when there is negative inner area drift by the fact that $\langle L \rangle$ and D can both vary for the same drift value. For example, if drift is -5, D and $\langle L \rangle$ can be 25 $\mu m^2 \, min^{-1}$ and 5 μm or 100 $\mu m^2 \, min^{-1}$ and 20 μm.

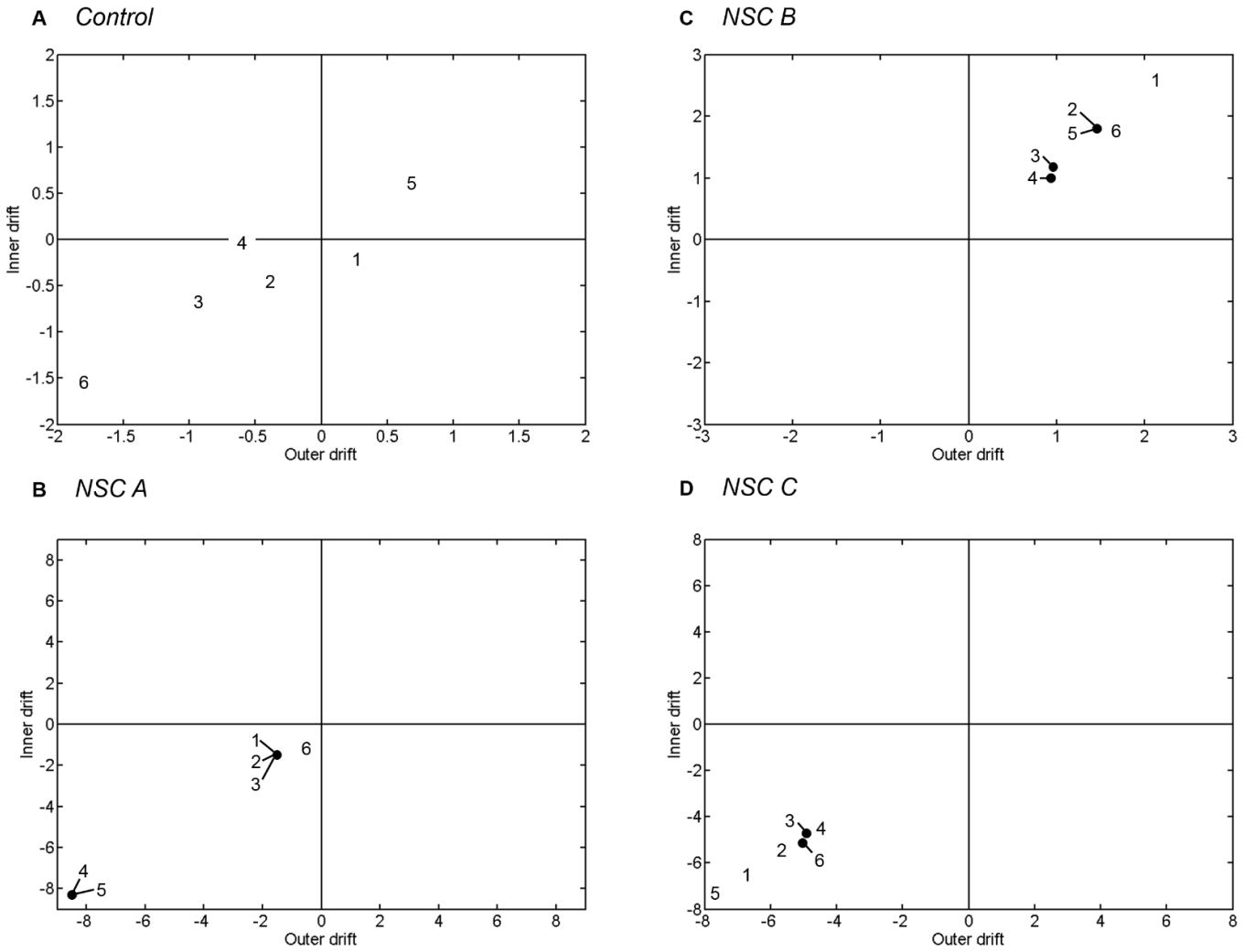

Figure 3. Experimental dynamics in drift space. The dynamics sets for experimentally-determined dynamics from chapter 3 are plotted in drift space. The numbers correspond to the different transition frequency values; where a line is drawn from a number to a dot, the dot represents the location. Drift units are μm min^{-1}.

The particular combinations of $\langle L \rangle$ and D for any given drift value are likely to be important because in a negative drift regime in the inner area, one could hypothesise that greater $\langle L \rangle$, and thus D, could be advantageous for cortical targeting because it might give the microtubules in the inner area more chance to reach the outer area. The fact that in the first set of experiments with dynamics sets 1-3, larger $\langle L \rangle$ gave rise to greater accuracy supports this notion.

For this reason, it would be difficult to investigate the dynamics sets from chapter 3 directly, since the theoretical average length is likely to be important in its relative magnitude compared to the cell size, or indeed, target length. Instead, the inner area negative drift, $\langle L \rangle$, and T_p can be systematically varied to determine how T_p and $\langle L \rangle$ affect cortical targeting accuracy for inner area negative drift regimes.

In these experiments, there are 3 principal dynamics sets, sets 11-13, which have inner area drifts of -0.56 μm min^{-1} (11), -2 μm min^{-1} (12), and -4.17 μm min^{-1} (13). Within these sets, $\langle L \rangle$ is varied in terms of its relative magnitude to the model cell size: in set 11, $\langle L \rangle$ starts at 80.54 μm and is lowest at 7.88 μm; in set 12, maximum $\langle L \rangle$ is 51.56 μm and minimum, 7.86 μm; in set 13, the greatest $\langle L \rangle$ is 30.56 μm and the smallest $\langle L \rangle$ is 7.79 μm. The reasoning for these values of $\langle L \rangle$ are that the greatest value is larger than the target length, the second value is similar to the target length, and the third and fourth values are progressively smaller. In sets 12 and 13, the greatest value of $\langle L \rangle$ cannot reach that attained in set 11, and in set 13, the largest $\langle L \rangle$ attainable is still smaller than the target length. This is due to the progressively larger negative drift in these sets. However, particular $\langle L \rangle$ values will still be comparable between the sets, allowing an investigation of the effect of negative drift. This relative length will be referred to as the relative theoretical average length, or relative $\langle L \rangle$.

Note that, because drift increases from set 11 to 13, for the values of $\langle L \rangle$ that are similar between sets, D is greater in the sets with larger negative drift. In addition to this, each $\langle L \rangle$ value in each set is run for five simulations with differing pause time percentage values: 10, 20, 40, 60 and 80. Moreover, each single combination of drift, $\langle L \rangle$ and T_p is repeated three times. Finally, outer drift is also varied to allow better exploration of drift space within quadrant 3, meaning that there are 2 more sets of 3 dynamics: sets 11-13 have an outer drift of -10.06 μm min^{-1}; sets 14-16 correspond to 11-13, but have an outer drift of -5.38 μm min^{-1}, and sets 17-19 again correspond to 11-13, but have an outer drift of -0.96 μm min^{-1}. Again, for a more detailed explanation of these dynamics sets, refer to section BII and the appendix tables (section E).

Firstly, we can consider how the theoretical average length of the inner area affects the accuracy of cortical targeting, in the different inner and outer area drift backgrounds; the results are plotted in figure 4. Here we see that for all negative inner area drift, increases in inner area $\langle L \rangle$ increase accuracy, as was hypothesised. Furthermore, increases in inner area T_p decrease accuracy for all inner and outer area drift combinations. The relationship between theoretical average length and accuracy is remarkably similar for all inner and outer area drift combinations, though note that at the combinations of the smallest inner and outer area negative drift values (fig. 4G), the accuracy levels off between the two largest values of

$\langle L \rangle$, which does not occur for the larger inner area negative drift dynamics sets at this outer area drift (fig. 4H and I).

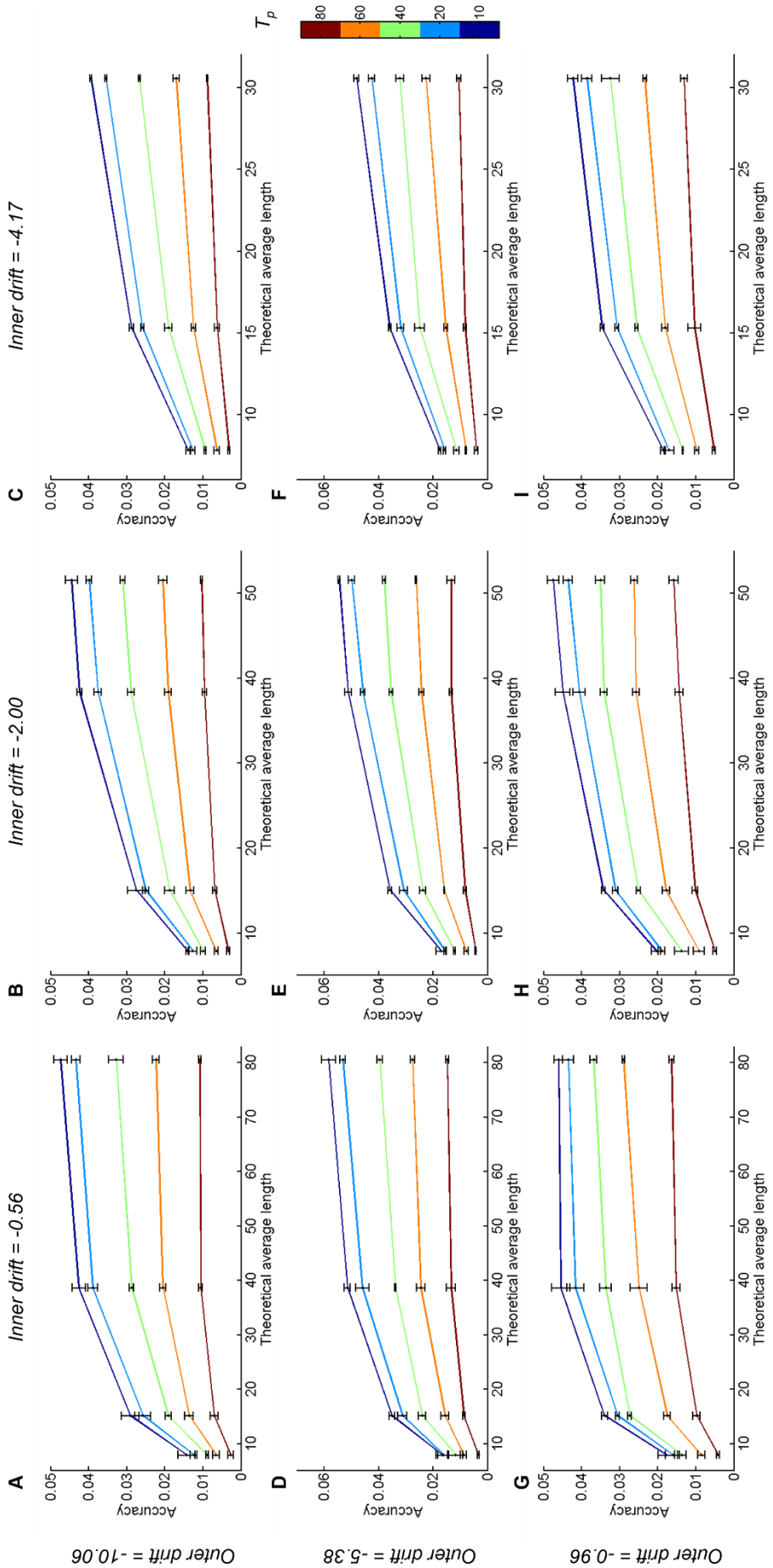

Figure 4. Accuracy and theoretical length for dynamics sets 11-19. Sets 11-19 have different inner and outer drift (refer to text), thus, for each combination of inner and outer drift (shown in italics: inner drift is columns; outer drift is rows), the accuracy as a function of theoretical inner area length is shown for the different pausing time percentages, T_p, indicated by the colour bar. Note the different y-axis scale for outer drifts of -5.38 (D, E and F). Drift units are µm min^{-1} and theoretical average length units are µm

The effect of T_p is more evident in figure 5. Here, we can see that for any combination of inner and outer area negative drift, and indeed for any $\langle L \rangle$, an increase in T_p results in a decrease in accuracy. Therefore, pausing in the inner area in a negative drift regime is adverse for accurate cortical targeting.

Having found that increased $\langle L \rangle$ and decreased T_p in a negative inner area drift regime produce more accurate cortical targeting, we can now consider more explicitly the effects of the magnitude of the negative inner and outer area drift on accuracy. Investigating this properly requires that the effects of T_p and $\langle L \rangle$ are taken into account. In figure 6, the accuracy is plotted as function of inner area drift, with each line corresponding to a particular $\langle L \rangle$ and rows and columns corresponding to outer area drift and T_p, respectively. Here we see that for any $\langle L \rangle$, T_p and outer area drift, changes in the inner area drift have very little effect on the accuracy of cortical targeting. Thus, where T_p and $\langle L \rangle$ have a clearly discernable effect on accuracy, inner area drift has very little influence on the accuracy.

Does outer area drift influence the accuracy? Shown in figure 7 is the accuracy plotted as a function of outer area drift, with each line again corresponding to a particular $\langle L \rangle$ and each column a particular T_p. Since outer area drift is now on the x-axis, inner area drift changes with the rows in figure 7. Unlike inner area drift, the outer area drift has a more interesting relationship with accuracy. At lower T_p values (up to and including T_p = 40) and equal to high relative $\langle L \rangle$, cortical targeting accuracy is at its greatest here for intermediate outer area drift. For higher T_p values and smaller relative $\langle L \rangle$, accuracy does not behave in a similar manner; instead, there is either a modest increase or similar values between intermediate and low magnitude outer area drift. In all cases, an intermediate outer area drift produces greater accuracy than the greatest magnitude outer area drift. This relationship between accuracy and outer area drift differs to the case in quadrant 4 of drift space, where accuracy increased with greater magnitude outer area negative drift.

That fact that the increase in accuracy as a function of outer area drift was marked for larger relative $\langle L \rangle$ than the smaller relative $\langle L \rangle$ suggested that a similar mechanism to that behind the poor accuracy in quadrants 3 and 4 in the first set of experiments with dynamics sets 1-3 was at work, where low magnitude negative outer drift effectively could not contain microtubules in the target area. To test this idea, the average lengths for the lowest T_p for each inner and outer area drift and relative $\langle L \rangle$ were found (fig. 8). Indeed, here we see that for all relative $\langle L \rangle$ and all inner area drift values, the average length undergoes a marked increase from the intermediate outer area drift value to the smallest magnitude outer area drift value. This increase, as would be expected, is greater for the high and equal relative $\langle L \rangle$ than for the mid and low relative $\langle L \rangle$. Therefore, the large increase in average length at low magnitude negative outer area drift is likely to be the reason that accuracy is lower at this outer area drift value compared to the intermediate outer area drift value; again, the low magnitude outer area drift cannot contain microtubules sufficiently.

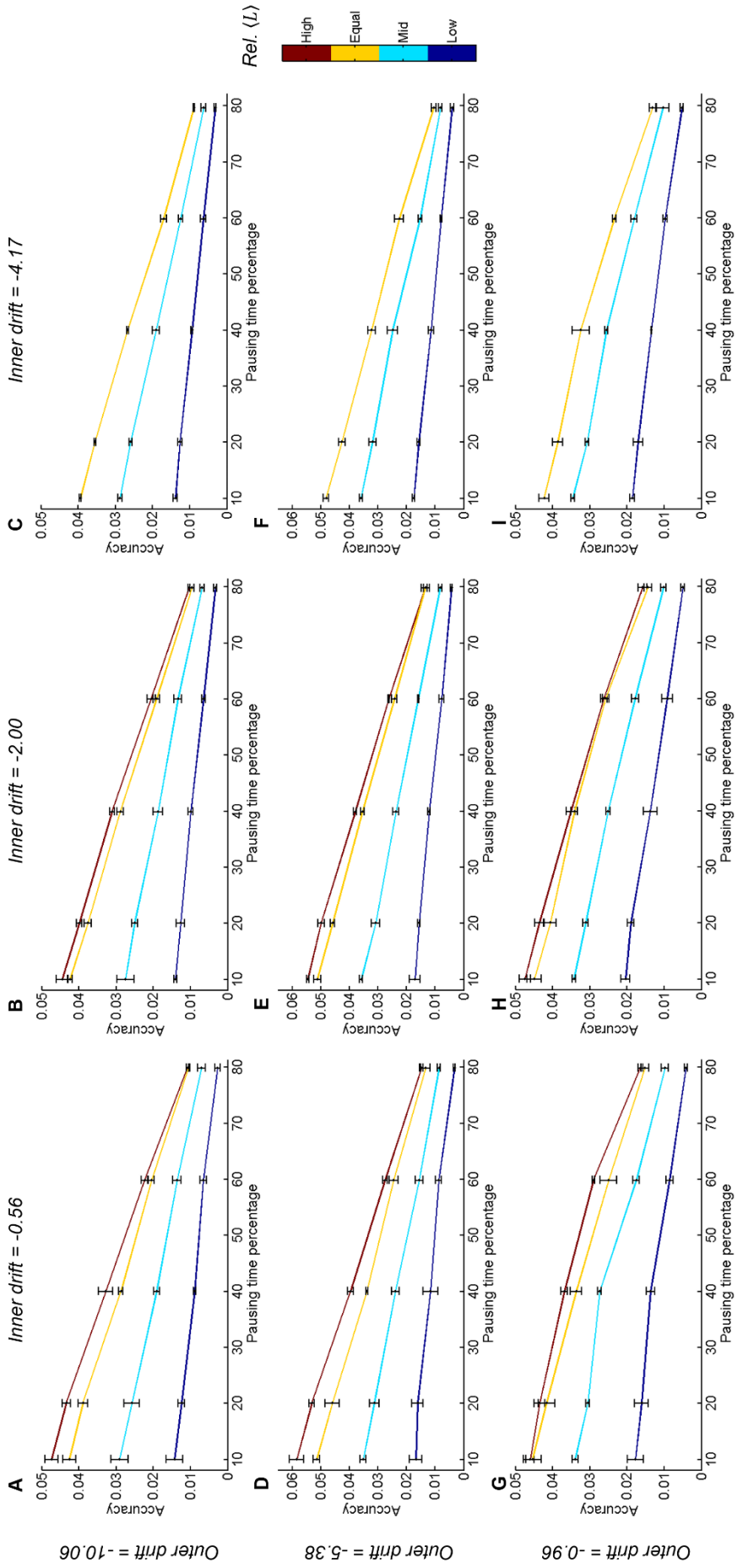

Figure 5. Accuracy and inner area pausing time percentage for dynamics sets 11-19. Each dynamics set has a fixed inner and outer drift, which are in columns and rows, respectively. Within each, relative length (rel. ⟨*L*⟩, see colour bar) and pausing time percentage vary. Thus, rel. ⟨*L*⟩ and pausing time percentage are indicated by colour and plotted on the x-axis, respectively.

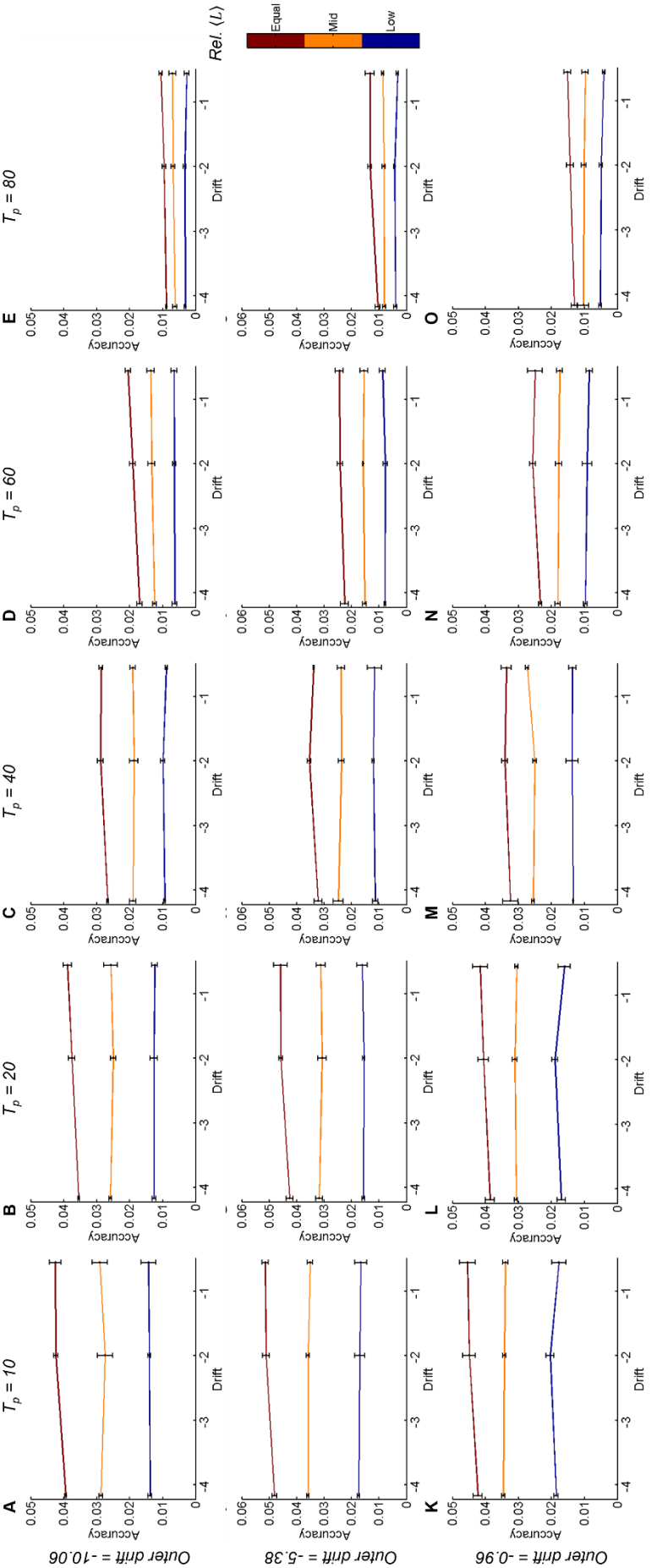

Figure 6. Accuracy and inner area drift for dynamics sets 11-19. Each dynamics set has a fixed inner area drift value; these are the three points plotted for each line in each plot, so in A, for example, the 3 point for the blue line correspond to set 11 at the smallest negative drift, set 12 at the middle drift, and set 13 at the largest negative drift; refer to text for more details. Each line corresponds to a common relative ⟨*L*⟩ (rel.⟨*L*⟩, see colour bar) between the sets, and the columns are for different pausing time percentage, T_p, values. The rows are for different outer area drift values. Drift units are μm min^{-1}

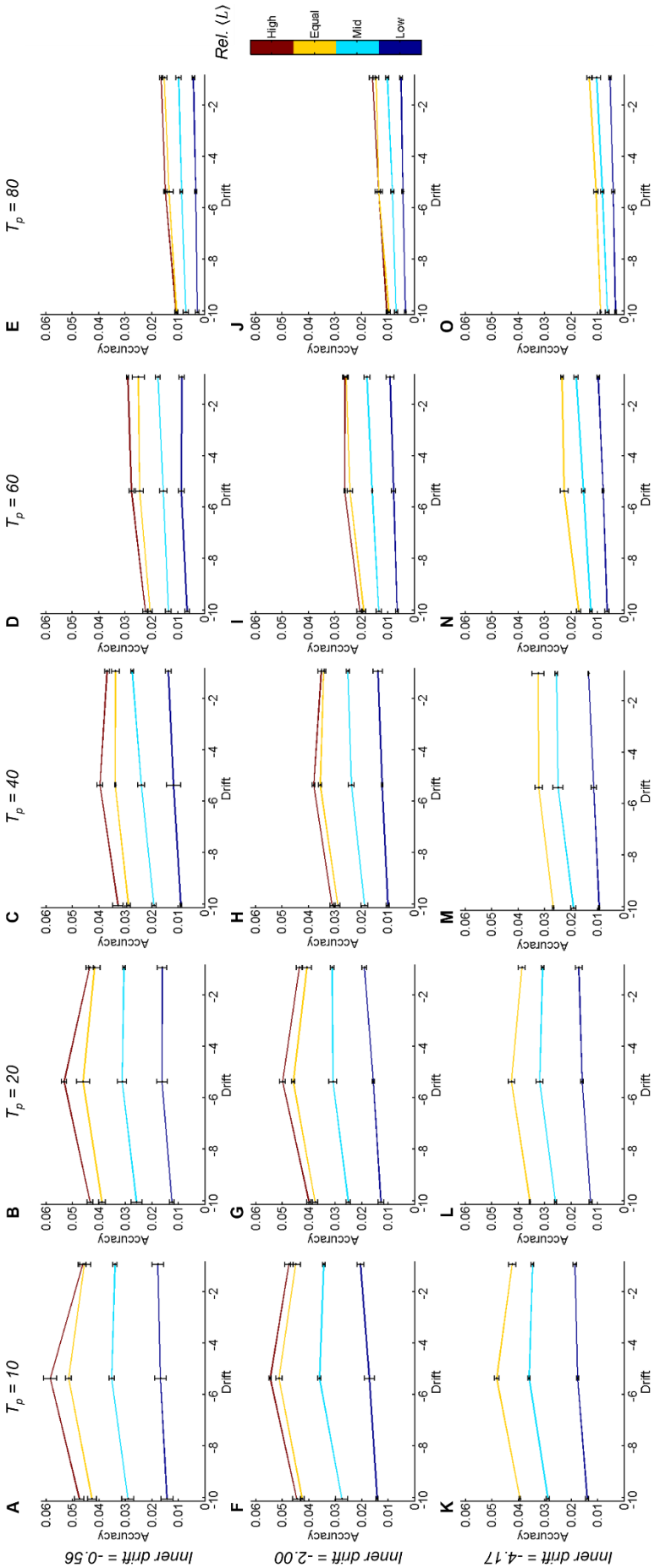

Figure 7. Accuracy and outer area drift in dynamics sets 11-19. Within each dynamics set, the relative theoretical length (rel. ⟨*L*⟩, see colour bar) and pause time percentage (T_p) was varied, and each rel. ⟨*L*⟩ and T_p was simulated with three different outer area negative drift values. Inner area drift is in rows, and Tp in columns, while rel. ⟨*L*⟩ is indicated by the colour of the line. Drift units are µm min^{-1}.

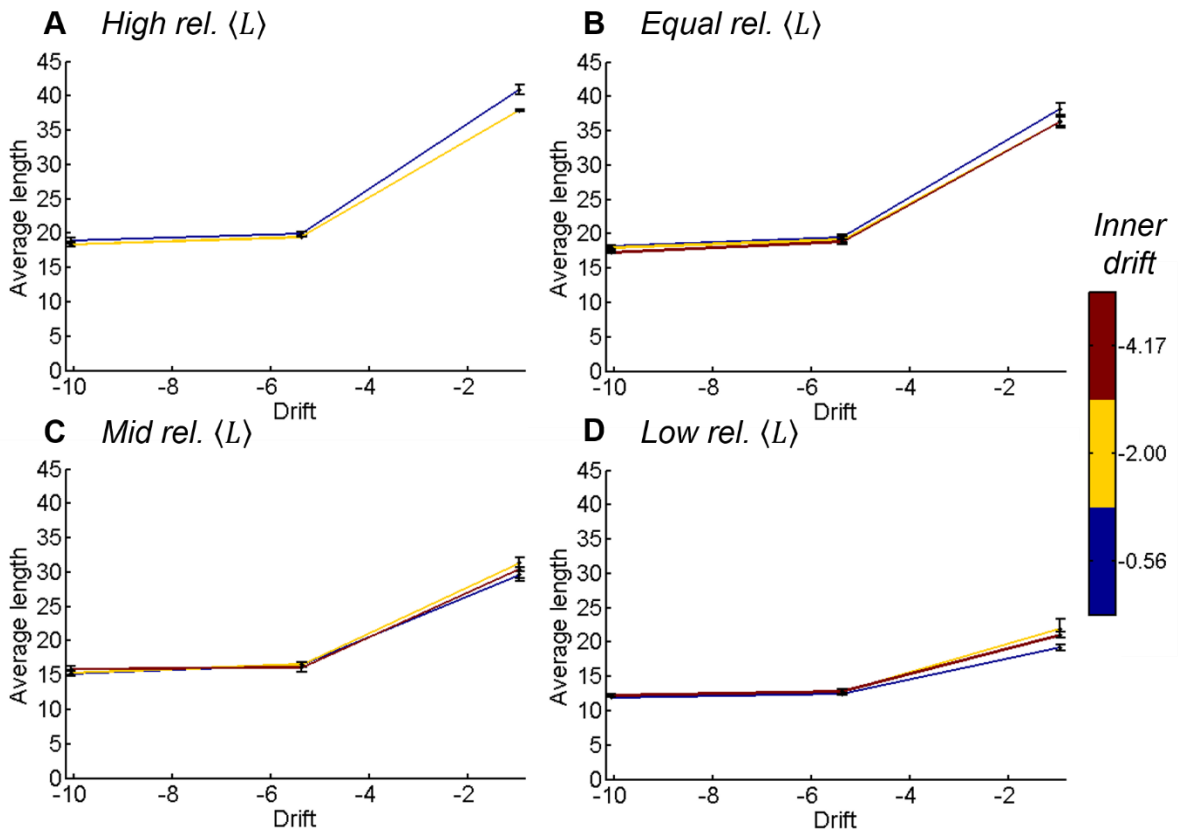

Figure 8. Average length for outer area drift regimes. For common relative theoretical lengths (rel. ⟨L⟩, i.e. high (A), equal (B), mid (C) and low (D) from different dynamics sets with different inner area drift values (indicated by colour; see colour bar) and different outer area drift values (plotted on the x-axis), the average length is shown. Average length units: μm; drift units, μm min^{-1}.

The results from negative inner and outer drift simulations indicate that accurate cortical targeting depends on the relative magnitude of the theoretical average length of the inner area compared to the size of the cell, and that the magnitude of the outer area drift also has an important role in determining accuracy. Interestingly, the magnitude of the inner area drift has little effect on accuracy; rather, theoretical average length and pausing time percentage are important determinants here. Note that, even though outer area drift can hinder accuracte targeting at high relative ⟨L⟩ for inner areas, the accuracy is always greater for higher relative ⟨L⟩ than for lower relative ⟨L⟩.

With these results in mind, we can discuss further the potential for accurate cortical targeting of the experimentally-measured dynamics sets. In figure 9, the inner area theoretical average lengths for the control and Rac1-inhibited conditions are shown. Of these, we see that the control dynamics condition has greater ⟨L⟩ in general, compared to the other condition sets. Sets 1 and 4 in the control condition have particularly large ⟨L⟩, while all sets in the Rac1-inhibited C condition (fig. 9C) have very low ⟨L⟩. Rac1-inhibited A sets have intermediate ⟨L⟩. In light of the model results, we can expect that higher accuracy could be achieved in the control sets compared to the Rac1-inhibited sets as a result of the larger ⟨L⟩.

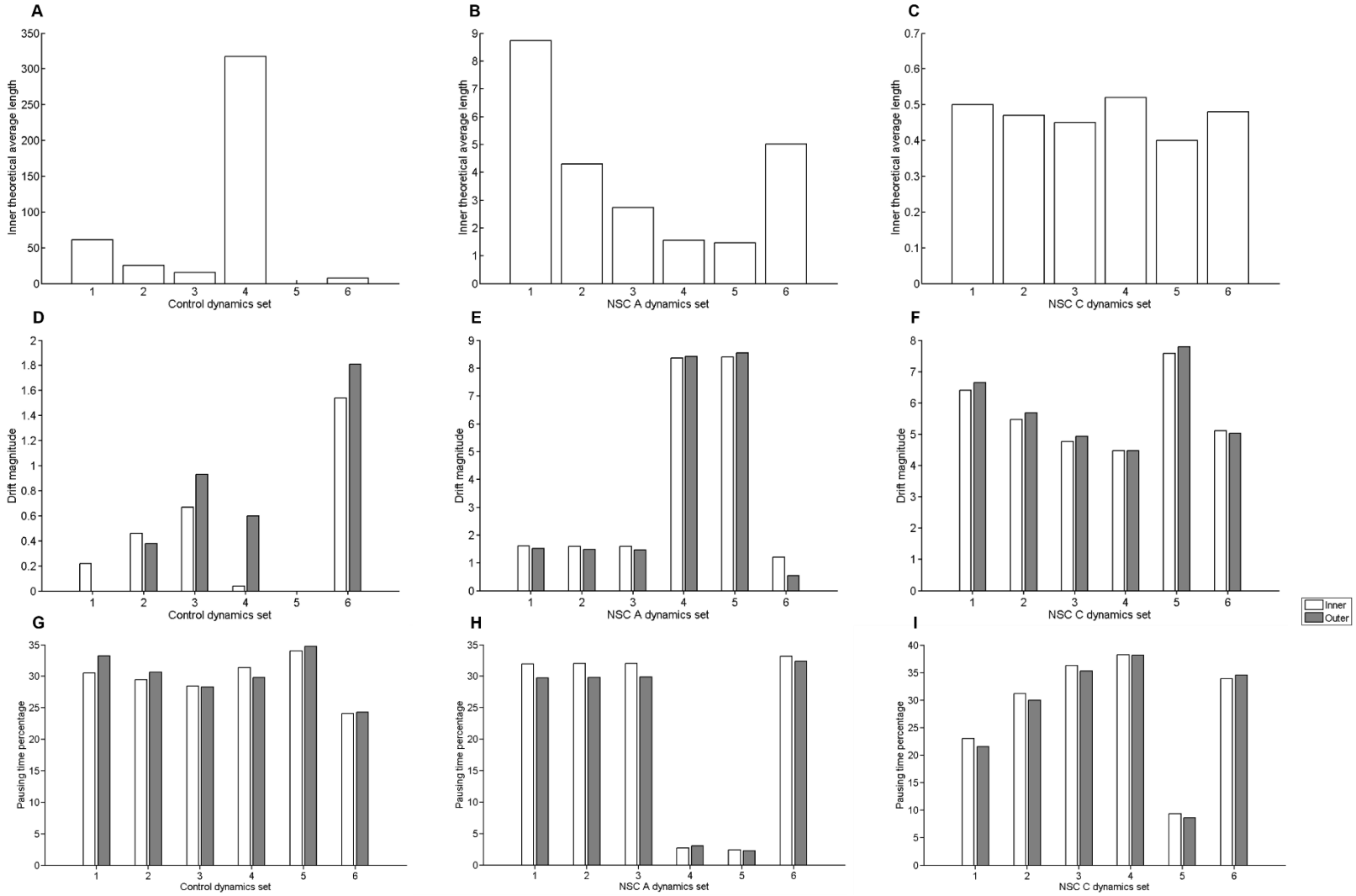

Figure 9. Inner area theoretical average length, inner and outer drift and pausing time percentages for experimental dynamics. For each of the experimental dynamics sets (1-6, on x-axis) in quadrant 3 of drift space, the inner area theoretical average length (A-C), the drift magnitudes both areas (D-F) and the pausing time percentage for both areas (G-I) is shown. Length units μm; drift units μm min^{-1}. Note that y-axes are different between plots.

However, as the modelling made clear, although $\langle L \rangle$ has an important role in dynamics regimes in quadrant 3 of drift space, the magnitude of the outer area negative drift is also important. The drift values for both areas are plotted as bar plots in figure 9D-F. Although control dynamics sets 1 and 4 had $\langle L \rangle$ values found to be good for cortical targeting in the model, these sets have positive outer drift (thus, it is not plotted in figure 9D) and low magnitude outer drift, respectively. As a result, cortical targeting accuracy is likely to be low in these cases, as it was found that negative outer drift of similar magnitude cannot maintain a low average length. In fact, all dynamics sets in the control condition have low magnitude outer area drift, apart from set 6 that has intermediate drift magnitude in both areas. However, this set may still yield low accuracy as a result of its low inner area theoretical average length of 7.44 μm (fig. 9A).

In the Rac1-inhibited condition, the combinations of inner area $\langle L \rangle$ and outer area drift magnitude generally are those found to be poor for cortical targeting accuracy. In Rac1-inhibited A, we see that for those sets that produce greater $\langle L \rangle$ in the inner area (fig. 9B), thus holding potential for good targeting, have low magnitude outer area drift (fig. 9E). Those sets that have high magnitude outer are drift have low $\langle L \rangle$ in the inner area. In Rac1-inhibited C, all inner area $\langle L \rangle$ are very small, but the drift magnitude in the outer area here are large.

Finally, the modelling suggested that pausing time is a significant factor of accurate cortical targeting. In the control dynamics sets, pausing time percentages are all quite similar, with set 6, which so far has the dynamics combinations most likely to produce accurate cortical targeting in light of the modelling, having the lowest values for both inner and outer areas. Indeed, earlier modelling suggested that increased *Tp* in the outer area was desirable for accurate cortical targeting, while the modelling in this chapter shows that decreased *Tp* in the inner area are better for accuracy. However, in the control condition, there are only small differences in the pausing time percentages. This may of course be an artefact of the fact that the two undetermined transition frequencies in chapter 3 both pertained to the pausing state.

As in the control condition, in the Rac1-inhibited condition A and C dynamics sets, inner and outer T_p are similar within each set. However, there is greater deviation between dynamics sets here in T_p, and again, this is likely to be an artefact of the undetermined transitions frequencies; in Rac1-inhibited A sets, both F_{cat} and F_{res} are low in comparison to the other transition frequencies, even when F_{p2s} and F_{s2p} are varied in magnitude but equal to each other (i.e. sets 1-3). Thus, in this case, variations in the latter two transition frequencies are unlikely to affect T_p to a great extent because they are always large; they do not affect the systems movement of microtubules through the three states. In sets 4 and 5, F_{s2p} takes on values of F_{cat} and F_{res}, respectively, and so T_p will be smaller here as a result of the small values of F_{cat} and F_{res}. Again, this is in evidence in set 5 of Rac1-inhibited C sets, where F_{cat} is large compared to F_{res}; here, in set 5 where F_{s2p} is equal to F_{res}, T_p is small.

Without a great difference in T_p between inner and outer dynamics sets, it is unlikely that pausing would play an instrumental role in targeting accuracy; it would hinder accuracy in the inner area and promote it in the outer area. However, note that in the control condition,

where theoretical average length was large, i.e. sets 1 and 4, and especially in set 4, where outer area negative drift is also relatively large, higher T_p here may aid targeting accuracy.

D. DISCUSSION

I. Chapter 3 dynamics in context

a. Comparisons of dynamics

The first part of this chapter was concerned with comparing microtubule dynamics, both as they are traditionally measured, i.e. in terms of transition frequencies and growth and shrinkage speeds, and by the abstract parameters used in chapter 4. The aim of this was to obtain an idea of how the measured dynamics compared with previous reports of microtubule dynamics. With the exception of the shrinking speed and F_{res} and F_{cat} in the Rac1-inhibited condition, the measured dynamics were comparable to previously-reported measurements of microtubule dynamics. The control condition F_{cat} and F_{res} were in fact the largest values of the survey, with the inner area F_{cat} being largest, and the outer area F_{res} being greatest. As was discussed in chapter 3, these values may be slightly overestimated, and thus the extent to which conclusive comparisons can be made here is limited. However, it is important that these transition frequencies were not so large as to appear unrealistic.

The surveyed dynamics were then compared by finding their abstract measures. There, most of the surveyed dynamics had positive drift, while the control condition, albeit with estimated F_{p2s} and F_{s2p}, had predominantly negative drift, and the Rac1-inhibited condition had negative drift for sets A and C, where F_{cat} was equal to and ten times greater than F_{res}, respectively, whereas Rac1-inhibited set B, where F_{res} was ten times greater than F_{cat}, had positive drift values more comparable to the surveyed dynamics. How can the differences in drift be explained? Just a glance at the drift values for the surveyed and measured dynamics shows that they are quite variable, but where many are positive and the measured sets are generally negative, a fundamental difference in the growth properties is evident. One difference between the measured and surveyed dynamics is the methodology; although some of the surveyed dynamics were based on tracking of +TIP proteins, none used plusTipTracker. In future work, comparisons of dynamics measured in this way will elucidate this matter. Other than methodology, reasons for the differences in drift are not clear.

b. Surveyed dynamics and microtubule organisation

To what extent can the comparisons described above contribute to our understanding of microtubule organisation? The rationale here is that changes in microtubule dynamics should underlie changes in microtubule organisation. With the exception of the *Xenopus* extract system (Belmont et al., 1990) and dynamics measured specifically at the cell periphery (Komarova et al., 2002), the drift was found to be positive for all surveyed dynamics. Although the drift values do vary from 0.38 μm min^{-1} (Vasquez et al., 1997) to 22.72 μm min^{-1} (Komarova et al., 2009), any positive drift value indicates continual growth. It can be argued that the consensus between microtubule growth characteristics is an indicator that microtubule arrays have similar systems properties, despite variations in cell type, cell line,

and dynamics measurement (which necessarily involves interfering with the cell in some way).

However, the question remains as to how radiality is attained in a microtubule dynamics regime where microtubules will on average grow continually. In this respect, the previous studies of microtubule dynamics at the cell periphery and in central areas are informative; these studies (Komarova et al., 2009; Komarova et al., 2002; Mimori-Kiyosue et al., 2005; van der Vaart et al., 2013) found that peripheral dynamics did differ to central dynamics, and the results of these four studies collectively suggest that microtubules are more likely to switch between states at a higher rate, grow more slowly, and spend more time in pausing at the cell periphery.

These results are consistent with the findings of the model in the previous chapter, but how do they compare to the results of chapter 3? The results of chapter 3 have been extensively analysed. If one takes the measured, not predicted, pausing time percentage that was originally reported in chapter 3 and is reproduced in table V, those times, at 9.21 and 8.58 for control outer and inner areas, respectively, and 5.13 and 4.53 for Rac1-inhibited outer and inner areas, respectively, are low compared to the surveyed times and also (for the outer area) the model predictions from the previous chapter. However, they do have the appropriate relationship between areas; the outer area is greater than the inner area, and although this is also true for the Rac1-inhibited condition, the values are both lower than the control condition, and this suggests that one way in which Rac1-inhibited cells lose the radiality of their microtubules because they pause less frequently at the periphery.

The predicted pausing time percentages, however, do not generally differ by such an extent. One reason for this is that in order to calculate these values, the values of the two undetermined transition frequencies, F_{s2p} and F_{p2s}, had to be estimated based on comparison with other reports. With the exception of a few parameter values, the values chosen for F_{s2p} and F_{p2s} gave greater values of T_p that were more comparable to the reported values. Two points are of note following this: first, that the values for F_{s2p} and F_{p2s} were often of similar magnitude between the inner and outer areas, and secondly, although T_p with these F_{s2p} and F_{p2s} values were comparable to the literature, they were consistently lower. Therefore, perhaps further differences between the inner and outer area dynamics sets in the control and Rac1-inibited conditions lie in differences for these undetermined transition frequencies. Further experimental work to measure these is a future project.

II. Mechanisms of radiality

a. Comparison to previous modelling

In the previous chapter, it was noted that the accuracy of cortical targeting in quadrant 4 of drift space is better when $\langle L \rangle$ is small and large in outer and inner areas respectively, and this was explained by the fact that a smaller $\langle L \rangle$ will confine microtubules in a target area more effectively than a larger $\langle L \rangle$ for outer areas, and in inner areas, a larger $\langle L \rangle$ produces more microtubules that grow to the outer area. This explanation is supported by the results of this chapter where the three-state simulations in which negative inner drift regimes were explored

(i.e. sets 11-19). In these simulations, in the different negative inner drift regimes, the sub-sets of dynamics with a greater D and $\langle L \rangle$ always produced greater accuracy, regardless of the drift in either area.

Another interesting finding in this chapter is the fact that inner area drift had little effect on the accuracy of cortical targeting, and indeed, $\langle L \rangle$, T_p and outer area drift were found to have more of an effect on cortical targeting accuracy than inner area drift, which is not what might have been expected given the results of the previous chapter, where drift, albeit more for the outer area, was found to be so important. This is not to say that drift space is rendered invalid; rather, it still represents a useful framework for considering dynamics combinations between areas, and as stated when it was introduced, it is a guide, and actual accuracy is determined by the specific combination of the abstract parameters.

b. Radiality for measured dynamics

The model has been used to identify the mechanisms of cortical targeting, but is it able to explain the differences in the organisation of control and Rac1-inibited cells that were documented at the beginning of chapter 3? Control, unperturbed cells have good radiality; microtubules generally approach the cell cortex at perpendicular relative orientations, and in Rac1-inhibited cells, this radiality is lost. Both experimental conditions have dynamics regimes located in similar quadrants of drift space. Because two of these quadrants were found to produce poor accuracy, they were not investigated further, but the quadrant where both inner and outer drift are negative was found to produce reasonable accuracy, so the dynamics sets that were located there were investigated.

It is apparent that the control condition certainly has more suitable dynamics regimes in terms of theoretical average length; model simulations found that for high and equal relative theoretical average length in the inner area, accuracy was improved, so long as this was accompanied by negative outer drift of appropriate magnitude. Only one of the control dynamics sets had outer drift of an appropriate magnitude, but in this set, inner theoretical average length was quite low.

Related to this is the fact that in the Rac1-inhibited condition, all theoretical average lengths were found to be small in the set that gave most relevant drift combinations, set A, but that Rac1-inhibited cells are in general smaller than unperturbed cells. Previously, a link between microtubule dynamics and cell size has been postulated by Picone et al. (2010), so further investigation here might prove fruitful. Of course, this would probably require use of micropatterning technology as in Picone et al. (2010) to control for variations in cell shape.

Perhaps one of the most interesting features of the analysis of the experimentally-determined dynamics is that the control condition dynamics sets generally had a greater difference between the magnitude of inner and outer area negative drift. Indeed, the mean absolute difference between the inner and outer area drift values for dynamics sets was 0.29 $\mu m\ min^{-1}$ compared to 0.20 $\mu m\ min^{-1}$ and 0.15 $\mu m\ min^{-1}$ for Rac1-inhibited condition A and C sets. Although some of the differences in inner and outer area drift are what could be considered the wrong way around in light of the modelling, i.e. positive outer drift and negative inner

drift, the fact that there is a greater difference between the two areas in the Rac1-inhibited condition hints that Rac1 could function to co-ordinate dynamics between inner and outer areas.

III. Modelling for measured dynamics

a. Model evaluation

After testing general mechanisms for targeting, the experimentally-measured dynamics were examined. Because it was apparent that average theoretical length in the inner area may have had a role in cortical targeting, and modelling verified this, the experimentally-measured dynamics sets could not be directly modelled. However, dynamics sets that were similar to these, but for which the theoretical average length was controlled, were used to investigate cortical targeting accuracy in dynamics regimes similar to that of the experimentally-measured dynamics. Thus, this is a legitimate methodology; controlling for otherwise undetermined but important parameters of the model.

b. Model extensions

As discussed in the previous chapter, an interesting extension of the model would be to consider the effect of the residence time of a microtubule in the target area on cortical capture. Following on from this, it may be that the accuracy values found in simulations of dynamics regimes in quadrant 3 of drift space, which seem low if this type of mechanism was to contribute to radiality with these dynamics regimes, might actually generate reasonable accuracy if it were combined with other mechanisms, such as cortical capture. Another interesting experiment would therefore be determination of the relative times spent in target areas for the different regimes.

E. APPENDICES

Table X. Dynamics sets 11-19. Each sub-set within each dynamics set is shown, denoted by the letters in the "set" column. For each set, the outer area drift is also shown. The abstract measures theoretical average length, $\langle L \rangle$, drift, V, diffusion coefficient, D are shown for each dynamics sub-set. Note that they repeat, so, for example, the only difference between sets 11 and 14 is the outer area drift. Also note that for each dynamics sub-set (i.e. each table row), five values for the pausing time percentage were used: 10, 20, 40, 60 and 80. Thus each row represents 5 different parameter sets. Units: V, μm min^{-1}, $\langle L \rangle$, μm, and D, μm^2 min^{-1}.

Set	V	$\langle L \rangle$	D
Set 11, outer area drift = -10.06			
a	-0.56	80.54	44.75
b	-0.56	38.63	21.46
c	-0.56	15.09	8.38
d	0.56	7.88	4.38
Set 12, outer area drift = -10.06			
a	-2	51.56	103.13
b	-2	38.37	76.74
c	-2	15.00	30.00
d	-2	7.86	15.71
Set 13, outer area drift = -10.06			
a	-4.17	30.56	127.34
b	-4.17	15.31	63.81
c	-4.17	7.79	32.44
Set 14, outer area drift = -5.38			
a	-0.56	80.54	44.75
b	-0.56	38.63	21.46
c	-0.56	15.09	8.38
d	0.56	7.88	4.38
Set 15, outer area drift = -5.38			
a	-2	51.56	103.13
b	-2	38.37	76.74
c	-2	15.00	30.00
d	-2	7.86	15.71

Table X, contd.

Set 16, outer area drift = -5.38			
a	-4.17	30.56	127.34
b	-4.17	15.31	63.81
c	-4.17	7.79	32.44
Set 17, outer area drift = -0.96			
a	-0.56	80.54	44.75
b	-0.56	38.63	21.46
c	-0.56	15.09	8.38
d	0.56	7.88	4.38
Set 18, outer area drift = -0.96			
a	-2	51.56	103.13
b	-2	38.37	76.74
c	-2	15.00	30.00
d	-2	7.86	15.71
Set 19, outer area drift = -0.96			
a	-4.17	30.56	127.34
b	-4.17	15.31	63.81
c	-4.17	7.79	32.44

REFERENCES

Belmont, L.D., A.A. Hyman, K.E. Sawin, and T.J. Mitchison. 1990. Real-time visualization of cell cycle-dependent changes in microtubule dynamics in cytoplasmic extracts. *Cell*. 62:579-589.

Cassimeris, L., N.K. Pryer, and E.D. Salmon. 1988. Real-time observations of microtubule dynamic instability in living cells. *The Journal of cell biology*. 107:2223-2231.

Hayden, J.H., S.S. Bowser, and C.L. Rieder. 1990. Kinetochores capture astral microtubules during chromosome attachment to the mitotic spindle: direct visualization in live newt lung cells. *The Journal of cell biology*. 111:1039-1045.

Komarova, Y., C.O. De Groot, I. Grigoriev, S.M. Gouveia, E.L. Munteanu, J.M. Schober, S. Honnappa, R.M. Buey, C.C. Hoogenraad, M. Dogterom, G.G. Borisy, M.O. Steinmetz, and A. Akhmanova. 2009. Mammalian end binding proteins control persistent microtubule growth. *The Journal of cell biology*. 184:691-706.

Komarova, Y.A., I.A. Vorobjev, and G.G. Borisy. 2002. Life cycle of MTs: persistent growth in the cell interior, asymmetric transition frequencies and effects of the cell boundary. *Journal of cell science*. 115:3527-3539.

Mimori-Kiyosue, Y., I. Grigoriev, G. Lansbergen, H. Sasaki, C. Matsui, F. Severin, N. Galjart, F. Grosveld, I. Vorobjev, S. Tsukita, and A. Akhmanova. 2005. CLASP1 and CLASP2 bind to EB1 and regulate microtubule plus-end dynamics at the cell cortex. *The Journal of cell biology*. 168:141-153.

Picone, R., X. Ren, K.D. Ivanovitch, J.D. Clarke, R.A. McKendry, and B. Baum. 2010. A polarised population of dynamic microtubules mediates homeostatic length control in animal cells. *PLoS biology*. 8:e1000542.

Rusan, N.M., C.J. Fagerstrom, A.M. Yvon, and P. Wadsworth. 2001. Cell cycle-dependent changes in microtubule dynamics in living cells expressing green fluorescent protein-alpha tubulin. *Molecular biology of the cell*. 12:971-980.

Schulze, E., and M. Kirschner. 1986. Microtubule dynamics in interphase cells. *The Journal of cell biology*. 102:1020-1031.

Shelden, E., and P. Wadsworth. 1993. Observation and quantification of individual microtubule behavior in vivo: microtubule dynamics are cell-type specific. *The Journal of cell biology*. 120:935-945.

van der Vaart, B., W.E. van Riel, H. Doodhi, J.T. Kevenaar, E.A. Katrukha, L. Gumy, B.P. Bouchet, I. Grigoriev, S.A. Spangler, K.L. Yu, P.S. Wulf, J. Wu, G. Lansbergen, E.Y. van Battum, R.J. Pasterkamp, Y. Mimori-Kiyosue, J. Demmers, N. Olieric, I.V. Maly, C.C. Hoogenraad, and A. Akhmanova. 2013. CFEOM1-associated kinesin KIF21A is a cortical microtubule growth inhibitor. *Developmental cell*. 27:145-160.

Vasquez, R.J., B. Howell, A.M. Yvon, P. Wadsworth, and L. Cassimeris. 1997. Nanomolar concentrations of nocodazole alter microtubule dynamic instability in vivo and in vitro. *Molecular biology of the cell*. 8:973-985.

Verde, F., M. Dogterom, E. Stelzer, E. Karsenti, and S. Leibler. 1992. Control of microtubule dynamics and length by cyclin A- and cyclin B-dependent kinases in Xenopus egg extracts. *The Journal of cell biology*. 118:1097-1108.

Waterman-Storer, C.M., and E.D. Salmon. 1997. Actomyosin-based retrograde flow of microtubules in the lamella of migrating epithelial cells influences microtubule dynamic instability and turnover and is associated with microtubule breakage and treadmilling. *The Journal of cell biology*. 139:417-434.

Chapter 6
Frequency-based quantification of microtubule organisation

A. FREQUENCY-BASED ORGANISATION QUANTIFICATION: WHAT FOR?

I. Rationale

a. Organisational features hitherto unquantified

Since the microtubule cytoskeleton is so important for cellular organisation, its organisation, in turn, is also very important. Thus it comes as no surprise that there are a vast number of ways in which the organisation of the microtubule network can be modulated in the cell, as discussed in chapter 2. Previously in this thesis, we saw that changing microtubule dynamics parameters influenced the organisation of the network, and that other factors, such as cell boundaries, also influence the organisation of the array. Thus it is clear that microtubule dynamics, which by definition determine microtubule behaviour through time and space, are a major determinant of the organisation of the array. In some cases, however, microtubule organisation is dependent on more than just the length distribution of its individuals. Such cases include certain spatial properties, such as the orientation, alignment, and bending of microtubules. Indeed, chapter 3 established that there is a difference in microtubule bending between control and Rac1-inhibited cells. The diagrams in figure 1 demonstrate these concepts, and they are expanded upon in table I, which gives the "parameters" of the different features of organisation. Some of these parameters will be used later on in this chapter.

A means of quantitatively describing the organisation of the microtubule cytoskeleton in other terms, that reflect these organisational features, should be helpful. In this chapter, I address this problem for two of these: orientation and alignment. Before proposing a method for quantification of these types of organisational features, I will first elaborate on why these organisation features have important functional consequences for the cell, and why they might make useful organisational metrics. Where applicable, I will also review previous attempts at quantification.

Table I. Features of microtubule organisation. Various important properties of microtubule organisation are shown, with details and parameters. Shaded areas are those investigated here.

Feature	Details	Parameter(s)	
Length	Distribution of microtubule lengths	Type of distribution Distribution-specific parameters	
Alignment	Distribution of orientations of individual microtubules	*Normally distributed* Mean Standard deviation	*Uniformly distributed* Orientation range
Orientation	Predominant orientation of microtubule population	Circular mean of orientation	
Spacing	Distance between principal axes of individual microtubules	Mean distance Variance of distance	
Bending	Mode(s) of bending of individual microtubules	Number of modes Amplitudes of modes	

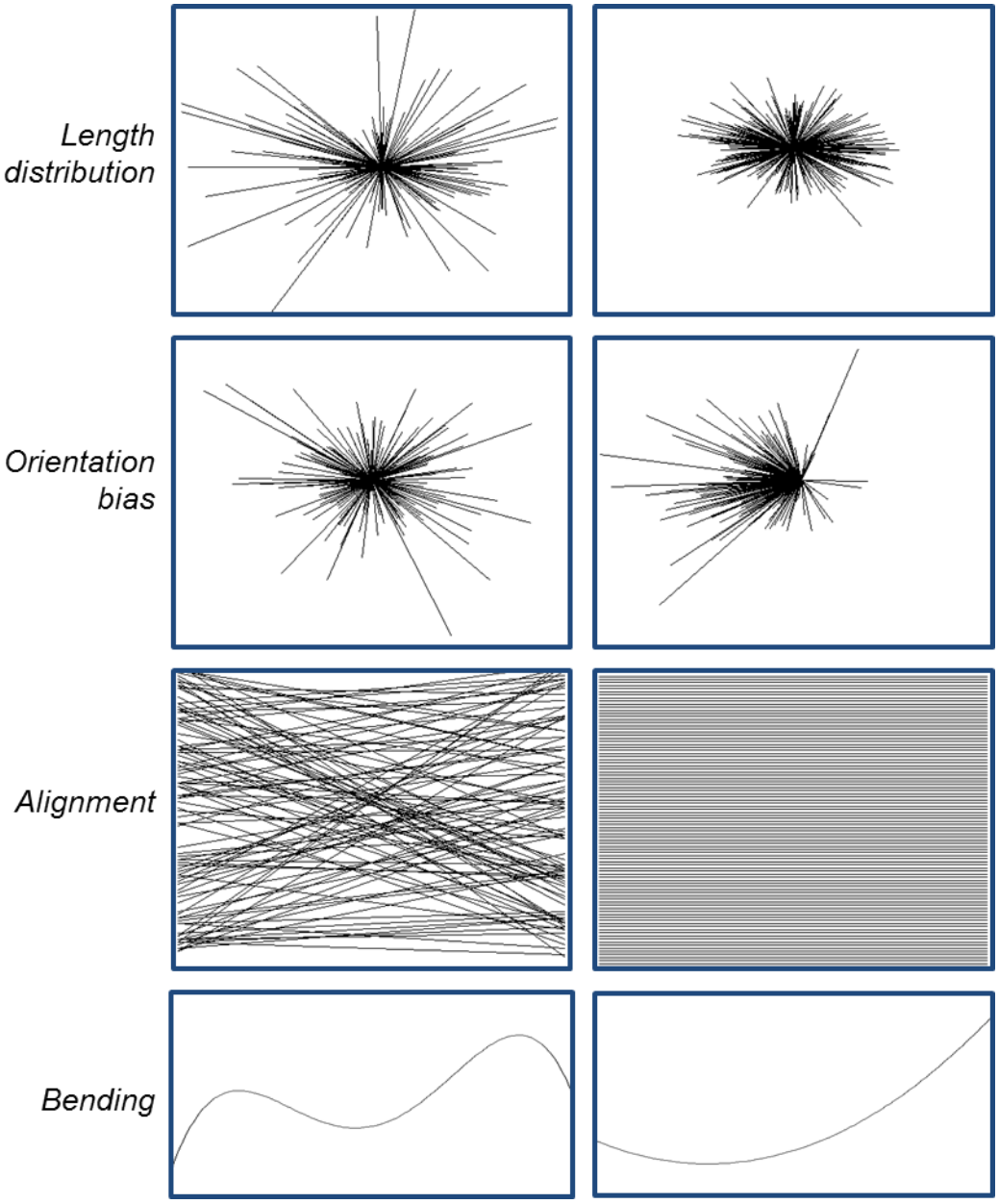

Figure 1. Microtubule organisation properties. Microtubule organisation can be considered in relation to the features shown; variations in each are shown in corresponding panels.

b. Microtubule orientation

Microtubule orientation is clearly an important feature of microtubule network organisation. The most obvious case to demonstrate this is the radial array in undifferentiated animal cells, whereby the distribution of orientations of the component microtubules is uniform on the interval [1°, 360°], perhaps the main functional consequence of which is proper transport throughout the cell. Moreover, as was discussed in chapters 2, and will be elaborated on in the next chapter, the orientation of plant cortical microtubules is a major determinant of plant morphology (Wasteneys and Ambrose, 2009), and in fission yeast cells, microtubules are oriented so that they run parallel with the principal axis of the cell, and this is an important factor in yeast cell growth and shape (Brunner and Nurse, 2000).

Microtubules can also re-orientate or fine-tune their orientation according to certain cues. For example, in plants, the predominant orientation of the cortical array can change in response to blue light (Lindeboom et al., 2013). In animal cells grown on micro-patterned substrates, it has been shown that microtubules target areas of cell-substrate adhesion, even though nucleation orientation is isotropic (Thery et al., 2006). Making use of micro-patterning again, in cells grown on thin, long substrates; microtubules have been shown to orientate parallel to the principal axis of the cell, in a similar manner to yeast microtubules (Picone et al., 2010). In some cases, biases in microtubule orientations are quite subtle. For example, in the *Drosophila* oocyte, a very slight but significant bias in microtubule orientation has been demonstrated, and this has important developmental functions (Parton et al., 2011). These studies make it clear that microtubule orientations can be indicative of important cellular processes.

How are microtubule orientations measured? One of the most thorough attempts of microtubule orientation quantification has been in the last study discussed above. Here, with images of plus tip protein EB1 labelled with GFP in the *Drosophila* oocyte, Parton et al. (2011) used a probabilistic threshold to assign a probability to each pixel that it "belonged" to an EB1-GFP particle. The probability was based on finding the intensity of the background at each pixel, and an estimation of the variation in intensity as a result of noise. The former was found using the median of the intensity over a number, *n*, of film frames before and after the current frame, this number being the time it takes an EB1-GFP particle to move from one pixel to another. The variation in intensity was defined as the mean of the standard deviations of intensity of the *n* frames before and after the current frame.

Finding the probability that a pixel is a "foreground" pixel (i.e. an EB1-GFP particle) involves subtracting the background intensity and variation (multiplied by some constant) and dividing by the background variation. Next, the probability images were segmented, and particles were linked into tracks using a previous method (Sbalzarini and Koumoutsakos, 2005). Once tracks are created, orientations can be determined, as was carried out in chapter 3 with plusTipTracker-created microtubule tracks. This probability-based method differs from that of Picone et al. (2010), where a conventional threshold was used to segment labelled microtubules from the background. Unfortunately, very few methodological details are provided, but after segmentation, presumably orientations were calculated according to gradients in the binary images.

Boudaoud et al. (2014) have implemented their method of quantifying microtubule orientation (and also alignment – see next sub-section) in "FibrilTool", an ImageJ/FIJI (Schindelin et al., 2012; Schneider et al., 2012) plugin. Based on gradients in pixel intensities, it gives the predominant orientation in an image, and it has previously been deployed in analysis of microtubule organisation the plant cortical array (Uyttewaal et al., 2012). In this method, images of labelled microtubules are subject to a pixel-by-pixel analysis of intensity; for each pixel, the gradient in intensity between it and those around it is found, giving a local gradient direction. The local gradients across the image are averaged, and this gives the predominant orientation.

Another method, developed by Lichtenstein et al. (2003) and also independently by Lindeboom et al. (2013), involves a rotating filter that resembles a microtubule or any filamentous structure. The microtubule-like filter is a line of given width, length and orientation, and by varying the orientation, one can determine the preferred orientation about the central pixel. Lindeboom et al. (2013) use summation of the intensities underneath the rotating kernel as a measure of preferential alignment, while Lichtenstein et al. (2003) take the correlation with the kernel. Both methods then employ a threshold step on the subsequent intensity or correlation to segment the stronger orientations from the background. The method of Lindeboom et al. (2013) is incorporated into the ImageJ plugin "LOCO", and has been used to measure orientation in the plant cortical array (Lindeboom et al., 2013).

In summary, the orientation of microtubules is an important factor in cell, and there have also been some good attempts at quantifying it, which have been varied in their methodology. Some involve segmentation, and in one case, use a probabilistic threshold, while others are based on the raw image, and others employ a filter-based approach. The FibrilTool method (Boudaoud et al., 2014) can be distinguished from the others by the fact that this requires absolutely no kind of threshold to delineate microtubules from the background; all others, whether it is the first step based on intensity (Picone et al., 2010), or a later step based on, e.g. probabilities (Parton et al., 2011) or correlation (Lichtenstein et al., 2003), set a point at which the signal is recognised over the background. Boudaoud et al. (2014) simply take the average image gradient direction to determine orientation; the method presented here will also not require any threshold or pre-processing step.

c. Microtubule alignment

The alignment in a network of microtubules goes hand-in-hand with orientation; the extent of alignment can be thought of as the extent of anisotropy in the orientation. Furthermore, the predominant orientation of a network of microtubules loses its relevance when there is no alignment; thus, an alignment score of some kind can be thought of as a proxy for the efficacy of the orientation estimate.

The alignment in microtubule networks varies between cell type and cycle stage, developmental stage, between organisms, and in response to environmental cues. For example, in plants, the anisotropy of orientations in the cortical microtubule array is a predictor of the extent of anisotropy in cell growth (Wasteneys and Ambrose, 2009); through its association with cellulose deposition in the cell wall (Paredez et al., 2006). Here, the so-called "growth continuum" paradigm posits that control of the organisation of the plant cytoskeleton is the main factor in the generation of diverse plant cell shapes; microtubule alignment is one such organisational property that is an important and highly modulated factor within this framework (Wasteneys and Galway, 2003).

In a theoretical study, it has been shown that the degree of alignment of a network is a major determinant of cargo transport, modulated by the extent of coupling between active transport and resulting cytoplasmic advection (Khuc Trong et al., 2012). Indeed, returning to the *Drosophila* oocyte, the slight bias in microtubule orientation is responsible for the correct

localisation of mRNA and protein with important developmental functions (Parton et al., 2011), and the theory in Khuc Trong et al. (2012) serves to elucidate why the microtubule network in the oocyte is not anisotropic to the extent one might expect in cases where unidirectional intracellular transport of various molecules is required: depending on the degree of coupling between active transport and the consequent advection, a weakly-biased network can actually localise molecules to a given target better than a strongly-biased network.

FibrilTool (Boudaoud et al., 2014) also quantifies the extent of alignment. Whereas the orientation is estimated as the circular average of the gradients in the image, the alignment, or orientation anisotropy, is taken to be the circular variance of the gradients in the image (see Mardia and Jupp (1999), for a good introduction to circular/directional statistics).

FibrilTool is a good example of user-friendly software to quantify alignment; indeed, other approaches at assessing alignment do not have such utility. For example, in a fascinating study of the effects of the protein Spiral 2 on the organisation of the plant cortical array, Wightman et al. (2013) use a statistical test (the type of which is not indicated) to discriminate between orientation distributions in different experimental conditions. Of course, this serves the purpose of being able to determine whether one condition is more or less aligned than another, but it does not permit comparison of many conditions, or different experiments.

The alignment of the microtubule network is also clearly an important factor in many instances. This feature of organisation is perhaps better-studied in plant biology, wherein it plays an essential part in development. However, there are cases in animal biology, for example the *Drosophila* oocyte, where microtubule alignment comes to the fore as a major force in development, but the extent to which it is involved in the proper functioning of animal cells is not clear; however, it is clear that, in theory, microtubule alignment can have a major effect on transport of molecules, which is one of the main functions of the microtubule network in animal cells. Moreover, previous work in the Mogensen laboratory has indicated that microtubule alignment is affected by the +Tip protein EB2, where its depletion caused an increase in microtubule alignment, and subsequent defects in cell differentiation (Goldspink et al., 2013). Thus, it is likely that there are at least certain cases where microtubule alignment is important in animal, as well as plant, cells. Next, I will introduce the concept of quantifying microtubule orientation and alignment based on the frequencies in an image.

d. The Fourier transform for microtubule organisation quantification

Here, I propose that the Fourier Transform (FT) of images of the microtubule network is ideally suited to quantify the orientation and alignment of microtubule networks. The FT is used commonly in image processing and elsewhere; it effectively transforms a signal (here, images are the signals) into its component frequencies. These frequencies are represented by complex exponential sinusoids, the magnitudes of which indicate the prominence of each frequency in the original signal.

When dealing with a two-dimensional image, the FT is taken in each direction, i.e., the result is 2-dimensional. In order to demonstrate the potential applicability of this method, an example image of the microtubule array is shown in figure 2 with its corresponding FT (specifically, it is the power spectrum that is shown; this is covered in the next section). In figure 2, the lowest frequencies are at the centre of the image, and the higher intensities at the borders. Immediately, it is possible to see that the greater intensities in the FT, indicated by brighter values, are generally located in a region that is oriented perpendicularly to the predominant direction of the microtubules in the original image. This is because the frequencies that are most prominent in the image are those that are perpendicular to the microtubules.

As an analogy, imagine walking over the original image, where the greater the intensity, the greater the altitude. Walking perpendicular to the microtubules means there will be a lot of ups-and-downs; plotting altitude as a function of position when walking this way will yield a signal that changes a lot. The FT can decompose this signal into a collection of sinusoids, of which there will be many contributing to the FT power spectrum in this direction. Walking parallel to the microtubules, however, and making the same plot, will yield a signal that does not change a great deal, because there will not be the same up-and-down profile as before. Thus, when decomposed by the FT, there will not be much contribution to the power spectrum in this direction.

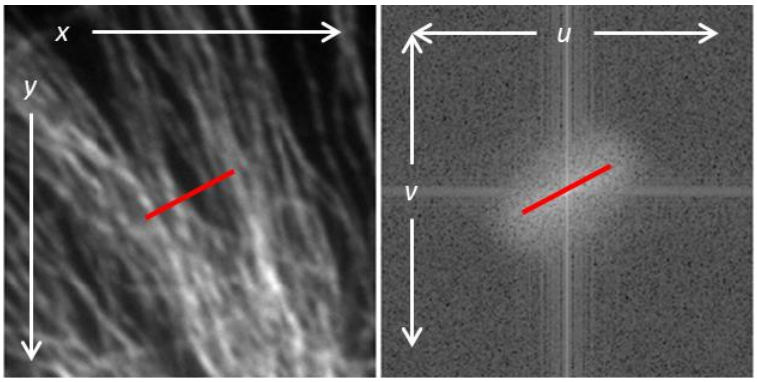

Figure 2. The Fourier transform (FT) of a microtubule image. An original image (left) and its FT power spectrum (right) are shown, with the highest intensities in the power spectrum in a region oriented perpendicularly to the prominent orientation of microtubules in the original image (indicated by the red line). Spatial information (x and y) is converted to frequency information (u and v), the latter of which is displayed so that the lowest frequencies are central.

These principles are the essence of all the work presented in this chapter. The next step in the process is to analyse the FT power spectrum and find the direction of the greatest intensities, and how spread these intensities are; these measures will indicate the predominant orientation and extent of alignment, respectively, of the microtubules. The purpose of this chapter is to establish the best means of analysing the power spectrum to quantify orientation and alignment in microtubule images, to test the method in a biologically-relevant situation, and further, to use the method to derive new information regarding the organisation of the microtubule network. Before I present these analyses, I will first summarise the principles of the FT and review its previous uses in biomedical image processing.

II. The Fourier transform

a. Principles

The Fourier transform originates with the man after whom it is named: Jean Baptiste Joseph Fourier, whose work on heat transfer lead to his theory that any periodic function can be expressed as a sum of sinusoids with different frequencies and amplitudes, and this concept is extendable to non-periodic functions, too; the former is known as a Fourier series, and the latter is known as the Fourier transform. Thus, any signal is converted into a collection of the frequencies that contribute to it, and what is more, this frequency domain information can be converted back again using the inverse Fourier transform. The formula for the Fourier transform in 2-dimensions is shown in equation 1:

$$F(u,v) = \sum_{x=0}^{M-1} \sum_{y=0}^{N-1} f(x,y)\, e^{-j2\pi\left(\frac{ux}{M} + \frac{vy}{N}\right)}, \quad (1),$$

where *u* and *v* are the frequency variables, and *f(x,y)* is the image of size *M*-by-*N*. Since Fourier's ideas were published in the 19th century, applications of his ideas have become widespread. The types of signals to which it is applied are usually those which vary in time or space, and as mentioned, in images the FT is 2-dimensional: one FT in the direction of each axis. Generally, analysis of signals with the FT involves the power spectrum, encountered in figure 2, the formula for which is below:

$$P(u,v) = |F(u,v)|^2, \quad (2).$$

Thus, the power spectrum is the magnitude of the Fourier transform, squared. All of the work in this chapter is based on the power spectrum. As was shown in figure 1, the power spectrum is usually shifted so that the lowest frequency is at the centre, and frequencies increase toward the borders of the spectrum. As a result, the power spectrum is symmetrical about the two principal axes.

The range of frequencies, Ω, in the power spectrum is dependent upon the rate at which the original function has been sampled, i.e. the sampling interval, ΔT:

$$\Omega = 1/\Delta T, \quad (3).$$

The sampling interval in images obtained from a microscope will be dependent firstly on the resolution obtainable with the microscope, and secondly, on the manner in which the continuous, optical image formed by the microscope is handled and converted into a digital image. Focussing on the former first, in microscopy, theory tells us that the resolution, commonly defined as the smallest resolvable distance between two objects, is a function of the numerical aperture (N.A.) of the microscope system (i.e. including the N.A. of the objective lens and the condenser; in epi-illumination systems, the objective also acts as the condenser), and the wavelength of the light being used to create the image. The smallest resolvable distance, *d*, is found like so:

$$d = 0.61\lambda/N.A., \quad (4),$$

where λ is the wavelength of the light used to create the image. Generally, for systems with magnification of 60x, N.A. can approach 1, and thus, for light at median wavelength (550 nm), *d* is about 0.3 μm, while for 100x systems, N.A. can reach 1.4, which, for similar light, gives values of *d* around 0.2 μm. Such calculations should be used as a guide; imperfect optics in the light path and fluorophores with different excitation and emission spectra will alter the resolution.

Moreover, the above equation is not all, since it applies to optical images, which are continuous functions in space, yet digital images are not continuous, but are instead represented by discrete elements, known as pixels. Hence, we arrive at the second issue mentioned above. The sampling interval is also determined by the area we choose to designate to each element in the camera attached to the microscope (which, in turn, gives us the area each pixel represents). Since pixels are square, we only need one figure to define the sampling rate. It is good practice in any signal processing, of which this analysis can be deemed an example, to sample at what is known as the Nyquist rate or criterion:

$$\Delta T = 2F_{max}, \quad (5),$$

where F_{max} is the maximum frequency, or likewise, the minimum resolvable distance, in the continuous signal (here, the optical image). The Nyquist criterion tells us simply that we must sample our continuous function, in this case the light emitted from fluorophores in the sample, at twice the greatest frequency in the function; abiding by this specification means that the highest frequencies in optical image will be represented in the digital image. In our case, this is 0.1 μm at best. Using the maximum expected frequency of 0.2 μm from calculations of *d*, and eq. 3, we can calculate the FT frequency range:

$$\Omega = 1/0.2 = 5\ cycles\ \mu m^{-1}, \quad (6).$$

This makes intuitive sense: the highest frequency in the FT will correspond to a signal that is varying at 5 cycles μm^{-1}, which, in the continuous optical signal, corresponds to 0.2 μm, for which the required sampling interval, according to eq. 5, for the digitised signal, is half that at 0.1 μm. Thus, the calculations agree, and in the frequency spectrum obtained from the FT, there will be a range from zero to 5 cycles μm^{-1}. Of course, as is clear by now, this changes according to the resolution of the microscope system.

Another pertinent factor is the resolution, or spacing, Δu, in the FT. This is dependent upon the total space sampled, *T* (in one dimension):

$$\Delta u = 1/T, \quad (7).$$

In microscopy images, *T* will typically vary between a sub-sample of a cell, on the order of microns, to a total cell, on the order of tens of microns:

$$T = 2\ \mu m,$$

$$\Delta u = 0.5\ cycles\ \mu m^{-1}, \quad (7a),$$

$$T = 50\ \mu m,$$

$$\Delta u = 0.02\ cycles\ \mu m^{-1}, \quad (7b).$$

We can see that the greater the space sampled, the smaller spacing we have in the FT, which means greater frequency resolution. Depending on the application, analyses of images are influenced by T and ΔT to varying extents. In this application, there is not the possibility of improving ΔT, since this is imposed by the physics of the imaging process, but T can be easily changed by changing the size of the image to be analysed. The extent to which frequency resolution matters for this particular application is debatable, since it is the direction(s) in which higher intensities in the power spectrum are positioned, rather than differences in frequencies. If the application was, e.g. an analysis of characteristic distances between microtubules, then T and ΔT might be more important.

Furthermore, there is essentially a trade-off between getting better frequency resolution and the heuristic use of the power spectrum. Although Δu decreases with increasing T, and thus resolution improves as T gets bigger, it may become more difficult to understand the correspondence between the frequencies resulting from the FT and the spatial distribution of intensities in the image. With smaller images, it is relatively easy to understand which parts of the image are represented by which parts of the FT; this becomes harder as T increases. Thus, any gains in frequency resolution resulting from increasing T are offset by the loss in understanding what the frequencies correspond to in the image. Later, in section B, this point is demonstrated.

One of the pitfalls of using the FT in image analysis is that the FT (and the inverse FT) are infinitely periodic (Gonzalez and Woods, 2006). This means that taking the FT of an image is analogous to assessing the frequencies in an infinitely-sized 2-dimensional tiled array of that image (fig. 3). Clearly, where the tiles meet, there is generally a large step, i.e. a discontinuity in most frequencies; the effect of this is to create a large signal, at every frequency, at these positions. Thus, in the power spectrum, there are high values at orientation corresponding to the principal axes, to which the tile edges are parallel. This is called an "edge effect", and analysis based on the FT must take measures to reduce them; without dealing with edge effects, there will be strong maxima in the FT along the principal axes, and this will hinder the identification of a principal orientation and calculation of alignment.

Once edge effects have been eliminated, an appropriate method of analysing the power spectrum must be chosen. The manner in which the power spectrum changes with orientation can be found with the following formula, which splits the power spectrum into radial sections (i.e. like the sections of a pie chart) and sums intensities in each (Gonzalez and Woods, 2006):

$$S(r) = \sum_{\theta=0^\circ}^{179^\circ} S_\theta(r), \quad (8),$$

where r is the radius of the circle from which the sections, oriented at θ, are taken. Hereafter, I refer to this function as the "orientation magnitude".

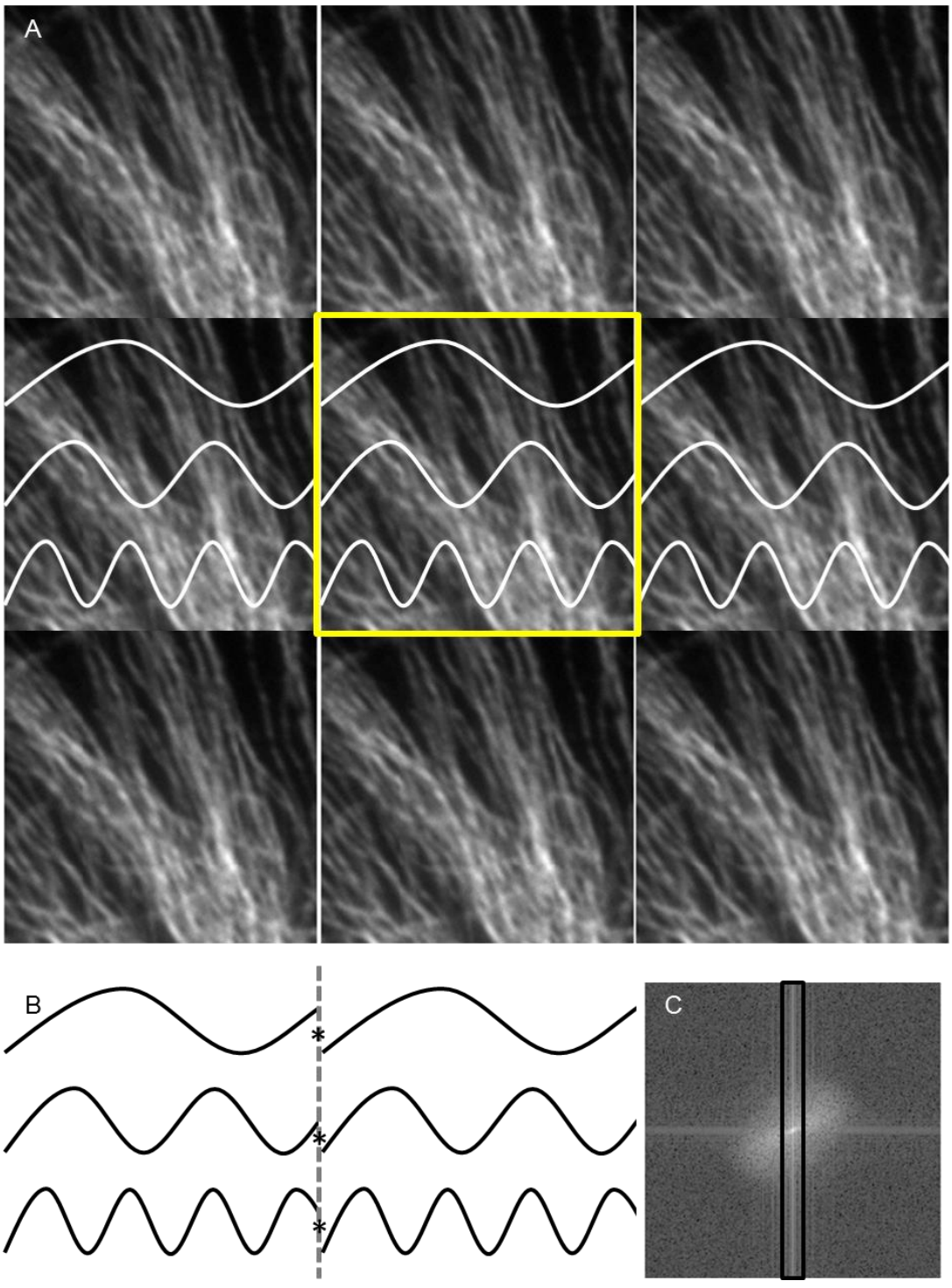

Figure 3. Edge effects. The FT treats images as being infinitely-tiled (A; original image in yellow square), leading to truncation of signals in the image (white lines in A; black lines in B) at the edges of the tiles. Where the signals are not continuous at the edges (asterisks at dotted line in B), a large signal is created at the same orientation as the tile edge in the power spectrum (black box in C). This example is for the y-axis; the same is true for the x-axis.

Here, I have discussed the principles of the FT and the pertinent image parameters that affect the analysis. But how can the power spectrum be analysed to quantify microtubule organisation? This is discussed later; before then, in the next section, I review cases where the FT has been used in similar situations, whether this has been for processing of biomedical images or an application from a different field.

b. Relevant applications of the FT

The aim of this section is to inform the next sub-section, where I assess the applicability of the FT for microtubule organisation quantification. In addition to being well-used in signal processing, the FT has been used extensively for diverse image processing applications. Many of these are not related to this application, and so reviewing them here would be superfluous; this only reflects the sheer applicability of the FT. Thus, I focus below on applications in analysis of filamentous structures; here, some of the applications are quite different to the one in this chapter, but similar methods of analysis justify their inclusion.

The principle of analysing frequencies using the power spectrum to derive information regarding the predominant orientation and the alignment in that orientation is not new. For example, Bayan et al. (2009) analysed the power spectra of images of collagen fibres with and without fibroblasts by taking the intensities of each orientation in the spectrum. Ayres et al. (2008) have used the FT in an analysis of scaffolds for tissue engineering generated by "electrospinning". In these scaffolds, the orientation and anisotropy of orientation of their constituent fibres are important in determining their material properties. Returning to collagen matrix organisation, Schriefl et al. (2013) used a similar approach to Bayan et al. (2009), summing power spectrum intensities at discrete orientations, to assess collagen fibre orientations in human abdominal aortas. The FT has also been used to detect structural changes in skin biopsies of patients diagnosed with Sjörgen-Larsson syndrome (SLS); here, histological staining of the biopsies was determined to be different between SLS sufferers and control patients in frequency components (Auada et al., 2006).

To determine the alignment in an image, some groups have defined a measure based on the "support" of the dominant orientation from the other orientations, i.e. the extent to which greater power spectrum intensities were at similar orientations to that which was determined to be dominant (Bayan et al., 2009). This type of method has the advantage that it includes all of the data; some other methods that use the maximum value in the orientation magnitude as an indicator of alignment (Ayres et al., 2008) (also the indicator of orientation, and dependent on the normalisation method – see below) effectively ignore all other data.

In a method related to the dominant angle support approach, Auada et al. (2006) calculated the resultant vector of the power spectrum. This group took frequency bands (i.e. annular sections of the spectrum) and, weighting vectors to each pixel by the intensity of that pixel, found the magnitude of the resultant vector for that frequency band. Thus, at discrete frequency bands, Auada et al. (2006) could use the magnitude of the resultant vector as an indicator of anisotropy; greater magnitude, greater anisotropy. Of course, since the power

spectrum is symmetrical, this method, and that of Bayan et al. (2009), requires that only half of the spectrum is used (it does not matter which half).

Moreover, with calculations of this kind, different spectrum halves have to be considered for each of the principal axes. This is because, e.g. a resultant vector calculated just for the interval of [90°, -89°], will always be positive for the x-axis direction, as all vectors are positive for x. The same can be said for the y-axis direction if the resultant is calculated over the interval [0°, 179°]. The fact that the power spectrum is symmetrical means that this type of manipulation is legitimate because the y-positive and x-positive areas correspond, so long as the "correspondence" is correct, e.g. an intensity at -80° will be the same as 100°. This will be expanded upon in a later section.

Another interesting method of quantifying alignment is that of Schriefl et al. (2013), who, after smoothing the orientation magnitude data, fit linear lines to the cumulative probability distribution of the orientation magnitude. Because isotropic orientation magnitude will have a linear cumulative distribution, those distributions that were not fit well by a linear line, defined according to a threshold R^2 value, were taken to be anisotropic (Schriefl et al., 2013).

"Benchmarking" is a common theme in analyses based on the FT; the idea is that some kind of "ground truth" is established, where the true characteristics of the image are known, to verify the accuracy of the method. Bayan et al. (2009) made efforts to benchmark their analysis based on synthetic image data, for which they knew the true dominant orientation and alignment, and Marquez (2006) has conducted a thorough analysis of the effect of fibre aspect ratio on detection of orientation using synthetic images. In that study, the FT-based quantification was found to work best for thin fibres.

In another study which compared methods to quantify orientation and alignment, in which, incidentally, the FT was found to be most reliable and quickest, synthetic images of "fibres" were created with varying numbers, predominant orientation and "anisotropy index" (i.e. some measure of anisotropy) (Sander and Barocas, 2009). This type of synthetic analysis is attractive since it allows exploration of a number of organisation parameters.

Where others have used synthetic images to benchmark their analysis, Ayres et al. (2008) use spaghetti. Here, spaghetti that was either left uncooked or had been cooked (5 min, *al dente*) for increased flexibility was arranged into various orientations and degrees of alignment. Importantly, cooked spaghetti was found to have a decreased alignment relative to uncooked spaghetti when arranged in similar orientations, verifying the efficacy of the method.

In some cases, benchmarking methods are based not on synthetic data or spaghetti, but on pre-assessment of the images to be analysed. For example, in their analysis of collagen organisation in human aortas, Schriefl et al. (2013) chose the threshold R^2 value in the fitting of linear lines to cumulative orientation magnitude probability distributions by labelling the images as isotropic or anisotropic first, and then chose the R^2 value that was in accordance with these labels.

Removal of edge effects is of course another important feature of FT analysis. In attempting to eliminate edge effects, Ayres et al. (2008) have used a circular window, where the image values outside the largest circle that fits into the image dimensions are set to increase from some given value at the borders of the images, to some unspecified higher value at the border of the image and circle window; other groups have employed similar methods (Schriefl et al., 2013). This method is similar to the windowing approaches employed in one-dimensional FT analysis, for which there are a number of functions to alter the image intensities so that edge effects are removed, each with slightly different characteristics.

Finally, to properly compare orientation magnitude plots, it is useful to normalise data in some way. Various approaches have been implemented, including seemingly *ad hoc* methods based on selection of one of the data points to subsequently divide the rest of the data by (Ayres et al., 2008), to "area normalisation", whereby the data is divided by the area so that the area under the data is equal to one (Bayan et al., 2009).

c. Suitability for quantifying microtubule organisation

The review above certainly contains promising indicators that the proposed method will be suitable for quantifying microtubule organisation, as there are a number of studies that have used similar methods to quantify the organisation of fibrillar structures, that are similar in appearance to microtubules. In particular, the analyses of electrospun scaffolds (Ayres et al., 2008), and of collagen matrices (Bayan et al., 2009; Schriefl et al., 2013) were carried out with aims similar to those here. Other cases, for example in the skin classification (Auada et al., 2006), suggest that FT analysis may also be useful for classifying cells based on the organisation of their microtubule cytoskeletons.

The review also highlights some methodological details that will be useful in this analysis. Firstly, it will be desirable to establish the applicability of ways to quantify orientation and alignment with some type of ground truth. Second, edge effect removal will need to be implemented. Third, to aid in comparison of data, a means of normalising the data will be required.

Another important point to come out of the above review is that there is generally not a consensus regarding ways to deal with the above points, i.e. orientation and alignment quantification, edge effect removal, and normalisation. Different groups have implemented their own methods, some overlap, and some are quite unique. Thus, appropriate methods for these will have to be determined; in this respect, ground truth data will be a useful tool.

Although some have made efforts to analyse not only orientation but also variations in frequency, given an orientation (i.e. the "frequency magnitude" as opposed to the orientation magnitude) (Auada et al., 2006), it is apparent that in most cases, only orientation information is taken into account, i.e. only pie-sections of the power spectra, and not annular sections, are considered. Thus, it will be sufficient to take a similar approach in this study.

In section B, these issues will be addressed in a preliminary analysis, involving ground truth images and some real microtubule images.

B. PRELIMINARY ANALYSES

I. Synthetic images

a. The need for synthetic images

By the end of section I, I will have carried out a thorough analysis of the FTs of synthetic images. The aim of doing this will be to have a benchmark against which to compare FTs of real cells. First, though, I briefly demonstrate why synthetic images are essential.

Figure 4 shows an image of fixed human retinal pigment epithelial, or ARPE-19, cells, visualised using similar parameters to all of fixed specimens under study throughout this thesis. We can see that the arrangement of the microtubule cytoskeleton varies between the cells, and within each cell. Some have well-aligned regions, while others are fairly disorganised, and some areas are well-aligned but bending. The power spectrum in figure 4b is for the whole image in figure 4a, while the power spectra of sections of the image are also shown in figure 4c.

Here, two important points become apparent. First, how can we be sure that certain features in the spatial domain relate to a given set of frequencies in the FT? Second, how do we go about quantifying the information in the FTs so as to enable us to compare microtubule networks? In relation to the first point, going backwards from the frequency information to the spatial domain can be informative: e.g. the power spectra for sections 2-4 show prominent frequencies oriented roughly perpendicular to the predominant orientation of the microtubules in the images. Thus, where there is a reasonable degree of alignment, it is quite simple to interpret the power spectrum; in cases where there is low alignment, or indeed a large image has been analysed, the power spectrum is more difficult to understand.

In relation to the second point, although it is easier to understand the power spectrum in smaller sections of an image, to do this for many images manually would be tedious and unfeasibly time-consuming. Hence, an automated method will be required, yet, one has to be sure that such a method behaves as it should; to establish a good automated method, candidate procedures can be tested on synthetic data, or compared against expert-labelled real data. Both approaches have been used previously, and here, I employ the former approach.

In summary, the argument for generation of synthetic data runs thus: thorough analysis of real images will require automation, but automation will require a method that we have confidence in. To do this, various approaches can be tested on data for which we know the parameters of interest: orientation and alignment, and we can then use them as a comparison when we look at real images.

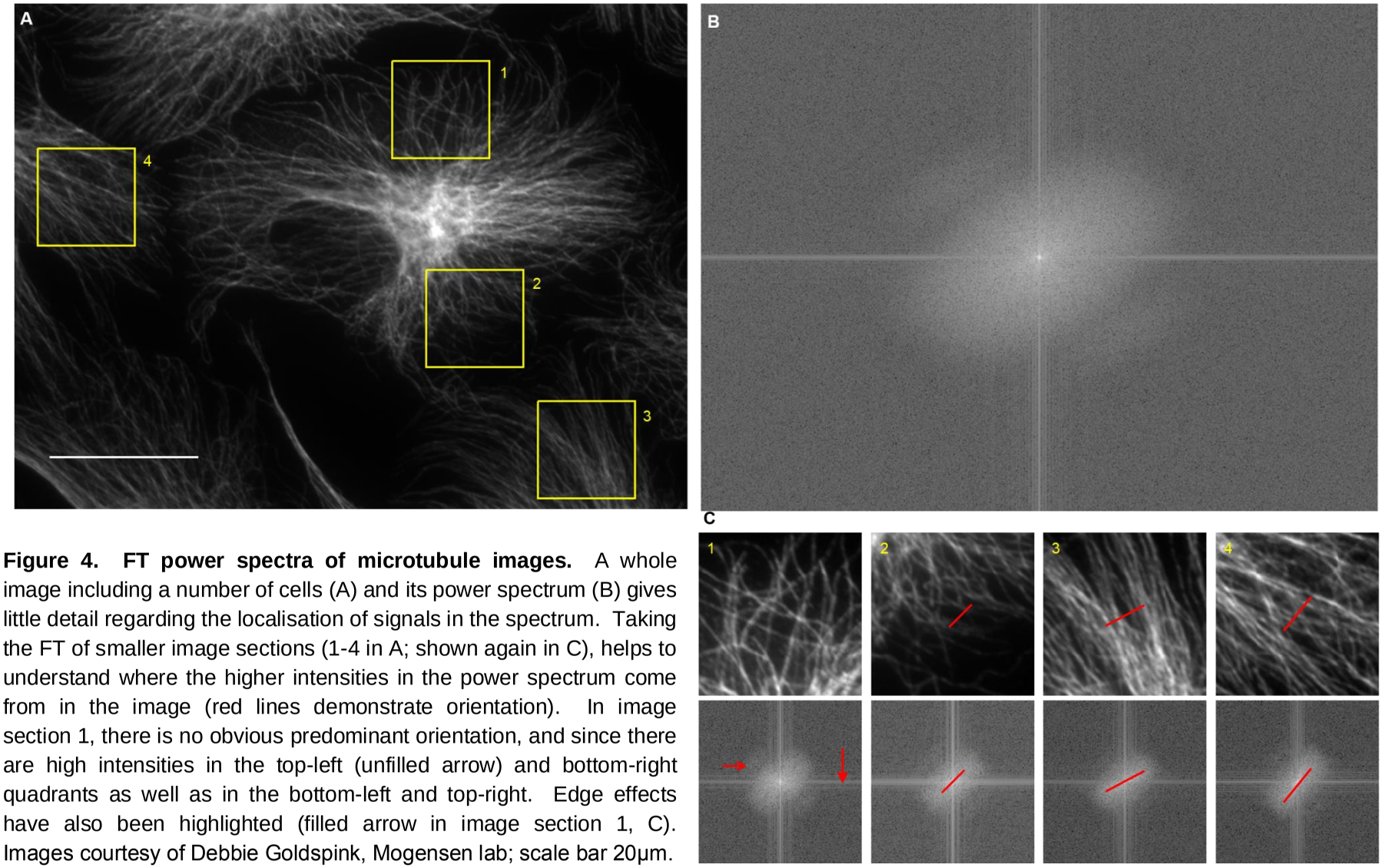

Figure 4. FT power spectra of microtubule images. A whole image including a number of cells (A) and its power spectrum (B) gives little detail regarding the localisation of signals in the spectrum. Taking the FT of smaller image sections (1-4 in A; shown again in C), helps to understand where the higher intensities in the power spectrum come from in the image (red lines demonstrate orientation). In image section 1, there is no obvious predominant orientation, and since there are high intensities in the top-left (unfilled arrow) and bottom-right quadrants as well as in the bottom-left and top-right. Edge effects have also been highlighted (filled arrow in image section 1, C). Images courtesy of Debbie Goldspink, Mogensen lab; scale bar 20µm.

b. Construction of synthetic images

How do we go about constructing these images, and what are the parameters we will vary? In a similar manner to Sander and Barocas (2009), I create a set of binary images with "fibres" with normally-distributed orientations with a given mean, μ, and standard deviation, σ (fig. 5). From here on, the mean and standard deviation in the synthetic images will be referred to as the "synthetic mean", or just predominant orientation, and the "synthetic standard deviation". For each combination of μ and σ, there are 20 images.

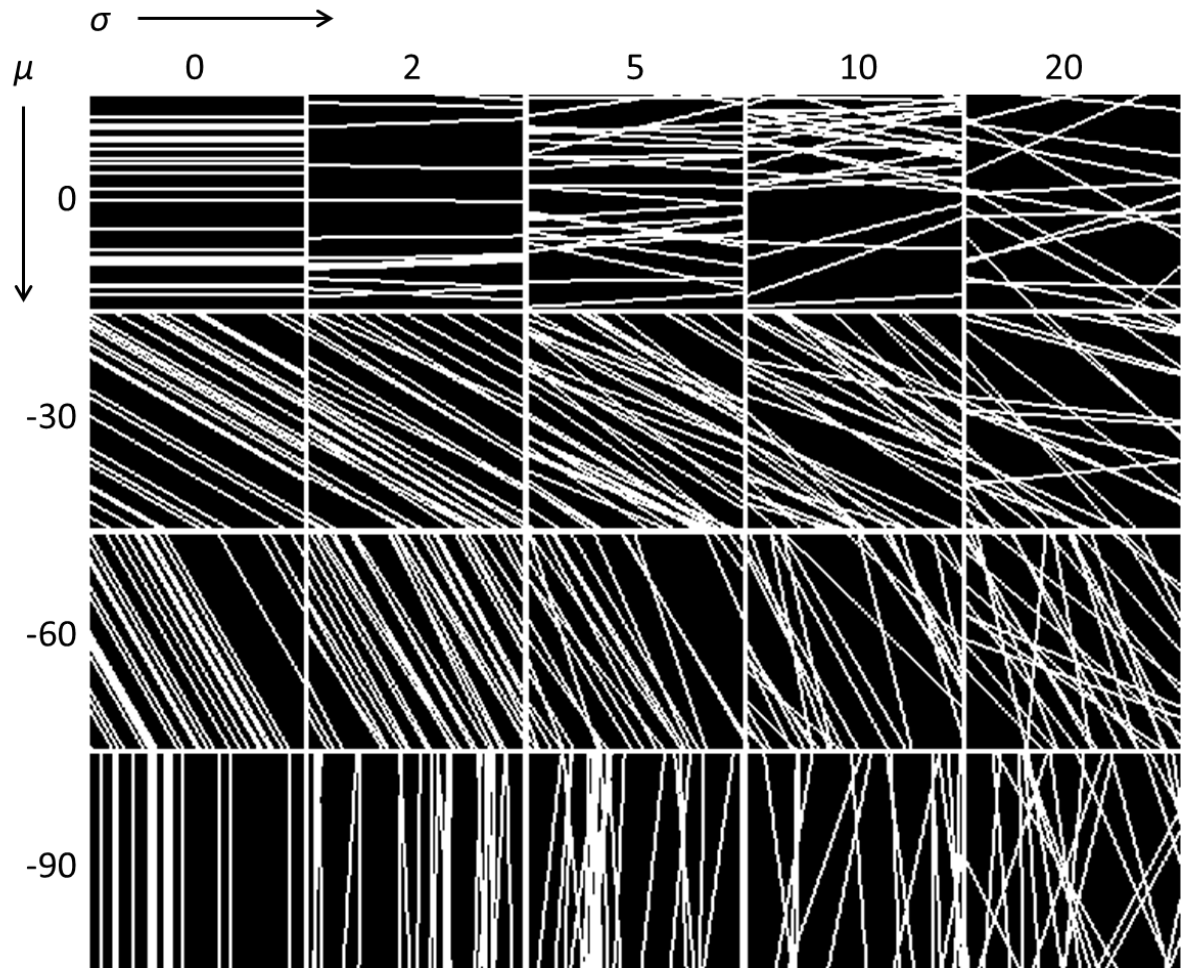

Figure 5. Summary of synthetic image set. Synthetic "fibres" are created, imitating microtubule images, with varying principal orientation, μ, and standard deviation, σ, about the predominant orientation.

c. Obtaining the orientation magnitude

The orientation magnitude, touched upon earlier, and found with the following formula:

$$S(r) = \sum_{\theta=0^\circ}^{179^\circ} S_\theta(r), \quad (8),$$

is an appropriate way of analysing how the power spectrum changes with orientation, and hence, the orientations present in the image. Keeping *r* fixed means that this can be omitted from the formula:

$$S = \sum_{\theta=0^\circ}^{179^\circ} S_\theta, \quad (8b),$$

and thus, "orientation magnitude" and "*S*" will be used interchangeably hereafter.

The orientation magnitude is a one-dimensional function, for which taking statistical measures, such as the circular mean and standard deviation, allows us to quantify the characteristics of the FTs (Gonzalez and Woods, 2006). The question I aim to answer in this sub-section is: what is the best way of obtaining the orientation magnitude?

In carrying out the summation in eq. 8, there are some preliminary considerations. First, it is clear that, due to the symmetry of the power spectrum, we only need analyse half of it (this is why θ goes from 0° to 179°, and not 359°, in eq. 8). Note that the issue mentioned earlier in determining the predominant orientation and extent of alignment by resultant vectors or dominant angle approaches is discussed further in section BIf. Second, the sums could be made over discrete ranges of θ, or, instead, they could run continuously, with a "window" of specified size centred at each orientation. Important parameters here are the number of groups for the "discrete" method, and the window size for the "continuous" method. Figure 6 depicts both the discrete and continuous approaches on the power spectrum of an example synthetic image.

From here onwards, I will specify whether the method was continuous or discrete. Figure 7 shows three example synthetic images, and plots of the orientation magnitude obtained with both methods; it also shows two different pre-processing methods, which are discussed in the next sub-section. It is clear that, while the discrete method produces step-like changes in the orientation magnitude, the continuous method, as might be expected, tends to produce "smoother" data. Reassuringly, both methods agree on the locations of maximum orientations. In this section, both methods will be used, with the aim of coming to a conclusion as to which is better for subsequent analysis.

In terms of subsequent analysis, even a brief look at the orientation magnitude plots in figure 7 suggests that values such as the mean of the distribution might not be quite what we are after; here, we are interested in the anisotropy of the distribution of the orientation magnitude: high anisotropy should indicate strong alignment, while low anisotropy should indicate weak alignment. Thus, we want to calculate how the power spectra of the synthetic control images vary with orientation (eq. 8) and compare the values for each orientation with one another, i.e., the intra-data set differences. However, before we address this problem, we must first consider how we will pre-process the orientation magnitude data.

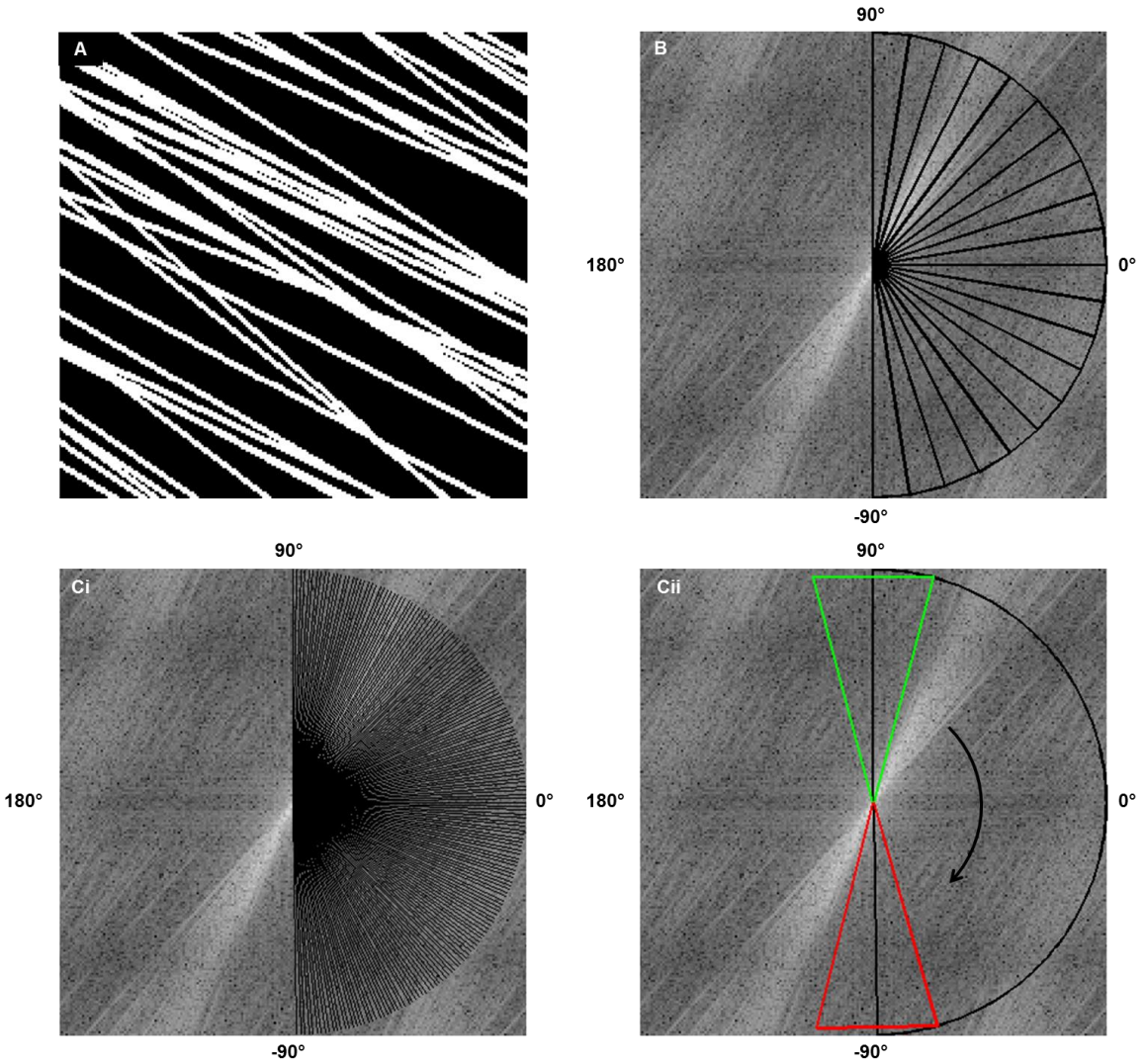

Figure 6. Methods of obtaining the orientation magnitude. The power spectrum of the synthetic image in A is analysed for orientation magnitude according to the "discrete" method (B) and the "continuous" method (C). In the discrete method, the areas analysed, from 90° to -90°, are depicted in black, and in the continuous method, the orientation at the centre of each area analysed is also shown in black (Ci). Cii depicts the first (green) and last (red) areas analysed as the central orientation sweeps from 90° to -89° (as indicated by the arrow).

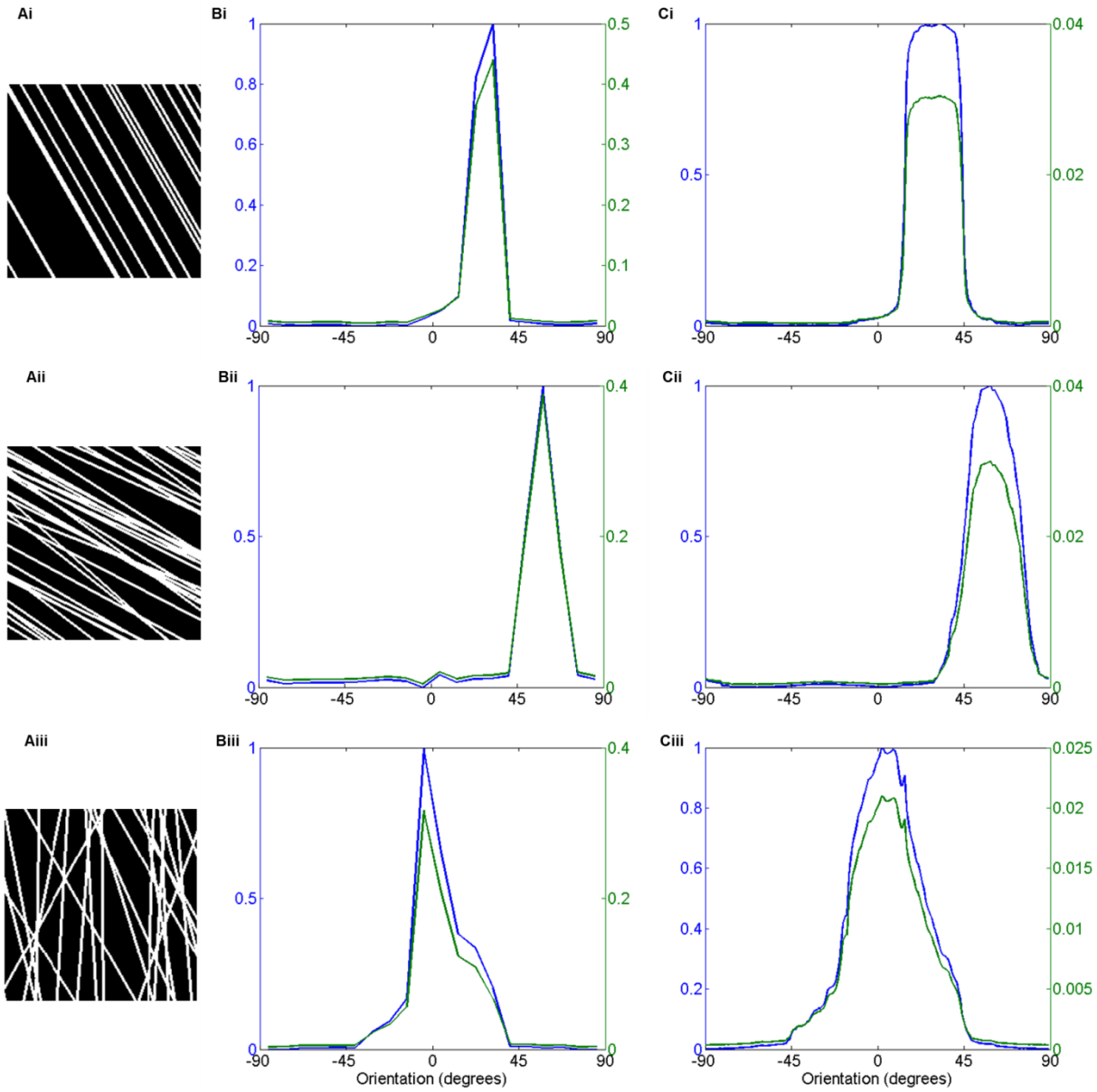

Figure 7. Orientation magnitude methods and pre-processing efficacy. For synthetic images with varying standard deviations and principal orientations, respectively: 0, - 60° (Ai), 5, -30° (Aii), and 20, -90° (Aiii), the orientation magnitudes are shown for the discrete (Bi-iii) and continuous (Ci-iii) methods, after pre-processing by either rescaling (blue lines) or normalisation (green lines).

d. Data pre-processing

A problem that arises in analysis of the orientation magnitude is that all of the data are very large values, and differences between them, may be small in comparison to their magnitude, making it difficult to detect any differences. Hence, some kind of pre-processing of the data should be required before any analysis. Furthermore, once we have compared values within single data sets, pre-processing should allow better comparison between data sets, since the results will not be affected by differences in magnitude between different sets. One form of pre-processing is to rescale the data so that all points are on the interval [0,1]. This is achieved with the following formula:

$$x' = \frac{x - x_{min}}{x_{max} - x_{min}}, \quad (9),$$

where, for each data point *x*, *x'* is the rescaled value, while x_{min} and x_{max} are the minimum and maximum values of the original data set, respectively.

Another form of pre-processing data is to normalise so that the area underneath a graph of the data is equal to one. This is achieved like so:

$$x' = \frac{x}{a}, \quad (10),$$

where, again, for each data point *x*, *x'* is the normalised value, and *a* is the area underneath the plot of the original data. This is the same method as that used by Bayan et al. (2009).

In figure 7, we can see that for the example synthetic images, both pre-processing methods, as with the different orientation magnitude methods, agree on where maxima are located in the data. Due to the differences in the two methods, we would of course expect quite different values, and this is indeed what we see, but both have similar shapes.

However, one concern with the rescaling method is that, because the maximum value takes the new value of one and the minimum takes the new value of zero, it might accentuate intra-data differences if the original distribution does not have a large maximum. Likewise, as figure 7 shows, the normalisation method appears to have smaller peaks at the predominant orientations relative to the other data; are either of these concerns valid? A simple analysis based on data with a clear maximum ("peaky" data) (fig. 8A) and another set with no clear maximum ("flat" data) (fig. 8D), can clear up the issue. Figure 8 shows that rescaling perfectly reproduces the shape of the original peaky data (fig. 8B), while normalisation tends to reduce the maximum slightly (fig. 8C). However, in the flat data, even though it appears that both rescaling and normalisation preserve the shape of the original data, comparison of the two appears to indicate differences between resultant data (fig. 8E-G).

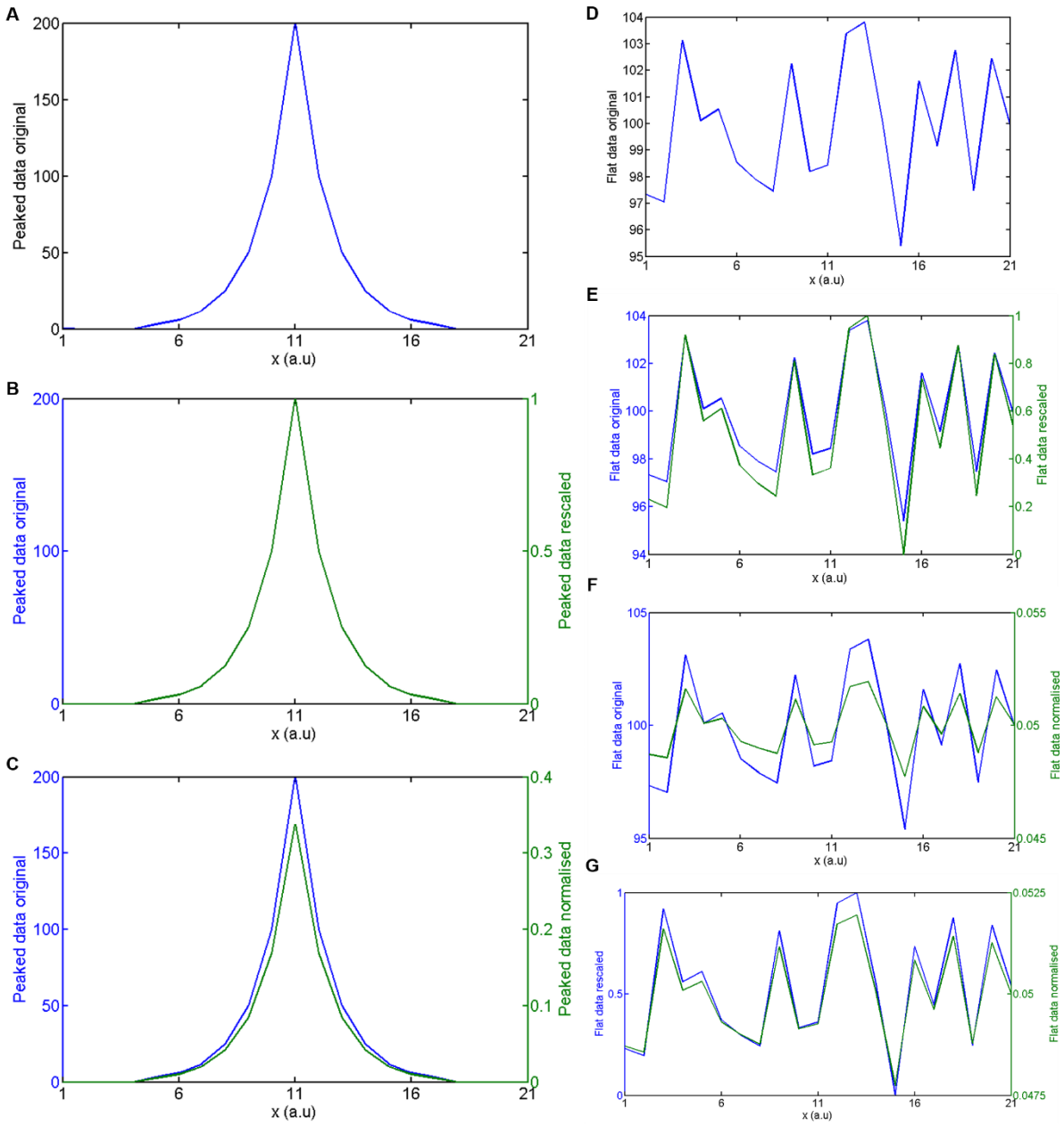

Figure 8. Further tests for pre-processing method efficacy. Data with a clear maximum ("peaked") (A) were tested with both rescaling and normalisation pre-processing, the results of which are presented in B and C, respectively, with both plotted with the original data. Relatively flat data (D) were also subject to the same analysis (E and F), and the results of rescaling and normalisation are also plotted together in G.

To better understand this, the ratios of the minimum to maximum, and mean to maximum, values of the data before pre-processing, and after pre-processing with both rescaling and normalisation, were calculated. Here, the aim was to quantify, to some extent, the shape of the data. The ratios are shown in table II, and as expected, rescaling deals well with the peaky data with both ratios, but so too does normalisation; perhaps the plotting process and axis scales used obscured the relationships within the data. The ratios for the flat data suggest that rescaling does indeed accentuate intra-data differences in situations where the original data was relatively uniform; the minimum to maximum ratio is zero, as would be

expected given that rescaling assigns zero to the former and one to the latter, whereas for the original and normalised data, this ratio is 0.919. The mean to maximum ratio is also misrepresented after rescaling the flat data: here, the value is 0.530, while for the original and normalised data, it is 0.962. Thus, caution should be exercised when using the rescaling method of pre-processing since it has the potential to change intra-data relationships. However, for the analysis of synthetic images, I will continue to employ both methods, where I can be sure that there is indeed a peak in the data at the predominant orientation.

Table II. Data metrics before and after pre-processing. Ratios of minimum to maximum value, and of the mean to the maximum value, are shown for original, rescaled, and normalised data. The discrepancies between the rescaled and original data are highlighted in grey.

	Original	**Rescaled**	**Normalised**
		Peaked data:	
Min/max	0	0	0
Mean/max	0.141	0.141	0.141
		Flat data:	
Min/max	0.919	0	0.919
Mean/max	0.962	0.530	0.962

e. Eliminating edge effects

Edge effects, and the various means that have been proposed to deal with them, were covered in section AII. Here, I investigate a number of potential means of reducing the effects of edge. The first way is to simply ignore them, and exclude the data at the principal axes from the analysis. This is not entirely satisfactory since, in the case that there is true strong alignment along one of the principal axes, it will not be detected. By taking into account that there are usually high values at these orientations, and including them if the values here are unusually high, is a possibility, and has been employed previously (Ayres et al., 2008). Another way would be to look at the power spectrum in all other directions, and if there are maxima here, it is likely the principal axes maxima are only edge effects; in essence, we are asking: is there information elsewhere in the FT, and if so, we will ignore the principal axes. However, this could be quite a complex and time-expensive analysis.

Another way to determine whether it is an edge effect or a real result from the information in the image is to take the FT and analyse it, then rotate the original image by a known amount and take the FT again. In this approach, if the principal axes maxima represent real information, there will now be maxima at the orientation of the angle the image has been rotated by. If they were edge effects, there will not be a new maximum at this orientation. This is a promising method, but as before, it could lead to a lengthy time of analysis, since it will double the number of images to analyse.

Although the above practises provide means of identifying edge effects and eliminating them from subsequent analyses, better approaches might aim to remove edge effects earlier, at the image stage, so they do not need to be identified. In this way, we would not risk removing legitimate data when trying to rid the analysis of edge effects. In signal processing, where the FT is used extensively, a process called windowing is employed to negate the effects of sub-

sampling sections of a 1-dimensional signal. This could be an option here, but it is only compatible with certain types of analysis; namely, those that are filter-based, and centre a window of some size on each pixel of the image. This type of method is described in a bit more detail in the full analysis; suffice to say that it is not the method of choice here, and so windowing cannot be considered.

A better-established method in image processing to eliminate edge effects before taking the FT is to pad the image. Here, the image is surrounded, or padded, by more sections of image. The idea of padding is to negate the effect of effectively abruptly truncating the wavelengths in the image at the image borders (demonstrated in fig. 3). The padding sections produce an area that softens this abrupt stop, and thus decreases the signal created by it in the FT.

There are a few options as to the positioning and content of these extra padding sections of image; here, I analyse zero, mean, and reflection padding. These approaches are summarised in figure 9. Zero padding consists of positioning rectangular sections of zeros around the image (fig. 9B). Whether padding at the top or bottom of the image or left and right, one of the dimensions of these sections clearly depends on the size of the image, while the other dimension that determines how "deep" the section is, is up to the user to decide. Generally, this dimension will correspond to the size of the image in some way; it might be the same size as the image, or it might be half the size. Another option is mean-padding. Here, instead of zeros, the image is padded with its mean value (fig. 9C). In some cases, this might be preferable because it could soften the transition at the border of the image to a greater extent than zero-padding. In addition to zero- and mean-padding, we can fill the padding sections with a reflection of the image (fig. 9D). We might expect that this approach is the best choice since the image is now more periodic; the FT algorithm expects periodic input; thus, it might perform better with a reflection-padded image.

The choice between these three approaches will usually be based on assessment of their corresponding FTs. It is to some extent a decision based on preliminary data rather than there being a definitive method. Later, we will examine these different approaches with a preliminary study to establish which is best-suited to our system of study.

There is an extension to the padding approaches described above, and this involves changing the shape of the image that is surrounded by padding sections (fig. 9). Here, the idea is that by removing the edges present in a square image, we should reduce the spurious signal created by these edges. Hence, instead of padding around a square image, we first remove sections of the image so that it is now in a circle. Of course, we will not want to make this circle too small, since we will start losing real signal from our image; good practice will be to use a circle of diameter similar to that of the smallest dimension of the image. As above, the choice as to whether padding is zero, mean or reflected is based on preliminary analysis; however, it is unlikely that reflection will be appropriate here, where there are no straight image borders.

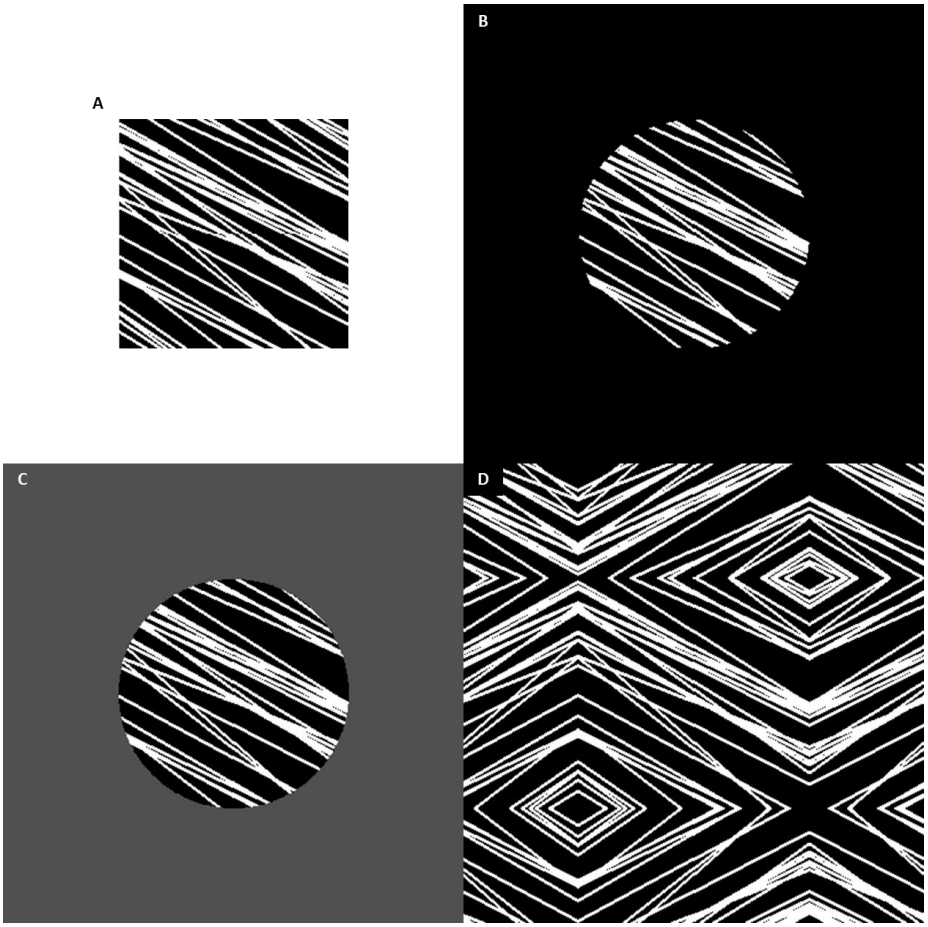

Figure 9. Padding approaches. A synthetic image (A) is padded either with zeros (B), the mean value of the circular "windowed" image (C), or reflected (D).

To determine which of these methods works best for this application, I carried out an analysis on the synthetic images, with data obtained using the discrete method and rescaling for pre-processing. In this analysis, for each types of padding, the mean orientation magnitude at the principal axes was found for synthetic images where the signal here would be expected to be low (i.e., predominant orientations -30° and -60°) and those where principal axis signal would be expected to be high (i.e., predominant orientations 0° and -90°). Finally, I then rotated the latter set of images by 45°, and found the mean orientation magnitude at the principal axes. A good padding approach should therefore give low signal in the first group, high signal in the second group, and low signal in the third. The results are plotted in figure 10.

It is clear to see from figure 10 that some padding approaches perform better than others. For example, zero and reflection padding increase the signal relative to non-padded images at the principal axes in the first group, which suggests enhancement of edge effects in some way, while mean padding decrease the signal for this group. All padding approaches conserve the signal in the second group, which is good, while, in the rotated set, mean padding reduces the signal best relative to the non-padded data. Thus, mean padding performs best in this analysis, and will be used hereafter to eliminate edge effects.

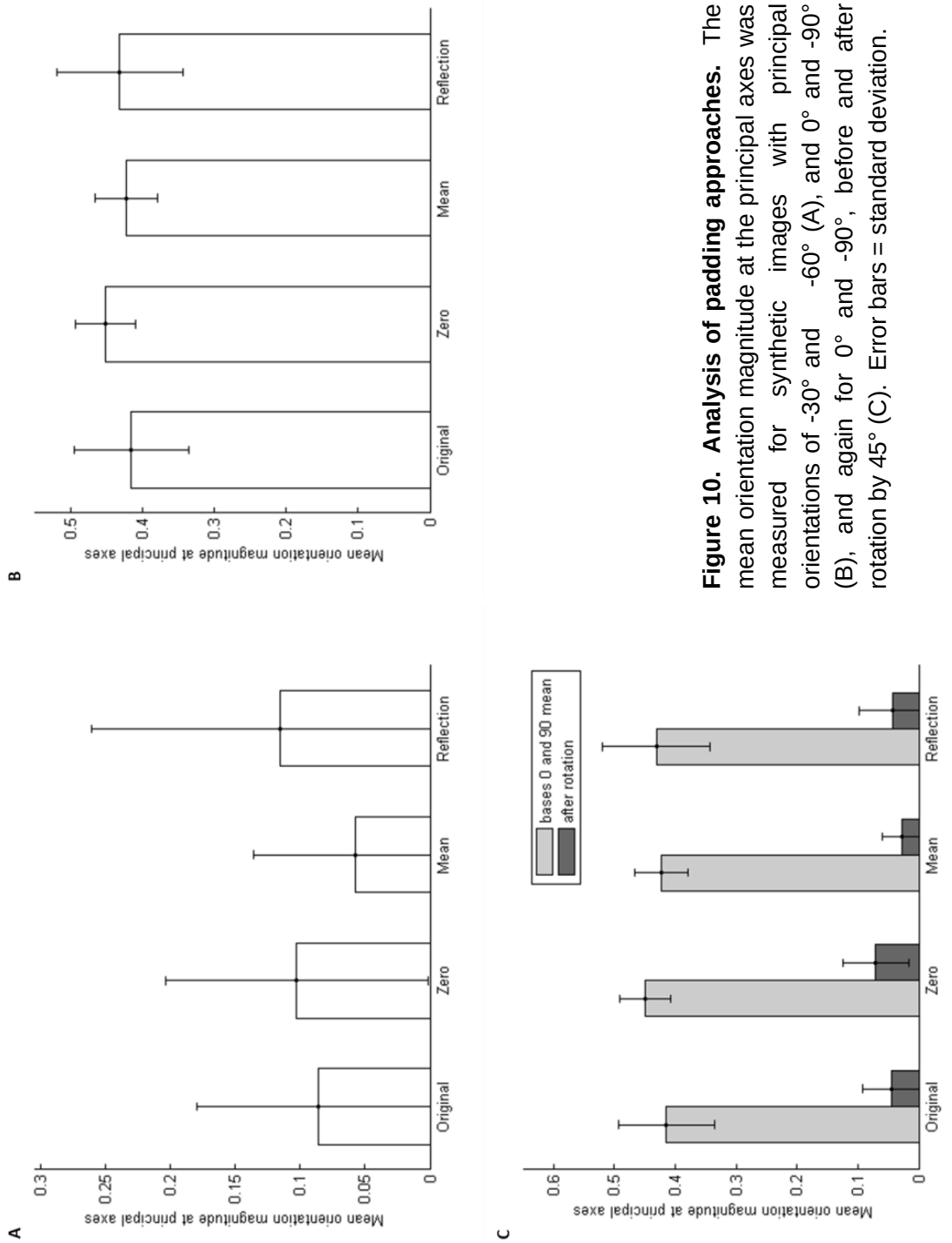

Figure 10. Analysis of padding approaches. The mean orientation magnitude at the principal axes was measured for synthetic images with principal orientations of -30° and -60° (A), and 0° and -90° (B), and again for 0° and -90°, before and after rotation by 45° (C). Error bars = standard deviation.

f. Analysis of the orientation magnitude

In this sub-section, I propose various methods to predict the predominant orientation from the orientation magnitude data, and also to quantify the anisotropy in the data, and after discussing their advantages and disadvantages, I test some of the more promising methods.

To recap, so far, we have seen that two methods of obtaining the orientation magnitude, the discrete and continuous approaches, are applicable, while we also have two methods to pre-process the orientation magnitude, rescaling and normalisation, albeit with some reservations as to the efficacy of the former. We have also seen that the most appropriate method for elimination of edge effects in the FT of the synthetic images is mean padding. Therefore, all analyses in this sub-section will be based upon images that have been mean padded prior to calculation of the FT, and both methods for obtaining the orientation magnitude and pre-processing will be used.

To predict the predominant orientation in an image, there are three potential methods:

1. Take the orientation at which the maximum magnitude occurs
2. Calculate the mean orientation of the data
3. Calculate the "dominant" orientation

These methods are summarised in table III. In many cases, these methods may give similar results; however, the latter two may be better means of estimating the predominant orientation because it takes into account all of the data. For example, if there is one outlying value that is a maximum, while there are many slightly lower magnitudes clustered elsewhere, then the mean orientation would indicate the predominant orientation better than simply taking the maximum value. Calling this the mean value can be misleading, since at first, one might think that, in any case, a mean value will not be a good indicator of where maxima are located in the data. However, it is not the mean value of the orientation magnitude, rather, it is the mean value of the orientations analysed, weighted by the orientation magnitudes. Hence, it is analogous to angle of the resultant vector, the magnitude of which is discussed as a means of quantifying alignment below. See Mardia and Jupp (1999) for a thorough guide on descriptive statistics for data that are collections of angles (i.e. "circular" data).

The second method suffers from a problem that is commonly encountered in analyses of circular data (Mardia and Jupp, 1999); what I call the "transition problem", in that, since the orientation magnitude is defined on an interval of 90° to -89°, if a peak were located across these angles, then the resultant vector would be small where it should be large, because the set of vectors, some clustered around +90° and some around -89°, would oppose one another. Thus, the second method is prone to giving spurious results, depending on where the principal orientation lies.

The third method maximises a function used to find what has been called the dominant orientation (Allard et al., 2010; Baulin et al., 2007), it is also used again, below, in one of the measures proposed to quantify alignment. Briefly, it is the orientation for which the

projection of all of the data in that direction, minus the projection of all of the data in the orthogonal direction, is at a maximum.

It may be the case that the third method is best suited to orientation magnitude data obtained by the continuous method, because, as table III outlines, it is calculated by maximising a function that has continuous input values of α, which is a set of angles from 0° to 179°; this can also be -89° to 90°. However, the third method will be tested with discrete orientation magnitude data; the particular combinations of methods is shown in table IV.

The third method does not suffer from the same problem as the second method, because, firstly, only the cosine of the difference between the input value α and a given angle θ is found, and it is squared; thus, $\sigma_s(\alpha)$ is at its minimum when θ is perpendicular to α, and it increases from this minimum for both differences less than and greater than 90°. Therefore, "opposing" angles such as 90° and -89° actually give the same value as "similar" angles, i.e. 90° and 89°.

Next, the measures that will be used to quantify the extent of alignment, or rather, the anisotropy in the orientation magnitude, will be defined. There are a number of measures that may be useful:

1. Take the proportion of the integral around the maximum value to the integral of the rest of the data
2. Subtract the proportion of the second biggest integral to the maximum integral from one
3. Subtract the proportion of the mean value to the maximum integral from one
4. Measure the kurtosis, or "peakedness" of the data
5. Find magnitude of resultant vector of data
6. Calculate an "order" parameter

The measures, and how they are calculated, are also summarised in table III. In some cases, as with the principal orientation prediction measures, it is clear that a particular measure is better suited to the discrete or continuous orientation magnitude approaches. For example, measures 1-3, that take the ratios of the integrals around the maximum value to the integrals of rest of the data (measure 1) and the second-highest value (measure 2), and the ratio of the integral around the maximum value to the mean value (measure 3), will be better suited to data obtained by the discrete method, since the smoothness of the continuous data, where many points make up a maximum, will likely make these measures obsolete. Again, the combinations of methods can be found in table IV.

Kurtosis is a standard descriptor of distributions; it is designed to indicate the extent to which data are peaked. There are variations on how kurtosis is calculated; the method used here is the built-in Matlab command, and with this method, distributions that are more likely to contain outliers, or rather, distributions where more of the area under the curve is concentrated in a peaked area, have a higher kurtosis. The normal distribution, according to the formula in table, has a kurtosis of 3; thus, values above 3 indicate that the data are more peaked than the normal distribution, and values below, less peaked data.

The fifth method suffers from the same transition problem as the direction of the resultant vector (method 2 for principal orientation prediction) suffers from. Here, a peak straddling the orientations of -89° to 90° will produce a small resultant vector where it should be large, again because the vectors oppose one another. Thus, the magnitude of the resultant vector is prone to giving spurious results, depending on where the principal orientation lies, and so will not be ideal for this analysis.

The sixth method is related to method 3 for principal orientation prediction. Again, this is based on work in Baulin et al. (2007) and Allard et al. (2010), and it quantifies the relative difference between the projections of the data in the principal orientation and the orthogonal direction. It takes values between 0 and 1, with 1 being perfect alignment, and 0, complete disorder.

To reiterate, the aim of using many methods with the synthetic is to obtain some idea as to which set of methods works best, and we can be confident that we can identify which is best as we know the ground truth; once we have determined which set of methods works best, we can then use just that set on real images. It has been clear that some of the methods proposed will not be suitable, thus, only some will be tested; these are shaded in grey in table III.

Table III. Summary of measures used to predict the principal orientation and to quantify the anisotropy of orientation magnitude data. For orientation prediction, measures 1-3 indicate the orientation at which the maximum value occurs, the mean orientation, and the "dominant" orientation, respectively. For anisotropy, measures 1-3 indicate the ratio of the maximum integral to the rest of the data integrated, the ratio of the second-largest integral to the maximum integral taken from one, and the ratio of the mean value to the maximum integral taken from one, respectively. Measure 4 is the kurtosis, or "peakedness" of the data, while measure 5 is the resultant vector of the data, and measure 6 is an order parameter indicating the extent of alignment in the data.

	Measure	**Formula**	**Notes**
	Principal orientation prediction		
1		$\theta_{max} = \max(S(\theta))$	
2		$\bar{\theta} = \begin{cases} \tan^{-1}(\bar{Y}/\bar{X}) & if\ \bar{X} \geq 0 \\ \tan^{-1}(\bar{Y}/\bar{X}) + \pi & if\ \bar{X} < 0 \end{cases}$	$\bar{X} = \frac{1}{n}\sum_{j=1}^{n} \cos(\theta_j)$ $\bar{Y} = \frac{1}{n}\sum_{j=1}^{n} \sin(\theta_j)$
3		$\Omega = \max(\sigma_s(\alpha))$	$\sigma_s(\alpha) = \frac{1}{n}\sum_{j=1}^{n} S(\theta_j)\cos^2(\alpha - \theta_j)$ $\alpha = \{0, \ldots, 179\}$
	Orientation magnitude anisotropy		
1		$m_1 = \frac{\sum_{s \in A} S(\theta)}{\sum_{s \in B} S(\theta)}$	
2		$m_2 = 1 - \left(\frac{\sum_{s \in C} S(\theta)}{\sum_{s \in A} S(\theta)}\right)$	
3		$m_3 = 1 - \left(\frac{\bar{s}}{\sum_{s \in A} S(\theta)}\right)$	
4		$k = \frac{E(s-\mu)^4}{\sigma^4}$	
5		$\bar{R} = (\bar{X}^2 + \bar{Y}^2)^{1/2}$	$\bar{X} = \frac{1}{n}\sum_{j=1}^{n} \cos(\theta_j)$ $\bar{Y} = \frac{1}{n}\sum_{j=1}^{n} \sin(\theta_j)$
6		$\rho = \sum_{j=1}^{n} S(\theta_j) \frac{(\cos^2(\theta_j - \Omega) - \sin^2(\theta_j - \Omega))}{\sum_{j=1}^{n} S(\theta_j)}$	

Table IV. Summary of combinations of methods and measures in synthetic image analysis. Both discrete and continuous methods of obtaining the orientation magnitude are combined with both recalling and normalisation, while particular sets of measures for principal orientation prediction and orientation magnitude anisotropy are used.

Orientation magnitude	Pre-processing	Principal orientation prediction	Orientation magnitude anisotropy
Discrete	Rescaling Normalisation	3	1-4,6
Continuous	Rescaling Normalisation	3	4,6

Later, when these measures are taken of real images of the microtubule cytoskeleton, it will be a simpler task to compare data sets, which would, in this case, be different cells, images, or parts of an image. In this case, the analysis will be based on relative data. However, it might also be useful to have some kind of absolute measure of alignment. Applying the measures in table III to the synthetic images will enable this; the values obtained from real image can be compared to those obtained from synthetic images for which we know the true alignment parameters, as summarised in figure 5.

Now that the combinations of methods to obtain the orientation magnitude, and means of estimating the principal orientation and quantifying the extent of alignment have been decided, they can be put to the test. Firstly, the accuracy of each combination of orientation magnitude data and pre-processing was assessed using the mean squared error of the predictions of principal orientation in the synthetic images. Remember, the orientations in the synthetic images are 0°, -30°, -60°, and -90°. Thus, the principal orientation in the magnitude data should be perpendicular to these, at 90°, 60°, 30°, and 0°. Table V shows the mean squared error for each combination and figure 11 has plots of the real orientation and the prediction of each combination for each synthetic standard deviation. Table V and figure 11 show that the continuous orientation magnitude, whether combined with rescaling or normalisation, has greater accuracy in principal orientation prediction than the discrete method.

Table V. Mean squared error of principal orientation prediction. For each orientation magnitude and pre-processing method, i.e., discrete (D), continuous (C), and rescaling (R), and normalisation (N), the mean squared error (MSE) in principal orientation prediction is shown; n = 400 for each combination.

	Method			
	D/R	**D/N**	**C/R**	**C/N**
MSE	2.25	2.25	0.35	0.35

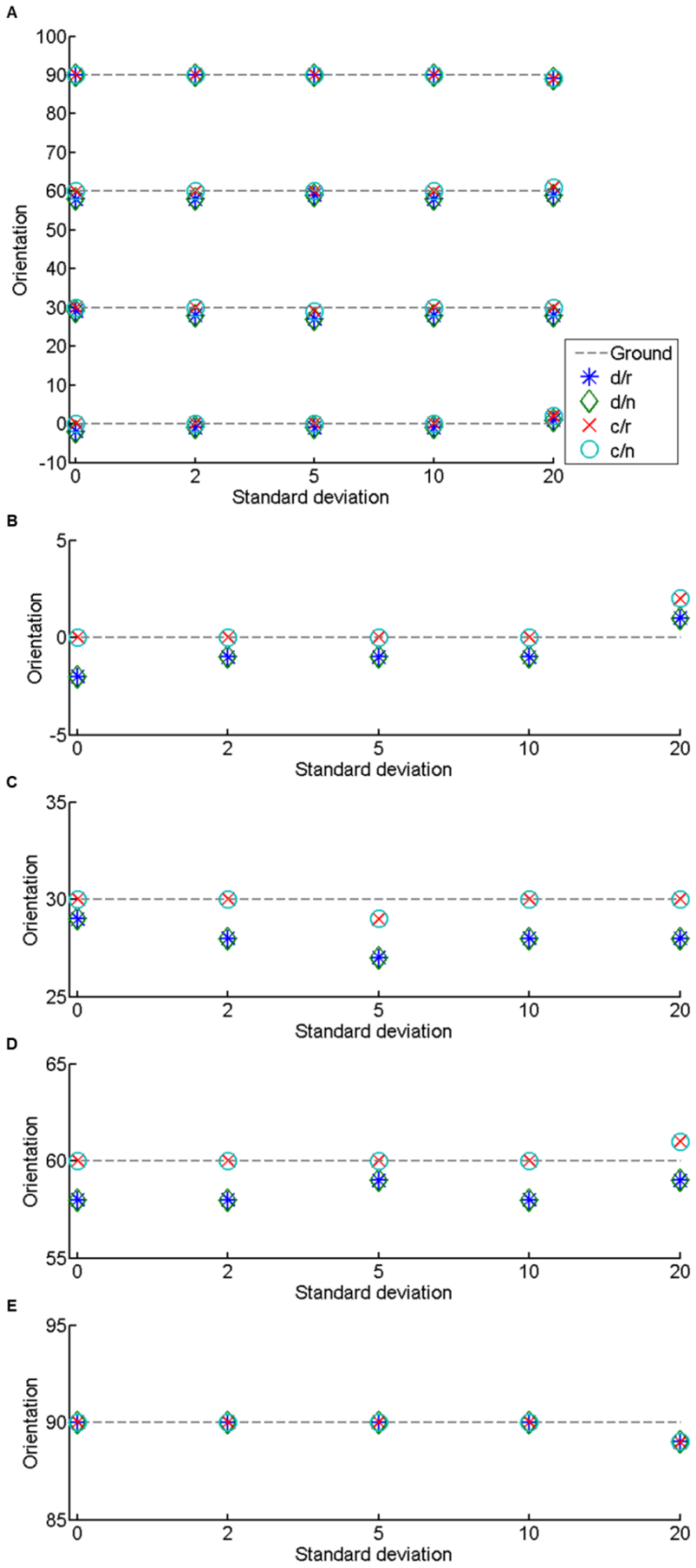

Figure 11. Principal orientation prediction for method combinations. For the discrete (d) and continuous (c) methods, combined with rescaling (r) and normalisation (n), the predicted principal orientation is plotted for each standard deviation and orientation (A), and enlarged for each orientation (B-E) with the real orientation (dashed line) also plotted; n = 80 for each point.

Next, we can consider how the alignment measures vary with the method combinations. For the order measure ρ, rescaling for pre-processing with both discrete and continuous produces greater values than the normalised counterparts (fig. 12A; table VI). However, all curves are similar in their trajectories, all indicating decreasing alignment with increasing synthetic standard deviation.

Table VI. Mean order, ρ, for synthetic images with different standard deviations. For each combination of treatment, i.e., discrete (D), continuous (C) and rescaling (R) and normalisation (N), the mean value, ± SD, for each standard deviation is shown; n = 80 for each treatment.

	Standard deviation				
Method	**0**	**2**	**5**	**10**	**20**
D/R	0.95 ± 0.02	0.94 ± 0.02	0.91 ± 0.04	0.88 ± 0.03	0.75 ± 0.07
D/N	0.91 ± 0.04	0.90 ± 0.04	0.86 ± 0.05	0.82 ± 0.04	0.68 ± 0.07
C/R	0.93 ± 0.01	0.92 ± 0.01	0.90 ± 0.01	0.86 ± 0.02	0.74 ± 0.06
C/N	0.89 ± 0.02	0.88 ± 0.02	0.85 ± 0.02	0.80 ± 0.02	0.67 ± 0.06

Kurtosis, which actually gave identical values for rescaling and normalisation in each type of orientation magnitude data, is heavily affected by changes in method combinations. Here, the discrete orientation magnitude produces a plot similar to that of ρ, with decreasing kurtosis as synthetic standard deviation increases (fig. 12B; table VII). The continuous orientation magnitude is very different to this, actually increasing slightly from standard deviation of zero to two, and thereafter decreasing, albeit at a slow rate (table VII). The cause of this difference is most likely to be the fact that the discrete orientation magnitude is generally more peaked (fig. 7), and the continuous data gives smoother peaks, and thus could result in a lower kurtosis.

Table VII. Mean kurtosis for synthetic images with different standard deviations. The values for both rescaled and normalised data are the same for either discrete (D) or continuous (C) orientation magnitude, so only one set of values for each is shown. Values are ± SD, and n = 80 for each treatment.

	Standard deviation				
Method	**0**	**2**	**5**	**10**	**20**
D	13.65 ± 3.58	12.51 ± 3.40	9.48 ± 2.05	6.18 ± 2.16	3.85 ± 1.40
C	4.26 ± 0.06	4.27 ± 0.04	4.20 ± 0.06	3.57 ± 0.29	1.40 ± 0.45

Measures 1-3, which were only used with discrete orientation magnitude data, gave varying responses to increasing synthetic standard deviation (fig. 12 C-E). First, measure 1, the ratio of the maximum integral to that of the rest of the data, follows a similar trajectory to ρ, decreasing with increasing standard deviation (fig. 12C). Here, rescaling and normalisation give similar results, with rescaling actually producing greater values (table VIII). Measure 2, the ratio of the second biggest integral to the maximum, taken from 1, is highly variable for each synthetic standard deviation, as indicated by the error bars on the plot (fig. 12D). Moreover, it does not behave as might be expected as synthetic standard deviation increases; first, it increases between standard deviations 0 and 5, and then decreases between 5 and 20 (table VIII). As the ratio of the second biggest integral to the maximum, taken from one, we

might expect this measure to high (i.e., close to one) with low synthetic standard deviation, and thereafter, decrease. However, this is not the case, and its variability and trajectory most likely render it and unsuitable measure of alignment. Both rescaling and normalisation produce similar results here. Measure 3, the ratio of the maximum integral to the mean value, taken from one, behaves in a similar manner to measure 1, but is apparently less sensitive at the lower synthetic standard deviations (fig. 12E, table VIII). Again, rescaling and normalisation produce similar results.

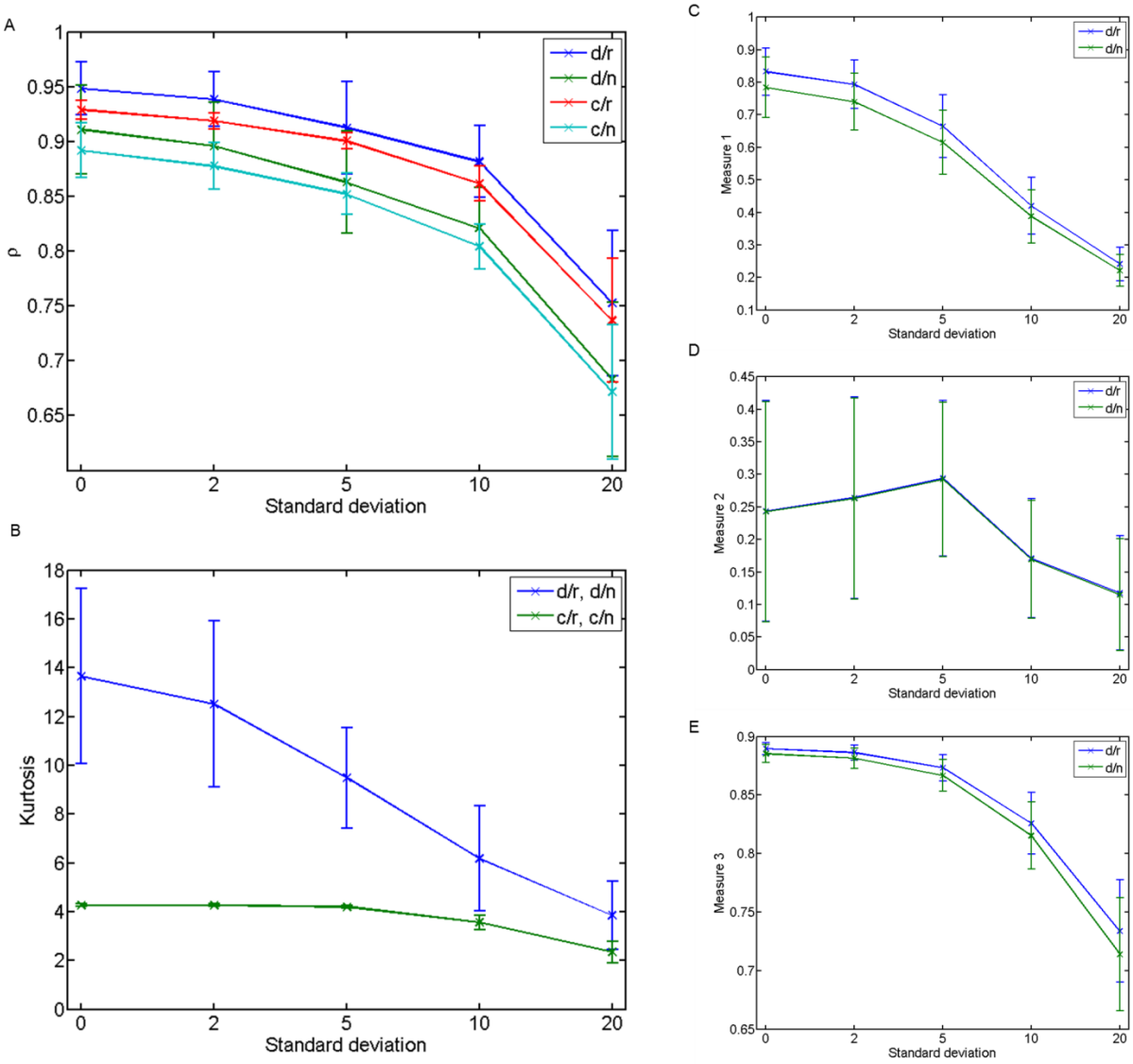

Figure 12. Mean alignment measures for method combinations. For discrete (d) and continuous (c) orientation magnitude data with rescaling (r) and normalisation (n) for pre-processing, the average values (mean ± SD, n = 80) for each synthetic standard deviation are shown for ρ (a), kurtosis (B) and measures 1-3 (C-E). For kurtosis, the values for both rescaling and normalisation were the same in each orientation magnitude data set, so only two curves are shown (B). The measures 1-3 were carried out only on discrete data, so only two curves, for rescaling and normalisation, are shown there (C-E). Refer to table III to recap each measure.

Table VIII. Mean values for measures 1-3 for synthetic images with different standard deviations. These measures were only conducted with the discrete orientation magnitude method, but both pre-processing methods of rescaling (R) and normalisation (N) were used. Values are ± SD, and n = 80 for each treatment.

Measure/Method	**Standard deviation**				
Measure 1	**0**	**2**	**5**	**10**	**20**
R	0.83 ± 0.07	0.79 ± 0.07	0.66 ± 0.10	0.42 ± 0.09	0.24 ± 0.05
N	0.78 ± 0.09	0.74 ± 0.09	0.62 ± 0.10	0.39 ± 0.08	0.22 ± 0.05
Measure 2					
R	0.24 ± 0.17	0.26 ± 0.16	0.29 ± 0.12	0.17 ± 0.09	0.12 ± 0.09
N	0.24 ± 0.17	0.26 ± 0.15	0.29 ± 0.12	0.17 ± 0.09	0.11 ± 0.09
Measure 3					
R	0.89 ± 0.01	0.89 ± 0.01	0.87 ± 0.01	0.83 ± 0.03	0.73 ± 0.04
N	0.89 ± 0.01	0.88 ± 0.01	0.87 ± 0.01	0.82 ± 0.03	0.71 ± 0.05

The plots in figure 12 and data in tables VI-VIII show how each measure tested behaves, and whether its behaviour is changed when the type of orientation magnitude data or pre-processing is changed. They also give an indication as to which combinations are likely to make useful measures later on in the analysis of real cells. For example, kurtosis with the continuous method looks unsuitable, as does measure 2, while measures 1 and 3, and ρ, look promising, as does kurtosis combined with the discrete orientation magnitude. However, to obtain a quantitative understanding of how these measures perform, we need a statistical measure of how well they perform in terms of distinguishing different synthetic standard deviations. Thus, for each set of method and measures, we need to assess the extent to which the data for each standard deviation differ from one another.

The results of this analysis are presented in tables IX-XI. For each combination of methods and measures, the analysis runs thus:

1. Establish whether the variances of the standard deviation data sets are similar with Levene's test; if so, a parametric test can be employed (if the data also satisfy normality criteria), and if not, a non-parametric test must be used.
2. In every case, the data were found to have unequal variances. Thus, the non-parametric equivalent of an analysis of variance, the Kruskal-Wallis test, is used to determine if there is significant difference between the standard deviation data.
3. In every case, there was a significant difference between the standard deviation data. Therefore, the non-parametric equivalent of a student's t-test, the Wilcoxon rank sum test, is used to compare adjacent standard deviation data (i.e., 0 is compared with 2; 2 with 5; 5 with 10; 10 with 20), giving four comparisons.
4. Because multi-comparison procedures like this are prone to statistical error (type 1 error), an adjustment is made to the significance level for which the p-value is judged to be significant. Here, the Bonferroni adjustment is used, which determines the new significance level by dividing the previous level by the number of comparisons; thus, here, it is 0.01/4 = 0.0025.

Table IX. Statistics for synthetic alignment quantified by order measure ρ. In each combination of methods, i.e., discrete (D), continuous (C) and rescaling (R) and normalisation (N), the data for each synthetic standard deviation were tested for homoscedasticity with Levene's test. A significant p-value (✓) indicates heteroscedasticity. A Kruskall-Wallis test was then conducted to test for significant (✓) differences between all standard deviation data. Individual standard deviation sets (SD#) were then compared with one another using a Wilcoxon rank sum test, with significance (no = x; yes = ✓) being tested against a p-value defined by the Bonferroni correction.

	Method			
Measure	**D/R**	**D/N**	**C/R**	**C/N**
Levene p	1.12×10^{-8}	5.55×10^{-7}	4.50×10^{-15}	3.35×10^{-17}
p < 0.01	✓	✓	✓	✓
Kruskal-Wallis p	2.86×10^{-60}	1.26×10^{-58}	6.31×10^{-78}	8.79×10^{-71}
p < 0.01	✓	✓	✓	✓
Wilcoxon rank sum SD# p < Bonferroni				
0 vs 2	0.01	0.01	1.39×10^{-14}	2.52×10^{-5}
	x	x	✓	✓
2 vs 5	7.04×10^{-7}	2.82×10^{-6}	5.02×10^{-23}	1.39×10^{-10}
	✓	✓	✓	✓
5 vs 10	2.87×10^{-11}	1.52×10^{-10}	4.03×10^{-27}	7.85×10^{-24}
	✓	✓	✓	✓
10 vs 20	5.64×10^{-25}	1.03×10^{-24}	1.84×10^{-27}	1.27×10^{-27}
	✓	✓	✓	✓

For ρ, the only non-significant results were for the comparison of synthetic standard deviation 0 and 2 for both rescaling and normalisation with discrete data (table IX). Thus, ρ performs better when used with continuous data; there is not much to choose between rescaling and normalisation here, although rescaling does produce smaller p-values.

In all comparisons of synthetic standard deviations 0 and 2, kurtosis did not show a significant difference (table X). Therefore, the increase in kurtosis with the continuous data between standard deviations 0 and 2 is not a significant increase, and the large decrease for kurtosis with the discrete data is not also not significant; this is supported by the fact that these mean values have large standard deviations (fig. 12B, table VII). Thereafter, all standard deviations with both types of data are statistically distinguishable. In fact, although the differences between synthetic standard deviations for kurtosis with continuous data appeared to be indistinguishable in the plots (fig. 12B), these actually have smaller p-values than kurtosis based on the discrete data (table X).

Table X. Statistics for synthetic alignment quantified by Kurtosis. In each combination of methods, i.e., discrete (D), continuous (C) and rescaling (R) and normalisation (N), the data for each synthetic standard deviation were tested for homoscedasticity with Levene's test. A significant p-value (✓) indicates heteroscedasticity. A Kruskall-Wallis test was then conducted to test for significant (✓) differences between all standard deviation data. Individual standard deviation sets (SD#) were then compared with one another using a Wilcoxon rank sum test, with significance (no = x; yes = ✓) being tested against a p-value defined by the Bonferroni correction.

	Method			
Measure	**D/R**	**D/N**	**C/R**	**C/N**
Levene p	7.11E-19	7.11E-19	1.96E-23	1.96E-23
p < 0.01	✓	✓	✓	✓
Kruskal-Wallis p	6.25E-61	6.25E-61	3.85E-68	3.85E-68
p < 0.01	✓	✓	✓	✓
Wilcoxon rank sum				
SD#				
p < Bonferroni				
0 vs 2	8.33E-02	8.33E-02	2.10E-02	2.10E-02
	x	x	x	x
2 vs 5	4.79E-09	4.79E-09	2.03E-10	2.03E-10
	✓	✓	✓	✓
5 vs 10	1.55E-17	1.55E-17	2.39E-27	2.39E-27
	✓	✓	✓	✓
10 vs 20	2.10E-13	2.10E-13	6.54E-26	6.54E-26
	✓	✓	✓	✓

The analysis of measures 1-3 supports the previous conclusion that measure 2 is not ideally suited to quantifying alignment, since the first two comparisons, for synthetic standard deviations 0 and 2, and 2 and 5, were not significant (table XI). The low sensitivity of measure 3 at lower standard deviations is supported by the non-significant result between 0 and 2, but significant differences elsewhere. Measure 1 also has a non-significant difference between synthetic standard deviations of 0 and 2, but significant differences between all other groups. For every measure, these results are the same for rescaled and normalised data.

Table XI. Statistics for synthetic alignment quantified by measures 1-3. For only discrete orientation magnitude data, rescaled (R) and normalised (N) data for each synthetic standard deviation were tested for homoscedasticity with Levene's test. A significant p-value (✓) indicates heteroscedasticity. A Kruskall-Wallis test was then conducted to test for significant (✓) differences between all standard deviation data. Individual standard deviation sets (SD#) were then compared with one another using a Wilcoxon rank sum test, with significance (no = x; yes = ✓) being tested against a p-value defined by the Bonferroni correction.

	Method	
Measure 1	**R**	**N**
Levene p	9.44E-07	2.06E-07
p < 0.01	✓	✓
Kruskal-Wallis p	2.42E-71	3.67E-70
p < 0.01	✓	✓
Wilcoxon rank sum		
SD#		
p < Bonferroni		
0 vs 2	4.69E-03	6.98E-03
	x	x
2 vs 5	4.45E-14	1.72E-12
	✓	✓
5 vs 10	2.16E-24	8.71E-24
	✓	✓
10 vs 20	1.37E-24	2.16E-24
	✓	✓
Measure 2		
Levene p	2.55E-15	9.37E-16
p < 0.01	✓	✓
Kruskal-Wallis p	1.30E-16	5.42E-17
p < 0.01	✓	✓
Wilcoxon rank sum		
SD#		
p < Bonferroni		
0 vs 2	3.20E-01	3.54E-01
	x	x
2 vs 5	3.89E-01	4.08E-01
	x	x
5 vs 10	1.52E-10	1.39E-10
	✓	✓
10 vs 20	2.92E-04	1.83E-04
	✓	✓

Table XI, contd.

Measure 3		
Levene p	5.34E-27	1.55E-26
p < 0.01	✓	✓
Kruskal-Wallis p	2.42E-71	3.67E-70
p < 0.01	✓	✓
Wilcoxon rank sum		
SD#		
p < Bonferroni		
0 vs 2	0.005	0.007
	x	x
2 vs 5	4.45E-14	1.72E-12
	✓	✓
5 vs 10	2.16E-24	8.71E-24
	✓	✓
10 vs 20	1.37E-24	2.16E-24
	✓	✓

Clearly, the lower synthetic standard deviations, 0 and 2, are the most difficult to distinguish with the measures proposed here; indeed, they are more similar than any other of the standard deviations. The only measure that distinguishes between these data is ρ, with continuous data. Furthermore, ρ is a good candidate for the alignment measure since it can also distinguish every other synthetic standard deviation. Thus, it performs better than any other measure tested. In addition to this, its best performance is with continuous data, which also gives the best orientation prediction accuracy (table V), and the formula for ρ is also calculated using Ω, the means of estimating principal orientation. Thus, continuous data and ρ are methods of choice, but we must distinguish between rescaling and normalisation for the pre-processing step. Since there is very little to choose between them in the analysis here, we can return to the previous analysis of these methods, where it was found that normalisation reproduced characteristics of the original data better than rescaling; thus, normalisation will be used for pre-processing form hereon.

g. Window size in the continuous orientation magnitude

The continuous method of obtaining the orientation magnitude was found to be preferable in the last sub-section, and, although the order measure ρ was determined to be preferable, the other available measure for continuous orientation magnitude data, kurtosis, will also be used here, to check whether it improves in its utility in this analysis. One facet of the continuous method that was briefly mentioned above but discussed no further was the size of the "window" used. The easiest measure for window size is just the size of the angle that it covers; for example, in the previous sub-section, the window size was 30°, meaning that the area that contributed to one point in the orientation magnitude data was the sum of an area of the FT that spanned 30°. As yet, we have no idea as to how, if at all, the window size affects the orientation magnitude data and subsequent analyses; thus, the focus of this sub-section is to investigate window size.

The window sizes analysed here are: 5°, 10°, 20°, 30° and 40°. Data were generated as before, using the synthetic images and normalisation as the pre-processing method. Table XII shows how changing window size affects the accuracy of orientation prediction, quantified by the mean squared error. The smallest window size of 5° degrees achieves total accuracy for the synthetic images with zero standard deviation, yet, this window size and that of 10° are less accurate than the larger windows when synthetic images with larger standard deviations are tested. Overall, taking the mean squared error of all predictions over all standard deviations indicates that the window size of 30° is the best all-rounder. Thus, the sacrifice of increased accuracy at smaller synthetic standard deviations for better predictions at greater standard deviations produces a better overall score. Moreover, the likelihood that, in real images, we are unlikely to encounter perfect alignment, as in the zero standard deviation case, supports the choice window sizes 20° - 40°, which perform better at intermediate and large synthetic standard deviations.

Table XII. Mean squared error of principal orientation prediction for each synthetic image standard deviation and overall, for each window size. The mean squared error of orientation prediction is given for each combination of synthetic image standard deviation (SD) and window size, as well as the overall value for each window size. For each mean value, n = 80.

	Window size (°)				
SD	**5**	**10**	**20**	**30**	**40**
0	0.0000	0.0125	0.0125	0.0125	0.0125
2	0.2500	0.3125	0.3125	0.3000	0.3125
5	1.5750	1.4875	1.5000	1.5000	1.5125
10	4.2625	4.1375	4.1125	4.2250	4.1375
20	19.0125	19.1000	18.6875	18.5500	18.6250
Overall	5.0200	5.0100	4.9250	4.9175	4.9200

How does changing window size affect alignment scores? Figure 13 shows the orientation magnitude for these different window sizes, plotted in groups of synthetic image standard deviation, for the synthetic images with a principal orientation of -60°. Remember, according to the rule that the maxima in the FT are perpendicular to the direction of best alignment in the image, the peaks in the orientation magnitude are at approximately 30° in figure 13. For each synthetic image standard deviation group, there is an example orientation magnitude plot, taken from one instance of the 80 repeats for each, and the mean orientation magnitude.

The most striking feature of the plots at lower standard deviations is how much more peaked the data are for smaller window sizes, for both the single examples and averages. Thus, decreasing window size increases the size of peaks in the orientation magnitude at lower standard deviations. This is to be expected, since where there is a tightly localised maximum in the FT, the orientation magnitude will elicit a greater response at smaller window values, which do not decrease the intensity of the maximum through averaging with adjacent, lower values.

The increased peak size is consistent with the findings in table XII that the smallest window size of 5° has excellent accuracy at lower standard deviations, since this is probably a result of unambiguous localisation of the peak, due to its size. However, again in agreement with the data in table XII, the peaks for smaller window sizes are quickly diminished as the standard deviation increases. In both the single and average cases, the smallest window size is still responsible for the greatest orientation magnitude at the larger standard deviations, but those of larger window sizes approach much closer here, especially in the average cases.

Furthermore, as we might expect, where smaller window sizes produced larger orientation magnitudes from less averaging in the lower standard deviations, at the larger standard deviations, the lower amount of averaging makes the orientation magnitude plot more "noisy", since it will now be more sensitive to variations in the FT. In all cases, the width of the peaks in orientation magnitude increase with increasing standard deviation.

To test whether these differences in orientation magnitude across the window sizes has an effect on the quantification of alignment, the mean values of order, ρ, and kurtosis were found for each synthetic standard deviation and window size combination. I re-examine kurtosis here, even though it performed poorly with continuous data in the previous analysis, simply to determine if changing window size affects the performance of this measure. The data are plotted in figure 14.

For the order measure ρ, the values behave in a similar manner with increasing standard deviation for each window size; the effect of increasing window size is to shift the data so that each value for ρ is greater (fig. 14, table XIII). This agrees with the orientation magnitude plots (fig. 13), where smaller window size produced larger peaks. Thus, for ρ, although changing window size has a quantitative effect on absolute scores of alignment, it does not change the relationship between synthetic image standard deviation and alignment quantification.

The same is not true of kurtosis, where decreasing window size not only quantitatively affects the result, but qualitatively changes the relationship between standard deviation and alignment quantification (fig. 14, table XIII). Again, the increase in kurtosis with smaller window size will be a result of the more peaked orientation magnitude data, though the origin of the qualitative relationship change is not immediately clear; it may be related to the problem of apparently reduced anisotropy when the peak spans the -89°-90° transition, briefly discussed earlier. This is an issue from which some of the other alignment measures, such as the resultant vector, suffer, and it results and decreased alignment score, because the peak is effectively split within the data. The reason it could contribute less when window size is small is because these data have narrower peaks; narrower peaks are less likely to span the -89°-90° transition, and so the data will not present the same problem. The fact that the kurtosis scores are so dramatically enhanced for lower standard deviations supports this notion, since, in these cases, peaks are even narrower than their higher standard deviation counterparts. Moreover, the kurtosis value for window size 5° and standard deviation of 20 are of a similar magnitude to those of larger window size.

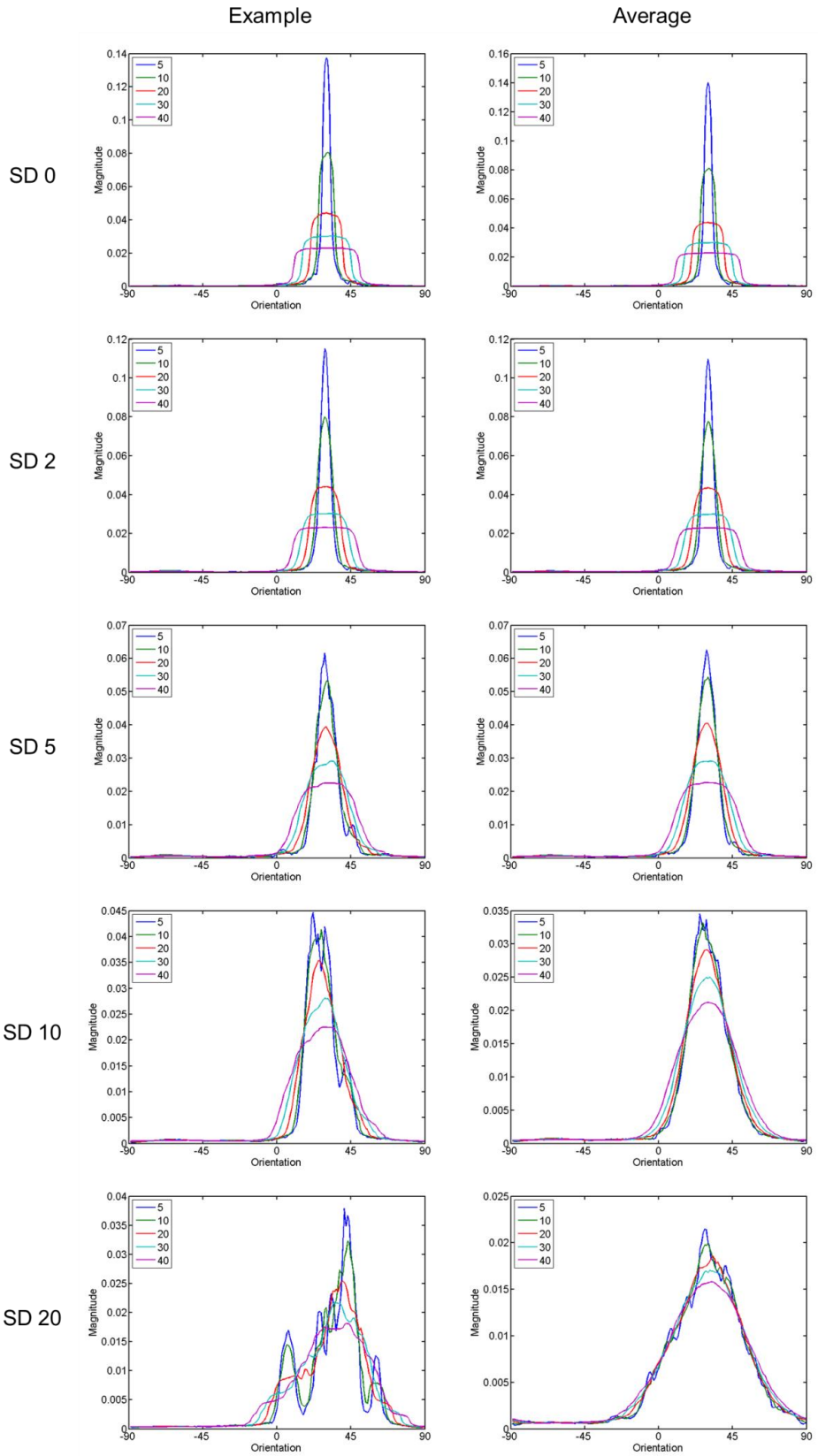

Figure 13. Orientation magnitude depends on synthetic standard deviation and window size (previous page). Plots of single data sets ("example"; left panels) and averages ("average"; right panels, n = 80) for synthetic images with varying standard deviation (SD) and principal orientation -60°, for each window size.

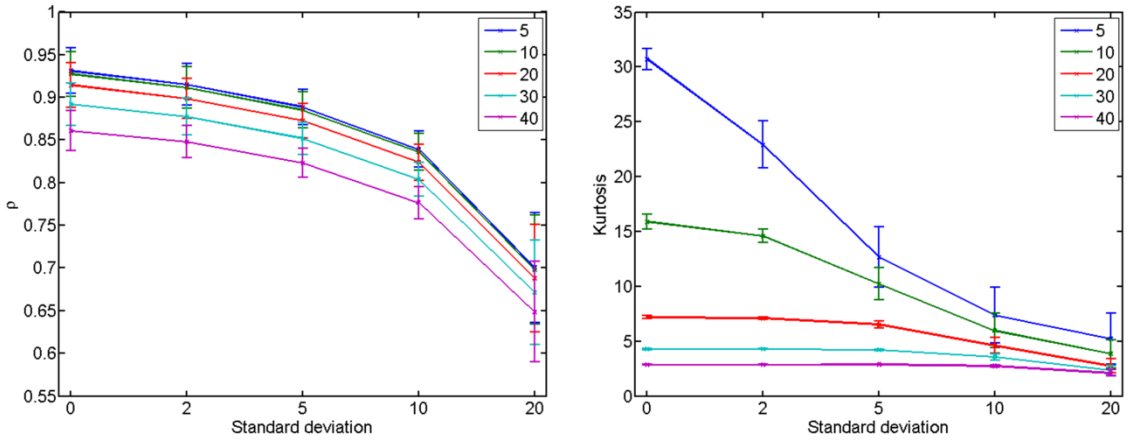

Figure 14. Mean order, ρ, and kurtosis for each synthetic image standard deviation and window size. Left and right panels show average values of ρ and kurtosis, respectively, as synthetic standard deviation increases, colour coded by window size.

Table XIII. Mean order, ρ, and kurtosis for synthetic images with different standard deviations for each window size. The mean order, ρ, and kurtosis for orientation magnitude is given for each combination of synthetic image standard deviation (SD) and window size. Values are ± standard deviation, and n = 80 for each.

	Window size (°)				
	5	**10**	**20**	**30**	**40**
ρ					
SD					
0	0.93 ± 0.03	0.93 ± 0.03	0.91 ± 0.03	0.89 ± 0.02	0.86 ± 0.02
2	0.92 ± 0.02	0.91 ± 0.02	0.90 ± 0.02	0.88 ± 0.02	0.85 ± 0.02
5	0.89 ± 0.02	0.89 ± 0.02	0.87 ± 0.02	0.85 ± 0.02	0.82 ± 0.02
10	0.84 ± 0.02	0.84 ± 0.02	0.82 ± 0.02	0.80 ± 0.02	0.78 ± 0.02
20	0.70 ± 0.06	0.70 ± 0.06	0.69 ± 0.06	0.67 ± 0.06	0.65 ± 0.06
Kurtosis					
SD					
0	30.72 ± 0.97	15.91 ± 0.67	7.19 ± 0.15	4.26 ± 0.06	2.84 ± 0.03
2	22.91 ± 2.15	14.60 ± 0.59	7.10 ± 0.11	4.27 ± 0.04	2.86 ± 0.02
5	12.68 ± 2.77	10.22 ± 1.46	6.52 ± 0.29	4.20 ± 0.06	2.88 ± 0.02
10	7.35 ± 2.53	5.97 ± 1.59	4.59 ± 0.72	3.57 ± 0.29	2.74 ± 0.10
20	5.21 ± 2.33	3.83 ± 1.31	2.75 ± 0.67	2.34 ± 0.45	2.08 ± 0.29

Given the principal orientation prediction and alignment data, how do we evaluate which window size is best? Clearly, some window sizes are better at predicting principal orientations than others, depending on the standard deviation in the synthetic image (table XII). The alignment measures show that some window sizes may not be suitable if we wish to persevere with both alignment measures, i.e., a window size of 40° may yield kurtosis quite unhelpful to discriminate grades of alignment (fig. 14). On the other hand, the kurtosis values appear to be remarkably reproducible, with low standard deviation (table XIII).

To better grasp the utility of each window size and the complementary alignment measures, we can turn to an analysis similar to that of the previous sub-section. Here, for each window size, if all of the data are found to be significantly different in some way with an analysis of variance, then the data for standard deviation are compared with the data for adjacent standard deviations, testing for significant difference between them with a t-test or non-parametric equivalent. The aim is to establish which combination of window size and alignment measure is best, taking "best" to be that which distinguishes adjacent standard deviation data with statistical significance.

The results of this analysis are shown in table XIV. For each measure and for every window size, it was found that the data for each standard deviation did not have equal variance (Levene's test, $p < 0.01$), and that there were significant differences between them (Kruskal-Wallis, $p < 0.01$). Hence, adjacent data sets were tested against one another, with all but one comparison being significantly different at the level of Bonferroni adjustment for multi-comparison statistics (Wilcoxon rank sum test, $p < 0.01/4$). The two sets of data that were not significantly different were those previously determined to not be different, for kurtosis with window size 30°, standard deviations 0 and 2.

The significant differences between data sets for kutosis at all window sizes apart from that mentioned is quite surprising, given that, in figure 14 and table XIII, they appear, in many cases, to be quite similar. However, as already mentioned, those values have very small standard deviations, and that is consistent with the statistical findings here.

Continuing with kurtosis, although there is significant difference between standard deviation data for window sizes of 30° and 40°, it is unlikely that this window size and alignment measure combination will be useful in the analysis of real images, since the kurtosis actually increases before decreasing, as synthetic image standard deviation increases. Two things are of note here: first, that, although there are significant differences at the synthetic standard deviations tested, in real images, levels of disorder that are intermediates of the synthetic standard deviation may prove indistinguishable, and second, in order to limit the number of comparisons in the multi-comparison statistical tests, only adjacent data were tested against one another; we do not know if distant groups are statistically different from one another or not.

For ρ, it would be difficult to choose between window sizes based on the analysis in table XIV. Indeed, the p-values are similar for each adjacent data set across the window sizes tested. This is consistent with the plot of ρ in figure 14, where the data followed similar trajectories, the only difference being the position on the y-axis.

To conclude this section and fix the last variable in the pipeline of analysis, the average accuracy of orientation prediction afforded by window sizes of 20°-40° certainly makes those sizes more attractive. Moreover, although smaller window sizes allow excellent orientation prediction at smaller synthetic standard deviation, such high degrees of order are unlikely to be encountered in real images. However, choosing window sizes of this size will prohibit the use of kurtosis as an alignment measure, though ρ performs just as well as kurtosis, so the

need for two measures is negated somewhat. In terms of ρ, since there is nothing to choose between window sizes for distinction of synthetic standard deviations (table XIV), then the choice is dictated by orientation prediction (table XII), for which window size 30° performs best, particularly at the greatest standard deviation, which may well be representative of a similar level of disorder found in real cells. Thus, for the preliminary analysis of real cells in the next section, orientation magnitude will be obtained by the continuous method with a window size of 30°, normalised, and subsequently analysed for anisotropy using only the order measure ρ.

Table XIV. Statistics for synthetic alignment for window sizes quantified by ρ and kurtosis. For each window size, the data for each synthetic standard deviation were tested for homoscedasticity with Levene's test. A significant p-value (✓) indicates heteroscedasticity. A Kruskall-Wallis test was then conducted to test for significant (✓) differences between all standard deviation data. Individual standard deviation sets (SD#) were then compared with one another using a Wilcoxon rank sum test, with significance (no = x; yes = ✓) being tested against a p-value defined by the Bonferroni correction.

	Window size (°)				
	5	**10**	**20**	**30**	**40**
ρ					
Levene p	9.50E-17	8.29E-17	7.44E-17	3.35E-17	1.29E-17
p < 0.01	✓	✓	✓	✓	✓
Kruskal-Wallis p	4.43E-70	4.71E-70	3.15E-70	8.79E-71	1.97E-71
p < 0.01	✓	✓	✓	✓	✓
Wilcoxon rank sum SD# p < Bonferroni					
0 vs 2	9.37E-06 ✓	9.82E-06 ✓	1.20E-05 ✓	2.52E-05 ✓	9.66E-05 ✓
2 vs 5	3.90E-09 ✓	5.76E-09 ✓	2.18E-09 ✓	1.39E-10 ✓	2.94E-12 ✓
5 vs 10	6.82E-23 ✓	7.81E-23 ✓	3.82E-23 ✓	7.85E-24 ✓	1.23E-24 ✓
10 vs 20	1.32E-27 ✓	1.32E-27 ✓	1.32E-27 ✓	1.27E-27 ✓	1.27E-27 ✓
Kurtosis					
Levene p	9.91E-04	1.75E-09	2.54E-26	1.96E-23	3.53E-33
p < 0.01	✓	✓	✓	✓	✓
Kruskal-Wallis p	9.83E-77	4.27E-78	1.17E-76	3.85E-68	5.43E-64
p < 0.01	✓	✓	✓	✓	✓
Wilcoxon rank sum SD# p < Bonferroni					
0 vs 2	9.75E-28 ✓	4.34E-22 ✓	1.85E-04 ✓	2.10E-02 x	1.81E-08 ✓
2 vs 5	1.42E-27 ✓	1.32E-27 ✓	1.13E-25 ✓	2.03E-10 ✓	2.76E-10 ✓
5 vs 10	1.26E-20 ✓	2.48E-24 ✓	2.99E-27 ✓	2.39E-27 ✓	4.72E-25 ✓
10 vs 20	1.36E-10 ✓	1.27E-15 ✓	1.81E-24 ✓	6.54E-26 ✓	3.28E-26 ✓

II. Real images: introducing "MtFT"

a. The data

The extensive analysis of the various components of the FT-based analysis to derive microtubule organisation can now be put together in an analysis of real microtubule images. This analysis pipeline, consisting of image mean-padding, taking the FT, analysing the power spectrum to obtain the orientation magnitude using the "continuous" method with a window size of 30°, and quantifying orientation and alignment using the dominant angle, Ω, and the order parameter, ρ, is encompassed in what will be referred to as "MtFT", for Microtubule Fourier Transform.

Here, I analysed sections taken randomly from images of the microtubule cytoskeleton in cells depleted of the plus-tip protein EB2, discussed in the introductory chapter, and compared them to control, scramble-siRNA cells (analysis of full images is discussed in section C). Here, EB2 is depleted with siRNA, and the control cells are treated with scramble siRNA; methods are detailed in the appendix (section E). Previously in the Mogensen lab, depletion of EB2 has been shown to give rise to straighter, better-aligned and perhaps more bundled microtubules (Goldspink et al., 2013). In that study, microtubule alignment was quantified by manually counting the number of occurrences of microtubules crossing each other (fig. 15).

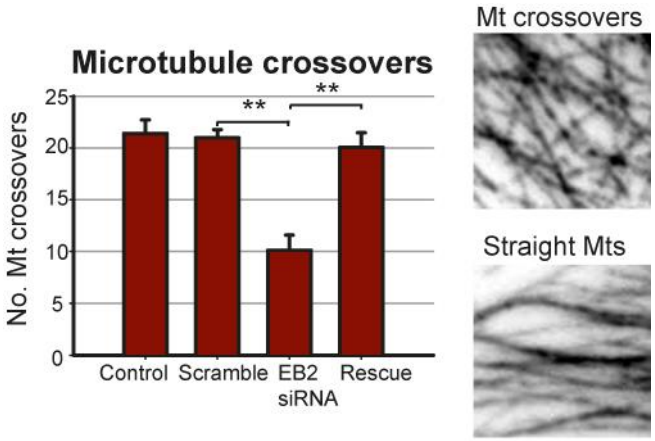

Figure 15. Previous analysis of EB2-siRNA microtubule organisation. EB2 depleted cells (bottom right) were found to have significantly better-aligned microtubules than control cells (top-right), quantified by numbers of microtubule crossover events (left). From Goldspink et al. (2013).

Using images that have previously been shown to differ in microtubule organisation means that we already have some idea that there are differences in microtubule alignment, otherwise it will be difficult to assert that the alignment measures are effective, and that MtFT is useful. Rather than try to quantify organisation in the whole of each image, for this preliminary analysis, I will take a section from each image.

b. Quantifying microtubule organisation

Both experimental treatments were subject to the same analysis: first, the FT was taken of each region, and the orientation magnitude was found using the continuous approach with a window size of 30°, and normalisation as the choice of pre-processing. Then, the principal orientation was predicted using the dominant angle and the anisotropy of the orientation magnitudes was quantified using the order measure, ρ. This analysis pipeline is summarised in figures 16 and 17 for the control and EB2-depleted regions, respectively.

A general inspection of the FTs and orientation magnitude plots in figures 16-17 suggests that there is indeed a difference between the two treatments: first, the FTs in the control regions tend not to have any discernable maxima in a specific direction, agreeing with the region images, while those for the EB2-depleted regions appear to have higher intensities in the FTs at particular locations that correspond to the apparent principal orientations in the images. Second, these observations are borne out in the orientation magnitude plots, where the absolute values of data tend to be lower in the control treatment than in the EB2-depleted treatment, and, furthermore, the shapes of the control orientation magnitude do indeed appear to be more isotropic than those of the EB2-depleted regions.

On this note, the choice of normalisation for pre-processing finds support from the fact that some of the orientation magnitude plots for the control condition (fig. 16) resemble the "flat" data used earlier (fig. 8); there, it was found that rescaling did not reproduce some characteristics of this type of data as well as normalisation (table II).

The values in figures 16-17, for ρ, serve to justify the initial conclusions that were made upon inspection of the FTs and orientation magnitudes of each treatment. We can see that the values for control regions are consistently lower than those for control cells; indeed, the maximum value for the control regions, 0.28, is still 0.15, over half its value, lower than the minimum, 0.43, for the EB2-depleted regions. The individual ρ values are collected in table XV, with the mean value also shown. A one-sample Kolmogorov-Smirnov test for both the control and EB2-depleted conditions, against a standard normal distribution, verified that they satisfied normality (null hypothesis of normality, $p > 0.01$ for both treatments), and the data were found to have equal variances with both a Bartlett's and Levene's test (null hypothesis of equal variances, $p >> 0.01$). The non-significant value for the Bartlett's test also supports the result of the Kolmogorov-Smirnov test, since Bartlett's test can return significant p-values if used with non-normal data. Thus, as the data satisfied the normality and equal variance requirements of the t-test, a two-sample, two-tailed t-test was used to test for a difference between the conditions. The ρ values for control and EB2-depleted regions were found to be significantly different ($p < 0.001$).

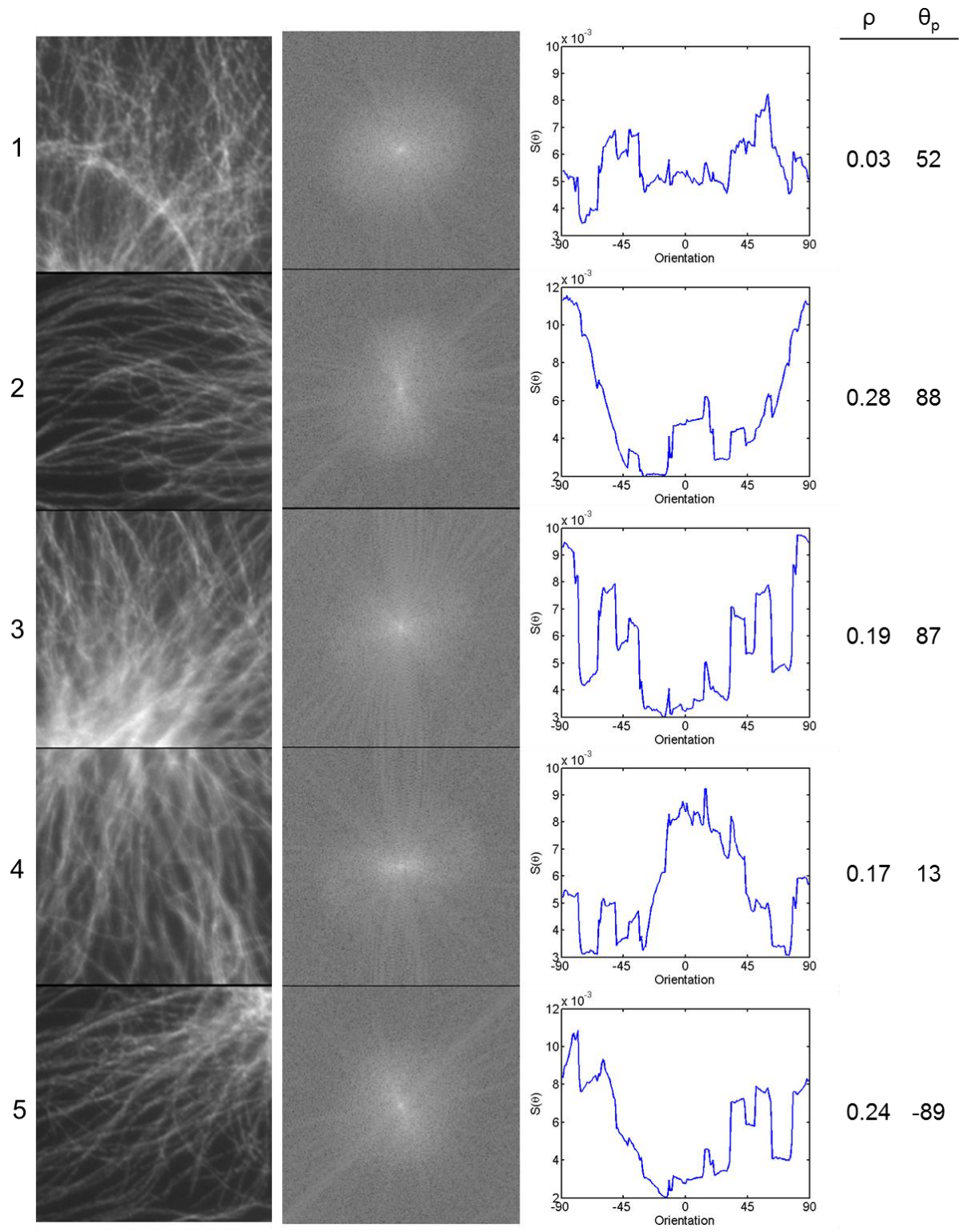

Figure 16. Preliminary analysis of real cells, scramble treatment. Regions of control, scramble cells (left panels), their FTs (middle left panels) and corresponding orientation magnitude plot (middle right panels), and order, ρ, and predicted principal orientation (θ_p).

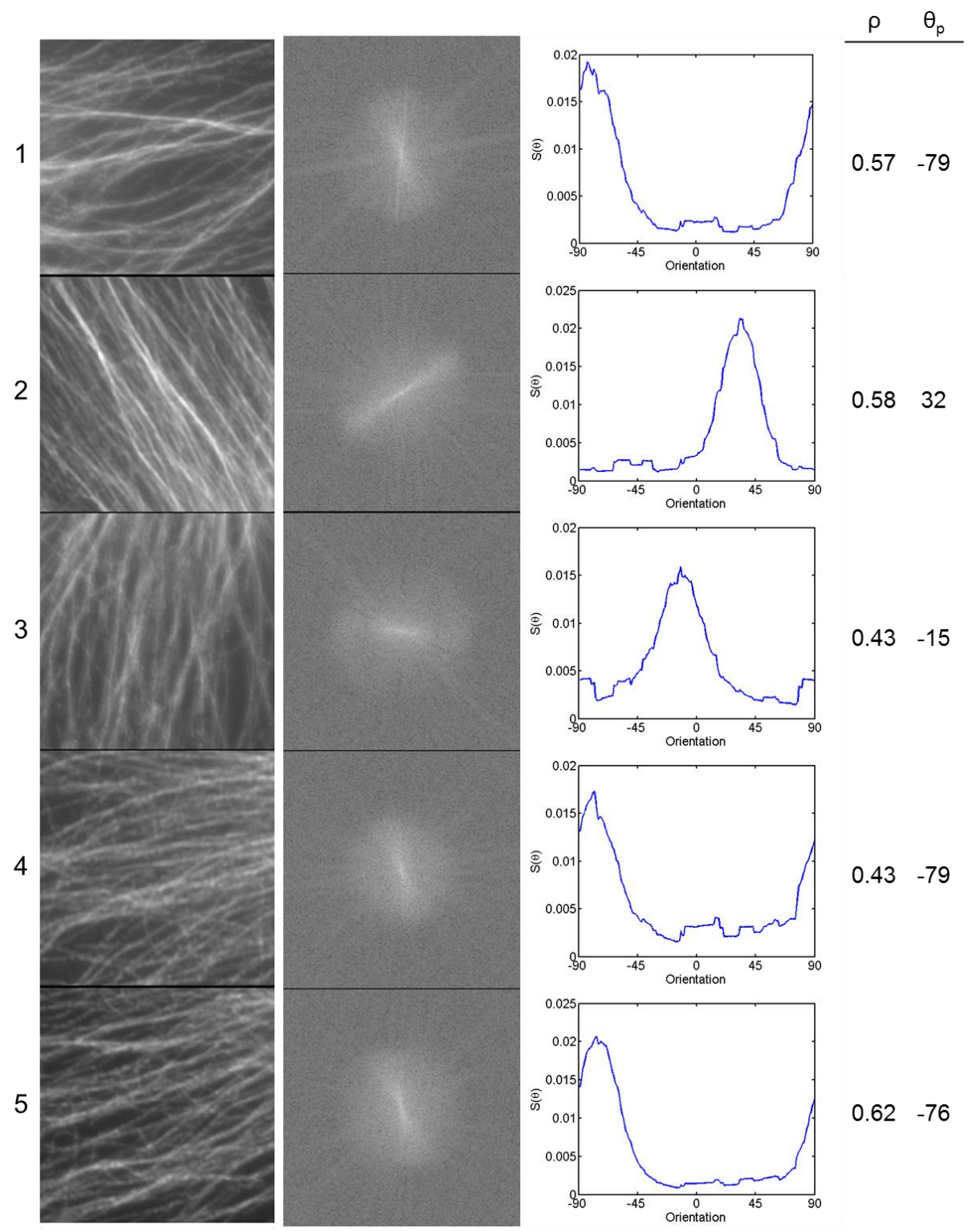

Figure 17. Preliminary analysis of real cells, EB2-siRNA treatment. Regions of EB2-siRNA cells (left panels), their FTs (middle left panels) and corresponding orientation magnitude plot (middle right panels), and order, ρ, and predicted principal orientation (θ_p).

Table XV. Microtubule alignment and orientation in real scramble and EB2-depleted cells, quantified by order, ρ. The orientation magnitudes in regions 1-5 in figures () and () were quantified for anisotropy with ρ, and the mean value was also determined.

Region	Treatment			
	Scramble		EB2-siRNA	
	Alignment			
1	0.03		0.57	
2	0.28		0.58	
3	0.19		0.43	
4	0.17		0.43	
5	0.24		0.62	
Mean	**0.18**		**0.53**	
	Orientation			
	Original	Adjusted	Original	Adjusted
1	52	-38	-79	11
2	88	-2	32	-58
3	87	-3	-15	75
4	13	-77	-79	11
5	-89	1	-76	14

The significant difference in microtubule alignment between control and EB2-depleted regions supports the efficacy of the method presented in this chapter, providing strong evidence that it is applicable to quantification of the organisation of the microtubule cytoskeleton, since the cells used for this preliminary analysis were previously found to have differences in alignment using a different method. To further evaluate the method, the next sub-section describes comparison with a previously-published method to quantify microtubule orientation and alignment.

c. Comparison with an established method

To further evaluate the efficacy of MtFT, I compare it here to the method developed by Boudaoud et al. (2014), who created "FibrilTool" to quantify microtubule, or any other fibrillar structure, orientation and alignment. FibrilTool was used on the same images as in the previous sub-section (figs. 16-18) and the results are shown in table XVI, with the values from my method repeated for ease of comparison. The tool required that a region-of-interest (ROI) is first defined, and the enclosed area is analysed. Thus, ROIs were created that encompassed the majority of each image (fig. 18).

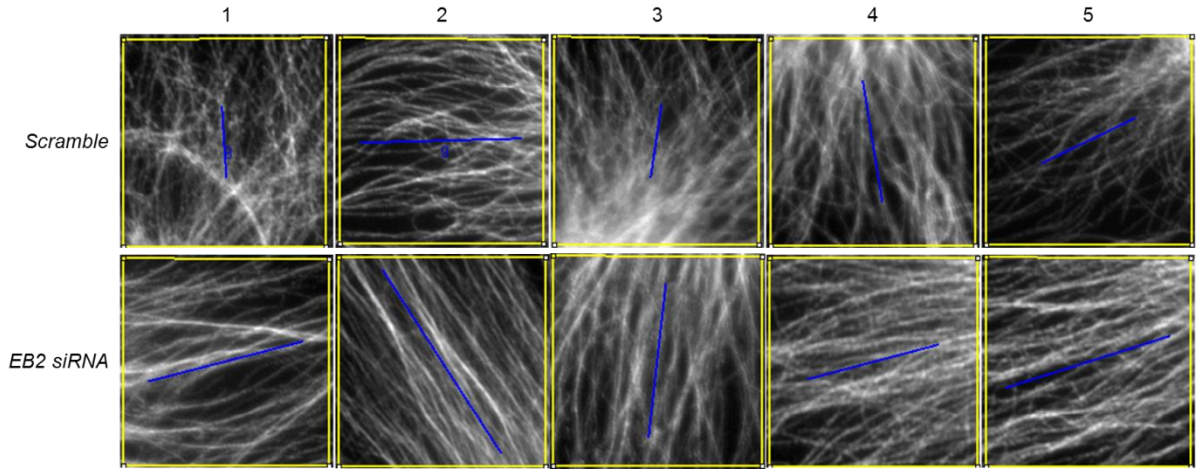

Figure 18. Analysis of preliminary images with "FibrilTool". ROIs (yellow) were defined that covered most of each image (1-5) in each treatment. FibrilTool plots a line on the image that is oriented in the direction of the principal orientation (blue), with length according to the degree of alignment in this direction. Scramble indicates the scramble siRNA-treated cells, and FibrilTool is explained in the text.

The alignment scores from FibrilTool also satisfy normality and equal-variance criteria (2-sample F-test, $p > 0.05$). While the alignment scores from each method for the scramble condition were not significantly different from one another (2-sample t-test, $p > 0.05$), they were in the EB2-depleted condition (2-sample t-test, $p < 0.05$). However, FibrilTool alignment scores for the two conditions were significantly different from one another (2-sample t-test, $p < 0.05$).

The results from FibrilTool and MtFT thus agree qualitatively on the difference in alignment between the two conditions. Quantitatively, this agreement is stronger for the scramble condition, where both methods report low alignment scores. MtFT returns a lower average value for the scramble condition and higher average value for the EB2-depleted condition, hence MtFT finds a greater difference between the two. In terms of orientation prediction, the two methods estimate similar values in situations where the alignment is stronger; in the EB2-depleted condition, therefore, the orientation predictions are close to one another. However, in the scramble condition, the two image regions that visually look most difficult to interpret (numbers 1 and 3) are those that yield the greatest disagreement between the two methods. In the other three cases, where a predominant orientation is perhaps more easily identified by visual inspection, orientation predictions are not as similar as in the EB2-depleted condition, but they are more similar than image regions 1 and 3.

Table XVI. Comparison of FibrilTool and MtFT for orientation prediction and alignment. For each experimental condition, the alignment scores and orientation predictions from each method are shown.

Region	Alignment		Orientation	
	FibrilTool	MtFT	FibrilTool	MtFT
Scramble				
1	0.17	0.03	-85.92	-38
2	0.39	0.28	1.3	-2
3	0.18	0.19	81.43	-3
4	0.29	0.17	-81.17	-77
5	0.25	0.24	25.76	1
Mean	**0.26**	**0.18**		
EB2-siRNA				
1	0.38	0.57	14.52	11
2	0.52	0.58	-57.08	-58
3	0.37	0.43	83.51	75
4	0.32	0.43	14.64	11
5	0.41	0.62	17.43	14
Mean	**0.40**	**0.53**		

In this sub-section, only a low number of regions of these cells have been analysed, and, although these were selected from similar intracellular locations and that they also returned a statistically significant difference, it will be important to analyse whole cells to further validate the method, and moreover, to look for interesting differences between the two treatments, and within cells. Moreover, images of cells where further experimental manipulations have been made will also be subject to analysis by MtFT. This is the focus of the next section.

C. FULL ANALYSIS

I. Approaches to whole-image MtFT analysis

Here, I now look to analyse whole images of the cells subject to preliminary analysis in the previous section. Previously, only selected regions were analysed for principal orientation and alignment, so means of dealing with a large image was not an issue. Here, we have this problem: how should we deal with an entire image? Should the FT be taken of the whole image, or just parts of it? Or should a filter-based approach be implemented with an FT for each pixel of the image?

Recalling the introduction to this chapter, we know that we obtain better frequency resolution in the FT if the image is larger (eq. 7). However, it was also noted that we sacrifice the ability to understand where certain frequency components have originated if the image is big, so there is a trade-off between frequency resolution and diagnostic power, so to speak. For the sake of estimating principal orientations and alignment, however, the frequency resolution is not as important to us as if we wanted to pinpoint a *scale* of alignment. This is demonstrated by the nature of the analysis up to this point: we have not considered the power spectrum as a function of frequency, only orientation (eq. 8); thus, analogous to "orientation magnitude", we do not obtain the "frequency magnitude". Therefore, our choice of how to implement this method with whole images should be dictated less by frequency resolution constraints, and more so by the need to locate the parts of the microtubule cytoskeleton that produce certain principal orientation and alignment values.

There are also practical considerations. Briefly mentioned above was a filter-like approach, where, for each pixel in the image, an area of given size is centred on it, and the FT is taken of that area. This continues for every pixel in the image, and the output would be arrays of principal orientation and alignment scores the same size as the input image. However, with this "filter" approach, for images with dimensions on the order of hundreds to thousands of pixels, it is clear that this approach might be costly in terms of computation time; for one image of 1,000-by-1,000 pixels, we would have 1,000,000 FTs! Add to this the question of whether there would be much to gain in terms of localising information, since areas for adjacent pixels would have a large overlap, and it is clear that this approach has some disadvantages.

Another way is to take the FT of distinct areas of the image. In image compression, such as with the JPEG file format, images are split into regions, usually eight of equal size, and the FTs are taken of these (Gonzalez and Woods, 2006). This "blocked" method allows localisation of frequency information, since we know it has originated from a specific image sub-section. A similar method can be applied to the images under analysis here. As with the filter method, this approach also has disadvantages, for example, certain regions of interest in an image may be partitioned into separate areas, thus making it difficult to localise characteristics to that region.

So each potential method has good and bad points; here, I opt to use the blocked method, as, since this is less computationally expensive, it is a good starting point; the filter method can

be tested at a later date. Furthermore, there is still some degree of sub-cellular analysis permitted with the blocked method, and this will be demonstrated in the results (next section).

II. EB2-depleted cells

For the whole-image MtFT analysis, 5 images of the control (scramble siRNA) and EB2-depleted cells were used; in each condition, images were similar and thus chosen at random. Notable, EB2-depleted cells are generally larger, and this may affect the extent to which conclusions can be made in any analysis of differences within cells. However, the main aim here is to test MtFT on two sets of cells treated differently, and the "blocked" analysis uses blocks smaller than a cell to limit such effects regardless. Examples of these images are shown in figure 19. Each image was subject to the blocked analysis, as described above. Furthermore, images of cells where the small GTPase Rac1 had been inhibited (with inhibitor NSC), in the backgrounds of scramble and EB2 siRNA, were analysed, and these images, of which there were again 5, are also shown in figure 19.

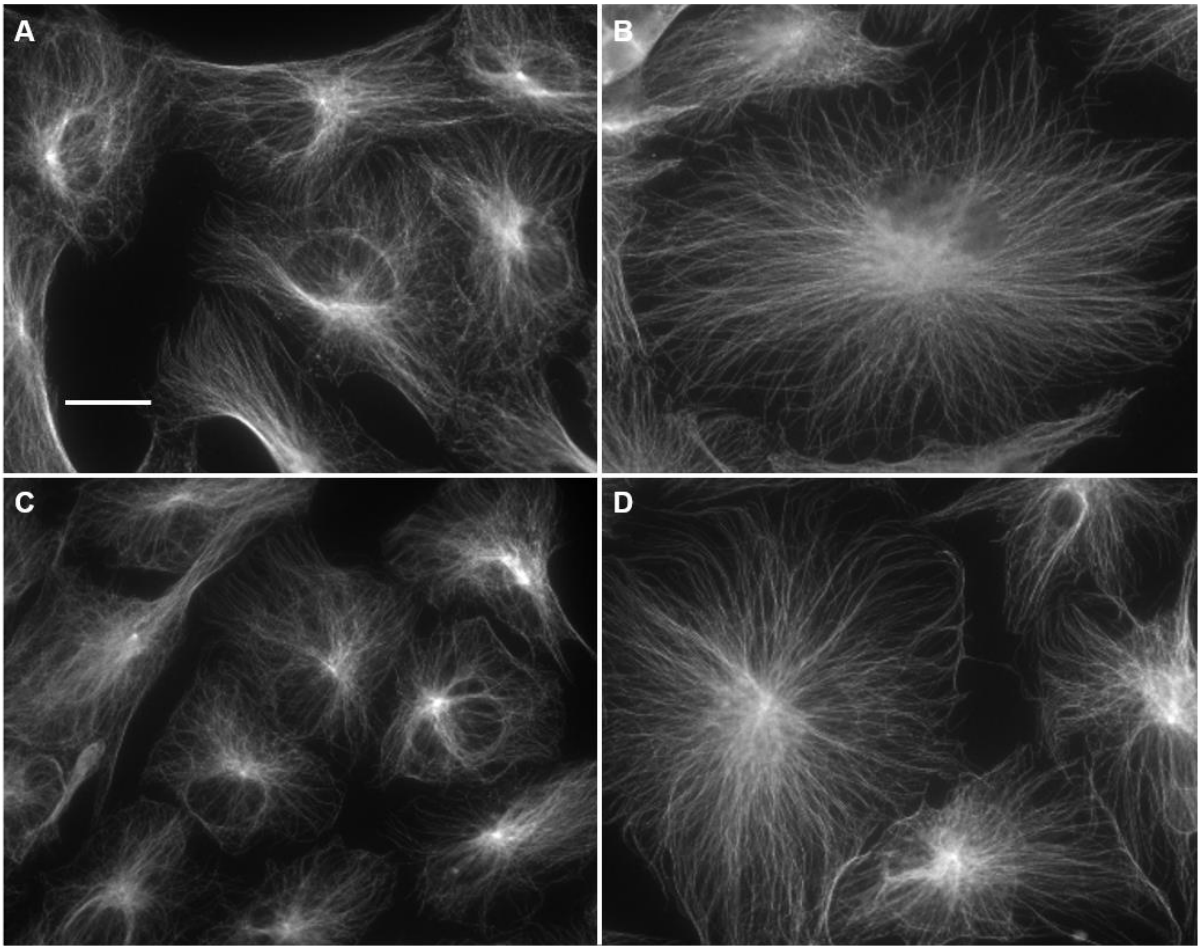

Figure 19. Examples of images used. Control (scramble siRNA, A), EB2-depleted (B), Rac1-inhibited (C) and EB2-depleted, Rac1-inhibited (D) cells were used. For each experimental condition, 5 images were used. Images courtesy of Debbie Goldspink, Mogensen lab; scale bar 20 μm.

The blocked analysis runs thus:

1. An area dimension "range" is decided upon. This is simply the permissible dimensions, in pixels, of the blocks.
2. To choose block dimensions from this range, the smallest value in the range that gives the smallest remainder when it is divided into the image dimension is identified as the best choice. This is done for both x and y dimensions.
3. The minimum size of the mean padding area to be positioned around the image is half of the maximum block dimension, while it is increased in the direction of the minimum block dimension so as to produce a square image; this gives a better MtFT analysis, since the orientation magnitude is programmed to extend the same distance in all directions (i.e., it is semi-circular), and the radius of the semi-circle it defines is limited by the smallest dimension of the FT; thus, with a square image, more of the FT is surveyed.
4. The FT is taken of the mean-padded block, and the orientation magnitude is found, and the principal orientation and alignment is determined as in the preliminary analysis of these cells.

For this analysis, the range was chosen to be from 80 to 120 pixels; the reason for point number 1 is to try not to miss edges of the image. By specifying a range of acceptable block sizes, we can survey more of an image, while the FTs and resulting orientation magnitude, etc., should not be overtly affected by small changes in block sizes of this order. An example of an image split into blocks is shown in figure 20.

It is evident from the example in figure 20 that there are regions of the image that we may not want to include in the analysis. The most obvious of these is the space where there are no cells. To allow this, I created a simple interactive tool in Matlab whereby the image, with all blocks plotted, is displayed, and the user chooses which are to be analysed simply by clicking in the blocks of choice. Figure 21 shows an example of an image with only blocks selected that are positioned over cells.

To assist in visual inspection, the images can be displayed with blocks colour-coded according to the principal orientation estimate for that area, or for the value of ρ for that area. Examples of both of these are shown in figure 22. For the orientation prediction, the angles have been converted to predict the actual orientation now, rather than that of the orientation magnitude, which is situated perpendicular to the real image. The angles are also now on the interval 0° to 180° to make visual inspection simpler.

The example orientation plot in figure 22 demonstrates that this type of display will be useful to analyse microtubule orientations in cells. Further analysis could include calculation of dominant angles within a cell, or, orientation relative to intra- or extracellular features/cues, such as the centrosome or the edge of the cell.

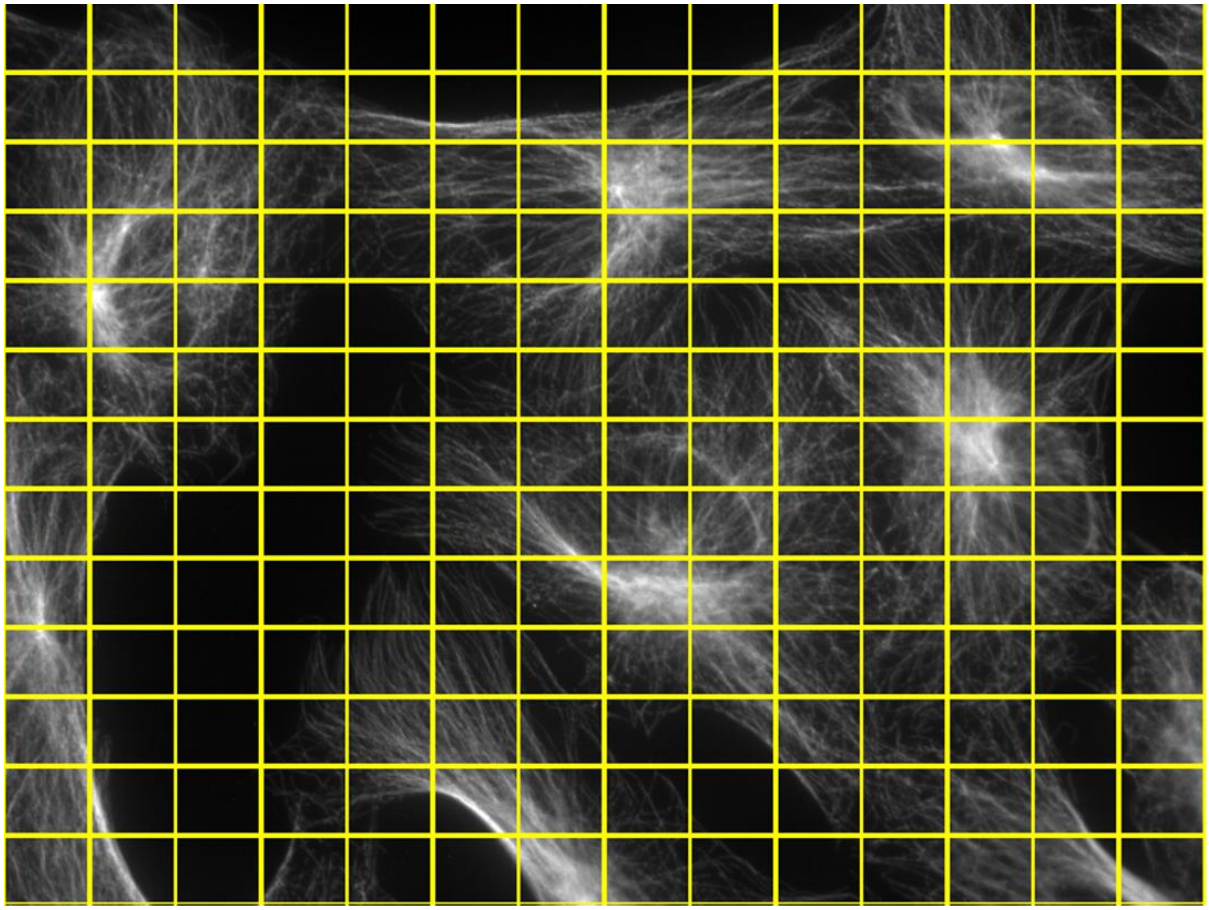

Figure 20. Example of a "blocked" image. Here, each block, or area, is analysed, thus, first, the FT is taken, then the orientation magnitude found with the continuous method, then the data is normalised, and then the principal orientation is estimated and the alignment measured. The algorithm for fitting blocks is based on a range of acceptable block dimensions, so that the size that leaves the least area at the bottom and right sides of the image can be chosen from the range. Image courtesy of Debbie Goldspink, Mogensen lab; scale bar 20 μm.

The results of this blocked analysis are shown in table XVII. The mean and median (due to non-normality, see below) alignment for each image was found, while the mean for all blocks, i.e., the mean for every single block measured, was also determined. To exclude possible effects of the blank spaces in images, the mean alignment in only the blocks positioned over cells (as in fig. 21) was also found; the results of this cell block-only analysis are shown in figure 23.

As table XVII shows, the results of the full analysis agree with the preliminary analysis; EB2 depletion generally increases microtubule alignment. Only one image (number 5) scored lower for alignment than images of scramble cells. The mean of all blocks analysed is also greater for EB2 depleted cells. Furthermore, although elimination of blank spaces in the image increases the mean alignment in both of these conditions, the increase is greater in EB2 depleted cells.

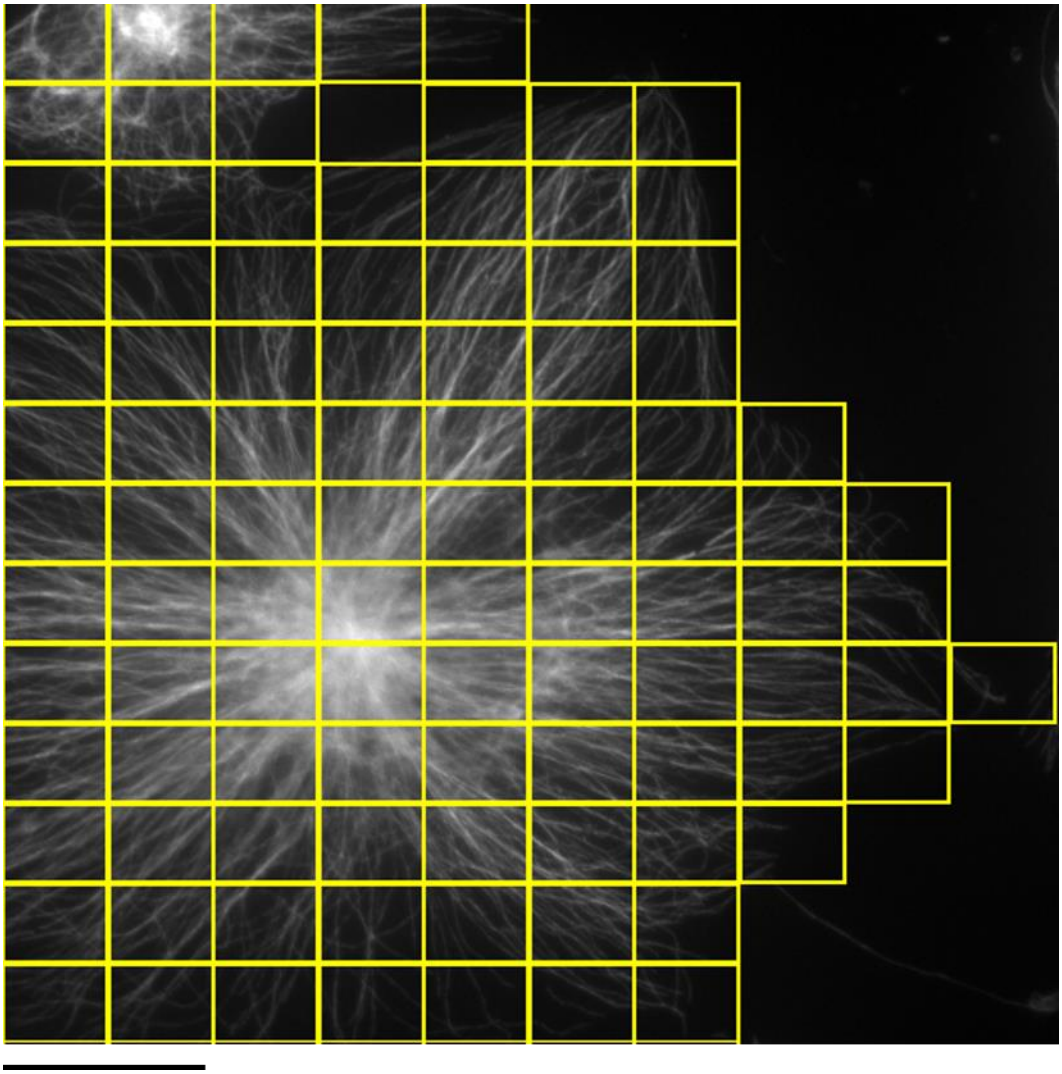

Figure 21. Block selection. Here, only blocks that are positioned over cells have been selected. Image courtesy of Debbie Goldspink, Mogensen lab; scale bar 20 μm.

Table XVII also shows the results for the other two treatments. Rac1 inhibition generally decreased microtubule alignment, as evidenced by the block and cell means, all of which are lower than the scramble cells. Only two images are greater than the lowest-scoring image in the scramble cells. Again, the omission of black spaces increased the alignment score in all treatments, as the cells value is greater than the blocks value.

Interestingly, the treatment where both EB2 was depleted and Rac1 was inhibited scored the highest for alignment. The reduction, just discussed, in alignment in the Rac1-inhibited cells makes this a surprising result because now, in combination with depletion of EB2, it has seemingly contributed to the opposite result.

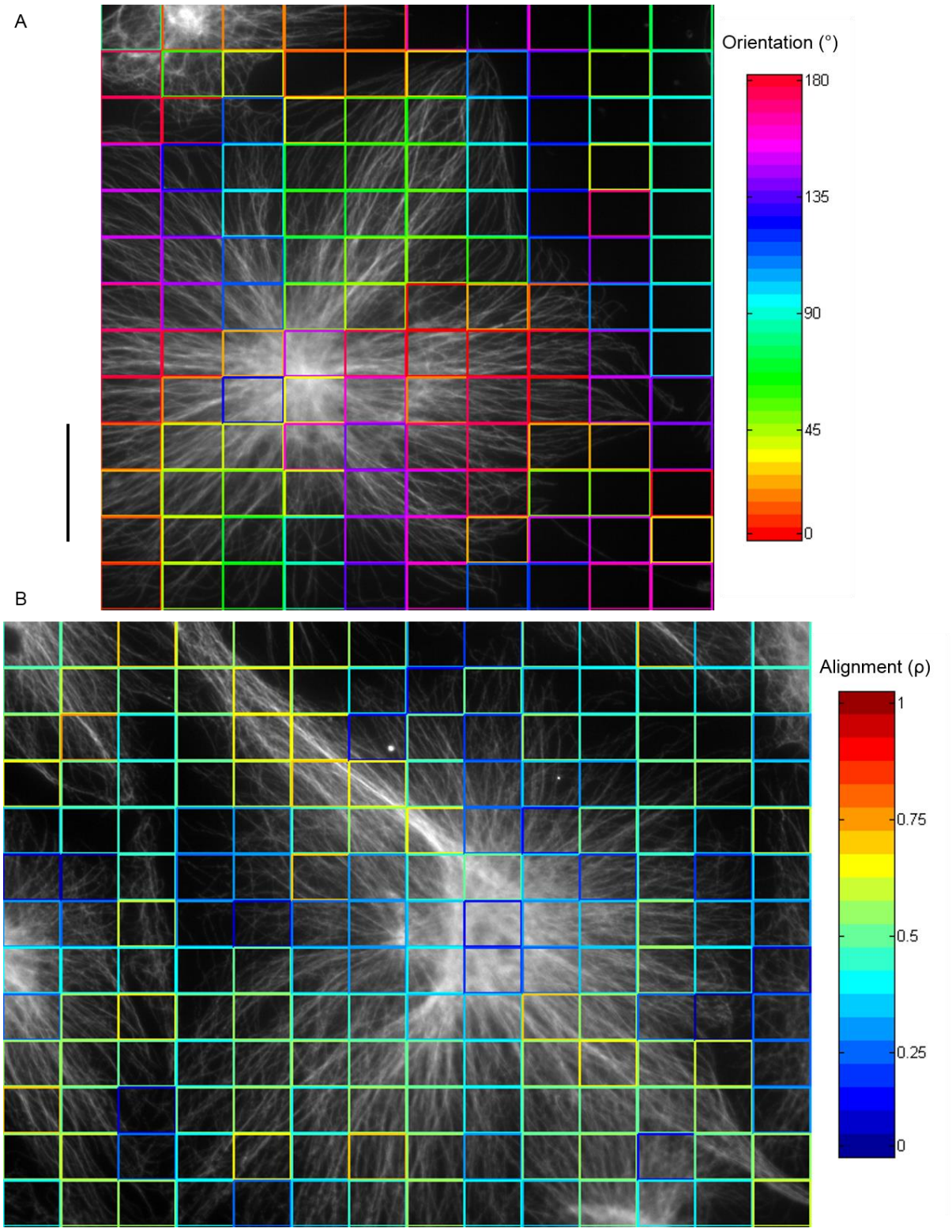

Figure 22. Blocks according to principal orientation prediction and alignment. Each block is colour-coded according to the principal orientation prediction (A) or alignment score (B) for that area. Images courtesy of Debbie Goldspink, Mogensen lab; scale bar μm.

Table XVII. Mean and median alignment values, ρ, for the different experimental conditions. The mean value, ± the standard deviation, for scramble, EB2-depleted, Rac1-inhibited (NSC) and EB2-depleted and Rac1-inhibited cells are shown for each image (1-5), for all blocks analysed (Blocks), and for only the blocks positioned over cells (Cells). The median and inter-quartile range (IQR) are also shown for blocks over cells. n = number of blocks.

	Scramble	**EB2 siRNA**	**NSC**	**EB2 siRNA + NSC**
Image				
1	0.3781 ± 0.16	0.4128 ± 0.14	0.3467 ± 0.13	0.4275 ± 0.15
2	0.3534 ± 0.14	0.3945 ± 0.17	0.3265 ± 0.14	0.4235 ± 0.14
3	0.3360 ± 0.13	0.4087 ± 0.15	0.3161 ± 0.17	0.4151 ± 0.18
4	0.3609 ± 0.13	0.4008 ± 0.15	0.2736 ± 0.17	0.4110 ± 0.14
5	0.3840 ± 0.15	0.3761 ± 0.14	0.3484 ± 0.15	0.4496 ± 0.16
Blocks				
Mean	0.3625 ± 0.14	0.3993 ± 0.15	0.3232 ± 0.15	0.4260 ± 0.15
n	910	882	826	871
Cells				
Mean	0.3638 ± 0.14	0.4051 ± 0.15	0.3323 ± 0.15	0.4265 ± 0.15
Median	0.3735	0.4194	0.3528	0.4374
IQR	0.21	0.21	0.21	0.22
n	857	793	601	777

The data for each condition were found to be non-normally distributed for both the blocks and cells analysis (chi-square goodness-of-fit test, $p < 0.01$), so non-parametric tests were employed. There was a significant difference between all groups (Kruskal-Wallis test, $p < 0.01$), and four groups were then individually compared with each other: scramble vs all other groups (3 comparisons) and EB2 siRNA vs EB2 siRNA + NSC. As before, the Bonferroni correction was employed to make the multi-comparisons more stringent. The three non-control groups differed significantly (Wilcoxon rank sum test, $p < 0.01/4$), while the EB2 siRNA + NSC group was not significantly different from the EB2 siRNA group at the most stringent significance level (Wilcoxon rank sum test, $p > 0.01/4$), but was so at a reduced significance level (Wilcoxon rank sum test, $p < 0.05/4$).

The method developed in this chapter, MtFT, has thus been able to detect, at a statistically significant level, differences in microtubule alignment between control and EB2-depleted cells, and this is in agreement with the previously published analysis of EB2 depletion and microtubule organisation (Goldspink et al., 2013). In addition, the method has also revealed an effect of Rac1 inhibition on microtubule organisation, where microtubules are apparently less well-aligned than control cells, and fascinatingly, a reversal of the effect of Rac1 inhibition on microtubule organisation when combined with EB2 depletion. In the latter scenario, microtubule alignment was also increased to a greater extent than in the EB2 depleted only condition.

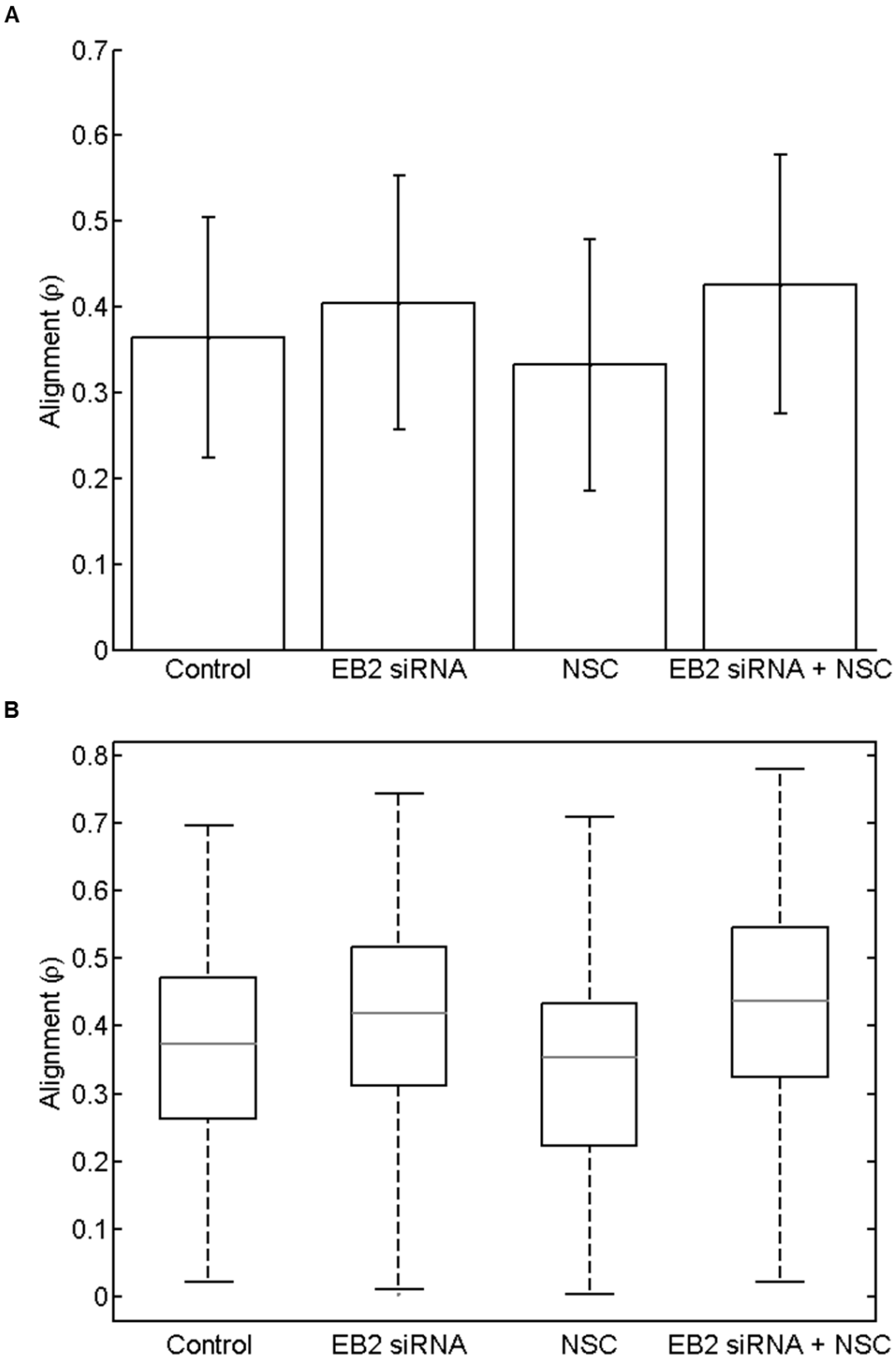

Figure 23. Mean (A) and median (B) microtubule alignment for blocks over cells. Values are ± standard deviation (A), and boxes extend to 25th and 75th percentiles (q1 and q3, respectively), whiskers to q1 – 1.5(q3 – q1) q3 + 1.5(q3 – q1).

III. Formin inhibition in EB2-depleted cells

Thus far, MtFT has been used to verify the effect of EB2 depletion on microtubule alignment, previously quantified by counting the number of microtubule crossovers by Goldspink et al. (2013). Furthermore, a potentially interesting interplay between EB2 depletion and Rac1 has been uncovered, since microtubule alignment was found to be significantly increased when Rac1 was inhibited in EB2-depleted cells.

In the previous study of EB2 depletion and microtubule organisation, it was found that depletion of EB2 not only increased microtubule alignment, but also induced re-organisation of the actin cytoskeleton, and co-alignment of microtubules and actin filaments (Goldspink et al., 2013). In their investigation into the processes involved in this phenotype, Goldspink et al. (2013) considered formins, which are a group of highly conserved proteins that are involved in remodelling both the actin and microtubule cytoskeleton (Wallar and Alberts, 2003), and "crosstalk" between these two systems (Bartolini and Gundersen, 2010). Goldspink et al. (2013) inhibited formins with SMIFH2 (Rizvi et al., 2009), and again quantified microtubule alignment by counting the number of crossovers (fig. 24). It was found that the inhibition of formins rescued the EB2-depleted phenotype, returning microtubules back to their less-aligned organisation.

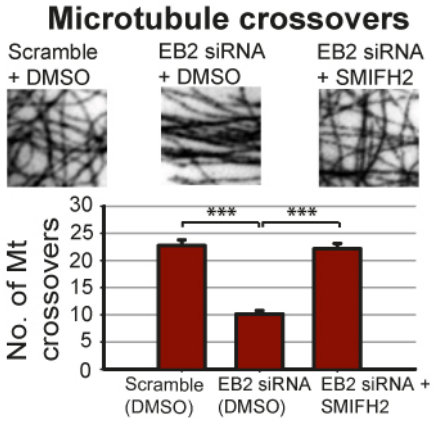

Figure 24. Microtubule alignment is rescued upon formin inhibition. In the EB2-depleted cells, formin inhibition produced less-aligned microtubules, similar to scramble, non-inhibited cells. From Goldspink et al. (2013).

To further assess the capability of MtFT, the same "blocked" analysis as before was carried out on images of four experimental conditions: 1) scramble, 2) formin-inhibited (SMIFH2), 3) EB2-depleted, and 4) EB2-depleted and SMIFH2. In this case, only the blocks over cells were analysed, as in the latter part of the previous analysis. The results are shown in table XVIII and in figure 25.

Table XVIII. Mean and median alignment values, ρ, for the different experimental conditions. The mean value, ± the standard deviation, median and inter-quartile range (IQR) for scramble, formin-inhibited (SMIFH2), EB2-depleted, and EB2-depleted and SMIFH2 cells are shown for only the blocks positioned over cells. n = number of blocks.

	Scramble	SMIFH2	EB2 siRNA	EB2 siRNA + SMIFH2
Mean	0.3047 ± 0.14	0.3087 ± 0.15	0.3745 ± 0.14	0.3223 ± 0.13
Median	0.3116	0.3154	0.3909	0.3322
IQR	0.21	0.24	0.19	0.19
n	533	502	733	385

Again, the depletion of EB2 in this set of experiments was found to result in increased microtubule alignment, and, in agreement with previous work, formin inhibition in EB2-depleted cells reduced the microtubule alignment. As in the previous analysis, the data for each condition were found to be non-normally distributed (chi-square goodness-of-fit test, $p < 0.01$), and there was a significant difference between all groups (Kruskal-Wallis test, $p < 0.01$). In this analysis, five comparisons were made: the scramble treatment was compared to all other treatments (3 comparisons), the SMIFH2 treatment was compared to the EB2 siRNA treatment, and the EB2 siRNA treatment was compared to the EB2 siRNA + SMIFH2 treatment. In a similar manner to the previous analysis, the Bonferroni correction was employed to make the multi-comparisons more stringent.

Here, the differences between the scramble condition and SMIFH2 and the EB2 siRNA + SMIFH2 treatments were not significant even at the non-corrected p-value (Wilcoxon rank sum test, $p > 0.05$). The EB2 siRNA condition was significantly different to the scramble condition (Wilcoxon rank sum test, $p < 0.001$). In the other two comparisons, the SMIFH2 and EB2 siRNA + SMIFH2 treatments were not significantly different, and again, this was even the case at the non-corrected p-value (Wilcoxon rank sum test, $p > 0.05$). Importantly, the EB2 siRNA + SMIFH2 condition was significantly different to the EB2 siRNA only treatment (Wilcoxon rank sum test, $p < 0.001$), supporting previous findings.

There, MtFT, has again been able to detect, at a statistically significant level, differences in microtubule alignment between control and EB2-depleted cells, and EB2-depleted only and EB2-depleted and formin-inhibited cells. These findings are again supported by previously published analyses on these experiments (Goldspink et al., 2013).

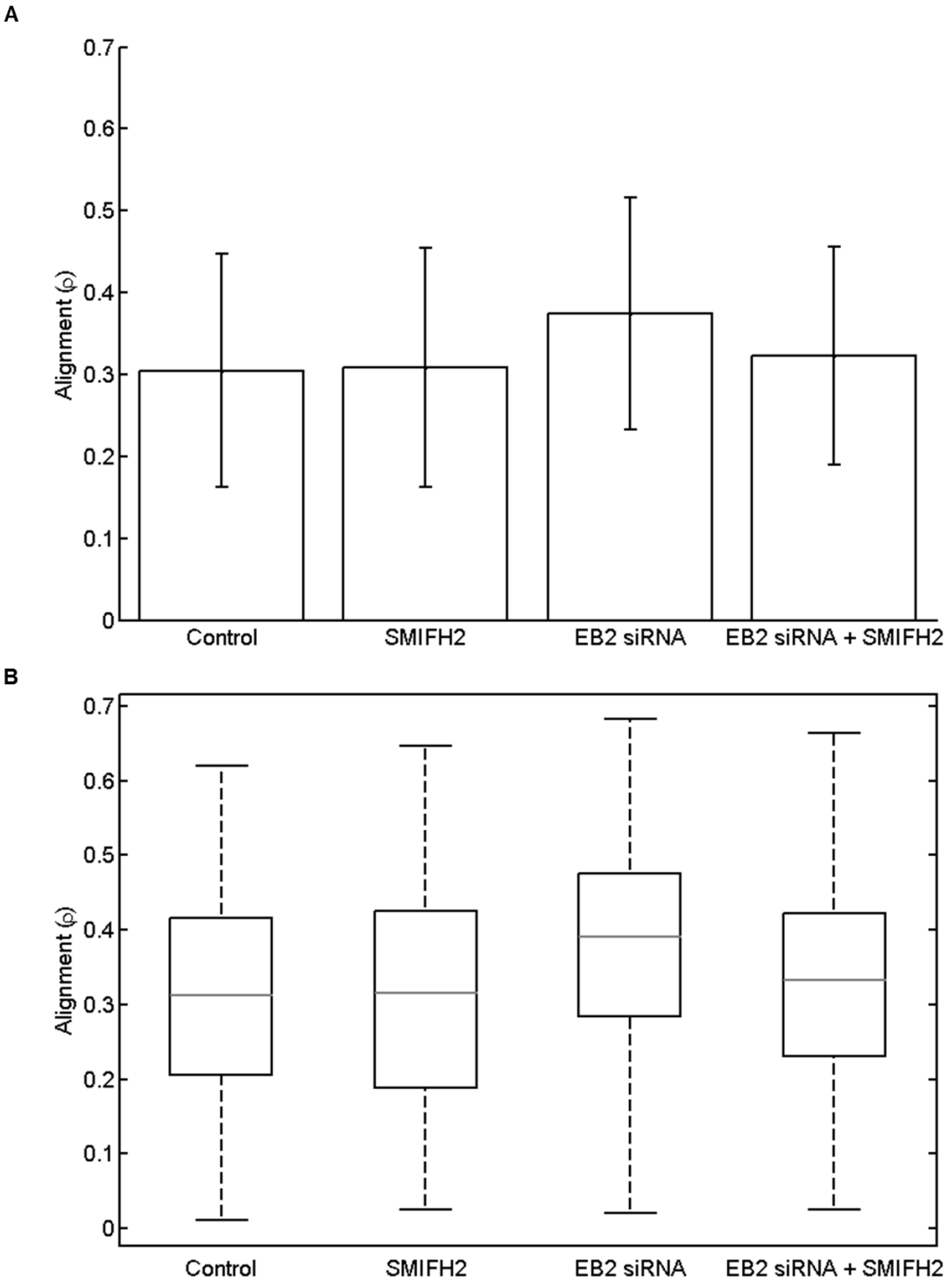

Figure 25. Mean (A) and median (B) microtubule alignment for blocks over cells. Values are ± standard deviation (A), and boxes extend to 25th and 75th percentiles (q1 and q3, respectively), whiskers to q1 – 1.5(q3 – q1) q3 + 1.5(q3 – q1).

IV. Microtubule alignment in plant cells

Finally, MtFT can be used in the analysis of plant microtubule organisation. As has been described already, plant microtubules exist in what is essentially a 2-dimensional system, known as the "cortical array", and the alignment of microtubules in this array is a major determinant of plant cell growth. Since microtubule alignment is such an important feature of plant development, it has received a lot of attention, and methods, including "FibrilTool" described and compared with MtFT earlier, have been developed to quantify it. Here, I am interested in whether MtFT can be used to detect differences in plant cortical microtubule organisation.

Images to be analysed here are kindly provided by the Turner laboratory at the University of Manchester; relevant methods are discussed in the appendix (section E). The Turner lab is interested in the mechanisms of plant cortical microtubule organisation, particularly the role of microtubule severing by the protein katanin, and modulation of its activity by spiral 2. The set consists of six images: 3 of pavement cells, and 3 of petiole cells; in each of these, there is an image for wild-type (WT), a katanin mutant (*bot1-7*) and a spiral 2 mutant (*spr1-2*) (fig. 26). As with earlier analyses, although cell shapes and sizes differ, blocks of sizes smaller than cells will be used to limit possible effects.

To recap, the wild-type organisation in pavement and petiole cells differs: in the former, microtubule organisation is more "net-like", while in the latter, microtubule are much more aligned. Katanin mutants have previously been shown to exhibit these net-like microtubule arrays, and in both pavement and petiole cells, this is the case (fig. 26). There is strong evidence to support the fact that katanin activity is somehow modulated by spr2 since, in spr2 plants, cortical arrays are well-aligned, in both pavement and petiole cells. Although the biochemical mechanism is currently unknown, spr2 appears to prevent severing of microtubule crossovers, protecting these from severing by katanin, thus permitting formation of net-like arrays.

Here, I use MtFT to quantify the extent of alignment in the cortical microtubule arrays in the images in figure 26. Since these images have many cells and there is thus less image for each cell, the acceptable block range is reduced for this analysis from 80-120 pixels, as before, to 60-80 pixels. Only blocks over cells were analysed.

The blocked MtFT analysis is shown colour-coded for alignment in figure 27. The most striking difference is that of the spr2 cells; here, the presence of many yellow boxes indicates greater values of ρ. After this, it is difficult to ascertain the differences, if any, between the other conditions. Table XIX shows the mean and median values for each condition; here we see that in WT, petiole cells have better-aligned cortical arrays, while in *bot1-7*, petiole cortical array alignment is reduced to a much greater extent than in pavement cells. As suggested in figure 27, the *spr2-1* plants have higher levels of microtubule alignment than any of the other conditions. Here, the *spr2-1* petiole cells have much greater alignment than the pavement cells, supporting the notion of Wightman et al. (2013) that these cortical arrays are "hyper-aligned".

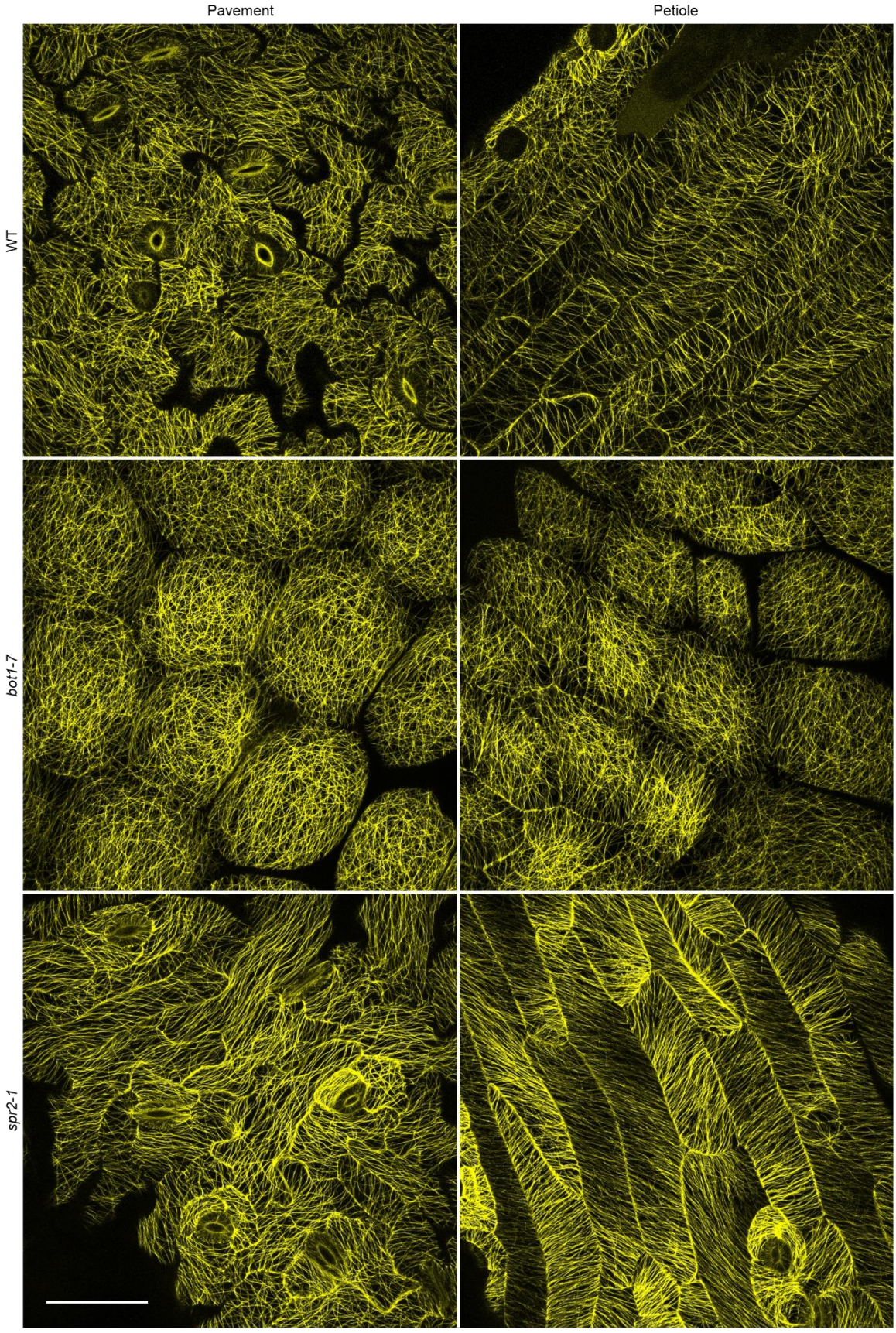

Figure 26. Plant microtubules in indicated cell types and mutant lines. Images courtesy of Ray Wightman, Turner lab (see text). Scale bar 50 μm.

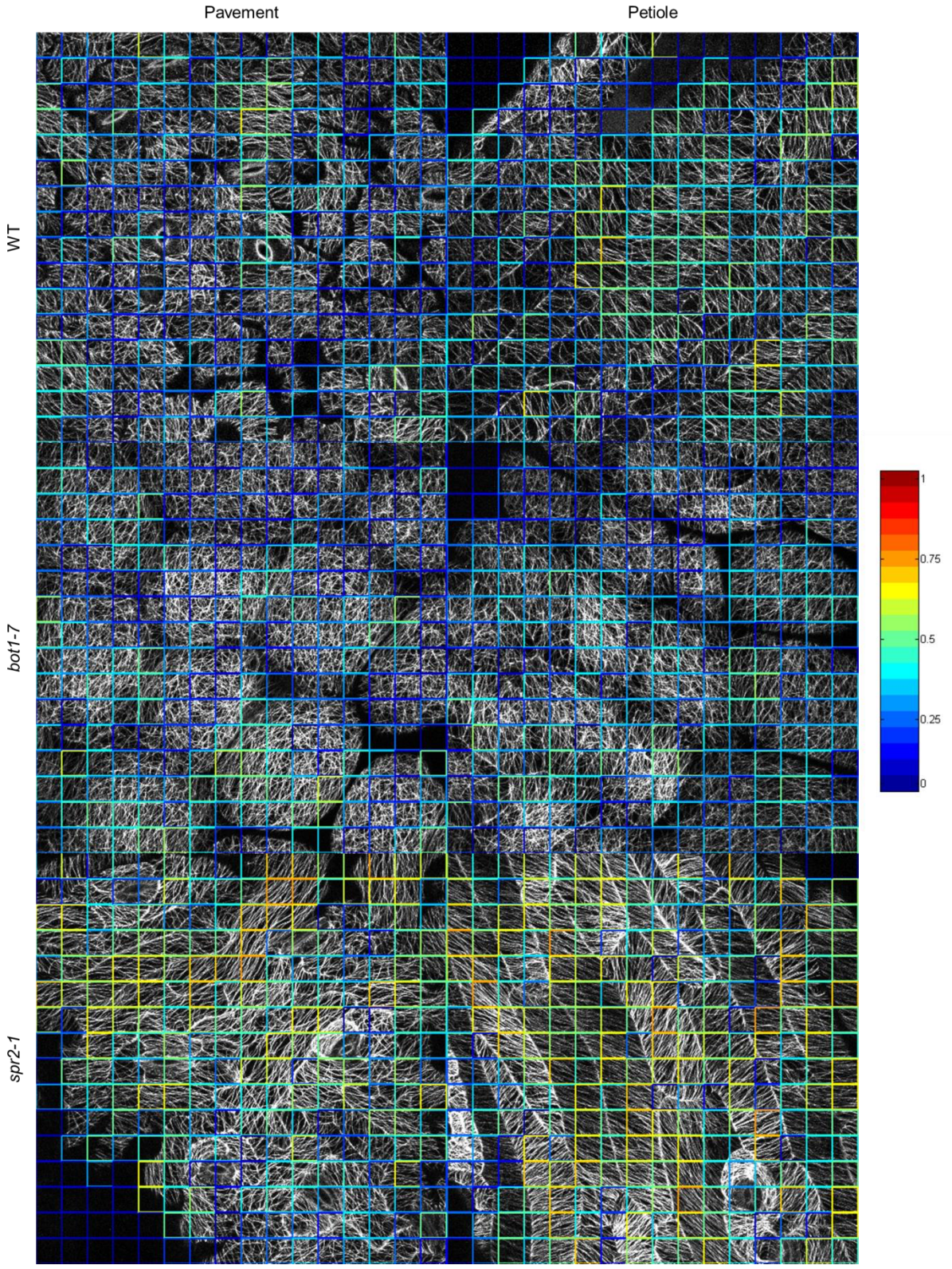

Figure 27. Alignment in plant microtubule arrays. Block colours indicate extent of alignment, quantified by MtFT. Only blocks positioned over cells were analysed, but all are shown here. Images courtesy of Ray Wightman, Turner lab (see text).

Table XIX. Mean and median alignment values, ρ, for the different experimental conditions. The mean value, ± the standard deviation, median and inter-quartile range (IQR) for wild-type (WT), mutant katanin (*bot1-7*) and mutant spiral (*spr2-1*) are shown for only the blocks positioned over cells. n = number of blocks.

	WT		***bot1-7***		***spr2-1***	
	Pavement	*Petiole*	*Pavement*	*Petiole*	*Pavement*	*Petiole*
Mean	0.2493 ± 0.12	0.3127 ± 0.15	0.2486 ± 0.13	0.2583 ± 0.11	0.3598 ± 0.19	0.4480 ± 0.17
Median	0.2456	0.3210	0.2322	0.2567	0.3853	0.4672
IQR	0.16	0.23	0.19	0.16	0.27	0.27
n	224	227	249	247	221	244

Although some of the alignment values were normally distributed, not all were (chi-square goodness-of-fit test, $p < 0.01$), so again, non-parametric tests were used. There were found to be significant differences between alignment values (Kruskal-Wallis test, $p < 0.001$), so comparisons were made between individual treatments, following the same statistical procedures as before. Here, the difference between WT pavement and petiole microtubule alignment was significant, as was the difference between *spr2-1* pavement and petiole alignment (Wilcoxon rank sum test, $p < 0.001$), while there was no significant difference between pavement and petiole microtubule alignment in the *bot1-7* condition (Wilcoxon rank sum test, $p > 0.05$).

Now comparing WT cells with the other two conditions, the difference between WT and *bot1-7* was significant only for petiole cells (Wilcoxon rank sum test, $p < 0.001$), and not for pavement cells (Wilcoxon rank sum test, $p > 0.05$). Between WT and spr2-1, both cell types had significantly increased alignment (Wilcoxon rank sum test, $p < 0.001$). Therefore, loss of *spr2-1* functionality clearly has great consequences for the organisation of the cortical microtubule array. Indeed, the increased alignment in spr2-1 in pavement cells was significantly increased compared to the WT petiole cell (Wilcoxon rank sum test, $p < 0.01$).

Again, microtubule alignment has been successfully measured with MtFT. Previously, this has only been measured by comparing orientation distributions (Wightman et al., 2013); thus, MtFT may assist further analyses in this respect.

D. DISCUSSION

I. Summary of MtFT

a. Development of MtFT

In this chapter, a new method for quantification of microtubule organisation, specifically, the orientation and alignment of microtubules, has been developed. Although there are previous instances of image processing methods based on the FT, none of these have been applied to microtubules, and have generally been confined to quantification of the properties of biological matrices, for example collagen fibres (Bayan et al., 2009; Schriefl et al., 2013).

The new method was then applied to real biological problems, for which there were previous results against which to benchmark the method to evaluate its efficacy, and in some cases, the particular problem was new.

b. Benchmarking of MtFT

The verification that MtFT worked as it should involved extensive analysis based on synthetic images for which the parameters of interest, i.e. orientation and alignment, were known. This approach has been used previously in the development of another FT-based image processing method (Bayan et al., 2009; Sander and Barocas, 2009), and it proved useful here, showing that MtFT could predict the image parameters, and that the accuracy of prediction depended on a number of variables of the processing algorithm, allowing appropriate parameters and the values of those parameters to be chosen.

Further benchmarking included comparison with another published method to quantify microtubule orientation and alignment. Here, the lower alignment scores for the scramble siRNA condition and higher alignment scores for the EB2-depleted condition when using MtFT suggests that it may be more sensitive to microtubule alignment than FibrilTool (Boudaoud et al., 2014), which is an exciting result. To be sure of this, further comparison will help, and perhaps use of synthetic data too.

In fact, this touches on a general point: there are many methods for quantification of microtubule alignment and orientation, but as yet, they have not been compared thoroughly on the same data. This will be a task for the future.

c. Extensions to MtFT

The most obvious extension to the method developed in this chapter is an analysis of the scale of alignment. Here, rather than taking the arc segments of the FT that were used to obtain the orientation magnitude, the analogous "scale magnitude" could be obtained by taking circumferential segments of the FT. Analysis of such a scale magnitude should allow quantification of the scale of the alignment, i.e. it could answer the question: how far apart are these aligned microtubules? And: is the spacing between these microtubules consistent, or does it vary? These would be interesting problems to investigate. Such analysis would also be applicable to other filamentous agents, for example, the actin cytoskeleton.

Additionally, the control synthetic images used in the benchmarking should also give us the opportunity to explore the effects of non-biological factors, i.e., noise, blurring, and the dimensions of the area being analysed. Noise is inherent to all microscopic imaging, for which there are a few potential sources, and blurring could be used to imitate defocussing, which may occur in these images since they have been taken using a widefield microscope and have a height, albeit not a very great one. It may also imitate the result of the fact that microtubules are smaller than the resolution of the microscope.

On this note, deconvolution has the potential to improve alignment quantification by re-assigning out-of-focus light, and thus allow the FT of the image to better represent the microtubule organisation. Moreover, confocal images may also have this attribute, but their use in anything other than almost 2-dimensional images will warrant development of MtFT for three dimensions, if it is to be truly applicable to data acquired as a set of slices in a stack.

We saw in the discussion of the principles of the FT that the size of the "window" being analysed is a determinant of the frequency resolution of the FT. An analysis of this type would be requisite for the extension of MtFT to quantify scales of alignment, since frequency resolution would be limiting in quantification of scale.

Finally, the blocked analysis implemented here could be improved on. Firstly, we should be able to identify areas of the image where there is not any information, i.e., where the cell is not. In these areas, we can abandon the sequential divisions of the image, which will help to speed up the analysis too. Secondly, areas that match one another in orientation or alignment could be kept together, and those that are different, separated. An output of such an analysis would be a map of areas of similar local alignment or orientation.

II. Mechanisms of microtubule alignment

a. In animal cells

The findings in this chapter, some of which were previously described by Goldspink et al. (2013) with different methods, suggest some interesting parallels between the mechanisms of microtubule alignment *in vivo* and *in vitro* actin-mediated organisation of microtubules, as described by López et al. (2014). There, actin bundles were observed persistently redirecting the growth of microtubules to match their orientation, and this depended on the presence of a specially-engineered minimal version of ACF7, which bound along the lattice of microtubules and actin so as to maintain the redirected orientation of the microtubule.

In cells, the situation appears to follow similar principles. Upon depletion of EB2, EB1 is observed along the microtubules (Goldspink et al., 2013) and microtubules are more aligned and furthermore, co-aligned, at least by eye, with actin filaments. In Rac1-inhibited cells, microtubules are less aligned, but when Rac1 is inhibited and EB2 is depleted as well, the microtubules are aligned to a greater extent than in an EB2-depleted background alone. As Rac1 can mediate microtubule-actin interaction, for example through IQGAP, a mechanism presents itself: microtubule-actin interactions, mediated or inhibited in some way by Rac1 and EB2, and promoted by formins and EB1, lead to greater microtubule alignment. EB2

must lie downstream to Rac1 in this proposed process, since inhibition of Rac1 leads to lower microtubule alignment; the precise mechanism for this is not clear; it may involve other Rac1 functions that mediate microtubule-actin interactions but are not dependent on EB2. Thus, when EB2 is depleted, EB1 can redistribute along the length of the microtubule and promote interactions with actin, while inhibition of Rac1 makes this phenotype stronger.

b. In plant cells

Previously, the organisation of the plant cortical microtubule array has been considered either by comparison of histogram distributions (Wightman et al., 2013) or by image processing techniques based on spatial (Lindeboom et al., 2013; Uyttewaal et al., 2012), rather than frequency, information. The contribution of the protein spr2 and the severing protein katanin to microtubule alignment was assessed here.

In the wild-type background, petiole cells have better-aligned microtubules compared to pavement cells, and this was verified here with MtFT. In the katanin mutant bot1-7, this alignment was nearly completely abolished, indicating that indeed, katanin does have a role in cortical microtubule alignment. Furthermore, in the spr2 mutant, alignment was increased relative to wild-type in both cell types, to the extent that the pavement cell alignment in spr2-1 was significantly greater than in wild-type petiole cells. Therefore, spr2 also has a role in microtubule alignment. Though the biochemistry of the mechanism is yet to be determined, it is probably given the localisation of spr2 to microtubule crossovers, that spr2 protects these sites from severing by katanin.

The facts that in both spr2-1 petiole and pavement cells, microtubule alignment was significantly increased over WT petiole cells suggests that spr2 still has some activity in petiole cells.

III. Biological significance of microtubule alignment

a. In animal cells

In animal cells, microtubule alignment has been investigated to a lesser extent than in plant cells. One of the main reasons for this is likely to be that in plants, microtubule alignment plays a pivotal role in the development of the plant. The extent to which microtubule alignment is a factor in development of animals in general, or in particular cases of cell differentiation, is an unknown entity. However, the theoretical study of Khuc Trong et al. (2012) served to demonstrate firstly that the alignment of a microtubule network is important for transport of a molecule and furthermore, that the interplay between the active transport and advection in the array can lead to unexpected results.

Theory aside, these potential effects of microtubule alignment have not really been addressed, but there are indications that it is important. For example, subtle orientation biases in the *Drosophila* oocyte described in Parton et al. (2011) are involved in correct segregation of fate determinants within the cell. Furthermore, the expression of EB2, which was also addressed here, changes with cell differentiation state in epithelial cells of the inner ear and intestinal crypt (Goldspink et al., 2013).

Interestingly, the less-aligned microtubule phenotype seen upon Rac1 inhibition in this chapter is consistent with the quantification of microtubule bending based on the plusTipTracker data in chapter 3. There, it was found that Rac1-inhibited microtubules produced growth tracks with greater relative orientation between track segments, indicating that their growth was more circuitous than a control microtubule. The modelling of chapter 5 was implemented with the aim of determining whether the Rac1-inhibited phenotype, in which microtubules have lost their radiality, is a result of aberrant microtubule dynamics modulation at the cell periphery. Thus, bending was not included, but the results in chapter 3 and those presented here that Rac1-inhibited microtubules are apparently more flexible, or not guided in the same manner as control microtubules, is worth investigating further. This will be another focus of future work.

b. In plant cells

The general significance of plant cortical microtubule alignment has already been briefly discussed above. The alignment of microtubules is thought to be important for the mechanical properties of the cell because proteins that deposit cellulose into the cell wall co-localise with microtubules (Paredez et al., 2006), and thus, the organisation of microtubules affects the organisation of the cell wall. In turn, the organisation of the cell wall affects how the cell behaves under pressure, and because plant cells are highly pressurised, with turgor pressure exerting outward forces on the cell wall, this is an important part of plant biology. Indeed, the mechanical properties of the cell determine its shape, and thus how development will proceed. Therefore, the activity of both katanin and spr2 is an important determinant of plant development; through the mediated severing of microtubules, these proteins can form different organisations, and consequently, control the physical properties of the cell.

In summary, the new method, MtFT, developed here, can quantify microtubule organisation in terms of alignment and orientation, and it has been used to address real biological problems, providing insight into mechanisms of microtubule alignment in animals and plants.

E. APPENDIX: MATERIALS AND METHODS

Cell culture, drug treatment and transfection

ARPE-19 human retinal pigment epithelial cells were maintained at 37° C in 5% CO_2, and passaged two times per week. Cells were cultured in DMEM/F12 containing 5mM Hepes and 2.5mM L-glutamine (Invitrogen), supplemented with 5% FBS.

Rac1 inhibition was carried out as described in the methodology section (appendix 1) of chapter 3. To inhibit formins, cells were treated with 10μM of the formin inhibitor SMIFH2 (Sigma) for 40 minutes. In control treatments, cells were treated with DMSO.

Cells were fixed, and subsequently immunolabelled as described in Bellet et al. (2009). Rabbit polyclonal antibodies against α-tubulin (ab15246, Abcam) were used to label microtubules. Secondary antibodies, conjugated to either AlexaFluor 488, 568, or 647 (Invitrogen) were used at a dilution of 1:1000.

Cells were treated with 27nM of siRNA (Qiagen), delivered by Oligofectamine (Invitrogen) as per manufacturers protocol twice, at 0 hours (the initial transfection) and 48 hours. For negative controls Allstar scramble siRNA sequence (Qiagen) was used. Human EB2 siRNA target sequences; EB2 siRNA (a) CAGCAGGTGCAGCTAAARCAA, EB2 siRNA (b) AACGCAGGTCATACAGCTTAA, EB2 siRNA (c) GACCTTATTAATAGGAGCATA, EB2 siRNA (d) CTCGATAACCCAAGAGACTAT. Any one of these four sequences were used, as all resulted in complete knockdown of EB2 at 96 hours post-initial transfection.

Microscopy

After fixation and immunolabelled, cells were imaged on a widefield Zeiss Axiovert 200M microscope.

Plant experiments

All wet lab work pertaining to the plant experiments was carried out in the Turner laboratory (University of Manchester), and methods can be found in Wightman et al. (2013).

REFERENCES

Allard, J.F., G.O. Wasteneys, and E.N. Cytrynbaum. 2010. Mechanisms of self-organization of cortical microtubules in plants revealed by computational simulations. *Molecular biology of the cell*. 21:278-286.

Auada, M.P., R.L. Adam, N.J. Leite, M.B. Puzzi, M.L. Cintra, W.B. Rizzo, and K. Metze. 2006. Texture analysis of the epidermis based on fast Fourier transformation in Sjogren-Larsson syndrome. *Analytical and quantitative cytology and histology / the International Academy of Cytology [and] American Society of Cytology*. 28:219-227.

Ayres, C.E., B.S. Jha, H. Meredith, J.R. Bowman, G.L. Bowlin, S.C. Henderson, and D.G. Simpson. 2008. Measuring fiber alignment in electrospun scaffolds: a user's guide to the 2D fast Fourier transform approach. *Journal of biomaterials science. Polymer edition*. 19:603-621.

Bartolini, F., and G.G. Gundersen. 2010. Formins and microtubules. *Biochimica et biophysica acta*. 1803:164-173.

Baulin, V.A., C.M. Marques, and F. Thalmann. 2007. Collision induced spatial organization of microtubules. *Biophysical chemistry*. 128:231-244.

Bayan, C., J.M. Levitt, E. Miller, D. Kaplan, and I. Georgakoudi. 2009. Fully automated, quantitative, noninvasive assessment of collagen fiber content and organization in thick collagen gels. *Journal of applied physics*. 105:102042.

Boudaoud, A., A. Burian, D. Borowska-Wykręt, M. Uyttewaal, R. Wrzalik, D. Kwiatkowska, and O. Hamant. 2014. FibrilTool, an ImageJ plug-in to quantify fibrillar structures in raw microscopy images. *Nat. Protocols*. 9:457-463.

Brunner, D., and P. Nurse. 2000. CLIP170-like tip1p spatially organizes microtubular dynamics in fission yeast. *Cell*. 102:695-704.

Goldspink, D.A., J.R. Gadsby, G. Bellett, J. Keynton, B.J. Tyrrell, E.K. Lund, P.P. Powell, P. Thomas, and M.M. Mogensen. 2013. The microtubule end-binding protein EB2 is a central regulator of microtubule reorganisation in apico-basal epithelial differentiation. *Journal of cell science*. 126:4000-4014.

Gonzalez, R.C., and R.E. Woods. 2006. Digital Image Processing (3rd Edition). Prentice-Hall, Inc.

Khuc Trong, P., J. Guck, and R.E. Goldstein. 2012. Coupling of active motion and advection shapes intracellular cargo transport. *Physical review letters*. 109:028104.

Lichtenstein, N., B. Geiger, and Z. Kam. 2003. Quantitative analysis of cytoskeletal organization by digital fluorescent microscopy. *Cytometry. Part A : the journal of the International Society for Analytical Cytology*. 54:8-18.

Lindeboom, J.J., M. Nakamura, A. Hibbel, K. Shundyak, R. Gutierrez, T. Ketelaar, A.M. Emons, B.M. Mulder, V. Kirik, and D.W. Ehrhardt. 2013. A mechanism for reorientation of cortical microtubule arrays driven by microtubule severing. *Science (New York, N.Y.)*. 342:1245533.

López, M.P., F. Huber, I. Grigoriev, M.O. Steinmetz, A. Akhmanova, G.H. Koenderink, and M. Dogterom. 2014. Actin–microtubule coordination at growing microtubule ends. *Nat Commun*. 5.

Mardia, K.V., and P.E. Jupp. 1999. Directional Statistics. Wiley, West Sussex, England.

Marquez, J.P. 2006. Fourier analysis and automated measurement of cell and fiber angular orientation distributions. *International Journal of Solids and Structures*. 43:6413-6423.

Paredez, A.R., C.R. Somerville, and D.W. Ehrhardt. 2006. Visualization of cellulose synthase demonstrates functional association with microtubules. *Science (New York, N.Y.)*. 312:1491-1495.

Parton, R.M., R.S. Hamilton, G. Ball, L. Yang, C.F. Cullen, W. Lu, H. Ohkura, and I. Davis. 2011. A PAR-1-dependent orientation gradient of dynamic microtubules directs posterior cargo transport in the Drosophila oocyte. *The Journal of cell biology*. 194:121-135.

Picone, R., X. Ren, K.D. Ivanovitch, J.D. Clarke, R.A. McKendry, and B. Baum. 2010. A polarised population of dynamic microtubules mediates homeostatic length control in animal cells. *PLoS biology*. 8:e1000542.

Rizvi, S.A., E.M. Neidt, J. Cui, Z. Feiger, C.T. Skau, M.L. Gardel, S.A. Kozmin, and D.R. Kovar. 2009. Identification and characterization of a small molecule inhibitor of formin-mediated actin assembly. *Chemistry & biology*. 16:1158-1168.

Sander, E.A., and V.H. Barocas. 2009. Comparison of 2D fiber network orientation measurement methods. *Journal of biomedical materials research. Part A*. 88:322-331.

Sbalzarini, I.F., and P. Koumoutsakos. 2005. Feature point tracking and trajectory analysis for video imaging in cell biology. *Journal of structural biology*. 151:182-195.

Schriefl, A.J., H. Wolinski, P. Regitnig, S.D. Kohlwein, and G.A. Holzapfel. 2013. An automated approach for three-dimensional quantification of fibrillar structures in optically cleared soft biological tissues. *Journal of the Royal Society, Interface / the Royal Society*. 10:20120760.

Thery, M., V. Racine, M. Piel, A. Pepin, A. Dimitrov, Y. Chen, J.B. Sibarita, and M. Bornens. 2006. Anisotropy of cell adhesive microenvironment governs cell internal organization and orientation of polarity. *Proceedings of the National Academy of Sciences of the United States of America*. 103:19771-19776.

Uyttewaal, M., A. Burian, K. Alim, B. Landrein, D. Borowska-Wykret, A. Dedieu, A. Peaucelle, M. Ludynia, J. Traas, A. Boudaoud, D. Kwiatkowska, and O. Hamant. 2012. Mechanical stress acts via katanin to amplify differences in growth rate between adjacent cells in Arabidopsis. *Cell*. 149:439-451.

Wallar, B.J., and A.S. Alberts. 2003. The formins: active scaffolds that remodel the cytoskeleton. *Trends in cell biology*. 13:435-446.

Wasteneys, G.O., and J.C. Ambrose. 2009. Spatial organization of plant cortical microtubules: close encounters of the 2D kind. *Trends in cell biology*. 19:62-71.

Wasteneys, G.O., and M.E. Galway. 2003. Remodeling the cytoskeleton for growth and form: an overview with some new views. *Annual review of plant biology*. 54:691-722.

Wightman, R., G. Chomicki, M. Kumar, P. Carr, and S.R. Turner. 2013. SPIRAL2 determines plant microtubule organization by modulating microtubule severing. *Current biology : CB*. 23:1902-1907.

Chapter 7

Summary discussion and conclusions

A. SUMMARY OF THESIS

I. Overview of work

In this thesis, the mechanisms governing the organisation of the microtubule cytoskeleton, and means of quantifying it, were addressed. This work centred on one of the most common microtubule network organisations, the radial array, for which the dynamics of microtubule within it were measured, the contribution of a proposed two-area dynamics model to the radial array was assessed, and various associated processes contributing to the alignment of the microtubules within the network were examined.

The work has been interdisciplinary, involving biological experiments, image processing and computational modelling. These various approaches have been united in their application for understanding how the organisation of the microtubule network is determined.

The microtubule network within the cell is immensely complex; even our understanding of the basic mechanisms of microtubule dynamic instability is being updated by new work. Add to this the modulation by the vast number of MAPs, PTMs, motor proteins, and other components of the cell, including other cytoskeletal systems and signalling cascades, and we see that a full understanding of how the microtubule network is organised is quite incomplete. However, in this work, genuine progress has been made towards understanding common principles of how dynamics can be modulated to produce a radial array, and this allowed an assessment of how the dynamics in chapter 3 could explain the differences in organisation between unperturbed and Rac1-inhibited cells.

Additionally, the image processing developed in chapter 6, "MtFT", has been comprehensively characterised and benchmarked, which has allowed deployment of this frequency-based method that has been used in various settings but not for the microtubule cytoskeleton, and never standardised for this purpose, to quantify orientation and alignment in the microtubule network. Thus, the extensive work to understand how the frequency-based measurements behave with synthetic data has allowed use of MtFT to answer legitimate biological questions. There, the effects of the lesser-studied EB protein, EB2, Rac1 and formins on microtubule alignment, were assessed. Furthermore, its application to a plant cell biology problem demonstrates its generality, and also permitted quantitative comparison of cortical microtubule array organisation, so important in plant development, in various mutant lines.

Overall, we know more now about the organisation of the mechanisms of microtubule network organisation than we did at the beginning of this thesis; modulation of dynamics at the cell periphery can be a major factor in microtubule radiality, and microtubule alignment within the cell is affected by various associated proteins.

II. Putting the work into context

a. Main findings

In relation to the topics discussed at the beginning of this thesis in chapter 2, perhaps the most pertinent findings of the subsequent work are the general mechanisms identified as being important for microtubule radiality, and potential role for microtubule-actin interactions in the alignment of microtubules within the array.

b. Mechanisms of radiality

Firstly, the thorough examination of the dynamics regimes required in order to target microtubules accurately to a certain length, and thus a target area, with a model has allowed explicit statement of the modulation of dynamics that is needed for radiality. As was discussed in chapter 4, it is often assumed that microtubule dynamics are altered in some way at the periphery of the cell so as to assist in cortical capture of microtubules, but cases in which this notion has been explicitly tested are few. The introduction of the simple, 1-dimensional model allowed proper exploration of cortical targeting mechanisms, finding that dynamics that produce strong negative drift in an outer area, combined with dynamics that give rise to strong positive drift in the inner area produce most accurate cortical targeting, and in the model, pausing helped to increase accuracy when in the outer area, but was detrimental to accurate targeting when in the inner area. This provides a framework for future studies of microtubule dynamics and the role of modulators of dynamics in generation and maintenance of radiality in the radial array.

After the general mechanisms of good cortical targeting were elucidated in chapter 4, chapter 5 showed that the measured dynamics from chapter 3 were in some ways similar to previously reported dynamics from the literature, and in some cases, different. The experimental methodology probably played a part in some of the differences there. The experimental dynamics were modelled so as to assess their contribution to radiality, and to establish whether the differences in dynamics could explain the differences in organisation between unperturbed and Rac1-inhibited cells within this cortical modulation of dynamics framework. The majority of the measured dynamics were found to be in a quadrant of drift space that can give intermediate levels of accuracy, and the modelling verified that accuracy is lower for dynamics sets that were similar to the measured dynamics when compared to dynamics regimes that were in optimal locations of drift space. The fact that other processes contribute to microtubule radiality, for example cortical capture and subsequent stabilisation of microtubules, was posited as an explaining factor for the lower-than-optimal measured dynamics sets.

c. Mechanisms of microtubule alignment

Development of MtFT allowed quantification of microtubule organisation in cells depleted of EB2, finding that, in agreement with a previous quantification of microtubule alignment in these cells, microtubules were better-aligned when EB2 was depleted relative to scramble siRNA-treated cells. A new finding in chapter 6 was that Rac1-inhibited cells had significantly less-aligned microtubules, but when Rac1 was inhibited in conjunction with depletion of EB2, microtubules were actually better-aligned than in scramble siRNA cells. Again in agreement

with previous results, microtubule alignment quantified by MtFT was decreased back to normal levels, similar to scramble siRNA-treated microtubules when formins were inhibited in EB2-depleted cells.

Therefore, the previous results verified by MtFT, and the new results pertaining to Rac1 inhibition, and the fact that previously, EB1 was shown to redistribute along microtubules when EB2 was depleted and microtubules were co-aligned with actin filaments (Goldspink et al., 2013), suggests that microtubule-actin interactions are operating *in vivo* to control microtubule alignment. The potential mechanisms of this interaction were expanded upon in chapter 6, and indeed, these findings are consistent with the *in vitro* characterisation of microtubule-actin interactions. Since expression levels of EB2 are associated with changes in microtubule organisation during cell differentiation *in situ* (Goldspink et al., 2013), this suggests and exciting interplay between these two cytoskeletal systems, whereby they influence one another's organisation as cells undergo their differentiation programme.

B. FUTURE WORK

There are a number of ways in which the work in this thesis could be extended, and as such, they form part of a series of experiments, modelling and image processing studies that will contribute to our understanding of the organisation of the microtubule array. Future work has been proposed in the individual discussions in each of the research chapters, and below is a short summary of these proposals.

Perhaps the most obvious of these extensions is further measurements of microtubule dynamics in the radial array. Although the methods used, based on analysis of data obtained with the software plusTipTracker, are of course valid, there are a number of ways in which those measurements could be complemented. For example, the dynamics could be further characterised by obtaining values for the transition frequencies between the shrinking and pausing phases. The transitions were not observable with plusTipTracker, and instead, results were compared with the literature to obtain estimates of their value. In order to characterise these transitions, labelling of tubulin with a fluorescent protein would allow observation of the pausing and shrinking phases.

Aside from this, another avenue of future research is extensions to the modelling in chapters 4 and 5. Here, a model of cortical capture as a function of plus end residence time within a target area, i.e. near the cortex, would allow testing of the hypothesis that modulation of dynamics at the cell periphery contribute to radiality by making microtubule plus ends available more often to capture by cortical protein complexes. Another extension to the model that would go hand-in-hand with the first extension is to model a cell boundary, whereby microtubules can no longer grow beyond the outer area, and implement microtubule bending. The bending parameters determined in chapter 3 could then be used in such a model.

The image processing in chapter 6 can also be taken further. In terms of characterisation of the method, it was already discussed that some image properties could be addressed, such as blurring and noise. Furthermore, potential uneven illumination, and variations in intensity between images could be investigated further.

In terms of the utility of MtFT, it was discussed that it could be modified so that areas with no information, whether because there is not a cell within it or there is low anisotropy, are automatically recognised and subsequently discarded. Such a method would speed up analyses, and this might allow the pixel-by-pixel approach that was discussed in chapter 6. Building on this, a means of automatically "joining up" areas with similar anisotropy or orientations could be implemented, allowing the study of discrete areas of alignment and orientation. Finally, another extension discussed was to use the method to analyse scales of alignment.

C. CONCLUSION

The microtubule cytoskeleton is a fascinating example of persistent organisation emerging from the chaotic nature of the cell interior. Here, in the context of millions of molecules being bombarded by thermal forces, colliding and interacting with one another, tubulin subunits associate and dissociate, coupled with changes in their biochemistry, giving rise to the microtubule phases that have been the focus of this thesis. These phases in turn, though the transitions between them are essentially stochastic, are regulated by the cell in a multitude of ways so that the microtubule network organisation that we see when looking down a microscope appears remarkably static, yet ready to respond to any relevant cue to re-organise. The image processing and modelling in this thesis have helped to better understand certain instances of this regulation, and thus contribute to our understanding of dynamics-organisation relationships in the microtubule cytoskeleton. Hopefully, the future work summarised above will continue to further our understanding of this complex and beautiful biology.

REFERENCES

Goldspink, D.A., J.R. Gadsby, G. Bellett, J. Keynton, B.J. Tyrrell, E.K. Lund, P.P. Powell, P. Thomas, and M.M. Mogensen. 2013. The microtubule end-binding protein EB2 is a central regulator of microtubule reorganisation in apico-basal epithelial differentiation. *Journal of cell science*. 126:4000-4014.